

---

# **Radiatively-driven processes in forest fire and desert dust plumes**

**Bernadett Barbara Weinzierl**

---



München 2007



---

# **Radiatively-driven processes in forest fire and desert dust plumes**

**Bernadett Barbara Weinzierl**

---

Dissertation  
an der Fakultät für Physik  
der Ludwig-Maximilians-Universität  
München

vorgelegt von  
Bernadett Barbara Weinzierl  
aus Rosenheim

München, 9. November 2007

Erstgutachter: Priv. Doz. Dr. Andreas Petzold  
Zweitgutachter: Prof. Dr. Olaf Krüger  
Tag der mündlichen Prüfung: 10. Januar 2008

---

# Contents

---

ABSTRACT .....	III
ZUSAMMENFASSUNG.....	V
<b>1 INTRODUCTION .....</b>	<b>1</b>
1.1 The aerosol in the global climate system.....	1
1.2 Biomass burning and desert dust aerosol in the atmosphere.....	5
1.2.1 Biomass burning aerosol .....	5
1.2.2 Desert dust aerosol.....	7
1.2.3 Long-range transport of biomass burning and desert dust aerosol .....	10
1.3 Objectives of this thesis .....	11
1.4 Structure.....	14
1.5 Use of external data and software routines .....	14
<b>2 AEROSOL FUNDAMENTALS.....</b>	<b>17</b>
2.1 Aerosol in the atmosphere – sources, sinks and life cycle.....	17
2.2 Microphysical properties of aerosol particles .....	19
2.2.1 Aerosol size distribution.....	19
2.2.2 Aerosol mixing state.....	22
2.3 Optical properties of aerosol particles .....	23
2.3.1 Definition of key quantities .....	23
2.3.2 Scattering and absorption by particles.....	26
<b>3 METHODS .....</b>	<b>31</b>
3.1 Aerosol measurements aboard the Falcon research aircraft.....	31
3.1.1 The DLR research aircraft Falcon 20-E5.....	31
3.1.2 Condensation Particle Counter (CPC).....	32
3.1.3 Diffusion Screen separators (DS).....	35
3.1.4 Differential Mobility Analyser (DMA).....	37
3.1.5 Optical particle counters (OPC) .....	38
3.1.6 Particle Soot Absorption Photometer (PSAP) .....	42
3.1.7 Thermal Denuder (TD).....	44
3.1.8 The Falcon aerosol inlet .....	44
3.1.9 Data quality assurance .....	46
3.2 Field experiments.....	54

3.2.1	Measurement concept for airborne studies of aerosol properties .....	54
3.2.2	The ITOP study – Forest fire aerosol .....	56
3.2.3	The SAMUM study – Desert dust aerosol.....	62
3.2.4	Differences between ITOP and SAMUM.....	66
3.3	Data analysis .....	67
3.3.1	Volumetric units and aerosol modes.....	67
3.3.2	Time series of microphysical aerosol properties and data reduction.....	68
3.3.3	Size distribution data .....	68
3.3.4	Validation of the inversion algorithm.....	74
3.3.5	Volatility analyses – aerosol mixing state .....	75
3.3.6	Absorption data.....	77
3.3.7	Aerosol optical model.....	78
3.3.8	Heating rates.....	79
3.3.9	Combination of data .....	79
<b>4</b>	<b>PROPERTIES OF FOREST FIRE AND DESERT DUST PLUMES .....</b>	<b>83</b>
4.1	Forest fire aerosol (ITOP).....	83
4.1.1	Transport of forest fire plumes to Europe.....	83
4.1.2	Case study 22 July 2004 .....	84
4.1.3	Optical properties of the aged forest fire plume on 22 July 2004.....	88
4.1.4	Properties of other forest fire plumes during ITOP .....	91
4.2	Desert dust aerosol (SAMUM) .....	93
4.2.1	Properties of dust aerosol layers south of the Atlas Mountains.....	93
4.2.2	Desert dust layers at the boundary between source and long-range transport regime ...	105
4.2.3	Properties of aged dust layers .....	112
4.2.4	Optical properties of dust layers .....	114
<b>5</b>	<b>DISCUSSION AND CONCLUSIONS .....</b>	<b>119</b>
5.1	Hypothesis I – Self-stabilising effect.....	120
5.1.1	Heating rates.....	120
5.1.2	Static stability .....	126
5.1.3	Wave breaking and mixing.....	130
5.2	Hypothesis II – Sealed ageing effect.....	132
5.2.1	Nucleation and Aitken mode .....	132
5.2.2	Accumulation mode.....	135
<b>6</b>	<b>SUMMARY AND OUTLOOK .....</b>	<b>137</b>
6.1	Summary of results .....	137
6.2	Open scientific questions .....	141
	<b>ACKNOWLEDGEMENTS.....</b>	<b>145</b>
	<b>LIST OF ABBREVIATIONS .....</b>	<b>147</b>
	<b>LIST OF SYMBOLS.....</b>	<b>149</b>
	<b>REFERENCES.....</b>	<b>153</b>
	<b>INDEX .....</b>	<b>165</b>
	<b>LEBENS LAUF .....</b>	<b>167</b>

---

## Abstract

---

The absorption of solar radiation by atmospheric aerosol particles is important for the climate effects of aerosols. Absorption by aerosol particles heats atmospheric layers, even though the net effect for the entire atmospheric column may still be a cooling. Most experimental studies on absorbing aerosols so far focussed mainly on the aerosol properties and did not consider the influence of the aerosols on the thermodynamic structure of the atmosphere. In this study, data from two international aircraft field experiments, the Intercontinental Transport of Ozone and Precursors study (ITOP) 2004 and the Saharan Mineral Dust Experiment (SAMUM) 2006 are investigated. The ITOP data were collected before the work on this thesis started, while the logistics and the instrument preparation of the SAMUM campaign, the weather forecast during SAMUM and the in-situ aerosol measurements during SAMUM were done within this thesis. The experimental data are used to explore the impact of layers containing absorbing forest fire and desert dust aerosol particles on the atmospheric stability and the implications of a changed stability on the development of the aerosol microphysical and optical properties during long-range transport. For the first time, vertical profiles of the Richardson number  $Ri$  are used to assess the stability and mixing in forest fire and desert dust plumes. Also for the first time, the conclusions drawn from the observations of forest fire and desert dust aerosol, at first glance apparently quite different aerosol types, are discussed from a common perspective. Two mechanisms, the self-stabilising and the sealed ageing effect, acting in both forest fire and desert dust aerosol layers, are proposed to explain the characteristic temperature structure as well as the aerosol properties observed in lofted forest fire and desert dust plumes. The proposed effects impact on the ageing of particles within the plumes and reduce the plume dilution, therefore extending the plume lifetime.

This study combines experimental data, modelling of optical parameters and calculated heating rates to assess the role of forest fire and desert dust plumes. The microphysical, optical and chemical properties of forest fire and desert dust aerosol, and their vertical distribution, were measured with multiple instruments on the DLR Falcon 20-E5 research aircraft during ITOP and SAMUM. Aerosol size information and absorption data were analysed with respect to the aerosol mixing state, effective diameter and parameterisation of forest fire and dust size distributions. Altogether, about 90 size distributions for particles from different sources were extracted from multiple instruments and parameterised with multi-modal log-normal distributions. Subsequently, the optical properties were calculated for the different aerosol layers and compared with other independent measurements of the optical properties like the extinction coefficient determined with a High Spectral Resolution Lidar.

The aerosol optical properties serve as the basis for the radiative transfer calculations with libRadtran (library for radiative transfer). Finally, the aerosol microphysical and optical properties, the meteorological data and the heating rates are examined to investigate the proposed self-stabilising and sealed ageing effects.

The investigation of numerous forest fire and desert dust plumes in this study revealed characteristic aerosol properties: the aged (age: 4-13 days) forest fire aerosol is characterised by the absence of a nucleation mode, a depleted Aitken mode and an enhanced accumulation mode. In addition, more than 80% of the particles in the Aitken mode and nearly all particles in the accumulation mode of the forest fire plumes are internally mixed with a solid core. The desert dust aerosol exhibits two size regimes of different mixing states: below 0.5  $\mu\text{m}$ , particles have a non-volatile core and a volatile coating; larger particles above 0.5  $\mu\text{m}$  consist of non-volatile components and contain absorbing material. After regional-scale transport from the Sahara to South-western Europe, the volatile fraction in the dust plume did not significantly increase. The lofted forest fire plumes were found during ITOP at altitudes between 3 and 9 km above sea level (ASL), while the lofted desert dust plumes were found during SAMUM between 1 and 6 km ASL. The transition of the aerosol plumes to the free tropospheric background above and below the plumes was remarkably sharp and characterised by strong inversions. Within a height range of 200-300 m, the particle concentrations decreased by more than one order of magnitude. The results of plume dilution were evident only in the upper part of the lofted forest fire and desert dust plumes. The daily mean heating rates in the forest fire and desert dust plumes showed maximum values of  $\sim 0.2 \text{ K day}^{-1}$  and  $\sim 0.24 \text{ K day}^{-1}$ , respectively. Vertical profiles of the heating rate suggest that the processes caused by the interaction between the aerosol particles and the solar radiation stabilise the plume itself and decelerate plume dilution. Apparently, the aerosol in such plumes ages in an almost “closed” system, where suppressed entrainment of condensable gases from the surface inhibits particle nucleation and the formation of coated particles inside the plume. The processes described tend to extend the lifetime of the layer allowing the transport over long distances.

---

## Zusammenfassung

---

Die Absorption von solarer Strahlung durch Aerosolpartikel ist wichtig für die Klimaeffekte des atmosphärischen Aerosols. Als Nettoeffekt für die gesamte atmosphärische Säule mag zwar eine Abkühlung eintreten, doch können absorbierende Partikel ihrerseits wieder die sie umgebenden atmosphärischen Schichten erwärmen. Die meisten experimentellen Studien, die sich mit absorbierenden Aerosolpartikeln befassen, fokussieren auf die Untersuchung der mikrophysikalischen und optischen Aerosoleigenschaften, ohne auf die Interaktion zwischen den absorbierenden Partikeln und den thermodynamischen Eigenschaften der Atmosphäre einzugehen. Die vorliegende Studie verarbeitet Daten von zwei internationalen Messkampagnen, der „Intercontinental Transport of Ozone and Precursors“ (ITOP) Studie 2004 und des „Saharan Mineral Dust Experiment“ (SAMUM) 2006. Die ITOP Daten wurden vor Beginn dieser Arbeit gesammelt. Im Gegensatz dazu waren die Logistik, die Vorbereitung der Instrumente für das SAMUM Feldexperiment, sowie die Wettervorhersage und die in-situ Aerosolmessungen während SAMUM Teil dieser Arbeit. Mit den experimentellen Daten wird der Einfluss absorbierender Aerosolschichten auf die atmosphärische Stabilität und die Folgen einer veränderten atmosphärischen Stabilität auf die Alterung der Aerosolpartikel während des Ferntransports untersucht.

Diese Studie verwendet zum ersten Mal Vertikalprofile der Richardson Zahl  $Ri$  zur Untersuchung von Stabilität und Verdünnung von Waldbrand- und Wüstenstaubaerosolschichten. Sie diskutiert, ebenfalls zum ersten Mal, die Beobachtungen dieser zwei auf den ersten Blick ziemlich unterschiedlichen Aerosoltypen von einem gemeinsamen Blickpunkt aus. Es werden zwei Mechanismen, die Selbststabilisierung und die Aerosolalterung in einem nahezu „geschlossenen System“ als Erklärung für die beobachteten Aerosoleigenschaften in den Waldbrand- und Wüstenstaubschichten vorgeschlagen. Diese beiden Mechanismen reduzieren die Verdünnung der Schichten und beeinflussen die Alterung der Aerosolgrößenverteilung. Die Lebenszeit der Schichten wird erhöht; damit können die Schichten über größere Strecken transportiert werden und die Atmosphäre fern von der Partikelquelle beeinflussen. Bestimmt wurden die Aerosolgrößenverteilung, der Absorptionskoeffizient, der Aerosolmischungszustand und der effektive Durchmesser der Waldbrand- und Wüstenstaubaerosole. Insgesamt wurden etwa 90 Größenverteilungen für Aerosolpartikel von verschiedenen Quellen aus den Messdaten der einzelnen Instrumente berechnet und mit multi-modalen Log-Normalverteilungen parametrisiert. Anschließend wurden die optischen Eigenschaften der einzelnen Aerosolschichten mit einem Mie-Modell berechnet und die Ergebnisse mit unabhängigen Messungen, z.B. der direkten Messung des Extinktionskoeffizienten mit dem High Spectral Resolution Lidar (HSRL) verglichen. Die

optischen Eigenschaften der Partikel dienen als Eingangsparameter für die Strahlungstransferrechnungen mit libRadtran (library for radiative transfer). Letztendlich werden die mikrophysikalischen und optischen Aerosoleigenschaften, die meteorologischen Daten und die berechneten Erwärmungsraten kombiniert, um die vorgeschlagenen Selbststabilisierungs- und Alterungsprozesse zu diskutieren

Die Untersuchung von zahlreichen Waldbrand- und Wüstenstaubschichten in dieser Studie hat charakteristische Aerosoleigenschaften gezeigt: So kennzeichnen eine fehlende Nukleationsmode, eine abgereicherte Aitken Mode und eine verstärkte Akkumulationsmode gealterte Waldbrandschichten (Alter: 4-13 Tage). Darüber hinaus sind etwa 80% der Partikel in der Aitken Mode und nahezu alle Partikel in der Akkumulationsmode von Waldbrandaerosol intern gemischt und haben einen nicht-flüchtigen Kern. Auch die Wüstenstaubschichten weisen charakteristische Eigenschaften auf. Die Größenverteilung ist durch zwei Zonen gekennzeichnet: Unterhalb von  $0.5 \mu\text{m}$  haben die Partikel einen nicht-flüchtigen Kern und sind mit flüchtigem Material beschichtet; größere Partikel oberhalb von  $0.5 \mu\text{m}$  bestehen aus nicht-flüchtigem Material und enthalten absorbierende Materialien. Nach regional-skaligem Transport von der Sahara nach Südwest-Europa, zeigte sich der flüchtige Anteil der Partikel in der Wüstenstaubschicht nicht signifikant erhöht. Die abgehobenen Waldbrandschichten fanden sich in Höhen zwischen 3 und 9 km über NN, wohingegen die Wüstenstaubschichten vor allem zwischen 1 und 6 km Höhe auftraten. Der Übergang von den Aerosolschichten zum Hintergrundaerosol unterhalb und oberhalb der Schichten zeigte sich als deutlich ausgeprägt. Außerdem waren die Aerosolschichten durch starke Temperaturinversionen am Unter- und Oberrand gekennzeichnet. Innerhalb von etwa 200-300 m ging die Partikelkonzentration um mehr als eine Größenordnung zurück. Das Ergebnis von Verdünnung war nur im oberen Teil der abgehobenen Schichten sichtbar. Die über den Tag gemittelten Erwärmungsraten wiesen Werte von  $\sim 0.2 \text{ K Tag}^{-1}$  bzw.  $\sim 0.24 \text{ K Tag}^{-1}$  in den Waldbrand- bzw. Wüstenstaubschichten auf. Der Verlauf der Vertikalprofile der Erwärmungsrate legt nahe, dass durch die Interaktion der absorbierenden Partikel mit der solaren Strahlung die Prozesse angeregt werden, die die Schichten stabilisieren und die Verdünnung der Schichten verlangsamen. Offensichtlich altert das Aerosol in einem „geschlossenen System“, in dem das unterdrückte Einmischen von kondensierbaren Gasen die Partikelneubildung und die Bildung von beschichteten Partikeln verhindert. Die beschriebenen Prozesse tendieren dazu, die Lebenszeit der Schicht zu verlängern, was wiederum den Transport über weite Strecken erlaubt und ihre Klimawirksamkeit erhöht.

---

# 1 Introduction

---

## 1.1 The aerosol in the global climate system

Within the last century, global surface temperatures increased by  $0.76 \pm 0.19$  K (*IPCC*, 2007). Eleven of the twelve warmest years since beginning of the instrumental record of global surface temperature in 1850 occurred between 1995-2006 (e.g. *IPCC*, 2007). Rising surface temperatures can be ascribed to changes in the Earth's energy balance. The flux of incoming radiation from the sun must be approximately balanced by the outgoing flux of infrared and shortwave radiation. Any deviation from this balance drives the climate of the earth to a new warmer or cooler equilibrium state where the energy balance is satisfied again.

Whereas greenhouse gases reduce the outgoing thermal radiation to the space, causing a warming of the surface, aerosol particles like black carbon, sulphate or mineral dust particles influence both sides of the radiation balance causing either a warming or a cooling. In general, aerosol particles impact on the climate in two ways: *directly* through scattering and absorption of radiation and *indirectly* through their role as cloud condensation nuclei. There is a variety of indirect effects: clouds forming in a polluted environment contain a larger droplet number concentration of smaller drops for a fixed water content (*Twomey*, 1974) than clouds forming in pristine environments. The increased droplet number concentration increases the reflection of solar radiation back into the space, and therefore leads to a climate cooling. This effect is named the *first indirect effect*. Keeping the condensed moisture in the cloud constant, but enlarging the aerosol concentration, results in a decreasing droplet radius. The precipitation efficiency of these clouds decreases, while the cloud lifetime (*Albrecht*, 1989) and the cloud thickness (*Pincus and Baker*, 1994) increase. In turn, the amount of clouds increases. This effect is known as the *second indirect effect*. *Ramanathan et al.* (2001) suggest that as a consequence of the reduction in surface solar radiation, together with the precipitation suppression, the hydrological cycle reduces in strength. Another effect is the absorption of shortwave radiation by particles, which causes a heating of the troposphere that alters the relative humidity and the stability of the troposphere, and influences cloud formation processes and cloud lifetime. This mechanism is called the *semi-direct effect* (e.g. *Hansen et al.*, 1997; *Ackerman et al.*, 2000).

In this study, biomass burning<sup>1</sup> and desert dust aerosols are investigated on the basis of experimental data. The global importance of aerosols, especially of biomass burning and desert dust aerosols can be illustrated by means of aerosol optical depth (*AOD*). The *AOD* is a measure that indicates the amount of incoming solar radiation inhibited to reach the Earth's surface due to the presence of aerosols. Figure 1 shows the mean annual *AOD* at  $\lambda = 550$  nm for the year 2006 based on daily MODIS measurements. For the grey shaded areas no *AOD* could be derived, white areas have small *AOD*, whereas dark orange areas exhibit high *AOD*. Several areas of very high annual *AOD* and therefore high aerosol concentrations are striking: the region over central and western Africa (a mixture of Saharan dust and biomass burning aerosol), northern India and north-eastern China (anthropogenic pollution), Indonesia (biomass burning aerosol) and Russia (biomass burning). Absorbing constituents are not present in all aerosol types, but in biomass burning and desert dust aerosols, and in anthropogenic pollution aerosols originating from fossil fuel burning. All regions with high *AOD* in Figure 1 contain absorbing particles, and the presence of either biomass burning or mineral dust particles can explain the high mean annual *AOD* in three out of the five most burdened regions. Due to the widespread occurrence of mineral dust and biomass burning aerosols and their large optical depth, the effects of both aerosol types on the radiation budget are important relative to those of other aerosols. The high aerosol concentrations over the Atlantic Ocean in Figure 1 demonstrate that the influence of aerosols is not only confined to areas close to the source. In fact, aerosol layers are transported over long distances and can affect air quality far downwind of the source. Long-range transport is one of the most important factors controlling the spatial and temporal variability of aerosols and atmospheric load. Especially biomass burning and desert dust plumes are transported over long distances, even between continents. The long residence time of biomass burning and desert dust aerosol layers in the atmosphere, makes them an even more important player in the global climate system.

In general, the direct and indirect interaction of various aerosol species with the global climate is assessed by means of *radiative forcing*  $\Delta F$ . The radiative forcing is a measure in  $\text{W m}^{-2}$  of the change in the Earth-atmosphere's radiation budget when some parameter is changed, such as for example the concentration of aerosols or the concentration of atmospheric greenhouse gases like carbon dioxide ( $\text{CO}_2$ ), methane ( $\text{CH}_4$ ) or nitrous oxide ( $\text{N}_2\text{O}$ ) (*Shine*, 2000). The radiative forcing is usually defined at the top of the atmosphere (TOA) (*IPCC*, 2001). Key parameters for the assessment of the direct effect are aerosol optical properties like single-scattering albedo  $\omega_0$ , specific extinction coefficient  $\sigma_{ep}$  and the scattering phase function  $P_s$ , which vary as a function of the wavelength and the relative humidity, and the atmospheric loading and horizontal and vertical distribution of the aerosols, which vary as a function of time (*IPCC*, 2007). The key parameter for the determination of the indirect effects is the ability of particles to act as cloud condensation nuclei (*IPCC*, 2007). The chemical composition of an aerosol particle is crucial to the ability of a particle acting as a cloud condensation nuclei (*Rosenfeld*, 2006), but the size distribution, a property easier to measure than chemical composition of such aerosols, can explain most of the variability in their ability to nucleate cloud droplets (*Dusek et al.*, 2006). The result stated by *Dusek et al.*

---

<sup>1</sup> Biomass burning refers to the burning of living and dead vegetation (boreal/tropical forests, savannas, agricultural land), including human-induced burning of vegetation for land clearing and land use purposes. In this thesis the term "forest fire" refers to fires in boreal forests.

(2006) reduces the relative role of the chemical composition of the particles compared to the size of the particles and makes it easier to treat aerosol effects on cloud physics and climate.

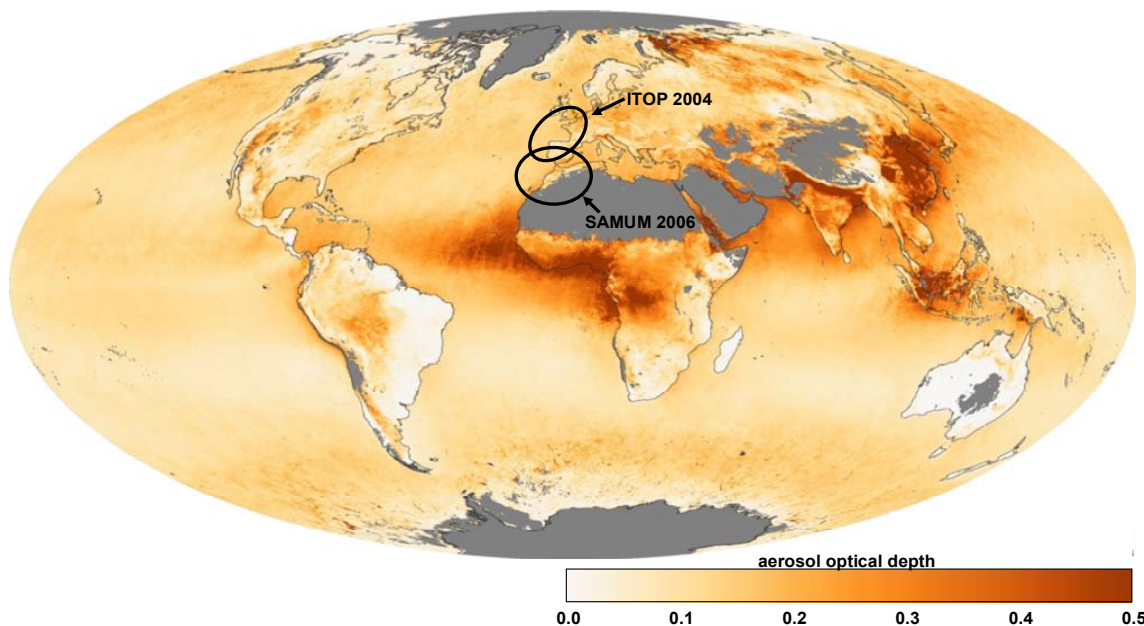


**Figure 1.** Mean annual aerosol optical depth at  $\lambda = 550 \text{ nm}$  for the year 2006 calculated from daily MODIS retrievals. The black circles mark the domain in which the ITOP and the SAMUM data were taken (adopted from [http://earthobservatory.nasa.gov/Newsroom/NewImages/images.php3?img\\_id=17575](http://earthobservatory.nasa.gov/Newsroom/NewImages/images.php3?img_id=17575)).

The total direct radiative forcing of all aerosol types is estimated to be  $-0.5 \pm 0.4 \text{ W m}^{-2}$ , and the scientific understanding is rated to be medium to low (IPCC, 2007). However, the direct radiative forcing of individual aerosol species is less certain, for example the forcing of biomass burning aerosol is estimated to be  $+0.03 \pm 0.12 \text{ W m}^{-2}$ , and for the mineral dust a forcing of  $-0.1 \pm 0.2 \text{ W m}^{-2}$  is given in the last IPCC report (2007). The estimated forcing for biomass burning aerosols does not include the semi-direct effect or the black carbon (BC) impact on snow and ice surface albedo. Moreover, the forcing of biomass burning aerosol is significantly more positive, when it overlies clouds (IPCC, 2007). The sign and the magnitude of the radiative forcing of aerosols depends crucially on the vertical distribution of the aerosols, and the presence of clouds underneath the aerosol layers (IPCC, 2007); it depends further on the chemical composition of the particles, the insolation, the amount of clouds and the underlying surface reflectance. All aerosol types lead to a reduced solar radiation at the surface, whereas at the TOA the forcing effect of BC opposes the cooling effect of non-absorbing sulphates. Satheesh and Ramanathan (2000) point out that the aerosol induced changes in the solar radiation flux at the surface far exceed the changes at the TOA. Hansen *et al.* (1997) showed that the climate response to an imposed forcing varied with altitude by a factor of about two. Since satellite sensors provide only column integrated aerosol optical properties like AOD, and lidar instruments do not deliver in-situ data on aerosol microphysical properties like particle size distribution, it is essential to conduct aircraft-based measurements to gather in-situ data on the vertical distribution of aerosol properties.

In the estimates of aerosol radiative forcing a large source of uncertainty is associated with aerosol absorption (IPCC, 2007). Sato *et al.* (2003) inferred absorption from AERONET

measurements and found an underestimate of aerosol absorption in global aerosol models by a factor of two to four. The absorption of radiation by aerosol particles is important for both the direct and semi-direct aerosol effects. The magnitude of the absorption and its contribution to global warming is subject to considerable uncertainty (e.g. *Hansen et al.*, 2002; *Stier et al.*, 2006; *Kinne et al.*, 2006; *Stier et al.*, 2007). Most studies address the aerosol forcing at the TOA (*IPCC*, 2001). However, absorbing aerosols are one of the climate forcing mechanisms for which radiative forcing is not always indicative of the climate response (*Hansen et al.*, 2005), since absorption by aerosols heats atmospheric layers, even though the net effect for the entire atmospheric column may still be cooling (*Pilewskie*, 2007). For example, in a modelling study by *Perlwitz et al.* (2001), desert dust layers have been found to cool the surface, while the dust layer itself was heated. A heating in the middle of the atmosphere changes the atmospheric lapse rate and can influence atmospheric dynamics. Atmospheric solar heating is a major source of uncertainty in the aerosol forcing effect as current estimates are mostly derived from model studies (*Ramanathan et al.*, 2007). *Ramanathan et al.* (2007) investigated atmospheric brown clouds, which are mainly the result of biomass burning and fossil fuel combustion, at altitudes between 0.5 and 3 km over the Indian Ocean. They found that the brown clouds enhance solar atmospheric heating by about 50%. They suggested that atmospheric brown clouds contribute about equally to the regional lower atmospheric warming trends as the recent increase in anthropogenic greenhouse gases do. The findings of *Ramanathan et al.* (2007) emphasize the importance of determining how aerosol forcing varies with altitude (*Pilewskie*, 2007). In most general circulation models, the effect of absorbing aerosols upon the atmospheric heating rates is not included in the dynamical evolution of the atmosphere, although recent modelling studies (*Perlwitz et al.*, 2001; *Wang and Christopher*, 2006; *Tegen et al.*, 2006; *Pérez et al.*, 2006; *Heinold et al.*, 2007; *Helmert et al.*, 2007; *Yin and Chen*, 2007) reveal an important aerosol feedback on atmospheric dynamics.

The impact of absorbing aerosol layers on the climate is poorly understood. Since aerosol properties show large regional variations, the regional impact of aerosols can be quite different, which is the main reason why the importance of aerosols is poorly characterised in climate models (*Satheesh and Moorthy*, 2005). To accurately assess the impacts of absorbing aerosols on the global climate, vertically resolved measurements of aerosol properties are required. The climate impact of aerosols can be significantly different, when a cloud layer is present above or below the aerosol layer, even when the aerosol column properties are the same (e.g. *Satheesh and Moorthy*, 2005). The reduction of aerosol properties to aerosol column properties does not sufficiently cover the real impacts of particles on the climate. Therefore, airborne measurements of microphysical and optical aerosol properties are crucial. In this study, we investigate biomass burning and desert dust aerosols, both of which are natural aerosols with a significant anthropogenic contribution (*IPCC*, 2007), on the basis of experimental data. The data were gathered during two international field experiments, the Intercontinental Transport of Ozone and Precursors (ITOP) study and the Saharan Mineral Dust Experiment (SAMUM), which were conducted in summer 2004 and late spring 2006, respectively. The circles in Figure 1 mark the domain in which the airborne measurements were conducted. The data collected during ITOP (mainly forest fire aerosol) and SAMUM (mainly desert dust aerosol) deliver in-situ data on the vertical distribution of aerosol properties like particle size distribution, and add new aspects to our understanding of the effects of absorbing aerosol plumes on atmospheric stability and on the development of

aerosol microphysical and optical properties within the lofted<sup>2</sup> plumes. The current knowledge on biomass burning and desert dust aerosol is summarised in the following sections.

## 1.2 Biomass burning and desert dust aerosol in the atmosphere

### 1.2.1 Biomass burning aerosol

Once believed to be a phenomenon of the tropics only, *biomass burning* has been proven by satellite observations to be a regular feature of boreal forests also (Levine, 1991). Every year, large areas of boreal forests are destroyed by fires in Canada and Alaska (Figure 2), and also in Russia and Siberia.

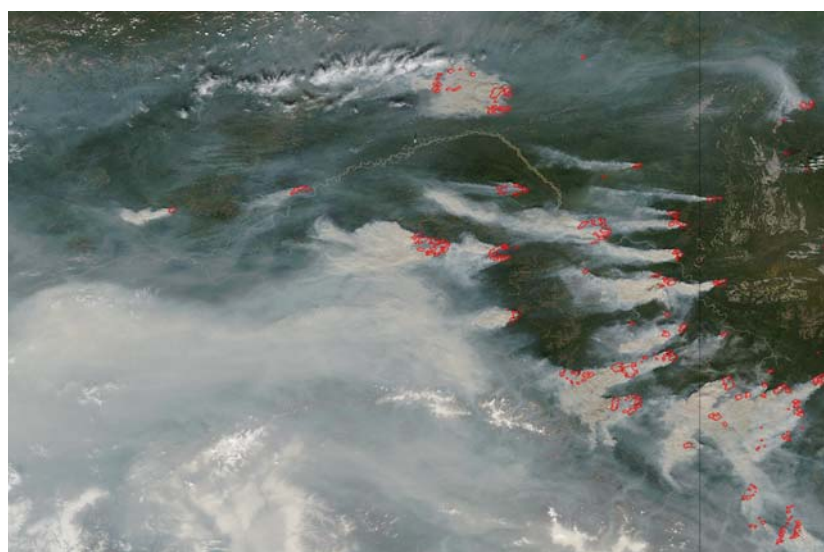


**Figure 2.** Large wildfires over Alaska and Canada captured by the Moderate Resolution Imaging Spectroradiometer (MODIS) flying on NASA's Terra satellite on 29 June 2004. Areas where MODIS detected actively burning fires are outlined in red (adopted from [http://earthobservatory.nasa.gov/NaturalHazards/natural\\_hazards\\_v2.php3?img\\_id=12209](http://earthobservatory.nasa.gov/NaturalHazards/natural_hazards_v2.php3?img_id=12209)).

Biomass burning and fossil fuel burning are contributing about equally to the global emission of BC (IPCC, 2001). Worldwide, biomass burning is one of the largest sources of accumulation mode particles ( $D_p < 1 \mu\text{m}$ ) (Reid *et al.*, 2005a). On average, smoke particles contain ~50-60% organic carbon (OC) and ~5-10% BC (Reid *et al.*, 2005a). BC is the most efficient particulate absorber of atmospheric solar radiation (Bond and Bergstrom, 2006) and therefore has a strong impact on the atmospheric radiation budget. Aerosol layers containing BC can contribute to a large atmospheric solar absorption (Grassl, 1975) leading to a reduction of the solar radiation that reaches the surface (negative forcing). Very recently, the existence of light absorbing carbon that is not black (“brown carbon”) has been discovered (e.g. Andreae and Gelencsér, 2006). Brown carbon may be “invisible” in the red and near-

<sup>2</sup> In this study, the term “lofted (aerosol) layer/lofted plume” refers to atmospheric layers containing aerosol laden air. The lofted layers extend from an altitude  $z_2$  to an altitude  $z_3$  and are situated above the boundary layer (see Figure 5b, p. 12).

infrared part of the light spectrum, and may bias the measurements of atmospheric light absorption (*Andreae and Gelencsér, 2006*). *Andreae and Gelencsér (2006)* point out that the biases they describe could question even the sign of the direct radiative forcing of carbonaceous aerosols. In addition to direct radiative effects, smoke particles have indirect effects, for example, they may act as condensation nuclei for the formation of cloud droplets, delay the onset of precipitation, and suppress low-level aerosol washout (*Andreae et al., 2004*). BC in dark (solar-absorbing) hazes is found to reduce tropical cloudiness and to stabilise the structure of the boundary layer (*Ackerman et al., 2000*).

In the course of the nuclear winter research, several studies on the effect of forest fire smoke to surface temperatures were conducted (*Robock, 1988;1991; Westphal and Toon, 1991*). The smoke was found to produce a daytime cooling of several degrees, but had no night-time effects. *Robock (1988)* reports a case, where smoke from fires was trapped in a valley by an inversion for three weeks. With the plume preventing surface warming by solar radiation, daily maximum surface temperatures steadily decreased, while the inversion strengthened. *Robock (1988)* proposed a positive feedback loop: the increased atmospheric stability in the boundary layer caused by the radiative properties of the smoke aerosol traps more smoke and enhances the radiative effects of the smoke aerosol. Very recent simulations with a coupled aerosol, radiation and meteorology model (*Wang and Christopher, 2006*) verify the proposed smoke self-trapping mechanism. *Wang and Christopher (2006)* point out that such a feedback together with favourable weather conditions may have crucial consequences for air quality and hydrological processes. *Radke et al. (1990)* focussed on the radiatively-driven self-lofting of fresh (several hours) smoke plumes from burning of aviation fuel: the smoke plumes were seen to rise rapidly from the ground to the temperature inversion on top of the boundary layer. After an initial stabilisation at the temperature inversion the solar radiation warmed the smoke plume and the temperature in the plume started to exceed ambient values. Two to three hours later the smoke had risen about 800 m. Similar observations were made by *Herring and Hobbs (1994)* in plumes of the Kuwait oil fires: the radiative heating (net daytime heating rates between 56-94 K day<sup>-1</sup>) lofted the plumes at a rate of 0.1 m s<sup>-1</sup>. All above-mentioned processes refer to fresh smoke (several hours) and plumes in the vicinity of fires.

Qualitatively, the properties of smoke particles are well understood, but the impact of smoke plumes on the meteorology of a region is highly uncertain (*Reid et al., 2005a; Reid et al., 2005b*). The possibility of an interaction between absorbing aerosols from severe forest fires and the large-scale meteorological situation was pointed out by *Pace et al. (2005)*: they observed an unusual aerosol load over a large fraction of the Mediterranean basin together with a persistent high pressure system over Western Europe during the summer heat wave in 2003. From trajectory analyses, forest fires over south-eastern Europe were identified as the aerosol source. In their study, they conducted radiative transfer calculations and estimated a heating rate of up to 2.8 K day<sup>-1</sup> at 20° solar zenith angle due to forest fire aerosols within the layer. The authors expected this heating to lead to increased atmospheric stability and thus the persistent forest fire layers may have helped to maintain the anomalously hot and dry conditions during summer 2003.

Climate change and the trend towards hotter and drier weather conditions may affect the number of wildfires in the world. Most general circulation models predict the largest future warming at high latitudes and over land (*IPCC, 2001;2007*); the region where boreal forests

are situated. With the more frequent occurrence of droughts and the increased direct human impact, an increased fire activity is expected at Northern latitudes (*Mollicone et al.*, 2006). In fact, the area burned annually by forest fires in Canada has shown a pronounced upward trend over the past four decades during which time the summer temperatures have increased (*Gillett et al.*, 2004). Studies by *Flannigan et al.* (2000, 2005) and *Stocks et al.* (2002) suggest a considerable increase in future area burned, although there are large regional variations in fire activity.

The increasing occurrence of wildfires in the world makes it necessary to better understand the influence of lofted forest fire layers on the meteorology and on the stability of the atmosphere. From the presented observations in forest fires plumes during ITOP (Section 4.1, p. 83ff) new insight into the ageing process and the interaction of aerosols and atmospheric dynamics can be provided. For the first time, forest fire plumes of various ages (4-13 days) were investigated with the same instrument combination within one field experiment during ITOP. The parameters measured covered the particle size range from 4 nm to 100  $\mu\text{m}$ , the absorption coefficient, and the aerosol mixing state for several particle size fractions. The measurement of the aerosol mixing state was performed for the first time on the Falcon. This thesis aims to contribute to the understanding of radiatively-driven processes in forest fire plumes and their impact on atmospheric stability.

## 1.2.2 Desert dust aerosol

The largest and most persistent sources of desert dust are located in an area extending from the west coast of North Africa, over the Middle East, Central and South Asia, to China, whereas the Southern Hemisphere is free of major dust activity (*Prospero et al.*, 2002). The Saharan desert covers an area of about 9 million  $\text{km}^2$  and is the largest desert on Earth, contributing to about 50-70% (*Mahowald et al.*, 2005) of the annual global dust emissions. Desert dust was identified as having a significant anthropogenic component (*IPCC*, 2007), and therefore mineral dust radiative forcing may play a significant role in a changing climate. Several authors (e.g. *Tegen and Lacis*, 1996; *Sokolik and Toon*, 1996; *Prospero et al.*, 2002; *Tegen et al.*, 2004) gave different estimates on the anthropogenic fraction of dust. In the latest IPCC report (*IPCC*, 2007), a best guess of 0-20% anthropogenic dust burden is given with still a large uncertainty. Dust is exported from the African continent in all seasons (Figure 3) and is frequently transported across the Atlantic Ocean towards the American continent throughout the year. *Moulin and Chiapello* (2006) report a significant intensification of Atlantic dust export since 1965. Their analysis suggests that this trend might be explained by anthropogenic soil degradation due to land use in certain parts of the Sahel.

Dust storms are a significant source of coarse mode particles (e.g. *Schütz and Jaenicke*, 1974; *Schütz and Jaenicke*, 1978; *d'Almeida and Schütz*, 1983; *de Reus et al.*, 2000). Similar to carbonaceous aerosols, mineral dust particles scatter and partly absorb solar radiation. Moreover, dust particles have the potential to alter the outgoing terrestrial radiation flux due to their large sizes (e.g. *Haywood et al.*, 2005). The sign of the TOA radiative forcing of mineral dust aerosol is uncertain, in view of the competing nature of the negative solar radiative forcing and the positive terrestrial radiative forcing (e.g. *IPCC*, 2001; *Haywood and Boucher*, 2000). Similar to layers containing BC, the presence of atmospheric dust reduces surface temperatures. Furthermore, the presence of dust alters atmospheric heating rates, impacts on the hydrological cycle (e.g. *Rosenfeld et al.*, 2001; *Miller et al.*, 2004), and the

formation of ice clouds (e.g. *Ansmann et al.*, 2005). *Otto et al.* (2007) simulated the atmospheric radiative effects of an in-situ measured Saharan dust plume measured on Tenerife during the Aerosol Characterisation Experiment (ACE-2) in 1997 (*Raes et al.*, 2000a). The calculations of *Otto et al.* (2007) indicate that the large particle fraction has a predominant impact on the optical properties. They show that the large particles strongly absorb and contribute at least 20% to the atmospheric radiative effects of a dusty atmosphere. *Moorthy et al.* (2007) investigated dust absorption over the Indian desert on the basis of ground-based and satellite-based remote sensing. They derived a warming of lower atmosphere of 0.7-1.2 K day<sup>-1</sup> due to the presence of dust.



**Figure 3.** This image of two different-coloured dust plumes blowing northward off the coast of Libya was captured by MODIS on 26 October 2007 (adopted from [http://earthobservatory.nasa.gov/Newsroom/NewImages/images.php3?img\\_id=178175](http://earthobservatory.nasa.gov/Newsroom/NewImages/images.php3?img_id=178175)).

Due to the lack of adequate measurement data, estimates of the radiative impacts of dust result mainly from modelling studies. The spatial and temporal distribution of the radiative properties of dust are poorly understood over many regions of the world (e.g. *Moorthy et al.*, 2007). *Sokolik et al.* (2001) point out that the major unknowns concerning dust aerosols are: the size distributions of the particles that spans a range from 0.01  $\mu\text{m}$  to about 100  $\mu\text{m}$ ; the vertical and spatial variability within the dust plumes, and optical properties like complex refractive index, absorption coefficient, single-scattering albedo, particle shape or the scattering phase function. The single-scattering-albedo is the most important factor for the shortwave radiative forcing of mineral dust, whereas the longwave forcing of dust is dependent on the vertical distribution of the dust (*IPCC*, 2007).

In the past few years, several field experiments focussing on desert dust were performed. The Saharan Dust Experiment (SHADE) was conducted in September 2000 in the Cape Verde area. The main aim of SHADE was to determine parameters relevant for computing the direct radiative effect of dust (*Tanré et al.*, 2003). The experiment was considered to be a success, but *Haywood et al.* (2003a) pointed out that one of the optical particle counters responsible for the measurement of particles in the size range between 1 and 23.5  $\mu\text{m}$  did not work correctly. As a result, dust size distributions in the super-micron size range had to be estimated from surface-based sun photometry. Similar problems with the optical particle

counter occurred during the Southern African Regional Science Initiative (SAFARI) 2000 (Haywood *et al.*, 2003b). The Puerto Rico Dust Experiment (PRIDE) took place in the Caribbean in June/July 2001. Data from a light aircraft, remote sensing and ground-based measurements were used to study the dust after the transport across the Atlantic into the Caribbean region (Reid *et al.*, 2003b; Maring *et al.*, 2003b). One result of PRIDE was the discovery of particles larger than consistent with Stokes gravitational settling (Maring *et al.*, 2003a). Assuming a continuous upward velocity of  $0.33 \text{ cm s}^{-1}$ , the authors could explain the existence of the large particles. However, Maring *et al.* (2003a) were not sure which physical process(es) caused the hypothesised upward velocity that partly counteracted the gravitational settling. Reid *et al.* (2003a) compared size and morphological measurements of coarse mode dust particles from Africa gathered during PRIDE and found large differences between optical particle counters and aerodynamic methods. Both experiments, SHADE 2000 and PRIDE 2001, took place in the outflow area of dust on Cape Verde, several hundreds of km away from the major dust sources so that the dust properties may have been transformed during transport. The results of SAFARI, SHADE and PRIDE suggest that there is still a need for the exact quantification of the dust size distribution up to sizes of  $100 \mu\text{m}$ . One possibility to gather data on the particle size distribution of Saharan/Sahelian dust was given by the African Monsoon Multidisciplinary Analysis (AMMA) 2006 field study. However, this large international experiment focussed mainly on the understanding of dynamical processes such as tropical thunderstorms and the African Monsoon, and involved only a minor airborne aerosol component.

Although several field experiments conducted in the past few years have improved our understanding of dust microphysical and optical properties, the interaction of desert dust with atmospheric stability has been rarely investigated on the basis of experimental data. In a recent study, Pérez *et al.* (2006) included mineral dust radiative effects in a numerical weather prediction model. They found that with the dust feedbacks included, low-level warm and upper-level cold temperature biases of the model are reduced. However, they admitted several limitations of the study: for example, the particle size distribution was confined to dust particles smaller than  $10 \mu\text{m}$  and the optical properties of dust, which are a function of location, were calculated with refractive indices from the Global Aerosol Data Set. They concluded that experimental data from the Saharan Mineral Dust Experiment (SAMUM) experiment could improve the model results. SAMUM was conducted in southern Morocco in May/June 2006 and focussed on the microphysical, optical, and radiative properties of pure dust aerosol in a vertical column over the Sahara and during transport to Western Europe. The investigation of the SAMUM in-situ measurements is part of this work. For the first time during the SAMUM field experiment, measurements with extended aerosol instrumentation close to the Sahara including ground-based, airborne and satellite-based measurements were performed. The airborne in-situ aerosol instrumentation covered the whole particle size spectrum from the smallest nucleation mode particles to dust particles in the far super-micron range, and an airborne High Spectral Resolution Lidar (HSRL) was employed. The absorption coefficient was measured at three wavelengths and instead of measuring the aerosol mixing state for several size fractions only, the non-volatile size distribution was recorded in the size range between  $4 \text{ nm}$  and  $2.5 \mu\text{m}$ . In this study, a large number of measurements of dust microphysical properties such as particle size distributions are presented, and the interaction of the dust microphysical properties with the stability of the atmosphere is investigated in detail.

### 1.2.3 Long-range transport of biomass burning and desert dust aerosol

Biomass burning and desert dust plumes are observed to be transported over long distances, even between continents. Although, the long-range transport of anthropogenic pollutants from Northern America or Asia to Europe has been reported in numerous studies (e.g. *Huntrieser and Schlager, 2004; Huntrieser et al., 2005; Stohl et al., 2007*), here we focus only on examples for the long-range transport of desert dust and biomass burning plumes. Lofted forest fire plumes have been observed to circle around the world within less than three weeks (*Damoah et al., 2004*). In August 1998 severe forest fires destroyed more than 10 000 ha of boreal forests in Canada. Plumes from these fires were transported across the Atlantic (Figure 4) and caused pronounced haze layers and enhanced carbon monoxide (CO) mixing ratios in Europe (*Forster et al., 2001*). *Petzold et al. (2002)* and *Fiebig et al. (2002)* studied the 1998 Canadian forest fires also as part of the Lindenberg Aerosol Characterisation Experiment LACE 98, after the plumes had been transported across the Atlantic. They observed a pronounced accumulation mode and absorption coefficients up to  $20 \text{ Mm}^{-1}$  in the plume. *Wandinger et al. (2002)* reported an *AOD* of 0.1 over Germany ( $\lambda = 550 \text{ nm}$ ) for an aged forest fire plume originating from the 1998 Canadian forest fires. *Fiebig et al. (2003)* investigated the ageing of smoke particles in a Canadian forest fire plume after its long-range transport across the Atlantic Ocean and found that the plume dilution was inhibited in the lower part of the plume. Recently, *Stohl et al. (2006)* observed elevated concentrations of light absorbing aerosols throughout the entire Arctic as a result of long-range transport from North American boreal forest fires during summer 2004. The transport of forest fire plumes across the Atlantic Ocean towards Europe in summer 2004 is a focus also of recent studies by *Clarke et al. (2007)*, *Petzold et al. (2007)*, and *Real et al. (2007)*.

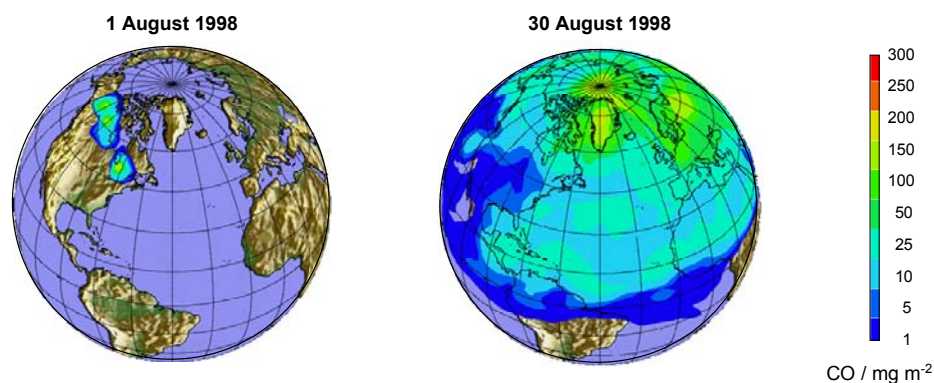


**Figure 4.** ECHAM simulation of CO mixing ratios (colour coded) originating from the 1998 Canadian forest fires, which were investigated by several groups as part of the Lindenberg Aerosol Characterisation Experiment LACE (courtesy: C. Kurz, DLR). Within one month the forest fire plumes spread over the entire Northern Hemisphere and caused enhanced CO mixing ratios and pronounced haze layers in Europe (see text).

Similar to the long-range transport of forest fire plumes, desert dust is transported all the way around the globe. *Husar et al. (2001)* investigated two Asian dust storms in April 1998. One dust cloud crossed the Pacific Ocean within five days and led to a significant increase in surface aerosol concentration across Northern America. Dust was observed also to be transported from China to the French Alps (*Grousset et al., 2003*). Saharan dust is exported across the North Atlantic towards the American Continent quite regularly (e.g. *Colarco et al.,*

2003; *Moulin and Chiapello, 2006*). Several studies report dust transport from the Sahara to south-western Europe and the Mediterranean, sometimes even reaching Germany and parts of Northern Europe (e.g. *Müller et al., 2003*).

The transport of lofted aerosol layers to Europe is a frequently monitored atmospheric phenomenon: *Müller (2007)* investigated the frequency with which lofted aerosol layers have been transported to Leipzig on the basis of lidar observations in the years 1997-2004. On average, these layers were detected in at least 30% of the regular annual measurements. In spring and summer, lofted layers occurred in about 60% of the regular measurements. *Müller (2007)* pointed out that their maximum occurrence in spring and summer coincides with the forest fire season in boreal areas that starts in spring and reaches its maximum intensity in summer.

### **1.3 Objectives of this thesis**

In this study, forest fire and desert dust plumes are investigated with data gathered during ITOP 2004 and SAMUM 2006. The main objective of this thesis is to investigate the impact of radiatively-driven processes in biomass burning and desert dust aerosol layers on the microphysical and optical properties of the particles in these layers. At first sight, biomass burning and desert dust aerosols appear to be quite different, but both aerosol types have an absorbing component and are observed to be transported over long distances, even around the globe. Both desert dust and biomass burning particles are natural aerosols. However, a certain component of biomass burning and desert dust particles originates from anthropogenic sources, mainly from agricultural practices (harvesting, overgrazing). Besides forest fire and desert dust aerosol, there is only one other source of absorbing particles: fossil fuel burning. However, fossil fuel burning – which is not discussed in this thesis – is a completely anthropogenic process. As described in the previous sections, absorbing aerosol layers like biomass burning and desert dust plumes can change the distribution of solar radiation by reducing it at the surface, absorbing it higher up. As aerosols cool the surface and warm the aerosol layer, the atmospheric lapse rate will be changed. Therefore the atmospheric stability will be influenced. The impact of radiatively-driven processes on the lifetime of the aerosol layer and atmospheric stability is examined in this thesis on the basis of airborne observations. The regular transport of lofted forest fire and desert dust plumes across long distances on hemispheric scales raises several scientific questions:

- Why are layers containing absorbing particles transported over such long distances, and why are they so long-lived?
- Are the microphysical and optical properties of absorbing particles responsible for the long atmospheric residence time of forest fire and desert dust plumes?
- Is the heating of the aerosol caused by the interaction of solar radiation and the absorbing particles seen in the measured temperature profiles? How large is the heating?
- Limited dilution has been observed in lofted forest fire and desert dust layers, but what causes the limited dilution?
- How are the microphysical properties of forest fire and desert dust particles modified during transport?
- How do the large coarse mode particles behave during transport?

Most experimental studies, except some studies mentioned in Section 1.2.1, focus on aerosol properties and do not consider the influence of the aerosols on the thermodynamic structure of the atmosphere. This study investigates the impact of absorbing aerosol particles on atmospheric stability and the implications of a changed stability on the development of the aerosol microphysical and optical properties during transport. For the first time, vertical profiles of the Richardson number  $Ri$  are used to assess the stability and mixing in forest fire and desert dust plumes. For the first time, the conclusions drawn from the observations of forest fire and desert dust aerosol, at first sight quite different aerosol types, are discussed from a common perspective. Two mechanisms, the **self-stabilising** and the **sealed ageing effect**, valid for both forest fire and desert dust aerosol layers are proposed to explain the characteristic temperature structure as well as the aerosol properties observed in lofted forest fire and desert dust layers.

### Self-stabilisation hypothesis

Aerosol layers containing light absorbing aerosol particles such as biomass burning or desert dust particles absorb solar radiation and are thereby heated (Figure 5b). Thus, the plume is stabilised at the bottom. In contrast, it is destabilised near the top (Figure 5c) generating an unstable lapse rate. The presence of this unstable lapse rate will produce mixing and entrainment from above. The lapse rate above the aerosol plume determines if entrainment is taking place from above. As long as the aerosol layer is topped by a stable stratified layer, mixing will be suppressed. If the temperature in the interface layer exceeds the temperature of the overlying air, mixing can take place, and the interface layer can grow in depth. This situation is called encroachment. Whether it grows in depth and if, how far because of the encroachment depends on the presence of any large-scale subsidence, which counteracts the turbulent encroachment. Subsidence does not only suppress the growth of the unstable layer. If the subsidence is sufficiently intense, it lowers the height of the top and may cause the whole layer to descend (*Carson, 1973*). As the air descends, it is warmed adiabatically and typically a subsidence inversion will form. This subsidence inversion is a barrier to mixing. In the regions where the lofted aerosol layers were observed during ITOP and SAMUM, large-scale subsidence could be accounted for by the presence of a subtropical high pressure system.

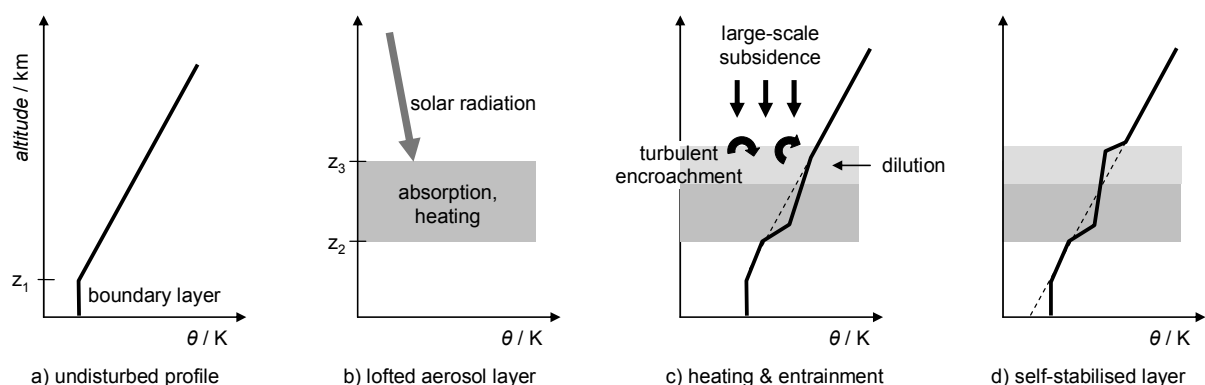


**Figure 5.** Schematic of the processes in a heated aerosol plume containing absorbing particles.

The mixing process and the large-scale subsidence leave the aerosol layer with nearly neutral stratification inside the layer and strong inversions at the bottom and at the top (Figure

5d). Furthermore, the entrainment of tropospheric air from above the plume has diluted the particle concentration in the upper part of the plume. This will change the heating distribution in the plume by reducing the heating rate near the plume top. The changed stability profile and the changed heating distribution in the plume will influence the evolution of the profile by exerting a stabilising effect on the layer. The processes described tend to extend the lifetime of the layer allowing the transport over long distances.

### **Sealed ageing hypothesis**

The self-stabilising effect gives rise to the sealed ageing effect. The lower boundary of the forest fire/desert dust layers is “sealed”, while the upper boundary of the layer is permeable. As a result, the aerosol layer can be considered as being isolated from the underlying airmass.

The aerosol processing within this almost “closed” system results in a characteristic shape of the aerosol size distribution (Figure 6, left panel). In general, several processes can modify the particle number concentration and the size distribution of a particle population. These processes include dilution due to mixing of the aerosol laden air with ambient air, nucleation of new particles from the gas phase, self-coagulation<sup>3</sup>, inter-modal coagulation<sup>4</sup> and dry deposition. In a “closed system”, the suppressed entrainment of condensable gases from the surface inhibits particle nucleation and the formation of coated particles inside the layer. Then coagulation changes the shape of the size distribution. The inter-modal coagulation decreases the particle number concentration in the Aitken mode and increases the particle number concentration in the accumulation mode. Self-coagulation in the accumulation mode leads to a narrowing (Figure 6, right panel) of the accumulation mode. In the coarse mode, no coagulation is expected, but parts of the large particles are expected to settle due to gravitation. The result of ageing within a sealed layer is the absence of a nucleation mode, a depleted Aitken mode and an enhanced accumulation mode.

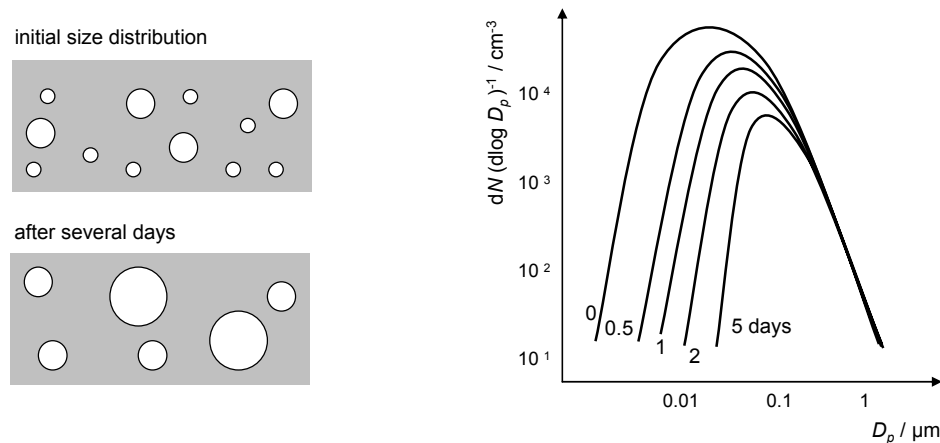


**Figure 6.** The left panel sketches the development of a size distribution in “closed” system. The right panel illustrates the evolution of a particle population during a period of five days (adopted from Butcher and Charlson, 1972).

<sup>3</sup> Self-coagulation means coagulation of particles within one size range. Self-coagulation decreases the number of particles in this size range.

<sup>4</sup> Inter-modal coagulation refers to coagulation of particles in size range  $i$  with particles in the larger size range  $j$ . Inter-modal coagulation decreases the particle number concentration in the smaller mode  $i$  and does not change the concentration in the larger mode  $j$ .

## **1.4 Structure**

This thesis is organised as follows: the aerosol fundamentals including the atmospheric life cycle of aerosols, sources and sinks, microphysical and optical properties of aerosols are described briefly in Chapter 2. In addition, all fundamental equations used for the analysis of data are summarised here.

Chapter 3 describes not only the measurement methods, and the transfer functions of the various aerosol in-situ instruments, but also the efforts made to ensure a high quality of all experimental data. These efforts include the evaluation of the FLEXPART performance for the cases investigated, the evaluation of the inversion algorithm, sensitivity tests of the instrument response on assumptions that entered the data analysis procedure, and the evaluation of possible error sources in the measurement data. Furthermore, an overview of the two field experiments ITOP (forest fire aerosol) and SAMUM (desert dust aerosol), and a summary of the flight missions is given. These experiments provided the data sets investigated here. The ITOP data were collected before the work on this thesis started, while the logistics and the instrument preparation of the SAMUM campaign, the weather forecast during SAMUM and the in-situ aerosol measurements during SAMUM were done within this thesis. Chapter 3 ends with a concept for the combination of the various data to test the hypotheses stated in Section 1.3.

In Chapter 4 the microphysical and optical properties observed in forest fire and desert dust aerosol layers are presented. The aerosol properties were derived with the methods introduced in Chapter 3 and include complete particle size distributions derived from the in-situ measurements for approximately 70 forest fire and desert dust encounters, calculated optical properties for about 20 forest fire and desert dust encounters, the lower and upper boundaries of the lofted forest fire and desert dust plumes, potential temperature gradients which will prove to be characteristic for absorbing forest fire and desert dust plumes, and several more microphysical and meteorological parameters for the investigated plume encounters. In addition, the observations are compared with independent measurements of optical aerosol properties for validation purposes. The results are shown separately in Chapter 4 for forest fire particles (ITOP) and desert dust particles (SAMUM).

Chapter 5 follows with the discussion of the results presented. In this section the self-stabilisation and the sealed ageing hypothesis are tested on the basis of experimental data. A summary of the results and scientific questions arising for future research are given in Chapter 6.

## **1.5 Use of external data and software routines**

The realisation of this study required the collaboration with several persons who provided results achieved outside this work. These contributions are summarised below. Excess CO data were provided by Dr. Heidi Huntrieser (DLR), and FLEXPART trajectory calculations were provided by Dr. Andreas Stohl (NILU). The evaluation of the FLEXPART performance during ITOP and the classification of forest fire plumes on the basis of FLEXPART trajectory calculations and excess CO measurements were part of this study. Ulrich Hamann (DLR) performed the calculation of heating rates. The basis for the heating rate calculations were the microphysical and optical forest fire and desert dust aerosol properties derived in this study.

For the SAMUM analysis, extinction measurements provided by Michael Esselborn (DLR) were additionally used in the heating rate calculation. The combination of the heating rates with the measurement data was part of this study. The derivation of the particle size distributions from the optical particle counters requires an assumption on the refractive index of the aerosol. For the ITOP data, the refractive index was estimated from the absorption measurements. For the SAMUM data, the refractive index data were provided by Katharina Rasp (DLR). The aerosol optical model for the calculation of optical forest fire and desert dust aerosol properties was provided by Dr. Markus Fiebig (DLR/NILU). Application of this model for the calculation of optical properties was one of the major parts of this study.



---

## 2 Aerosol fundamentals

---

The following chapter gives an overview over atmospheric aerosol particles, their sources, their life cycle, transformation and ageing. Furthermore, all equations relevant for the processing of the experimental aerosol data and interpretation of the results are summarised. More detailed information on aerosols is given for example in *Seinfeld and Pandis* (1998) or *Hinds* (1999), the optical properties of aerosols are extensively described in *Bohren and Huffman* (1983).

### 2.1 Aerosol in the atmosphere – sources, sinks and life cycle

The atmosphere of the Earth contains significant concentrations of aerosol particles. Although often synonymously used to denote the particles, the term *aerosol* refers to both, the suspension of liquid or solid particles in a gaseous medium<sup>5</sup>. The diameters  $D_p$  of atmospheric aerosol particles cover a wide range of sizes from a few nanometres ( $10^{-9}$  m) to some hundred micrometers ( $10^{-4}$  m). The aerosol particles have various shapes (spherical/aspherical) and are composed of different chemical constituents such as sulphate, ammonium, organic material, black carbon or crustal material. The morphology and chemical composition of the aerosol particles is mainly determined by the source of the particles, but it also contains information on transformation processes acting on aerosol particles during atmospheric residence time. Aerosol sources are natural and anthropogenic: the particles originate directly from emissions of particles (*primary aerosol*) and by chemical reactions from the gas-to-particle conversion by nucleation of gaseous vapours (*secondary aerosol*). Examples of natural primary aerosols are wind blown dust and sea spray. Emission of soot particles from burning of fossil fuels is an example for anthropogenic primary aerosols. Gaseous precursors of secondary aerosols include for example  $\text{SO}_2$ , organic compounds, dimethyl sulphide (DMS),  $\text{H}_2\text{S}$ , as well as  $\text{NO}_x$  ( $\text{NO} + \text{NO}_2$ ) and  $\text{NH}_3$ . Table 1 summarises particle sources and the estimated annual emissions. Desert dust contributes to about half of the global particle emissions, with the Sahara accounting for about 60% of the global dust emissions. Averaged over the globe, aerosols produced by human activities, account for about 15% of the total amount of aerosols in the atmosphere (Table 1).

Aerosol particles are traditionally divided into two size classes, the sub-micron ( $D_p < 1 \mu\text{m}$ ) and the super-micron ( $D_p > 1 \mu\text{m}$ ) particles. This reflects the two major

---

<sup>5</sup> The term aerosol does not include cloud droplets, ice particles and rain droplets.

formation mechanisms (secondary and primary). Both formation mechanisms strongly overlap in the range  $0.1 < D_p < 1 \mu\text{m}$ . Whereas particles  $< 1 \mu\text{m}$  are produced by gas-to-particle conversion or emission, particles  $> 1 \mu\text{m}$  can only be produced by mechanical processes such as break-up of bulk material by wind. Atmospheric concentrations of particles  $D_p < 1 \mu\text{m}$  generally range between 10 and  $10^6$  per  $\text{cm}^3$ , whereas particles  $D_p > 1 \mu\text{m}$  typically occur at concentrations around 10 per  $\text{cm}^3$ .

**Table 1.** Sources and estimates of global emissions of atmospheric aerosols (adopted from Hinds, 1999).

Source	Amount / $\text{Tg yr}^{-1}$ ( $10^6$ metric tons $\text{yr}^{-1}$ )	
	Range	Best estimate
<b>Natural</b>		
Soil dust	1000 – 3000	1500
Sea salt	1000 – 10000	1300
Botanical debris	26 – 80	50
Volcanic dust	4 – 10000	30
Forest fires	3 – 150	20
Gas-to-particle conversion	100 – 260	180
photochemical	40 – 200	60
<b>Total for natural sources</b>	<b>2200 – 24000</b>	<b>3100</b>
<b>Anthropogenic</b>		
Direct emissions	50 – 160	120
Gas-to-particle conversion	260 – 460	330
Photochemical	5 – 25	10
<b>Total for anthropogenic sources</b>	<b>320 – 640</b>	<b>460</b>

Once an aerosol particle is suspended in air, it is subject to processes altering the chemical composition and the size of the particle (*ageing*) through condensation of vapour species on the particle or by evaporation, by coagulation with other particles, by chemical reactions, or by activation in the presence of supersaturated water vapour to become fog or cloud droplets. Figure 7 (Raes *et al.*, 2000b) summarises the microphysical processes that influence the size and chemical composition of atmospheric aerosol particles during their lifetime.

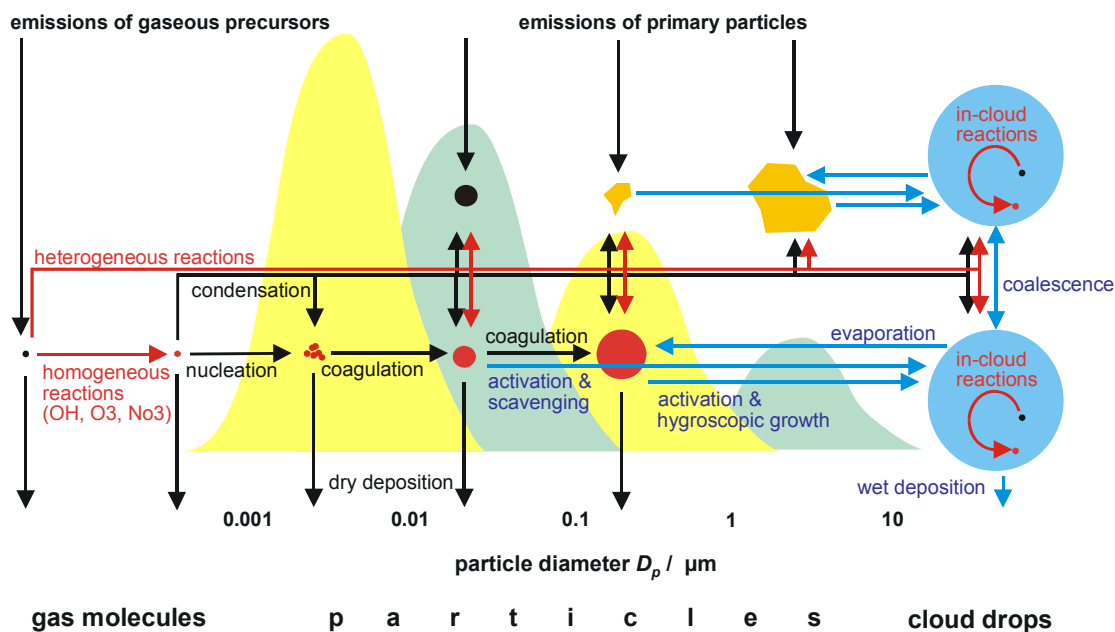


**Figure 7.** Scheme of microphysical processes influencing the size and chemical composition of atmospheric aerosol particles (adopted from Raes *et al.*, 2000b).

Aerosol particles are removed from the atmosphere by deposition processes (Figure 5). During wet deposition processes the particles are first incorporated into droplets and then transported to the Earth's surface via precipitation. Dry deposition is the transport of gaseous and particulate species from the atmosphere to the ground level, where they are adsorbed onto a surface without precipitation. Within dry deposition two mechanisms are discriminated: deposition and sedimentation. During deposition, particles are transported to surfaces as a result of Brownian motion. Brownian diffusion is dependent on the particle size and is very effective for ultrafine particles ( $D_p < 0.05 \mu\text{m}$ ) and decreases with increasing particle size. Sedimentation refers to the settling of particles due to gravity and increases with the square of the particle diameter. Small particles are often not removed, but they are transformed into larger particles, for example by coagulation. For particles in the size range  $0.05 < D_p < 1 \mu\text{m}$  no effective dry deposition mechanisms exist. This is the reason, why aerosol is accumulated in this size region (Seinfeld and Pandis, 1998). Enhanced accumulation mode concentrations are characteristic for aged aerosols. The settling of particles  $D_p > 20 \mu\text{m}$  is governed by gravitational settling. When the particle is released in air, it quickly reaches terminal *settling velocity*  $v_{TS}$ , a condition where the drag force of the air from Stokes' law is balanced by the gravity force. The settling velocity can be calculated easily by equating the force due to gravity by the drag force and solving for velocity. For particles of a density  $\rho_{particle}$ , much larger than the density of air  $\rho_{air}$ ,  $v_{TS}$  can be approximated by the following equation (Hinds, 1999)

$$v_{TS} = \frac{\rho_{particle} \cdot D_p^2 \cdot g_a \cdot C_c}{18 \cdot \eta \cdot \chi} \quad (2.1)$$

where  $g_a$  is the acceleration of gravity,  $\eta$  the viscosity of the air,  $\chi$  the dynamic shape factor and  $C_c$  the Cunningham factor, which accounts for the slip correction. The dynamic shape factor accounts for the effect of shape on particle motion. For spherical particles,  $\chi$  is 1. In the case of aspherical particles ( $\chi \neq 1$ ), the *equivalent volume diameter* is used in Equation 2.1 (see also left panel in Figure 8). It can be thought of as the diameter of the sphere that would result if the irregular particle melted to form a droplet. The use of  $C_c$  extends the range of application of the Stoke's law to particles  $D_p < 1 \mu\text{m}$ . For a particle with  $D_p = 1 \mu\text{m}$ ,  $C_c$  is 1.15 for a temperature  $T = 293 \text{ K}$  and a pressure  $p = 1010 \text{ hPa}$ ; that is, the particle settles 15% faster than predicted without slip correction.

In general, the lifetime of particles depends on the size, the chemical composition and the height in which the particles occur. On average, it ranges between 3-10 days. After approximately 30 days, about 95% of the particles are removed from the atmosphere (Andreae, 2007).

## 2.2 Microphysical properties of aerosol particles

### 2.2.1 Aerosol size distribution

The most important parameter to characterise the behaviour of aerosol particles is the particle size. All properties of aerosol particles depend on particle size. For example, the particle size determines together with the chemical composition the dominating removal processes (diffusion, sedimentation), and therefore the atmospheric lifetime of a specific

particle. Particle size is essential for extinction or scattering properties of the aerosol. If the particle size and the concentrations of particles in a certain size range is known, every other distribution such as volume and surface distribution can be easily be calculated, as all those quantities are proportional to the particle size raised to a power (*moment p*). For example, the surface area is proportional to  $D_p^2$  (second moment,  $p = 2$ ) and the volume is proportional to  $D_p^3$  (third moment,  $p = 3$ ). Distributions of particle mass can be inferred under the assumption of a realistic particle density. Whereas liquid particles have a spherical shape, solid particles can have any irregular<sup>6</sup> shape. To account for irregular particles shapes, *equivalent diameters* are defined. An equivalent diameter is the diameter of a sphere that has the same value of a particular physical property as that of an irregular particle (see Figure 8). A very widely used equivalent diameter in aerosol technology is the *aerodynamic equivalent diameter*  $D_{aero}$ , which is the diameter of a standard density sphere ( $1 \text{ g cm}^{-3}$ ) having the same gravitational settling velocity  $v_{TS}$  as the irregular particle. In contrast to the aerodynamic diameter, the *Stokes diameter*  $D_{Stk}$  is defined as the diameter of a sphere that has the same density and settling velocity as the irregular particle.

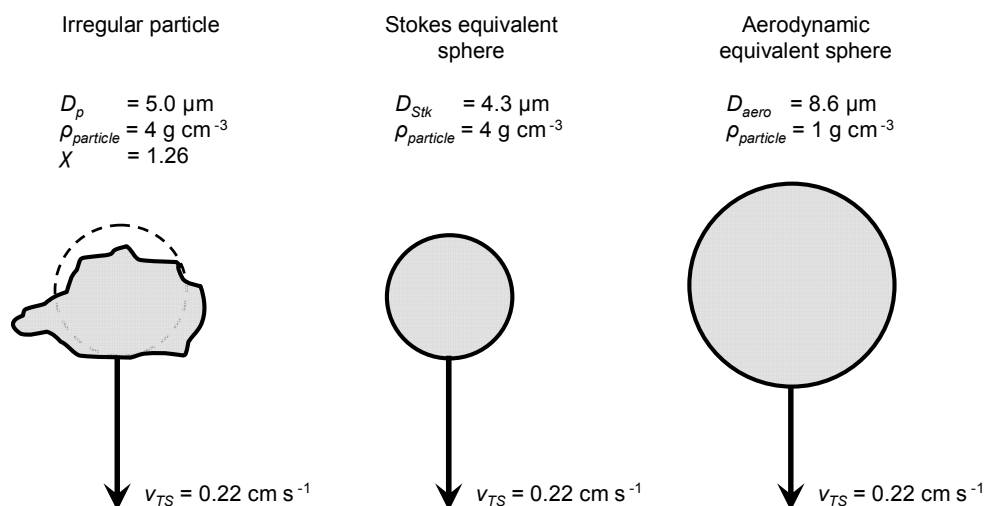


**Figure 8.** An irregular particle and its equivalent diameters (adopted from Hinds, 1999).

Atmospheric aerosols do not only occur at one specific size (*monodisperse aerosol*), they contain particles of different sizes (*polydisperse aerosol*). Monodisperse aerosols can be generated for example by controlled technical processes and are used for example to calibrate optical aerosol instruments. It is quite common to subdivide the atmospheric aerosol particles into four size classes, so called modes. The range of particles with  $D_p < 0.01 \text{ } \mu\text{m}$  is called *nucleation mode*, the range  $0.01 < D_p < 0.1 \text{ } \mu\text{m}$  *Aitken mode*, and the range  $0.1 < D_p < 1 \text{ } \mu\text{m}$  *accumulation mode*. The size range with  $D_p > 1 \text{ } \mu\text{m}$  is named *coarse mode*. In connection with air quality and health issues the particles are often classified as fine particle fraction ( $D_p < 2.5 \text{ } \mu\text{m}$ ) and coarse particle fraction ( $2.5 \text{ } \mu\text{m} < D_p < 10 \text{ } \mu\text{m}$ ). The term “PM” stands for particulate mass suspended in air. *PM2.5* is particulate mass with  $D_{aero} < 2.5 \text{ } \mu\text{m}$ . *PM10* comprises particulate mass with  $D_{aero} < 10 \text{ } \mu\text{m}$ , and it includes both, sub-micron and super-micron particle fractions. Aitken mode particles normally dominate the particle number concentration. Due to their small size, these particles contribute only minor to the total aerosol

<sup>6</sup> In the following the terms “irregular” and “aspherical” are used synonymously to describe non-spherical particles.

mass. The lack of an effective removal process in the accumulation mode leads to enhanced particle concentrations in this size range. The accumulation mode contributes much of the particle surface and the total aerosol mass.

The particle size distribution function describes the frequency with which a specific particle diameter occurs. Particle size distributions are characterised by statistical means like the diameter of highest occurrence frequency, the mean diameter or the median diameter. The sizes of aerosol particles and their concentrations  $n_i$  in a specific size range  $D_p$  to  $D_p + dD_p$  vary over several orders of magnitudes and the particle size distributions are highly asymmetric exhibiting a long tail at large particle sizes. To cover all the details of the size distribution, the size distribution is represented on a double-logarithmic scale. To describe particle size distributions in models, it is convenient to formulate a mathematical expression with a few adjustable parameters. The most popular expressions are the Junge power law, the *log-normal distribution* and a modified gamma distribution. In this work, the size distributions are parameterised with log-normal distributions. They are given by (Hinds, 1999)

$$\frac{dN}{d \log D_p}(\text{Mode } X_j) = \frac{N_j}{\sqrt{2\pi} \cdot \log GSD_j} \cdot \exp \left[ -\frac{1}{2} \left( \frac{\log D_p - \log CMD_j}{\log GSD_j} \right)^2 \right] \quad (2.2)$$

where  $N_j$  denotes the particle number concentration in mode  $X_j$ ,  $CMD_j$  is the count median diameter and  $GSD_j$  is the geometric standard deviation, respectively.  $GSD_j$  quantifies the width of the distribution, and 68% of the area below the curve is in the range  $CMD_j \pm GSD_j$ . The so called mode parameters  $N_j$ ,  $CMD_j$  and  $GSD_j$  completely describe one mode of the aerosol size distribution (Figure 9).

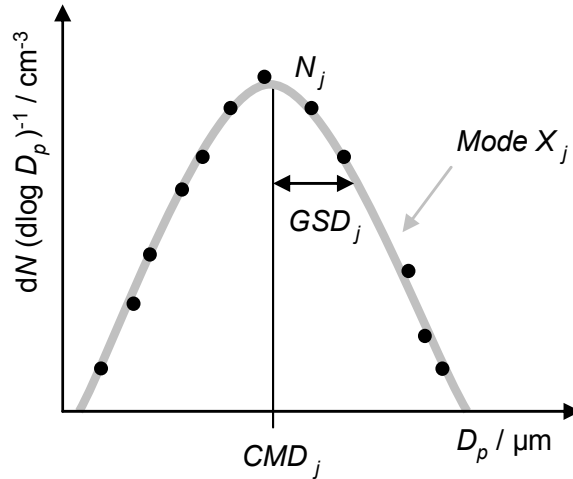


**Figure 9.** The log-normal size distribution is completely described by three parameters: the size distribution is centred at the count median diameter  $CMD_j$ ; the geometric standard deviation  $GSD_j$  quantifies the width of the distribution, and  $N_j$  denotes the particle number concentration in mode  $X_j$ .

A combination of 3-4 log-normal distributions fits the shape of most atmospheric size distributions quite well. The idea to represent atmospheric aerosol distributions by a combination of log-normal distributions was raised by Whitby (1978). A very useful feature of log-normal distributions is the fact that for any known log-normal distribution with known  $CMD$  and  $GSD$ , any type of average diameter can be calculated by the *Hatch-Choate*

equations (Hatch and Choate, 1929). All the conversion equations have the same form. The general conversion equation for the  $p^{\text{th}}$  moment average of the  $q^{\text{th}}$  moment distribution (Hinds, 1999) is given by

$$(D_{qm})_p = CMD_j \cdot \exp\left[\left(q + \frac{p}{2}\right) \cdot (\ln GSD_j)^2\right] \quad (2.3)$$

where the constants  $p$  and  $q$  depend only on the type of conversions. For example, with Equation 2.3 the diameter of average surface area ( $p = 2$ ) or average volume ( $p = 3$ ) can easily be calculated from the count mean diameter ( $q = 0$ ). More detail about the Hatch-Choate equations, including a list of coefficients  $p$  and  $q$  for the most common conversions, is given in Hinds (1999).

An important parameter characterising the size distribution of an aerosol is the *effective diameter*  $D_{eff}$  introduced by Hansen (1971), which is defined by

$$D_{eff} = \frac{\int_0^{\infty} D_p^3 \cdot n(D_p) dD_p}{\int_0^{\infty} D_p^2 \cdot n(D_p) dD_p} \quad (2.4)$$

The effective diameter  $D_{eff}$  differs from the mean radius by including the particle area as a weight factor multiplying the particle size distribution  $n(D_p)$ . This weight factor is introduced, since the amount of light scattered by a particle is approximately proportional to the area of the particle.  $D_{eff}$  is a significant characterisation of a particle size distribution for describing the scattering properties of that distribution. Satellite retrieval algorithms focus on the retrieval of  $D_{eff}$  together with optical depth. Various definitions of  $D_{eff}$  are used with each definition related to physically based parameters. The different definitions are summarised and compared in a review paper by McFarquhar and Heymsfield (1998). In this work, the definition stated in Equation 2.4 is used. The  $D_{eff}$  can either be calculated directly from the measured particle size distribution or, applying Equation 2.3, from the parameterised size distributions.

## 2.2.2 Aerosol mixing state

The atmospheric aerosol rarely consists of a single chemical component. Generally, it is a mixture of various constituents from numerous sources. The *mixing state* of the aerosol describes the distribution of chemical species among the particles. Figure 10 depicts different mixing states. An aerosol population is *externally mixed*, if each particle arises from only one source and consists of a single material. In an *internal mixture*, particles contain different components from different sources. Internally mixed particles can be formed by coagulation, coalescence of particles in clouds or by chemical reactions on particle surfaces. *Coated particles* can arise, if gaseous vapours condense on aerosol particles. This can happen for example during long-range transport. Aged aerosol particles typically show coatings.

It is important to identify the mixing state of the aerosol, because it affects both the microphysical and optical properties of the aerosol. For instance, hygroscopic growth and therefore the ability of a particle to act as cloud condensation nuclei is influenced by the

mixing state. Assuming an aerosol composed of hygroscopic and non-hygroscopic particles illustrates the different behaviour depending on the mixing state: in an external mixture, only the hygroscopic particles grow, whereas in an internal mixture every particle grows, if the relative humidity is increased. A soluble coating on an insoluble particle can reduce atmospheric lifetimes of those coated particles. Coating also changes aerosol optical properties (e.g. *Seinfeld and Pandis, 1998*). In theoretical calculations *Bauer et al. (2007)* showed that optical properties of coated dust particles started to differ significantly from uncoated ones, if coating layers on the particle exceeded 20% of the radius of the dust core. The analysis of the aerosol mixing state is a tool to investigate transformation and ageing processes acting on an aerosol population during transport from the source region to the far field.

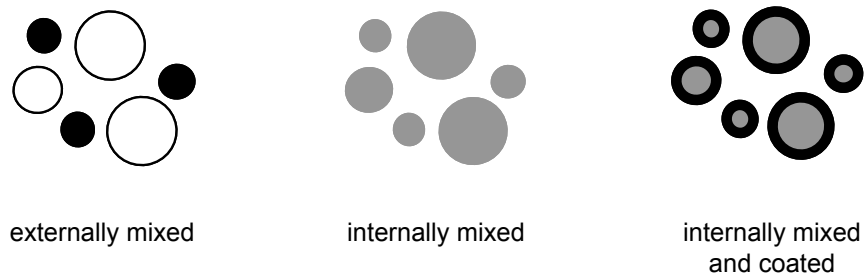


**Figure 10.** Mixing states of an aerosol composed of different chemical components. The picture on the left shows an externally mixed aerosol, the mid picture depicts an internally mixed aerosol, and the picture on the right illustrates an aerosol that is internally mixed and exhibits a coating.

## 2.3 Optical properties of aerosol particles

In the range of the visible wavelengths, the optical properties of the atmosphere are dominated by the interaction of aerosol particles with the radiation, while the air and other gases have only a small influence in the visible spectrum (e.g. *Horvath, 1996*). The optical properties of the aerosols are important for example for visibility, and also to assess possible impacts of aerosols on the climate system. This section summarises the basic principles of interaction of radiation with particles. More detail including the derivation of the equations is given for example in *Bohren and Huffman (1983)*.

### 2.3.1 Definition of key quantities

The *irradiance*<sup>7</sup>  $I$  is defined as the amount of energy that crosses a unit area perpendicular to the direction of light propagation per time. It is measured in  $\text{W m}^{-2}$ . The rate at which energy is scattered or absorbed by a particle or gas molecule  $W_{\text{scat/abs}}$ <sup>8</sup> is proportional to the incident irradiance  $I_0$  (*Bohren and Huffman, 1983*)

$$W_{\text{scat}} = C_{\text{scat}} \cdot I_0 \quad \text{and} \quad W_{\text{abs}} = C_{\text{abs}} \cdot I_0 \quad (2.5)$$

<sup>7</sup> Some authors (e.g. *Hinds, 1999*) refer to the irradiance as the “intensity”. In this thesis both terms are synonymously used.

<sup>8</sup> In this work the indices *scat/abs/ext* refer to the scattering, absorption and extinction of particles and gases, while the indices *sp/ap/ep* refer to the particulate component only.

where  $C_{scat}$  and  $C_{abs}$ , measured in  $m^2$ , are the scattering- and absorption cross-sections, respectively. The extinction cross-section  $C_{ext}$  can be interpreted as the “shadow area” of size  $C_{ext}$ , in which the particle or molecule interacts with the radiative energy passing the particle or molecule. This “shadow area” can be much greater, or smaller, than the particle’s geometrical shadow. Conservation of energy requires that the light removed from the incident beam is accounted for both, scattering and absorption. The attenuation of light along the direction of propagation is the result of the combined effect of scattering and absorption and is referred to as *extinction*. The extinction cross-section can be written as follows (*Bohren and Huffman, 1983*)

$$C_{ext} = C_{scat} + C_{abs} \quad (2.6)$$

For particles, the dimensionless scattering efficiency  $Q_{sp}$  refers the scattering cross-section  $C_{sp}$  to the particle’s cross-sectional area  $A_p$  projected onto a plane perpendicular to the incident beam ( $A_p = \pi D_p^2/4$  for a spherical particle of diameter  $D_p$ ) (*Bohren and Huffman, 1983*)

$$Q_{sp/ap/ep} = \frac{C_{sp/ap/ep}}{A_p} \quad \Rightarrow \quad Q_{ep} = Q_{sp} + Q_{ap} \quad (2.7)$$

When a parallel beam of incident irradiance  $I_0$  passes through an atmospheric column of length  $dL$ , the light is attenuated (Figure 11). The light attenuation is given by the Lambert-Beer law (*Bohren and Huffman, 1983*)

$$I = I_0 \cdot e^{-\int_{z_1}^{z_2} \sigma_{ext} \cdot dL} \quad (2.8)$$

with  $\sigma_{ext}$  being the extinction coefficient. The extinction coefficient is measured in  $m^{-1}$  and is the sum of the scattering coefficient  $\sigma_{scat}$  and absorption coefficient  $\sigma_{abs}$ . The extinction coefficient  $\sigma_{ext}$  (and also the absorption  $\sigma_{abs}$  and scattering coefficient  $\sigma_{scat}$ ) can be decomposed into contributions from gases ( $\sigma_{egas/sgas/agas}$ ) and particulate components ( $\sigma_{ep/sp/ap}$ ) in the atmosphere. The extinction coefficient  $\sigma_{ep}$  for an monodisperse aerosol consisting of  $N$  spherical particles of cross-sectional area  $A_p$  is given by (*Bohren and Huffman, 1983*)

$$\sigma_{ep} = N \cdot C_{ep} = N \cdot \frac{\pi \cdot D_p^2}{4} \cdot Q_{ep} \quad (2.9)$$

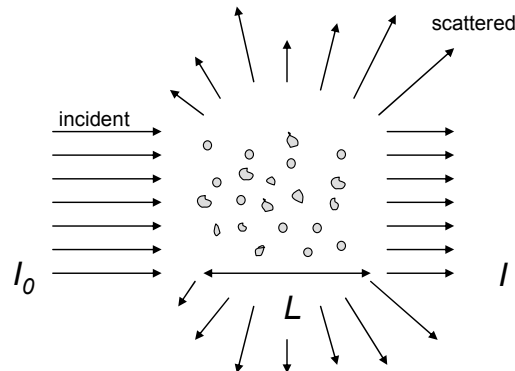


**Figure 11.** Extinction by a collection of particles (adopted from *Bohren and Huffman, 1983*).

The treatment of scattering by an ensemble of particles consisting of different sizes and concentrations is very complicated (*Seinfeld and Pandis, 1998*), unless the average distance between the particles is large compared to the size of the particles. In this case, scattering by an ensemble of particles can be treated as the sum of the scattering by the single particles. This assumption is satisfied even for particle concentrations ( $D_p = 1 \mu\text{m}$ ) of  $10^6 \text{ cm}^{-3}$ , which only occur in heavily polluted areas. For an ensemble of different-sized particles with a number size distribution function  $n(\log D_p) = dN/d\log D_p$ , the extinction coefficient  $\sigma_{ep}$  of the particle population is given by the following equation (*Seinfeld and Pandis, 1998*)

$$\sigma_{ep} = \int_{-\infty}^{\infty} \frac{\pi \cdot D_p^2}{4} \cdot Q_{ep}(D_p) \cdot \frac{dN}{d \log D_p} d \log D_p \quad (2.10)$$

Again, similar expressions can be written for the scattering  $\sigma_{sp}$  and the absorption coefficient  $\sigma_{ap}$  of a particle population. Note the wavelength-dependence of the scattering/absorption/extinction cross-section and efficiency, and the scattering/absorption/extinction coefficient.

The fraction of light extinction that is scattered is called the single-scattering albedo  $\omega_0$  and is also dependent on the wavelength. For demonstration, the wavelength-dependence is written explicitly in the equation defining the single-scattering albedo (*Bohren and Huffman, 1983*)

$$\omega_0(\lambda) = \frac{\sigma_{sp}(\lambda)}{\sigma_{ep}(\lambda)} = \frac{\sigma_{sp}(\lambda)}{\sigma_{sp}(\lambda) + \sigma_{ap}(\lambda)} \quad (2.11)$$

The single-scattering albedo  $\omega_0$  is a key parameter for the assessment of the direct radiative effects of aerosols on the climate. It determines whether an aerosol causes a negative radiative forcing ( $\omega_0 > 0.95$ ; cooling) or a positive radiative forcing ( $\omega_0 < 0.85$ ; warming) in the atmosphere. Depending on the albedo of the underlying surface and the altitude of the aerosol layer, a change in  $\omega_0$  from 0.8 to 0.9 can change the sign of the radiative effect (*Hansen et al., 1997*).

The dimensionless quantity aerosol optical depth *AOD* describes the integrated extinction of an aerosol layer extending from  $z_1$  to  $z_2$  (*Seinfeld and Pandis, 1998*)

$$AOD(\lambda) = \int_{z_1}^{z_2} \sigma_{ep}(\lambda) dz \quad (2.12)$$

The *AOD* of tropospheric aerosol layers ranges without clouds from less than 0.05 in pristine environments to close to 1.0 near sources of intense emissions such as forest fire plumes and can exceed 2 in intense dust storms. The *AOD* is the main product which can be derived from satellite sensors.

As most of the aerosol types do not absorb at infrared wavelengths, aerosol layers have a tendency to be relatively transparent at infrared wavelengths. This is why radiative effects of aerosols on the energy balance of the Earth are more or less confined to the solar and visible region of the spectrum. However, this is not the case for desert dust particles due to their large sizes. Depending on the underlying surface and the presence or absence of clouds, dust

forcing at solar wavelengths can be either positive or negative. However, it is always positive at infrared wavelengths (e.g. *Sokolik et al.*, 1998)

### 2.3.2 Scattering and absorption by particles

The interaction of electromagnetic radiation with particles gives rise to a number of spectacular atmospheric effects, like coloured sunsets or rainbows, but it can also cause reduced visibility. Electromagnetic radiation that impinges on a particle excites electrical charges in the particle to oscillatory motion. A particle scatters light, when the excited electric charges reradiate energy in all directions. A particle absorbs light, when (parts of) the excited electric charges are converted into thermal energy. The type of interaction of particles with radiation depends on the wavelength  $\lambda$  of the incident radiation, the size, chemical composition and shape of the particle. The interaction of radiation can be divided into three regimes with aid of the size parameter  $x$  (*Bohren and Huffman*, 1983)

$$x = \frac{\pi \cdot D_p}{\lambda} \quad (2.13)$$

#### Rayleigh scattering regime: $x \ll 1$

Is the particle small compared to the wavelength of the incident light, Rayleigh scattering takes place. The light is scattered symmetrically into the forward and backward direction (see Figure 12), almost regardless of the particle shape. With respect to the visible spectrum of light, particles with  $D_p \leq 0.1 \mu\text{m}$  are in the Rayleigh regime. The radiation scattered by a sphere which is small compared to the wavelength is proportional to  $\lambda^{-4}$ . As a consequence light of short wavelengths is scattered more efficiently than light of longer wavelengths. Rayleigh scattering of the incident solar radiation by molecules and small particles in the atmosphere is responsible for example for the bluish colour of the sky. In the evening, when the path of the light through the atmosphere grows, the blue components are scattered out of the line of sight causing reddish sunsets.

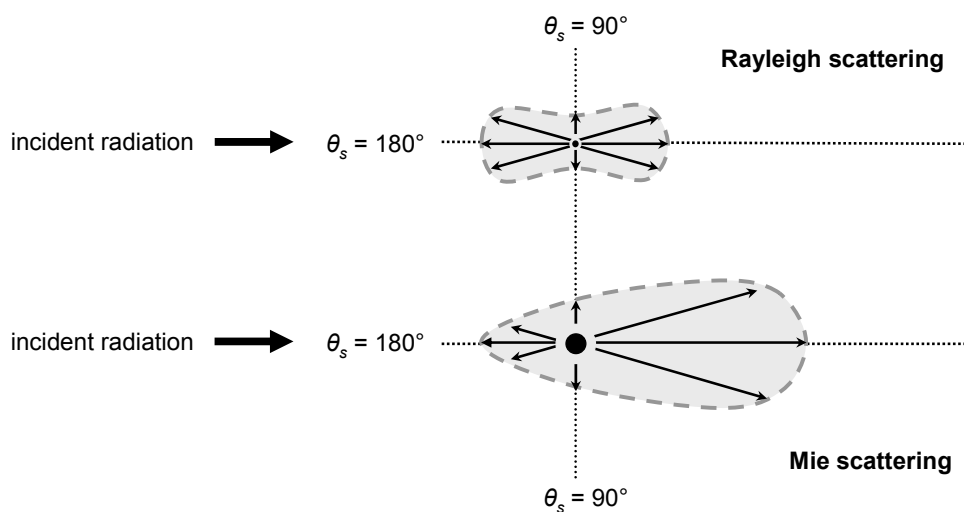


**Figure 12.** Angle-dependent distribution of scattered light for the Rayleigh (top) and Mie (bottom) regime. In the Rayleigh regime, the light is scattered symmetrically into the forward ( $\theta = 0^\circ$ ) and backward direction ( $\theta = 180^\circ$ ), whereas in the Mie regime with increasing particle size the scattering more and more peaks in the forward direction.

### Mie scattering regime: $x \sim 1$

Gustav Mie developed in 1908 a mathematical theory with which the optical behaviour of spherical particles of about the same size of the wavelength of the incident radiation is described. Mie theory allows the exact calculation of scattering  $C_{scat}$  and the absorption cross-sections  $C_{abs}$  for any spherical particle by solving the electromagnetic wave equations for a spherical boundary. Numerical Mie codes are wide spread, the Mie code used in this work (see Section 3.3.7) is based on the *Bohren and Huffman* (1983) Mie code for the treatment of spherical particles and the *Toon and Ackerman* (1981) Mie code for the treatment of coated spheres (see Section 3.3.7, p. 78). The interaction of non-spherical particles with radiation can be approximated with Chebyshev particles or calculated exactly by the T-matrix method (e.g. *Mishchenko*, 1990; *Borrmann et al.*, 2000). In contrast to the Rayleigh regime, where scattering is strongly dependent on the wavelength, in the Mie regime almost all wavelengths are scattered with similar intensity. Scattering of particles in the Mie regime is mostly responsible for the reduction of visibility in the atmosphere. Particles in the range between  $0.1 < D_p < 1 \mu\text{m}$  scatter light most efficiently. This can be illustrated by an examination of the mass-normalised extinction as a function of particle size (Figure 13).

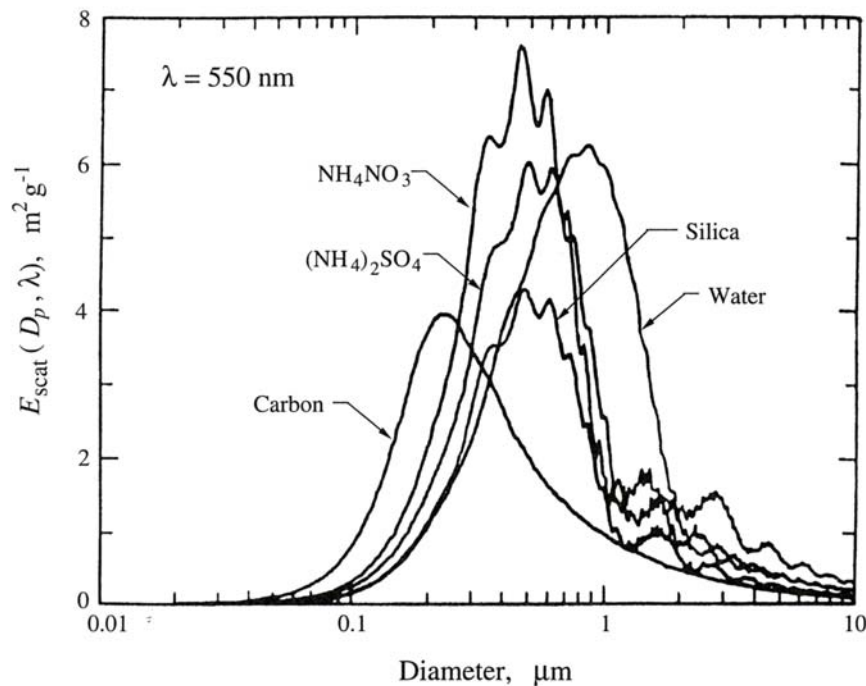


**Figure 13.** Mass scattering efficiencies  $E_{scat}$  ( $\lambda = 550 \text{ nm}$ ) of homogeneous spheres of  $(\text{NH}_4)_2\text{SO}_4$ ,  $\text{NH}_4\text{NO}_3$ , carbon, and silica (adopted from *Seinfeld and Pandis*, 1998).

### Geometric scattering regime: $x \gg 1$

For particles much larger than the wavelength of the incident light, scattering can be described by geometric optics of reflection, refraction and diffraction. In this regime, scattering is strongly dependent on the size and the orientation of the particles relative to the incoming beam of light. Atmospheric phenomena like rainbows or halos are described with geometric optics.

Whereas all particles scatter light, only particles consisting of some fraction of absorbing substances absorb light. The complex refractive index  $m$  (Bohren and Huffman, 1983)

$$m(\lambda) = n(\lambda) + i \cdot k(\lambda) \quad (2.14)$$

describes the optical properties of the particle relative to the surrounding medium and is a function of the wavelength. Both, the real part  $n$  and the imaginary part  $k$  of the refractive index are determined by the chemical composition of the particle. For non-absorbing particles,  $k$  is zero, while for absorbing particles  $k$  is larger than zero. Table 2 summarises refractive indices for substances contained in forest fire and desert dust aerosols. Usually, the refractive index  $m$  is normalised to the refractive index of the surrounding medium. Since the surrounding medium of atmospheric aerosol particles is air, which has a refractive index of unity, the normalised refractive index and that of the particle are quasi identical. Often, particles are composed of multiple components. The refractive index of multi-component particles is commonly approximated by an effective medium mixing rule (Ackerman and Toon, 1981; Ouimette and Flagan, 1982; Chýlek et al., 1988) under the assumption that the particle is a homogeneous mixture of the single components. Applying this approximation, the real and imaginary part of the refractive index for particles composed of  $j$  components can be calculated as a linear combination of the refractive indices of the individual components  $l$  weighted by their volume fraction  $f_l$

$$n = \sum_{l=1}^j n_l \cdot f_l \quad \text{and} \quad k = \sum_{l=1}^j k_l \cdot f_l \quad (2.15)$$

For example, applying Equation 2.15, the refractive index  $m_{mixture}$  for an aerosol composed of quartz ( $f_{quartz} = 0.6955$ ), haematite ( $f_{haematit} = 0.0045$ ) and kaolinite ( $f_{kaolinite} = 0.3$ ) is  $m_{mixture} = 1.5597 + 0.0041i$ .

**Table 2.** Refractive indices of atmospheric substances at  $\lambda = 550 \text{ nm}$ .

Substance	$n$	$k$	Source
Water	1.333	0.0000	Shettle and Fenn (1979)
H2SO4	1.430	0.0000	Shettle and Fenn (1979)
(NH4)2SO4	1.530	0.0000	Shettle and Fenn (1979)
black carbon	1.965	0.6350	Ackerman and Toon (1981)
quartz	1.543	0.0000	Sokolik and Toon (1999)
haematite	3.315	0.4882	Sokolik and Toon (1999)
kaolinite	1.572	0.0064	Arakawa et al. (1997)

Light scattering by particles can be divided into three groups: elastic scattering, quasi-elastic scattering and inelastic scattering. During quasi-elastic scattering processes, the wavelength shifts due to Doppler effects and diffusion broadening, while during inelastic scattering processes the emitted radiation has another wavelength than the incident radiation. Inelastic scattering processes include Raman scattering and fluorescence. For the interaction of solar radiation with aerosol particles, only elastic scattering processes are of relevance. When a beam of light is scattered elastically, the wavelength of the scattered light stays the same as that of the incident beam. The direction of the scattered light, however, can differ from the incident direction. The angle between the incident and the scattered beam is called *scattering angle*  $\theta_s$ . If the light is scattered into the forward direction ( $\theta_s < \pi/2$ ) it is referred to as forward scattering, whereas the backscattered light refers to range  $\theta_s > \pi/2$ . The angular

distribution of the light scattered by a particle at a given wavelength depends on the number of excited normal modes.

The (*scattering*) *phase function*  $P_s(\theta_s, x, m)$  describes the angle-dependent scattering of light impinging on a particle (*Seinfeld and Pandis, 1998*)

$$P_s(\theta_s, x, m) = \frac{I(\theta_s, x, m)}{\int_0^\pi I(\theta_s) \cdot \sin \theta_s \, d\theta_s} \quad (2.16)$$

With increasing particle size, the directional asymmetry of the scattering phase function becomes more pronounced (see Figure 12), and the scattering peaks more and more in the forward direction (Mie theory). The directional asymmetry of the scattering with its forward peak is the reason why visibility is decreased if one looks in the direction of the sun.

The *asymmetry parameter*  $g$  describes the irradiance-weighted average of the cosine of the scattering angle (*Seinfeld and Pandis, 1998*)

$$g = \frac{1}{2} \cdot \frac{\int_0^\pi \cos \theta_s \cdot I(\theta_s) \cdot \sin \theta_s \, d\theta_s}{\int_0^\pi I(\theta_s) \cdot \sin \theta_s \, d\theta_s} = \frac{1}{2} \cdot \int_0^\pi \cos \theta_s \cdot P(\theta_s) \cdot \sin \theta_s \, d\theta_s \quad (2.17)$$

For  $g = 0$ , the light is scattered equally in all directions, forward and backward; for  $g = 1$ , the light is scattered completely into the forward direction (at  $\theta_s = 0^\circ$ ), whereas for  $g = -1$  all the light is scattered backwards (at  $\theta_s = 180^\circ$ ).



---

## 3 Methods

---

The data used in this study for the assessment of aerosol microphysical and optical properties and their impacts on the atmosphere, were acquired from a (large) range of instruments. All instruments were operated on board the Falcon 20-E5 research aircraft of the DLR providing a unique, vertically and horizontally high resolved data set on properties of forest fire and desert dust particles. A high quality data set requires several conditions, an excellent preparation/calibration of the instruments, a data quality assurance procedure, favourable weather conditions during a field experiment and the combination of measurement data and model calculations. This chapter not only describes the measurement methods, the transfer functions of the various aerosol in-situ instruments, and the two field experiments ITOP 2004 and SAMUM 2006, it also shows the results of the work done within this thesis to ensure high data quality of all experimental data. Since the instrumentation and the measurement concept used during ITOP and SAMUM differed significantly, a separate section summarising the differences between both field studies is added.

### ***3.1 Aerosol measurements aboard the Falcon research aircraft***

This sub-section provides an overview over the individual aerosol in-situ instruments and measurement techniques including a short description of the measurement platform, the Falcon 20-E5 research aircraft. Since the size of aerosol particles extends over several orders of magnitude, different measurement techniques (condensation, deposition, electrical mobility, light scattering and light transmission) are required to completely cover the relevant particle size ranges. The combination of all instruments covers the whole aerosol size range from smallest particles in the nucleation mode ( $D_p \sim 4$  nm) up to coarse mode particles in the far super-micron size range ( $D_p \sim 100$   $\mu\text{m}$ ), the non-volatile aerosol in the sub-2.5  $\mu\text{m}$  size range and the spectral absorption coefficient.

#### ***3.1.1 The DLR research aircraft Falcon 20-E5***

The meteorological research aircraft Falcon 20-E5 (D-CMET) has been operated by the DLR for more than 20 years. For the realisation of various in-situ and remote sensing instruments, the aircraft has been modified. Three large optical windows (diameter 40 cm) at the bottom and in the ceiling for optical measurements and a number of holes were built in the fuselage in order to draw air into the cabin to analyse it with numerous instruments. Furthermore, four wing-pods were added for the operation of the optical spectrometers like

PCASP-100X, FSSP-100 and FSSP-300, and cloud measuring instruments. Figure 14 depicts the Falcon during a scientific flight mission. On top of the fuselage the aerosol inlet and two trace gas inlets are visible. The optical spectrometers PCASP-100X FSS-300 and FSSP-100 are mounted under the wings. Multiple sensors are located in the front part for the measurement of meteorological parameters like static pressure, temperature and humidity (“Falcon standard instrumentation”). In addition, the aircraft is routinely equipped with a data acquisition system to measure the aircraft position (altitude, longitude, and latitude). The Falcon has a maximum take-off mass of 13.8 t and can carry a payload of 1100 kg. The absolute ceiling is 42000 ft. The flight time is limited to 4 h. The Falcon cruises on average with a speed of approximately  $200 \text{ m s}^{-1}$ .

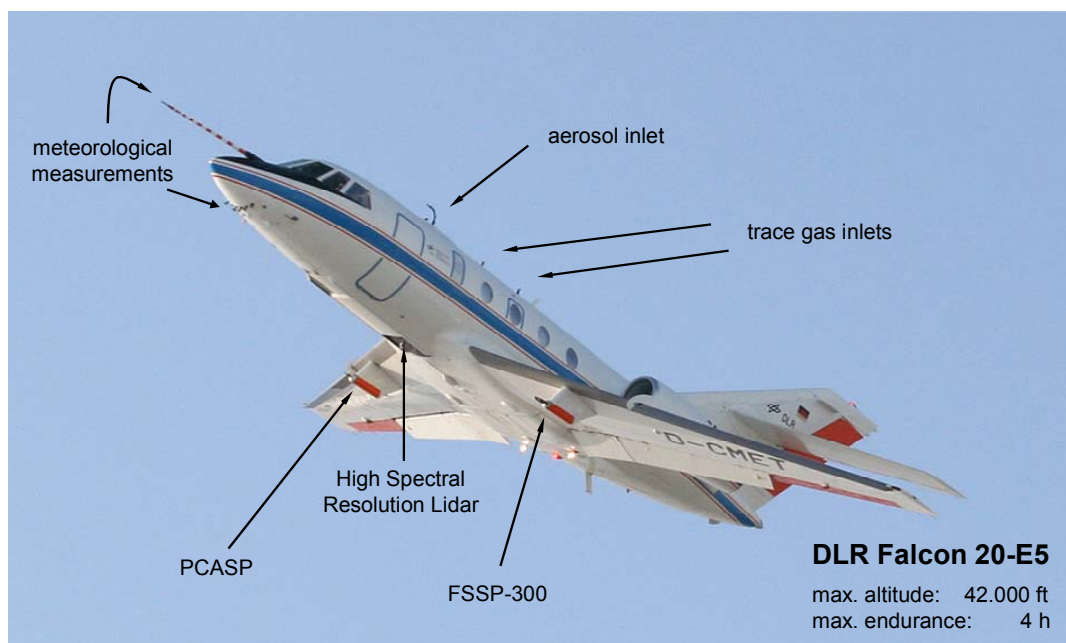


**Figure 14.** The Falcon 20-E5 research aircraft. The aircraft was highly modified for the realisation of various in-situ and remote sensing measurements (photo: A. Minikin).

During ITOP and SAMUM the Falcon served as an excellent measurement platform allowing the horizontal and vertical probing of forest fire and desert dust aerosol layers.

### 3.1.2 Condensation Particle Counter (CPC)

A Condensation Particle Counter (CPC) is a single-particle counting instrument, which provides the integral particle number concentration  $N$  above a certain cut-off diameter  $D_{p,50\%}$ . Sub-100 nm particles are too small for detection by light scattering, but these ultrafine particles can initiate droplet formation in a supersaturated environment by the Kelvin-effect. A CPC uses a condensation technique to enlarge sub-100 nm particles to sizes that can easily be detected by optical methods (Figure 15). The aerosol sample first passes through a chamber with saturated vapour (e.g. water, n-butyl alcohol<sup>9</sup>), where the sample is saturated with a condensable vapour. Then the aerosol sample is cooled down by about 20-30 K in the condenser. Due to the decrease in temperature, a supersaturated environment evolves and the vapour starts to condense on the particles (*heterogeneous condensation*). This process grows

<sup>9</sup> The working fluid in the DLR CPCs is n-butyl alcohol.

the particles to optical detectable sizes that are detected by light transition measurement. The saturation ratio  $S$  determines the minimum detectable particle diameter  $D_{p,50\%}$ <sup>10</sup> via the Kelvin equation (Hinds, 1999)

$$D_{p,50\%} = \frac{4 \cdot \sigma_{fluid} \cdot M_{fluid}}{R \cdot T_{cond} \cdot \rho_{fluid} \cdot \ln S} \quad (3.1)$$

where  $\sigma_{fluid}$ ,  $M_{fluid}$ ,  $R$ ,  $T_{cond}$  and  $\rho_{fluid}$  are the surface tension and the molecular weight of the condensing fluid, the gas constant, the temperature in the condenser and the liquid-phase density. The supersaturation that is required for the formation of droplets depends on the working fluid, and the saturation ratio is controlled by the temperature difference  $\Delta T$  between the saturation and the condensation path. An increased  $\Delta T$  causes a higher supersaturation resulting in a decreased minimum detectable diameter  $D_{p,50\%}$ . In the DLR CPC system  $\Delta T$  can be varied between 6 and 30 K, which corresponds to lower cut-off diameters of 4-20 nm.

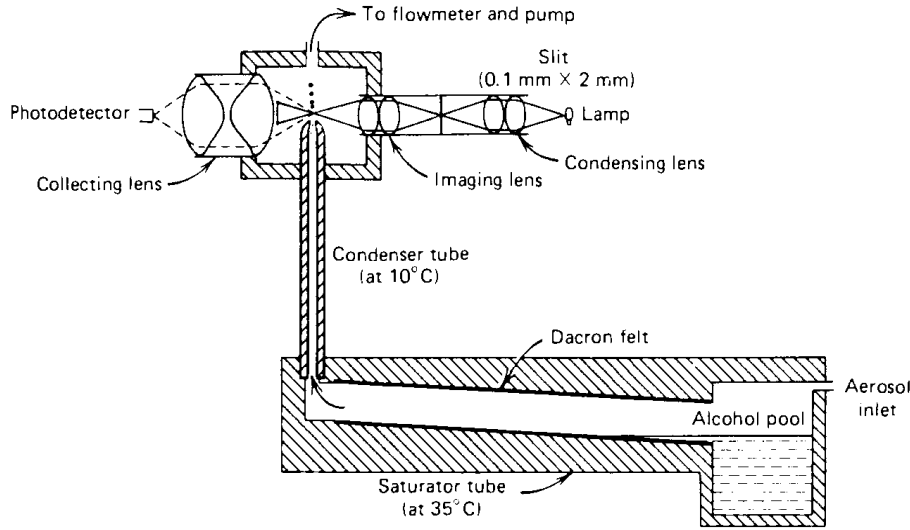


**Figure 15.** Functional principle of a condensation particle counter (CPC). Supersaturation is achieved by diffusive cooling.

As the saturation ratio is not exactly constant over the whole condensation path, the minimum detectable diameter is not a sharp boundary, but an s-shaped function. According to Banse *et al.* (2001) the CPC transfer function  $Tr_{CPC}(D_p)$  can be described by a sigmoidal function

$$Tr_{CPC}(D_p) = \begin{cases} a - b \cdot \left[ 1 + \exp\left(\frac{D_p - D_1}{D_2}\right) \right]^{-1} & ; \quad D_p \geq D_0 \\ 0 & ; \quad D_p < D_0 \end{cases} \quad (3.2)$$

with  $D_0 = D_2 \ln(b/a-1) + D_1$ . The parameters  $a$ ,  $b$ ,  $D_1$  and  $D_2$  are fitting parameters. The CPC transfer function can be determined experimental. Figure 16 shows the theoretical calculated

<sup>10</sup> The minimum detectable diameter  $D_{p,50\%}$  refers to the diameter with 50% counting efficiency.

(lines) and measured transfer function of CPSA<sup>11</sup> (symbol) module 1 for different minimum detectable diameters  $D_{p,50\%}$  (adopted from Stein, 2000).

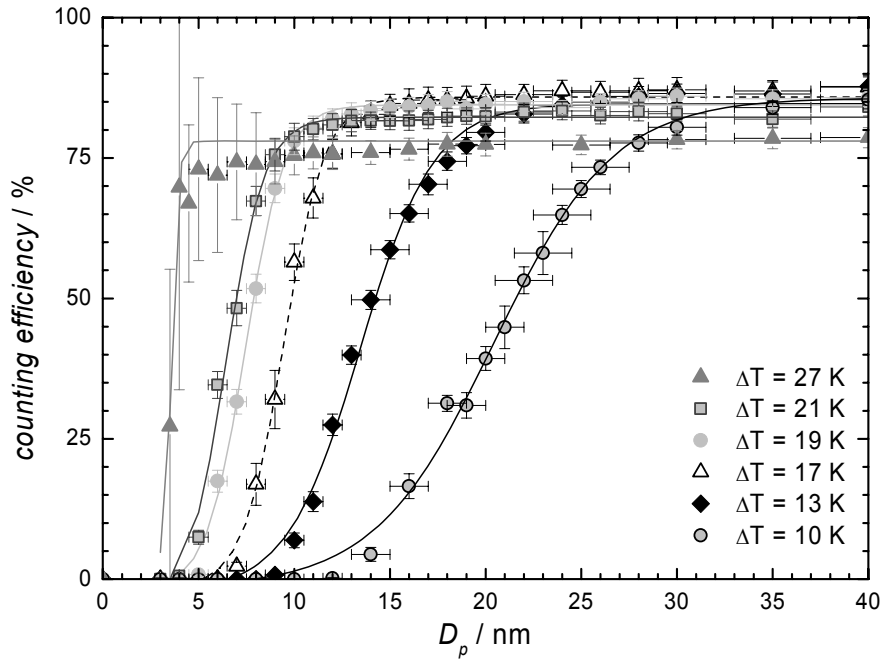


**Figure 16.** Transfer functions of CPSA module 1 for different saturation ratios achieved by different temperature settings (adopted from Stein, 2000). An increased temperature difference  $\Delta T$  shifts the minimum detectable diameter with 50% counting efficiency  $D_{p,50\%}$  to smaller particle diameters.

A CPC is capable of detecting very high particle concentrations ( $N > 10\,000\text{ cm}^{-3}$ ). The factor limiting the detection of particle concentrations  $N > 10\,000\text{ cm}^{-3}$  is coincidence, which means that two particles appear simultaneously in the optical field, but only one particle is counted. Furthermore, the supply of condensable vapour in the saturator is limited. That is, for high concentrations not every particle can grow to detectable sizes. The particle number concentrations can be corrected for coincidence losses with the following equation

$$N_{atmos} = N_{CPC} \cdot e^{(N_{atmos} \cdot q_{CPC} \cdot t_{pulse})} \quad (3.3)$$

In Equation 3.3,  $N_{atmos}$  and  $N_{CPC}$  are the number concentration in the atmosphere and the number concentration shown by the CPC, respectively. The parameter  $q_{CPC}$  denotes the flow rate through the CPC and  $t_{pulse}$  refers to the time needed to count one particle.  $N_{atmos}$  in the exponent of Equation 3.3 can be approximated by  $N_{CPC}$  (CPC manual). For particle concentrations of about  $10\,000\text{ cm}^{-3}$ , the atmospheric concentration is about 7% higher than the indicated concentration.

The accuracy of a CPC depends crucial on a constant flow rate through the system, because the CPC counts the number of particles that pass a photodetector in a second. These counts per second can be converted to number concentrations, if the flow through the system is known. The flow through the CPC can be tuned very precisely with a critical nozzle.

<sup>11</sup> The Condensation Particle Size Analyser (CPSA) is a self-build combination of four CPCs, operated on different cut-off diameters.

Critical nozzles make use of the following effect: if the pressure upstream of a nozzle is more than two times the pressure downstream of the nozzle, the gas is accelerated to sonic speed at the narrowest part of the nozzle. As sonic speed can not be exceeded in the flow, the volume flow through the system stays constant, even if pressure rises.

On board the Falcon research aircraft, a set of six CPC instruments is operated on different cut-off diameters  $D_{p,50\%}$  (e.g. 4 nm, 10 nm, 20 nm) and provides very high resolution data (1 Hz) of ultrafine particle number concentrations.

### 3.1.3 Diffusion Screen separators (DS)

Ultrafine particles in the size range between 20 and 100 nm are commonly measured by a differential mobility analyser (DMA; see Section 3.1.4, p. 37). However, the DMA needs about one minute for a complete scan. Therefore, a faster sizing measurement method is used to provide data with high time resolution in the size range between 20 and 100 nm. As the minimum detectable diameter can only be shifted to particle diameters of approximately  $D_{p,50\%} \leq 20$  nm for the commonly used working fluid n-butyl alcohol (e.g. Brock *et al.*, 2000; Stein *et al.*, 2001), the CPCs are combined with Diffusion Screen separators (DS) (Feldpausch *et al.*, 2006). DS are similar to a single stage of a screen-type diffusion battery. The application of diffusion batteries is reviewed by Knutson *et al.* (1999). A DS consists of a set of metallic meshes, which offer a surface for particle deposition (Figure 17).

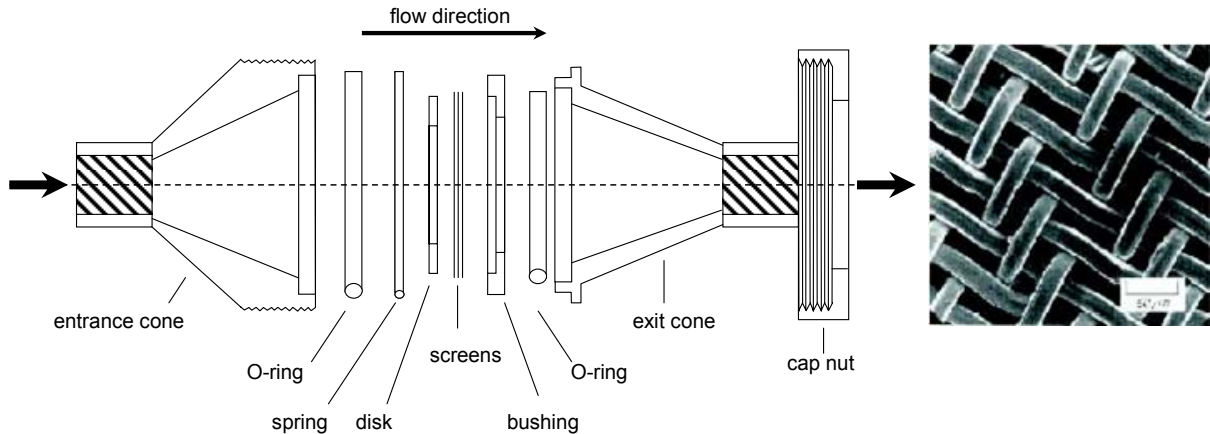


**Figure 17.** Schematic diagram of a diffusion battery (left panel) and microscopic image of a single screen (right panel).

Particles are deposited due to their diffusion coefficients on the meshes. The deposition efficiency is a function of the particles size, with small particles being deposited most efficient. The removal of small particles from an aerosol sample by a DS can be described by the theory of particle deposition on fibres or wires. The fraction of particles of a given size penetrating a fibrous filter is described by the penetration  $P$  of the filter. The deposited fraction is then  $1 - P$ . The penetration  $P$  (Cheng and Yeh, 1980) can be expressed as follows

$$P = \exp\left(-\frac{4 \cdot \alpha_s \cdot E_\Sigma \cdot t_f}{\pi \cdot (1 - \alpha_s) \cdot D_f}\right) \quad (3.4)$$

where  $\alpha_s$ ,  $t_f$  and  $D_f$  is solidity volume fraction of the filter material, the thickness of the filter or mesh, and the single-fibre diameter.  $E_\Sigma$  is the total single-fibre efficiency concerning particle removal. Particles are deposited on a fibre by interception ( $E_R$ ), impaction ( $E_I$ ), diffusion ( $E_D$ ), gravitational sedimentation ( $E_G$ ), and electrostatic attraction ( $E_q$ ) and enhanced diffusion ( $E_{DR}$ ) due to interception of diffusing particles. All these mechanisms are expressed by the total single-fibre efficiency  $E_\Sigma$ . More details on deposition are given in *Hinds (1999)* and *Feldpausch et al. (2006)*.

The validity of this penetration theory was originally tested for standard pressure conditions. *Feldpausch et al. (2006)* showed that the diameter with 50% penetration shifted to from 45 nm at 950 hPa to 100 nm at 200 hPa for a DS containing 3 screens. Their calibration experiments revealed that the theory of diffusion deposition can be extended from standard conditions down to pressure levels of 200 hPa. *Feldpausch et al. (2006)* concluded that combined DS-CPC systems can be applied for airborne measurements of upper tropospheric aerosol size distributions. To obtain the transfer function  $Tr_{DS}$  of a combined DS-CPC system (*Feldpausch et al., 2006*), the penetration  $P$  has to be multiplied by the corresponding transfer function of the CPC (see Equation 3.2, p. 33)

$$Tr_{DS} = P \cdot Tr_{CPC} \quad (3.5)$$

The penetration depends on the number of used screens and therefore determines the lower cut-off diameter of the combined DS-CPC system. An increasing number of screens in the DS shift the lower cut-off diameter to larger particles. Figure 18 presents transfer functions for combined DS-CPC systems with different numbers of screens. In the Figure 18, DS#1, DS#2 and DS#3 contained 3, 10 and 17 screens, respectively.

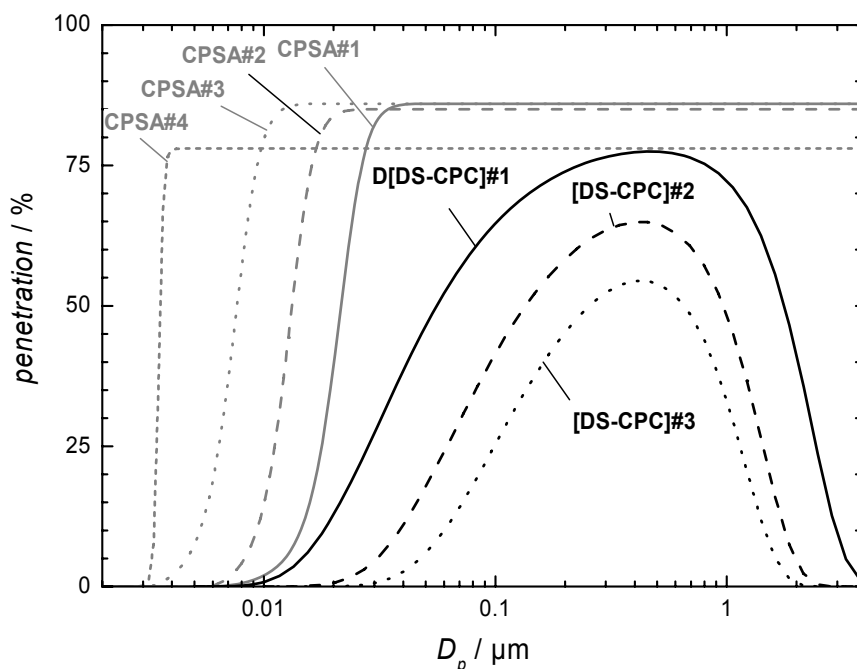


**Figure 18.** Transfer functions for a combined DS-CPC system (adopted from *Feldpausch et al., 2006*). An increasing number of screens in the DS shifts the lower cut-off diameter to larger particles.

### 3.1.4 Differential Mobility Analyser (DMA)

A Differential Mobility Analyser (DMA) is based on the electrostatic classification of aerosols. During the classification process, the particles are separated into size classes according to their electrical mobility  $Z$ , which is a function of particle size  $D_p$  (Hinds, 1999)

$$Z = \frac{n_e \cdot e \cdot C_c}{3 \cdot \pi \cdot \eta \cdot D_p} \quad (3.6)$$

where  $n_e$  denotes the number of elementary units of charges  $e$  ( $1.6 \cdot 10^{-19}$  C) of an electron,  $C_c$  is the Cunningham factor and  $\eta$  is dynamic viscosity. The electrical mobility is measured in  $\text{m}^2 (\text{V s})^{-1}$ .

The improved DMA introduced by Knutson and Whitby (1975b;1975a) consists of a coaxial cylinder condenser with two inlets and two outlets. Figure 19 sketches a DMA.

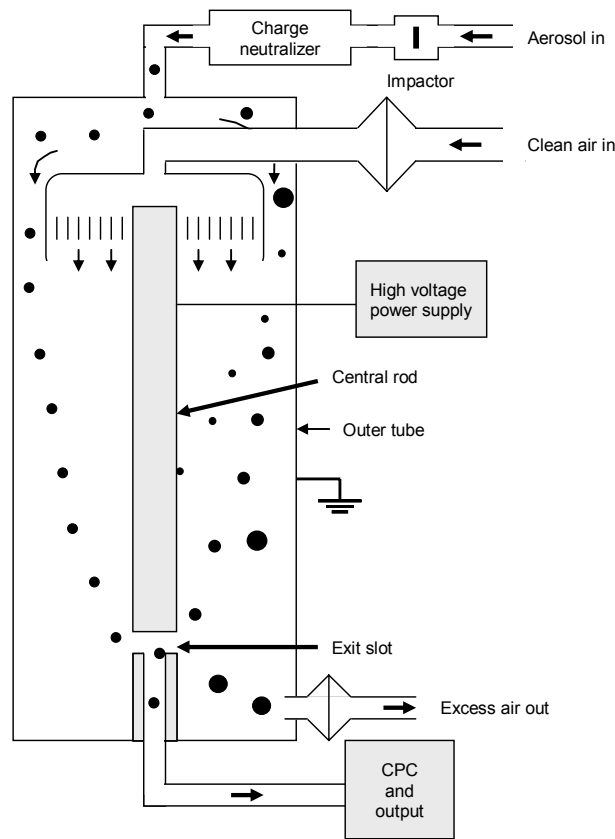


**Figure 19.** Schematic diagram of a differential mobility analyser (adopted from Hinds, 1999).

The aerosol sample passes through an impactor which removes particles larger than 10  $\mu\text{m}$ . To ensure a fixed percentage of particles carrying one unit charge, the particles pass a bipolar charger. After the neutralisation process, an equilibrium state is obtained, with a known percentage of particles carrying no charge, a single charge and multiple charges, respectively. The neutralised aerosol is then drawn into the classifier with the flow rate  $q_{aerosol}$ , where it surrounds as a thin aerosol layer the annular flow of clean air (flow rate  $q_{sheath}$ ). The flow of clean air forces the aerosol to flow downward close to the outer wall of the condenser. As the aerosol flows downward into the classifier, the electrical field in the condenser attracts

charged particles from the aerosol layer, forcing them to move across the clean air flow to the central rod. Particles with high electrical mobility deposit at the central rod before reaching the exit slot, particles with low electrical mobility are carried out with the excess air flow (flow rate  $q_{excess}$ ). Only particles in a narrow range of mobility can enter the exit slot and are detected with a CPC. The probability that an aerosol particle of mobility  $Z$  which enters the classifier can leave via the exit slot is given by the transfer function  $Tr(Z)$ . The transfer function can be obtained from particle trajectory analyses (for more detail see *Knutson and Whitby, 1975b*). *Knutson and Whitby (1975b)* derived a trapezoidal transfer function with a relative half-width of  $q_{aerosol}/q_{sheath}$  from particle trajectory analyses. *Roth et al. (1989)* showed that a Gaussian transfer function better fits the monodisperse aerosol leaving a DMA.

The aerosol size distribution can be derived from the number concentration of classified particles  $N_c$  in the output aerosol (*Reischl, 1991*). The effect of the multiple charged particles can be neglected for particles smaller  $0.2 \mu\text{m}$  (see DMA manual). For single-charged particles and a narrow transfer function, the number of classified particles is given by the following equation

$$N_c = Tr_{CPC}(D_p) \cdot \alpha(D_p, n_e = 1) \cdot \frac{q_{aerosol}}{q_{sheath}} \cdot \Psi(D_p) \cdot \left. \frac{dN}{d \log D_p} \right|_{D_p} \quad (3.7)$$

where  $Tr_{CPC}$  is the transfer efficiency of the connected CPC (see Equation 3.2) and  $\alpha(D_p, n_e = 1)$  the fraction of single charged particles.  $\Psi(D_p)$  represents the influence of the Cunningham slip correction factor on the resolution of the DMA.  $\Psi(D_p)$  approaches 0.5 for  $D_p \rightarrow 0$  and 1.0 for  $D_p \rightarrow \infty$ . The DMA selected aerosol is mainly singly charged and nearly monodisperse. By stepping through different voltages, particles with different sizes can be selected due to their electrical mobility. With this procedure a particle size distribution can be obtained. The DMA works best for particles in the size range  $0.01 < D_p < 0.2 \mu\text{m}$  (*Hinds, 1999*). In the DLR configuration, a several size steps take about one minute. The geometric design of a DMA determines the size range that can be detected and the aerosol flow rates with which the DMA can be operated. The properties of the resulting size distribution of the classified aerosol can be described with the DMA transfer function (*Reischl, 1991*). One important application of a DMA is the generation of monodisperse test aerosols of a known size. This is needed for the calibration of optical spectrometers like PCASP-100X or FSSP-300 (see Section 3.1.5., p. 38ff).

### 3.1.5 Optical particle counters (OPC)

The DLR uses a number of optical particle counters (OPC), which are described in more detail in the following sections. OPCs operate on the principle of light scattering and provide particle size distributions in a certain size range from the intensity of the scattered light. The scattered light is a function of the particle size. The intensity of the scattered light seen by the spectrometer is determined by the instrument-specific scattering cross-section  $C_{scat, OPC}$ , which is a function of particle size, refractive index and particle shape. The instrument-specific scattering cross-section can be calculated adopting Mie theory for several refractive indices. OPCs use a laser to illuminate a volume in an aerosol flow. As the particles pass through the laser beam they scatter light in all directions. Some of the light is collected and focussed on a photodiode. The particles are sized into different channels by comparing the peak amplitude of each pulse to preset voltage thresholds. The count is assigned to the channel which upper

and lower thresholds include the measured pulse height value. The OPCs used at the DLR only collect the light scattered through a certain solid angle in the forward direction. The restriction of the measurement to the forward scattered light is chosen to minimise the influence of the particle shape and the refractive index on the scattering properties of the particle (e.g. *Mishchenko et al.*, 1997).

### 3.1.5.1 Forward Scattering Spectrometer Probe (FSSP-300)

The FSSP-300 is designed to measure particle size distributions from 0.3 to 20  $\mu\text{m}$  (depending on the refractive index; for example, the upper detection limit shifts to larger particle sizes for absorbing particles). The operating principles for the FSSP-300 are described by *Baumgardner et al.* (1992). The scattering cross-sections are divided into 31 size classes (channels) with a higher resolution for smaller sizes. Particles are classified by the amount of light that is forward-scattered into the optics aperture during the particle interaction with a focused helium-neon laser ( $\lambda = 632 \text{ nm}$ ). Figure 20 illustrates the optical path of the FSSP-300. The laser beam is focussed to a small diameter at the centre of the inlet and impinges on the particles in the incoming aerosol flow. On the opposite site of the inlet a “dump spot” is situated on the prism. The “dump spot” blocks the main beam, while the forward scattered light enters a beam-splitting prism. The “dump spot” on the prism defines together with the lenses a collection angle from approximately 3-15° for the scattered light. The scattered light is divided into two components by a beam splitter and each is then detected by a photodetector. One photodetector is optically masked so that it receives the scattered light only when the particle passes to the centre of the beam  $\pm 0.5 \text{ mm}$ . Particles that fall outside that area are rejected when the signal from the unmasked detector exceeds that from the masked detector.

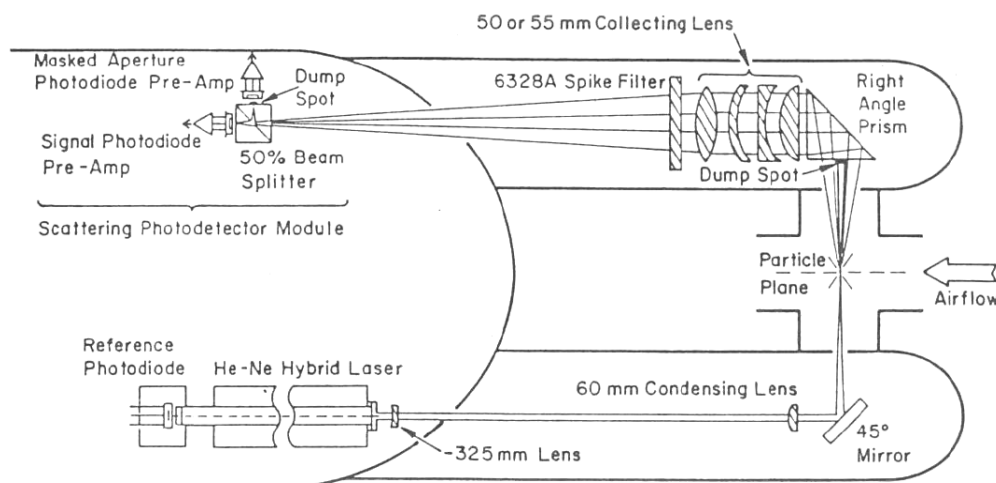


**Figure 20.** Optical path of the FSSP-300 (<http://www.eol.ucar.edu/raf/Bulletins/B24/fssp300.html>).

From the scattered light intensity, the particle size can be determined on the basis of the Mie theory, which relates the scattered light intensity to the particle size. Figure 21 shows the instrument specific scattering cross-section ( $C_{scat, FSSP-300}$ ) for three different refractive indices and illustrates how the scattered light varies with particle diameter. The scattering cross-section at the channel boundaries is marked by the grey horizontal lines. The particle

diameters at the lower and upper boundary of each channel vary according to the used refractive index. It is obvious from Figure 21 that the scattering cross-section at the channel boundaries  $C_{bound\ I}$  of a channel  $I$  can be ambiguous. To avoid errors in the interpretation of the data due to these ambiguities, adjacent channels, whose channel boundary is intercepting  $C_{scat, FSSP-300}$  several times, have to be grouped to one channel (secondary channels). For example, in the case of ammonium sulphate particles, the primary channels 7, 8 and 9 are grouped to one secondary channel. The grouping of primary channels to secondary channels and the related particle diameters at the channel boundaries are listed in Table 3 for ammonium sulphate. Similar tables exist for other chemical substances and constitute the basis for the data analysis of FSSP-300 data.

**Table 3.** Grouping of primary channels to secondary channels for ammonium sulphate ( $m = 1.53 + 0i$ ) particles. The first row shows the secondary channels, which result from the grouping of primary channels (second row). The third and fourth (fifth and sixth) row depicts the particle diameter  $D_p$  and their uncertainties at the lower (upper) boundary of channel  $i$ .

Secondary channel $i$	Primary channel $k$	$D_p$ at lower boundary of channel $I / \mu\text{m}$	Standard deviation	$D_p$ at upper boundary of channel $I / \mu\text{m}$	Standard deviation
1	1	0.356	0.009	0.436	0.014
2	2	0.436	0.014	0.477	0.012
3	3	0.477	0.012	0.517	0.013
4	4	0.517	0.013	0.574	0.025
5	5	0.574	0.025	0.636	0.018
6	6	0.636	0.018	0.682	0.021
7	7 8 9	0.682	0.021	1.291	0.303
8	10	1.291	0.303	1.605	0.023
9	11	1.605	0.023	1.631	0.027
10	12 13 14 15 16	1.631	0.027	5.812	1.134
11	17 18 19	5.812	1.134	10.108	1.581
12	20 21 22	10.108	1.581	13.982	0.879
13	23 24 25	13.982	0.879	17.405	1.564
14	26 27 28	17.405	1.564	24.018	2.015
15	29 30 31	24.018	2.015	34.631	2.836

Besides the FSSP-300, another FSSP-type spectrometer is operated at the DLR: the FSSP-100. The optical path of the FSSP-100 is identical with that of the FSSP-300. In most cases, the FSSP-100 serves as a backup instrument to the FSSP-300. It is capable of measuring particles up to an upper limit of 100  $\mu\text{m}$ , instead of 20  $\mu\text{m}$  in the case of the FSSP-300.

### 3.1.5.2 Passive Cavity Spectrometer Probe (PCASP-100X)

The passive cavity spectrometer probe (PCASP-100X) is designed for the measurement of particles in the size range between 0.1 and 3  $\mu\text{m}$ . The diagram in Figure 23 depicts the optical path of the PCASP-100X. A helium-neon laser ( $\lambda = 632\text{ nm}$ ) is focussed on the incoming aerosol flow. Particles that encounter this beam scatter light in all directions, some of which is collected by a mirror over angles from 35-120°. The collected light is then focussed on a photodetector and classified into one of fifteen size channels. The classification of the particles works similar as described for the FSSP-300. Figure 22 illustrates how the scattered light intensity varies with particle diameter for different refractive indices. The particle size distribution can be derived from the scattered light intensity on the basis of the Mie theory, similar as shown in detail for the FSSP-300.

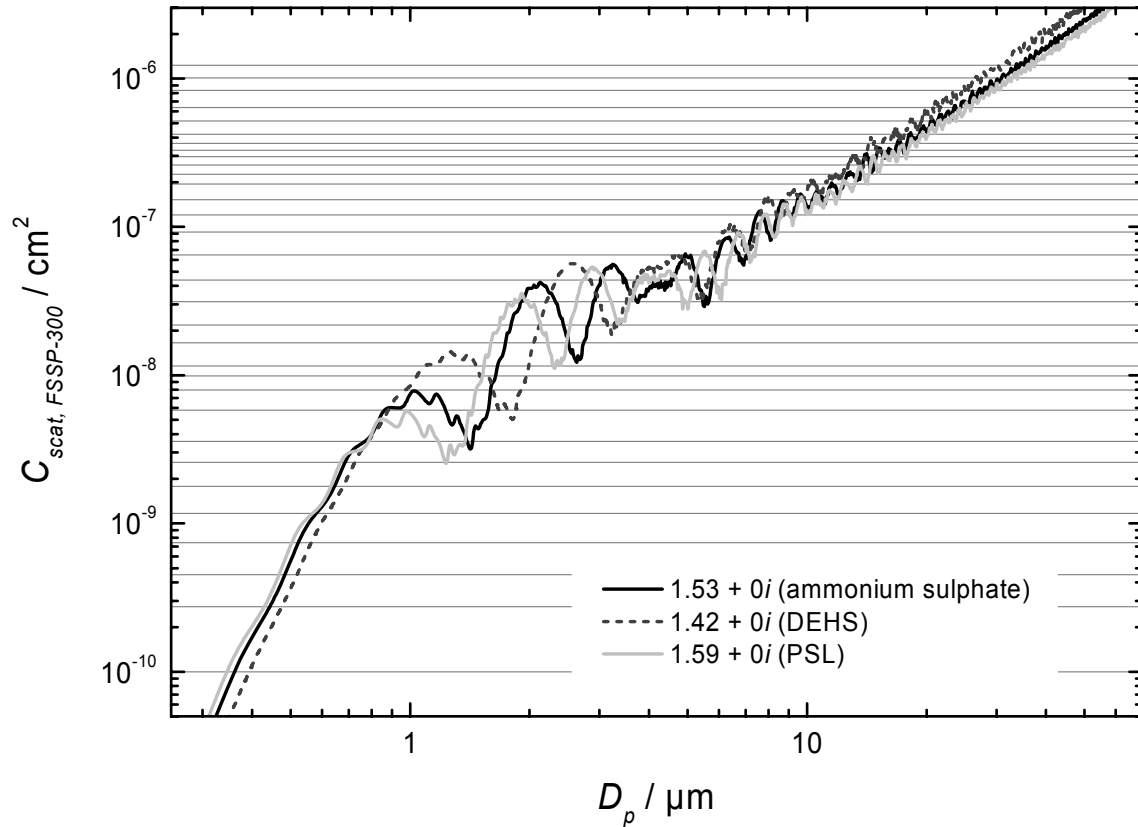


**Figure 21.** Theoretical response function of the FSSP-300 instrument for three refractive indices (courtesy: M. Fiebig).

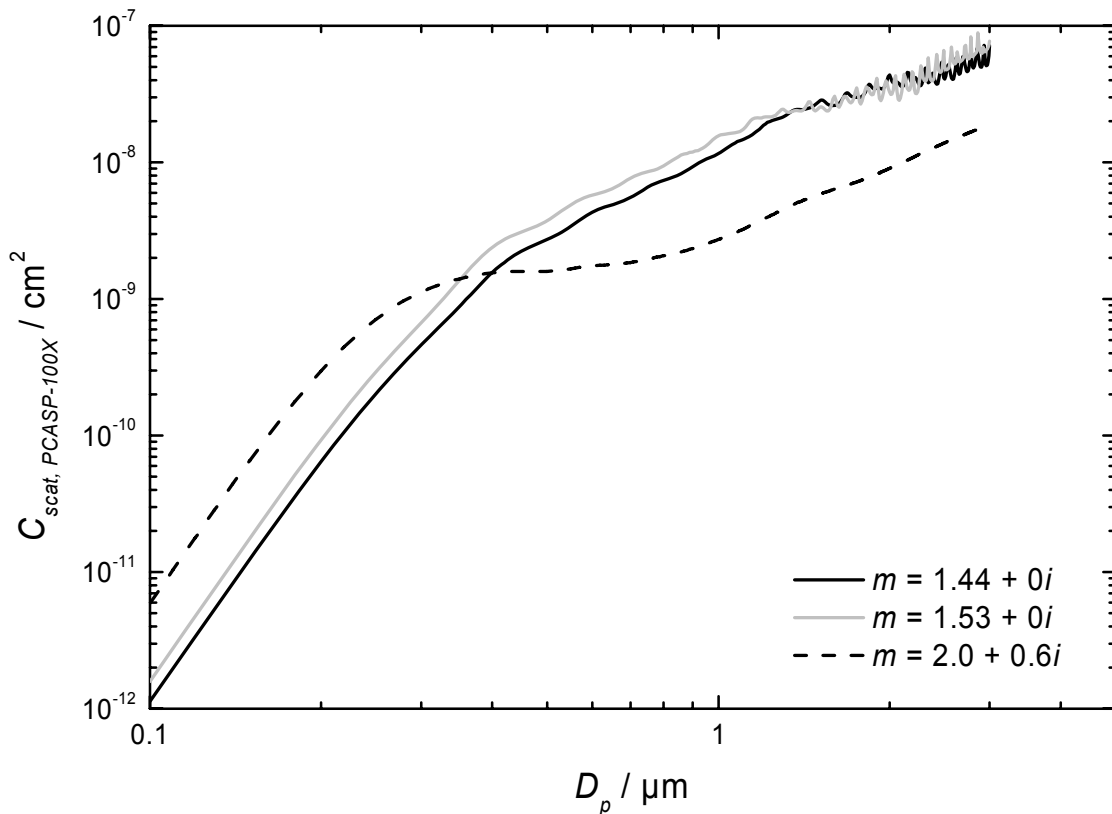


**Figure 22.** Theoretical response function of the PCASP-100X instrument for three refractive indices.

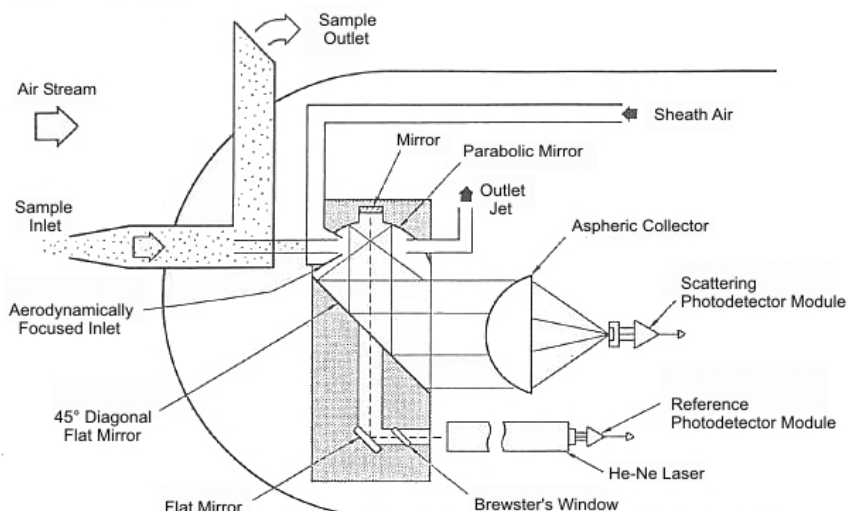


Figure 23. Optical path of the PCASP-100X.

### 3.1.5.3 Grimm OPC, model 1.109

The operating principle of the Grimm instrument is similar to those described for the FSSP-300 and the PCASP-100X. The Grimm OPC records the scattered light at  $90^\circ$  scattering angle with an aperture angle of  $30^\circ$ . The collected light is then classified into one of 31 size channels. Figure 24 shows the optical path within the Grimm instrument.

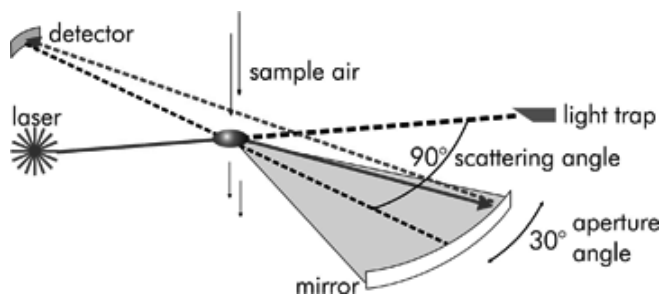


Figure 24. Optical path within the Grimm instrument.

The Grimm OPC allows the measurement of particles in the size range  $0.25\text{--}32\ \mu\text{m}$ . However, operated on board of the Falcon aircraft, the Grimm OPC is used for the measurement of the particle size distributions in the size range  $0.25\text{--}2.5\ \mu\text{m}$ . The limitation to an upper size of  $2.5\ \mu\text{m}$  is due to the aerosol inlet, which allows only particles  $< 2.5\ \mu\text{m}$  to enter the aircraft (see Section 3.1.8).

### 3.1.6 Particle Soot Absorption Photometer (PSAP)

The Particle Soot Absorption Photometer (PSAP) provides filter-based real-time measurements of absorption by particles. The aerosol is drawn through a filter, while the decrease of light transmission through the filter is monitored. From the light attenuation, the absorption coefficient  $\sigma_0$  can be derived by applying the Lambert-Beer law (e.g. Weingartner *et al.*, 2003)

$$\sigma_0 = \frac{A}{V} \ln \left( \frac{I_{t-\Delta t}}{I_t} \right) \quad (3.8)$$

where  $V$  is the volume of air drawn through the sample spot  $A$  during a certain period of time  $\Delta t$ .  $I_{t-\Delta t}$  and  $I_t$  is the filter transmittance before and after the time period  $\Delta t$ . To obtain a final value for the absorption coefficient, a number of corrections have to be made to the PSAP measurements. These corrections have been described in more detail in *Bond et al.* (1999).

Changes in transmission due to an increasing filter-load are corrected internally in the PSAP by the following equation

$$\sigma_{PSAPout} = \frac{\sigma_0}{2 \cdot \left( 0.5398 \cdot \frac{I_{t-\Delta t}}{I_t} + 0.355 \right)} \quad (3.9)$$

The presented calibration is only valid, if filter transmission ( $I_{t-\Delta t}/I_t$ ) is larger than 0.7 (*Bond et al.*, 1999). For comparison, for an unloaded filter the filter transmission is 1.

Inaccurate assumptions on the flow rate and spot size can result in significant errors. To avoid these errors the absorption coefficient needs to be corrected for these effects. Though the flow rate through the PSAP  $q_{PSAP}$  is recorded continuously, *Bond et al.* (1999) found an error in the internally measured flow rate up to 20%. They suggest to measure the flow  $q_{meas}$  directly with a high precision flow meter and to derive the flow correction factor as follows

$$f_{flow} = \frac{q_{PSAP}}{q_{meas}} \quad (3.10)$$

The PSAP is recording the volume flow with a mass flow meter. If the PSAP is operated at other conditions than standard conditions, for example on an aircraft, the flow has to be converted from standard conditions (STP; 273.15 K, 1013 hPa) to ambient conditions, by multiplication with the following conversion factor  $f_{STP}$

$$f_{STP} = \frac{V_{stp}}{V_{amb}} = \frac{T_{stp}}{T_{amb}} \cdot \frac{p_{amb}}{p_{stp}} \quad (3.11)$$

In this equation  $V_{stp}$ ,  $T_{stp}$ ,  $p_{stp}$ ,  $V_{amb}$ ,  $T_{amb}$ ,  $p_{amb}$  denote volume, temperature and pressure at standard conditions (273.15 K, 1013 hPa) and volume, temperature and pressure at ambient conditions, respectively.

As each PSAP instrument has a slightly different spot size due to small differences in fabrication of the filter holder, the spot size for each individual PSAP differs from the reference instrument. To account for these differences, the spot size diameter  $A_{meas}$  can be measured and used to correct the spot size  $A_{PSAP}$  of the reference PSAP calibrated by the manufacturer

$$f_{spot} = \left( \frac{A_{meas}}{A_{PSAP}} \right)^2 \quad (3.12)$$

*Bond et al.* (1999) estimated the total uncertainty of the corrected PSAP measurements at 60s averaging time and typical atmospheric levels to ~15%. Using all described corrections, the adjusted PSAP absorption coefficient is given by the following equation

$$\sigma_{adj} = \sigma_{PSAPout} \cdot f_{spot} \cdot f_{flow} \cdot f_{stp} \quad (3.13)$$

As both, scattering and absorption are contributing to a decreased light transmission, the PSAP derived absorption coefficient  $\sigma_{adj}$  overestimates absorption by 20-30% and therefore needs to be corrected for scattering. A simple empirical model for scattering correction is proposed by *Bond et al.* (1999). They assume that the instrument response is a linear function of both, the absorption coefficient  $\sigma_{ap}$  and the scattering coefficient  $\sigma_{sp}$

$$\sigma_{adj} = K_1 \cdot \sigma_{sp} + K_2 \cdot \sigma_{ap} \quad (3.14)$$

In a number of tests *Bond et al.* (1999) derived a value of  $0.02 \pm 0.02$  for  $K_1$ , and a value of  $1.22 \pm 0.11$  for  $K_2$ . The derived values for  $K_1$  and  $K_2$  are appropriate for correcting the PSAP absorption, if the single-scattering albedo  $\omega_0$  is larger than 0.80-0.85 (*Sheridan et al.*, 2005).

For absorption measurements on board the Falcon two types of PSAP were used: the original PSAP (1- $\lambda$ -PSAP), which is operated at a single wavelength ( $\lambda = 567$  nm) and an extended PSAP (3- $\lambda$ -PSAP) modified to measure at three wavelengths, namely 467 nm, 530 nm and 660 nm (*Virkkula et al.*, 2005). The 3- $\lambda$ -PSAP allows a determination of the wavelength-dependency of the absorbing component.

### 3.1.7 Thermal Denuder (TD)

A Thermal Denuder (TD) removes volatile/semi-volatile particles and precursors from an aerosol sample, leaving only the solid components. The volatilisation tube is a simple but effective technique (*Clarke*, 1991). The TD consists of a heated tube which heats the aerosol probe to a preset temperature (0 to 400°C). The volatile components in the aerosol evaporate, whereas the non-volatile components like dust, sea salt and carbonaceous components remain. More details on the separation of volatile and non-volatile aerosol particles by thermodesorption are given in *Burtscher et al.* (2001).

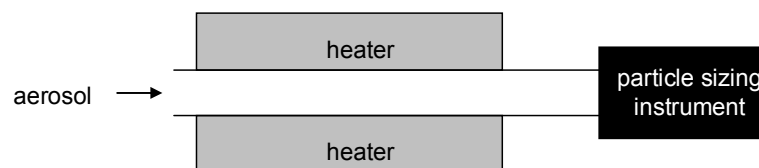


**Figure 25.** Schematic of the thermal denuder design.

A combination of a TD with particle sizing instruments like CPCs or a Grimm OPC allows the determination of the non-volatile particle size distribution. The TD used at the DLR was built and characterised at the DLR as part of a diploma thesis by *Fritzsche* (2002).

### 3.1.8 The Falcon aerosol inlet

In contrast to the optical spectrometers, which are mounted under the wings of the aircraft, part of the aerosol instruments, like the CPCs, DMA, Grimm OPC, TD, PSAP, are operated

inside the cabin of the aircraft (Figure 26). An inlet is required to transport the particles from ambient air to the instruments inside the aircraft, without changing the ambient particle properties or alternatively disturbing the aerosol sample as little as possible. Therefore, the DLR inlet is mounted outside the boundary layer of the Falcon aircraft in order to avoid a disturbance of the sampled air by the aircraft fuselage. The sampling is recommended to be isokinetic (*Wendisch et al., 2004*), which means that the velocity of the air through the inlet  $v_e$  is identical to the true air speed  $TAS$  of the aircraft. Isokinetic sampling avoids size sorting, heating, and cooling of the aerosol probe due to compression or expansion of the flow. It avoids disturbances of the ambient aerosol concentration and composition. For  $v_e > TAS$ , the flow is super-kinetic, with streamlines being bent inwards. In this case, large particles are not able to follow the streamlines and are missed in the measurements. For  $v_e < TAS$ , the flow is sub-kinetic, and large, inert particles are accumulated in the inlet.

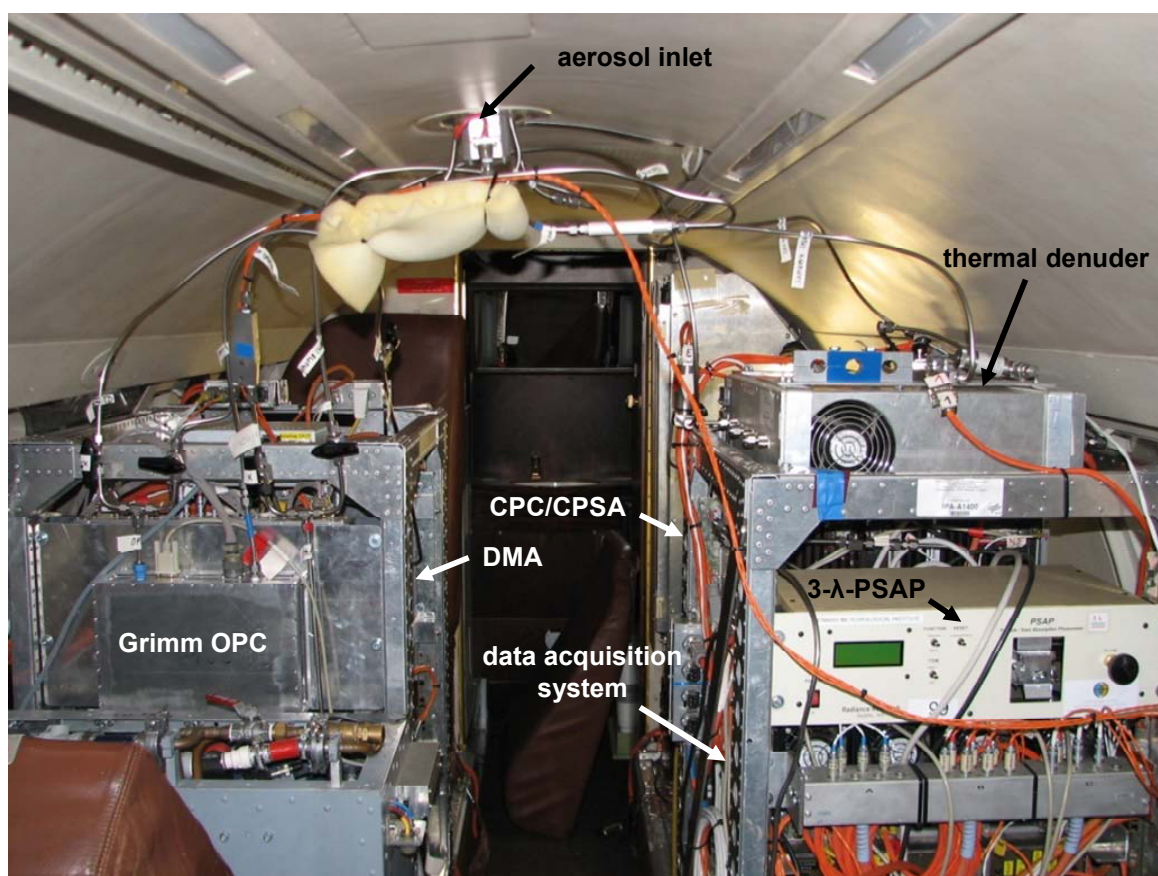


**Figure 26.** Aerosol instruments operated inside the cabin of the Falcon: Grimm OPC and DMA (left rack); 3- $\lambda$ -PSAP, impactor sampling, CPCs and optical particle spectrometer data acquisition system (right rack).

The  $TAS$  of the Falcon aircraft is  $\sim 200 \text{ m s}^{-1}$ . This means that the air has to be slowed down after entering the inlet, because such high velocities would cause turbulence in the sampling line. Figure 27 sketches the design of the aerosol inlet used on the Falcon, which can be used with backward and forward-facing configuration. The forward-facing part of the inlet allows near-isokinetic sampling of particles. Before entering the isokinetic inlet, the air passes a widening tube, the diffuser, where the flow is decelerated so that near-isokinetic sampling is ensured. With the non-isokinetic backward-facing configuration only interstitial

particles are collected. The backward configuration can be useful in the presence of ice crystals that would shatter on the leading edge of the inlet and lead to an artificially increased concentration of smaller particles.

The diameter  $D_{50\%,iso}$ , at which 50% of the particles passed the isokinetic inlet, was calculated by *Fiebig* (2001). At the ground level  $D_{50\%,iso}$  was  $\sim 2.3 \mu\text{m}$  and decreased to about  $1.5 \mu\text{m}$  at an altitude of 10 km. For the backward-facing configuration,  $D_{50\%,back}$  was  $0.19 \mu\text{m}$  at ground level and decreased to  $0.06 \mu\text{m}$  at 10 km altitude (*Fiebig*, 2001).

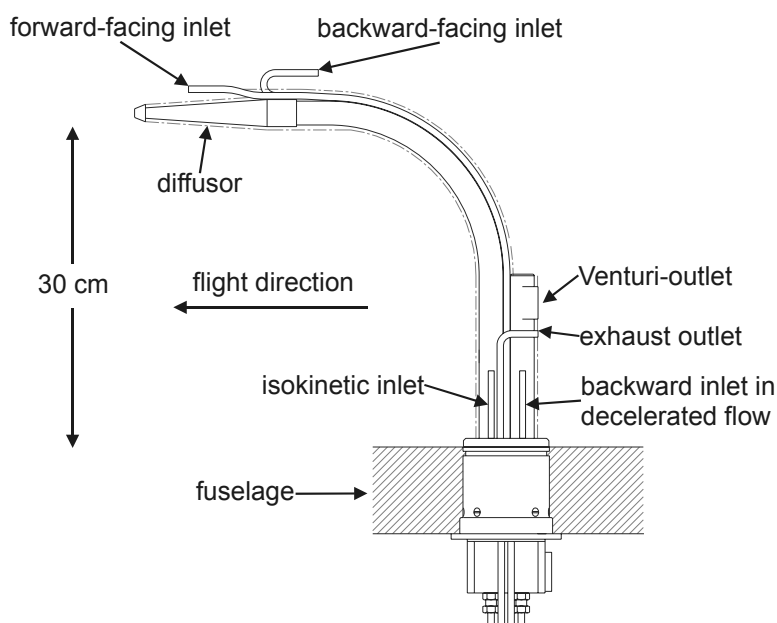


**Figure 27.** Inlet design of the inlet used at the DLR Falcon. The forward-facing inlet ensures near-isokinetic sampling, while with the backward-facing inlet only interstitial particles are collected.

### 3.1.9 Data quality assurance

To provide high quality data, it has to be assured that all instruments work properly. For that purpose, numerous calibration tests are performed. In this section only the major calibration tests for the condensation particle counters and the optical spectrometers are described in detail.

#### CPC calibration

As described earlier (Section 3.1.2, p. 32), the accurate determination of the flow rate through each CPC is crucial to derive correct particle number concentrations. The flow rate through a CPC is controlled by a critical nozzle. However, the flow rate can slightly differ from the default value of the critical nozzle or the nozzle can be blocked. Therefore the flow rate is calibrated with a gilibrator. Table 4 lists the CPC set-up, the default flow rate  $q_{default}$  and the calibrated flow rate  $q_{calib}$  for all particle counters used during ITOP and SAMUM. Values are given for both, the ITOP and the SAMUM field experiment. It can be seen from Table 4 that the average deviation between the default flow and the measured flow is 5%, but the deviation can be as large as 17%.

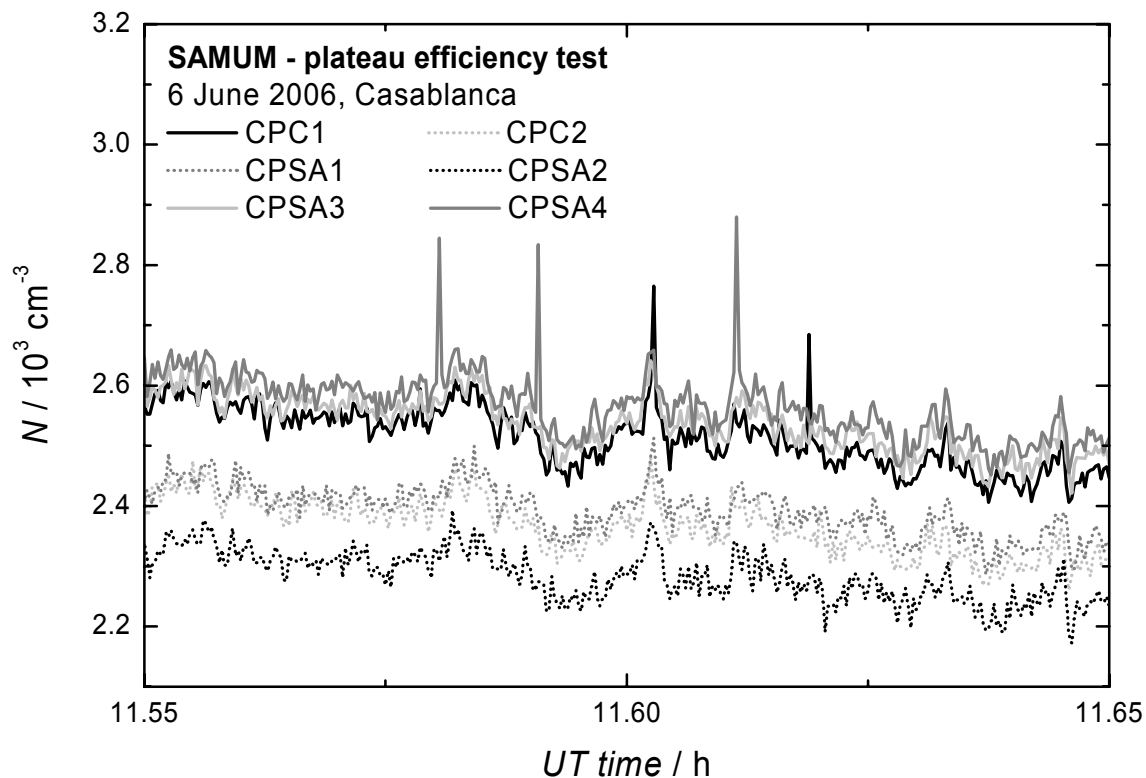


**Figure 28.** Time series of particle number concentration for all particle counters during the SAMUM plateau efficiency calibration on 6 June 2006.

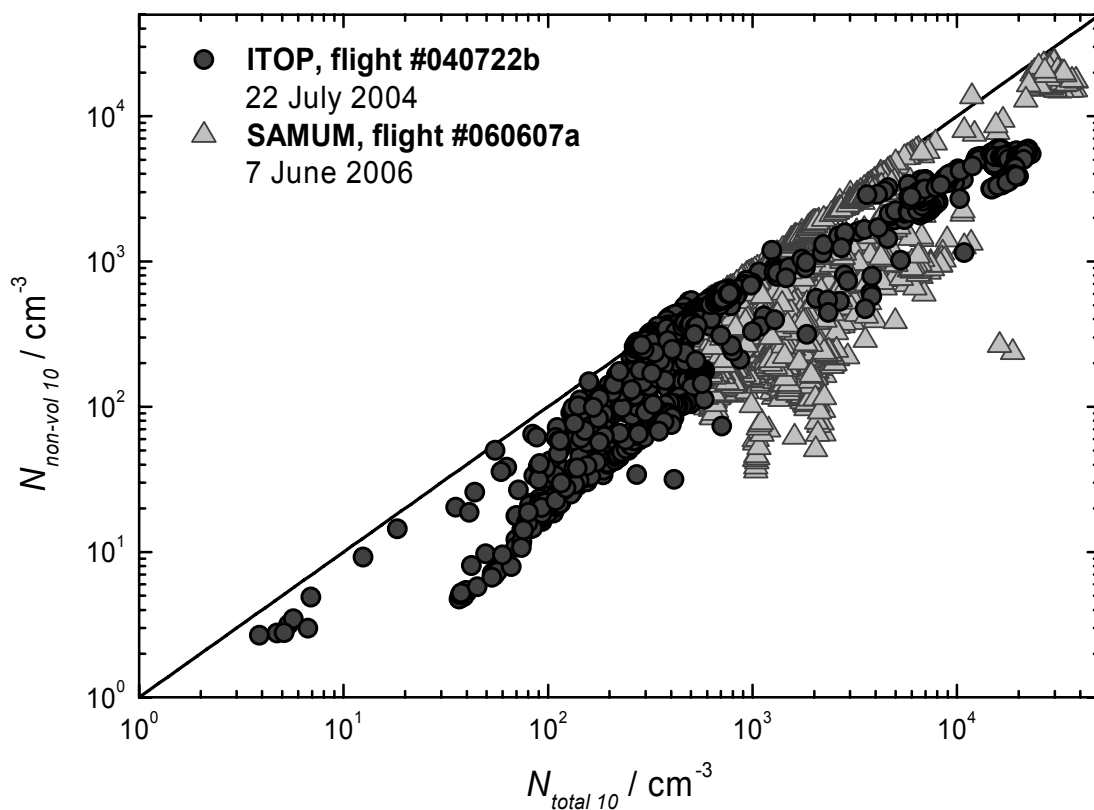


**Figure 29.** Plausibility check for plateau efficiency factors illustrated for the ITOP flight #040722b on 22 July 2004 and the SAMUM flight #060607a on 7 June 2006.

When operating several CPCs, it is important to ensure that all CPCs are counting the same particle number concentration when exposed to the same aerosol. The procedure that ensures equal counting rates is called plateau efficiency calibration. As CPCs are normally set to different lower cut-off diameters, the CPC efficiency calibration is performed with an aerosol containing only particles of sizes well above the lower cut-off diameters  $D_{p,50\%}$  of all CPCs. Therefore, the aerosol inlet is equipped with several DS containing 35 screens, which allows only particles  $D_p \gg 100$  nm to enter the sampling line. Figure 28 depicts a time series of particle number concentrations for all six CPCs during the SAMUM plateau efficiency calibration on 6 June 2006. The temporal evolution of the particle concentration curve is similar for all CPCs. However, the absolute concentrations are shifted by up to 11%. To correct for this shift, the relative plateau efficiency  $f_{efficiency}$  of every CPC with respect to a reference counter is calculated from the calibration data. CPSA 3, a very stable instrument, has been selected to be the reference counter. To get final CPC data, the number concentrations of each CPC are subsequently multiplied with the relative plateau efficiency factor. The plateau efficiency calibration is performed at least once in a field experiment. The derived plateau efficiencies are checked on plausibility by analysing scatter plots of the non-volatile particle and the total particle concentration. Figure 29 exemplifies such a scatter plot for particles  $> 10$  nm. The non-volatile particle concentration  $N_{non-vol 10}$  can not be larger than the total concentration  $N_{total 10}$  that means all data points need to be below the 1:1 line. Usually, sequences with totally non-volatile particles are encountered in every flight, so that some data points are expected to be on the 1:1 line. Missing sequences with totally non-volatile particles or a displacement of all data points parallel to the 1:1 line may indicate errors in the derived relative plateau efficiency factors. In Table 4, the relative plateau efficiency factors are summarised for all particle counters.

**Table 4.** Calibration of CPCs during ITOP and SAMUM. Besides the default flow rates  $q_{default}$ , the CPC set-up, the calibrated flow rates  $q_{calib}$  and the derived plateau efficiency factors  $f_{efficiency}$  are shown. The acronym DS in the CPC set-up column expresses that the CPC was combined with a diffusion screen separator; the number in brackets denotes the number of screens in the DS. TD means that the CPC was connected to the heated (250°C) sampling line, therefore measuring the non-volatile number concentration.

Particle counter	$q_{default} / \text{cm}^3 \text{ s}^{-1}$	CPC set-up (ITOP)	$q_{calib} / \text{cm}^3 \text{ s}^{-1}$ (ITOP)	$f_{efficiency}$ (ITOP)	CPC set-up (SAMUM)	$q_{calib} / \text{cm}^3 \text{ s}^{-1}$ (SAMUM)	$f_{efficiency}$ (SAMUM)
CPC1	25.0	> 4 nm, TD	25.2	0.968	DS (3), TD	23.4	1.009
CPC2	25.0	> 14 nm, TD	25.5	0.935	DS (10), TD	23.0	1.072
CPSA1	16.7	DS (3), TD	17.0	0.891	> 10 nm, TD	15.4	1.060
CPSA2	16.7	> 4 nm	15.7	0.919	> 4 nm	13.8	1.111
CPSA3	16.7	> 14 nm	16.9	1.000	> 10 nm	15.5	1.000
CPSA4	16.7	DS (3)	17.0	1.078	DS (3)	15.2	0.989

### OPC calibration

The sizing of the optical spectrometers (PCASP-100X, FSSP-300, Grimm OPC) is calibrated by means of test aerosols of known size and refractive index. The calibration of the OPCs is crucial, as under some circumstances the optics can be polluted or misaligned, which leads to large errors in the derived particle size distributions.

Two types of test aerosol particles are mainly used for the calibration: di-ethylhexyl sebacate (DEHS,  $m = 1.42 + 0i$ ) particles and polystyrene latex (PSL,  $m = 1.58 + 0i$ ) particles, which both have spherical shape. While PSL particles are available at several standardised sizes, DEHS is an oily substance that allows the generation of a polydisperse test aerosol. DEHS aerosol is generated with an atomiser type TSI. The atomiser is connected to a DMA to produce monodisperse aerosol particles of diameter  $D_p$ . The general DEHS calibration set-up is described in detail in *Pinnick and Auvermann (1979)*, a sketch of the calibration set-up used at the DLR can be found in *Fiebig (2001)*. Monodisperse PSL aerosol is generated with a nebuliser (*Hinds, 1999*). At the DLR, PSL particles up to 2  $\mu\text{m}$ , and DEHS particles up to 1  $\mu\text{m}$  are used. Larger size bins of the optical sondes can be calibrated with glass beads.

The calibration of the optical spectrometers with monodisperse test aerosol particles allows the determination of the limits between two adjacent channels. Figure 30 shows histograms with mean particle concentrations for monodisperse DEHS (left panel) and PSL (right panel) particles. The advantage of the DEHS calibration over the PSL calibration is that the bin limits can be measured directly. For example, to determine the bin limit between channel  $j$  and  $j + 1$ , the size of the test particles is varied with the DMA until both channels exhibit similar particle concentrations. The particle size at which both channels show the same particle concentration marks the limit between the two channels.

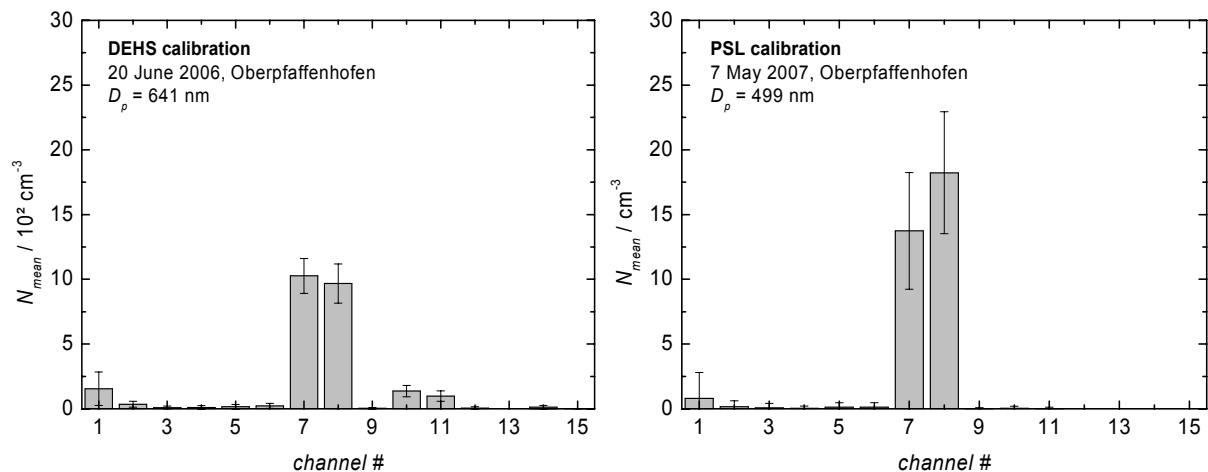


**Figure 30.** DEHS (left panel) and PSL (right panel) calibration of the PCASP-100X.

In contrast to DEHS, the determination of the bin limits from PSL calibration measurements requires some calculations, since PSL particles have discrete sizes. Figure 31 illustrates the determination of the bin limits with aid of discrete-sized PSL standards. The particles of a particular PSL standard, for example  $D_p = 499$  nm, are Gaussian distributed and are characterised by a narrow standard deviation  $GSD$ . The count median diameter  $CMD$  and the  $GSD$  are indicated by the manufacturer. When the  $CMD$  of a PSL standard, exactly matches the limit between two adjacent channels  $j$  and  $j + 1$ , 50% of the particles are detected in channel  $j$  ( $p_j = 50\%$ ) and  $j + 1$  ( $p_{j+1} = 50\%$ ), respectively (Figure 31a). In most cases, the  $CMD$  of a PSL standard does not exactly match the boundary between two adjacent channels. For example, for a particular PSL standard, a percentage  $p_j$  of all particles is counted in channel  $j$  and a percentage  $p_{j+1}$  of all particles in channel  $j + 1$  (Figure 31b). For a case with  $p_j < p_{j+1}$ , the  $CMD$  of the Gaussian-distributed particles is shifted towards larger particle sizes.

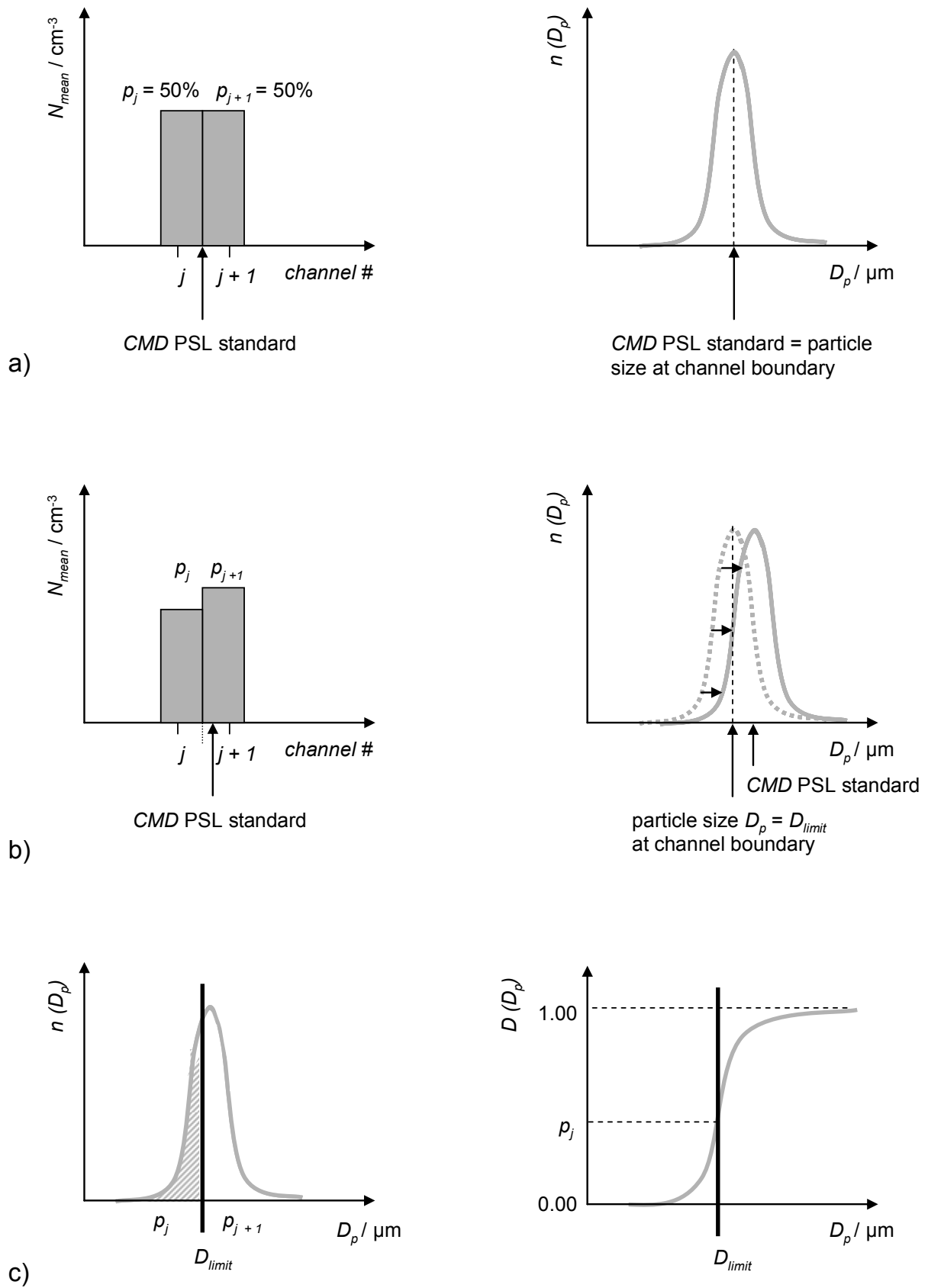
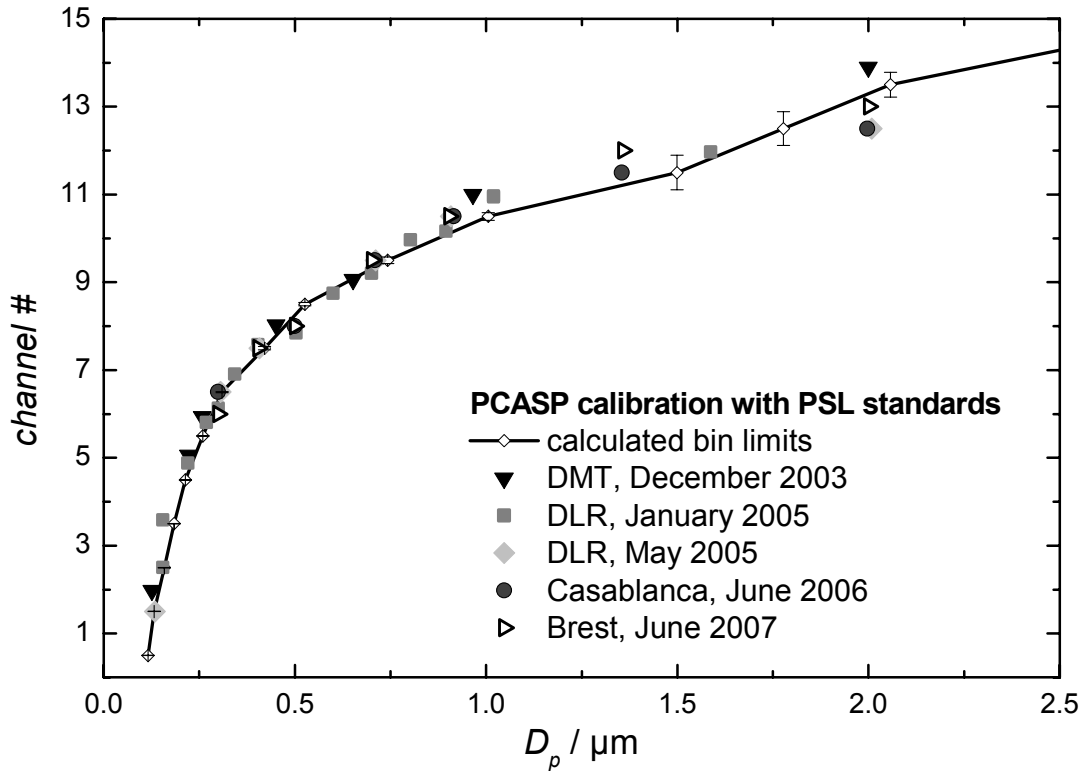
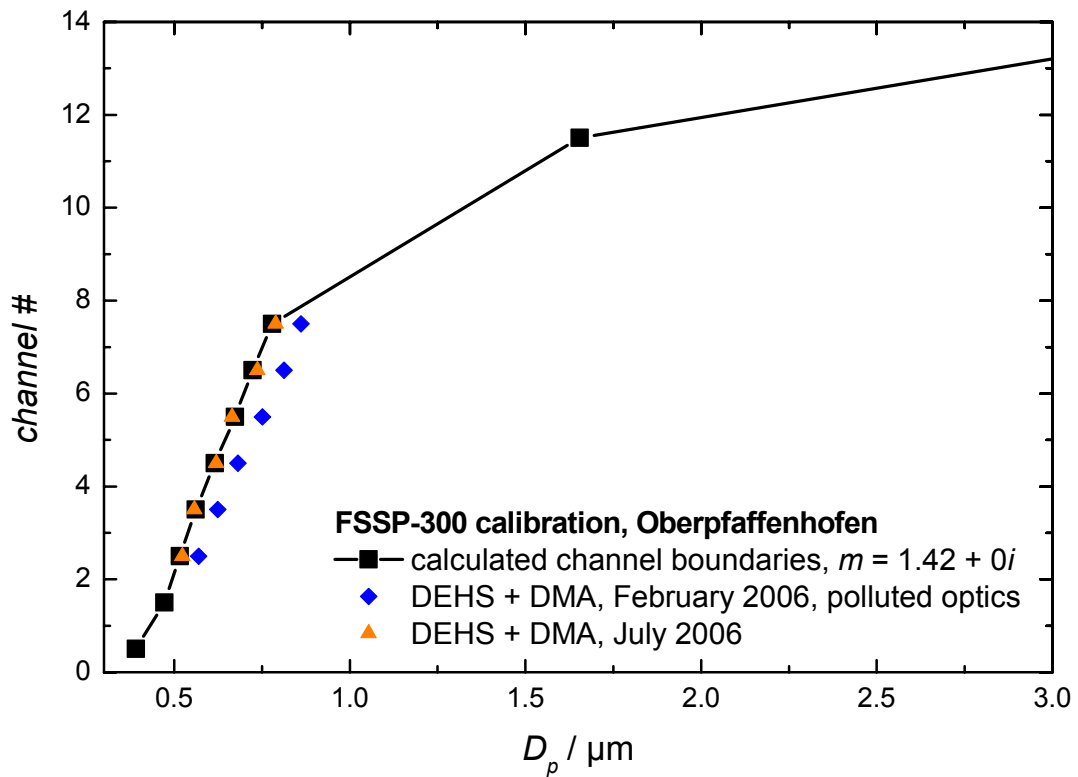


Figure 31. Schematic illustrating the calculation of bin limits from PSL calibration. See text.



**Figure 32.** Theoretical response function (black line) of the PCASP-100X for  $m = 1.58 + 0i$  and five size calibrations with PSL standards (symbols) performed between 2003 and 2007.



**Figure 33.** Theoretical response function (black line) of the FSSP-300 for  $m = 1.42 + 0i$  and DEHS calibration of the FSSP-300. The blue symbols show a calibration in February 2006, when the optics of the FSSP-300 was polluted and the orange symbols indicate the channel boundaries after cleaning the optics.

The bin limit can be calculated from these measurements by integrating the Gaussian distribution (Figure 31c), which gives the cumulative distribution function

$$D(D_p) = \frac{1}{GSD\sqrt{2\pi}} \cdot \int_{-\infty}^{D_p} e^{-\frac{1}{2} \left[ \frac{x-CMD}{GSD} \right]^2} dx = \frac{1}{2} \cdot \left[ 1 + \operatorname{erf} \left( \frac{D_p - CMD}{GSD \cdot \sqrt{2}} \right) \right] \quad (3.15)$$

where  $\operatorname{erf}$  is the error function. Setting  $D(D_p) = p_j$ , yields the boundary  $D_{limit}$  between channel  $j$  and channel  $j + 1$ . The “Gaussian method” is applicable for the determination of the FSSP-300 bin limits also.

Figure 32 shows the theoretical response function of the PCASP-100X for  $m = 1.58 + 0i$  (black line) together with five PSL calibrations (symbols) performed in the period 2003-2007. The channel boundaries were deduced using the “Gaussian method”. It is obvious from Figure 32 that the PCASP-100X is very stable over the time. In contrast to the PCASP-100X, which proved to be a very stable instrument, the optics of FSSP-300 was observed to be sometimes polluted or even misaligned. The blue symbols in Figure 33 show a case where the optics of the FSSP-300 was polluted. Particles that should be classified into channel  $j + 1$  due to their size, are classified into channel  $j$ . A size distribution derived from those measurements without redefining the thresholds of the size channels is systematically shifted towards smaller sizes. After cleaning the optics, the theoretical response function (black curve) and the measurements (orange symbols) corresponded again. The theoretical response function and the measurement are in very good agreement for both, PSL and DEHS. The validity of the theoretical response function for PSL and DEHS (e.g. Figure 32 and Figure 33) encourages the calculation of several sets of channel thresholds for both, non-absorbing and absorbing particles like biomass burning and desert dust particles. For each refractive index, the channel grouping also has to be calculated.

In addition to the size calibration of the optical spectrometers, the counting efficiency is checked. The counting efficiency of the PCASP-100X is determined by the synchronous measurement of the PCASP-100X and a CPC. The CPC collects the air in the sample outlet of the PCASP-100X (see Figure 23, p. 42). The results of these measurements are shown in Figure 34. The concentrations seen by the CPC are about 3-7% smaller than that measured by the PCASP-100X. This is the result of the calibration set-up: the CPC measures in the outlet of the PCASP-100X, so that some particles might not pass the inlet of the CPC. Considering the calibration set-up, the concentrations seen by the PCASP-100X are in very good agreement with that seen by the CPC. Due to the geometry of the FSSP-300, the counting efficiency can not be determined by the parallel operation of the spectrometer and a CPC. The accuracy of measuring the particle concentration with the FSSP depends upon the accurate measurement of the sampling volume, the active area. The flow through the active area and the size of it determines the particle concentration. Until now, the size of the active area has not been measured experimentally. A common procedure for the determination of the active area is the comparison of a size distribution derived from the PCASP-100X with that derived from the FSSP-300 (e.g. *Strapp et al.*, 1992). A few things have to be considered, when the active area is derived experimentally: first, to avoid artefacts due to humidity growth<sup>12</sup>, this

<sup>12</sup> The FSSP-300 measures particle sizes at ambient humidity, while the PCASP-100X dries the aerosol to about 30 % relative humidity before measurement.

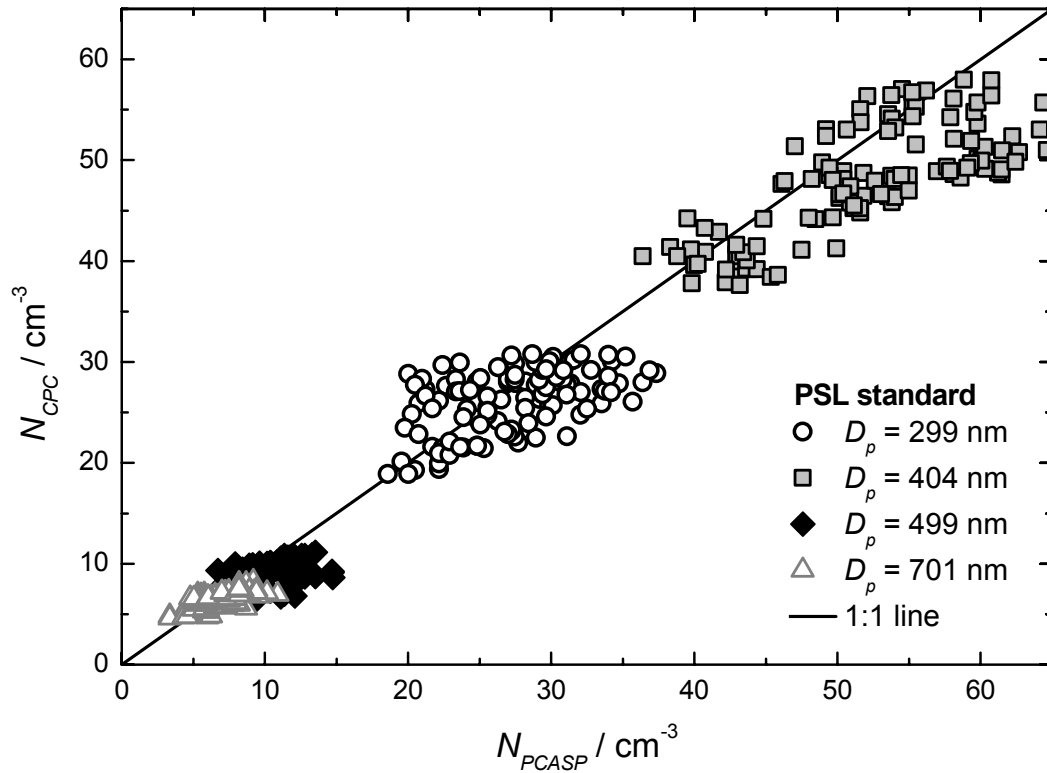


**Figure 34.** Calibration of the PCASP-100X counting efficiency for four different particle sizes (symbols).

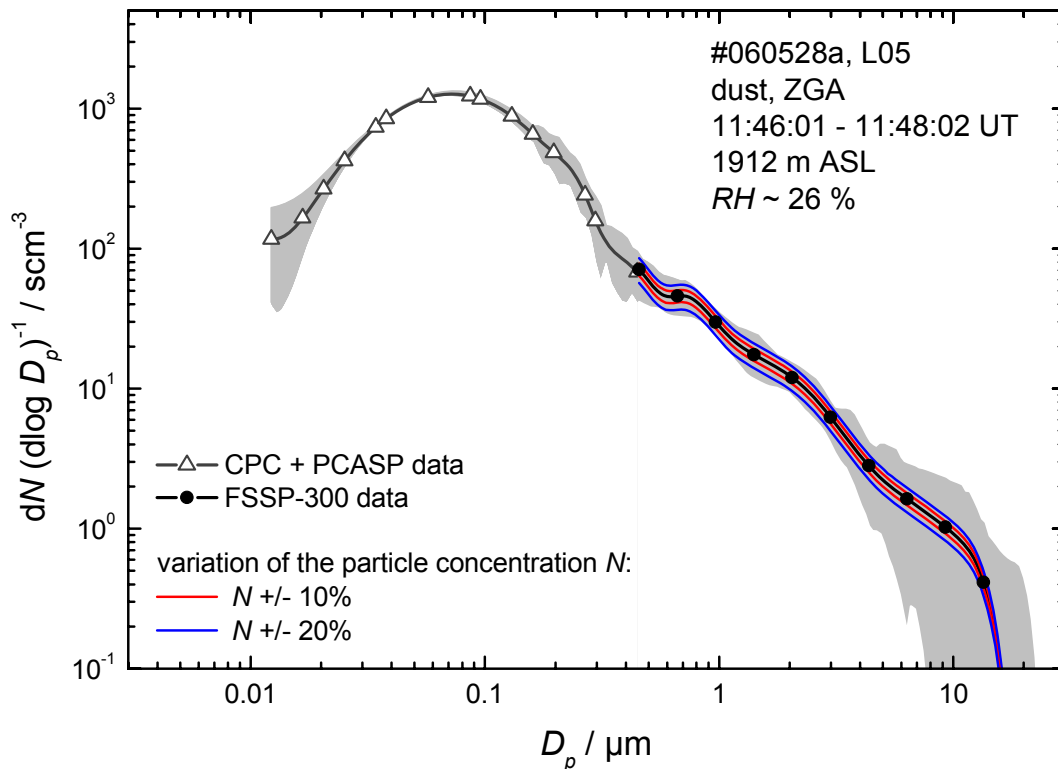


**Figure 35.** Determination of the active area of the FSSP-300 and effect of uncertainties in the active area on the derived particle number concentrations for standard conditions. The triangles and circles show data from the PCASP-100X and the FSSP-300, respectively. The red and blue lines mark 10% and 20% higher (lower) particle concentrations, respectively. The grey shaded area depicts the range of uncertainty of the measurements.

Comparison can only be done in dry air (relative humidity < 30%); second, the refractive index of the measured aerosol should be known. The active area was determined by the described procedure, and yielded a value of  $0.0004 \text{ cm}^{-2}$ . The validity of the experimentally derived active area was assessed by comparing the particle concentrations measured by the PCASP-100X and by the FSSP-300 for several cases in the range where the measurement range of both instruments overlap. One example of such an intercomparison is shown in Figure 35: the triangles and circles show data from the PCASP-100X and the FSSP-300, respectively. The grey shaded area depicts the range of uncertainty of the measurements which is dominated by fluctuations in the atmospheric particle concentration within the averaging period. The red (blue) lines in Figure 35 illustrate 10% (20%) variation in the particle concentration. An uncertainty of 10% in the active area leads to an uncertainty of approximately 10% in the derived particle number concentration. It is obvious that the particle concentrations agree within the uncertainty of the measurements, even assuming an uncertainty of 20% in the active area of the FSSP-300.

## **3.2 Field experiments**

The data sets to be discussed in this work were obtained during two different field experiments: the Intercontinental Transport of Ozone and Precursors (ITOP) field experiment in early summer 2004 and the Saharan Mineral Dust Experiment (SAMUM) in late spring 2006. Each field campaign focussed on a different aerosol type (ITOP: forest fire aerosol; SAMUM: desert dust aerosol), and therefore the Falcon research aircraft was equipped with a different combination of instruments. The ITOP data were collected before the work on this thesis started, while the logistics and instrument preparation of the SAMUM campaign (see <http://www.pa.op.dlr.de/aerosol/samum/>), the weather forecast during SAMUM and the in-situ aerosol measurements during SAMUM were part of this thesis. In this section, a general measurement concept for the DLR airborne aerosol measurements, the two field experiments and their main objectives are described. The airborne instrumentation and the procedures to identify the aerosol layers are presented separately for each study. Finally, the differences in the instrumentation and the data analysis are summarised in Section 3.2.4 (p. 66ff).

### **3.2.1 Measurement concept for airborne studies of aerosol properties**

The airborne measurement of miscellaneous aerosol types, originating from different sources, requires sophisticated flight planning and payload designs. To forecast the location and altitude of the aerosol layers before conducting a research flight is a challenge. The design of the flight mission, including descents and ascents through the aerosol layers, requires a combined approach of model forecasts studied before the flight, and monitoring of characteristic tracers during the flight. For the planning of DLR Falcon research flights, a detailed weather and plume forecast is made. The general weather forecasts during DLR field experiments are usually based on forecasts from the European Centre for Medium-Range Weather Forecasts (ECMWF). If the measurement of long-range transported aerosol layers is desired, the general weather forecast is supported by particle trajectory forecasts from models like FLEXPART (Stohl *et al.*, 1998; Stohl *et al.*, 2005) or LAGRANTO (Wernli and Davies, 1997). These models provide information on plume trajectories and the vertical extent of the plumes. Especially in the case of Lagrangian experiments (like ITOP), particle trajectory

models play a major role. Lagrangian experiments aim to track airmasses and to intercept the same airmass several times in order to investigate the ageing of atmospheric constituents within the airmass during transport.

Figure 36a sketches a flight track planned on the basis of weather and trajectory forecasts. The black line shows the flight altitude, the greyish areas denote the expected plumes, the orange area is a plume inhomogeneity not forecasted by the models. Based on the model forecast, the flight path is planned in such a way that the vertical and horizontal structure of the plume can be probed extensively. Once the aircraft is airborne and reaches the forecast position of the aerosol plumes, the forecasts have to be verified by monitoring tracer concentrations. For example, CO is enhanced in forest fire layers (e.g. *Crutzen et al.*, 1979; *Kasischke and Penner*, 2004; *Pfister et al.*, 2006), and can therefore be used as tracer. Sometimes the flight route has to be adapted to the atmospheric conditions during the flight mission. Figure 36b illustrates the advantage of an airborne lidar system that is optimised for the measurement of aerosols (e.g. the High Spectral Resolution Lidar, HSRL): the combination of in-situ instruments and an airborne lidar system allows the online monitoring and measurement of the three-dimensional structure of the atmosphere, especially the structure of the aerosol layers. The lidar can act as a path finder to direct the aircraft into the plumes, including plume inhomogeneities not forecasted, to take in-situ measurements.

The flight missions are aimed to gather data representative for the plumes and to investigate the whole extent of the plumes. To get good statistics and a large number of data points in a particular plume, constant-altitude sequences (of about 5-10 minutes duration) are flown leading to a stepped flight profile. The measurement on constant-level (CL) sequences is especially important for the analysis of the PSAP data, because the PSAP filter is sensitive to pressure changes in the sampling line during ascent and descent of the aircraft between different flight levels. To avoid artefacts, the PSAP data analysis is reduced to CL sequences. Furthermore, the incoming flow on the optical spectrometers may be disturbed if the aircraft climbs too fast. As a result, the measured particle concentrations may be too small. The described data acquisition concept was used for both, the ITOP 2004 and the SAMUM 2006 field experiment. An airborne lidar was employed only during SAMUM.

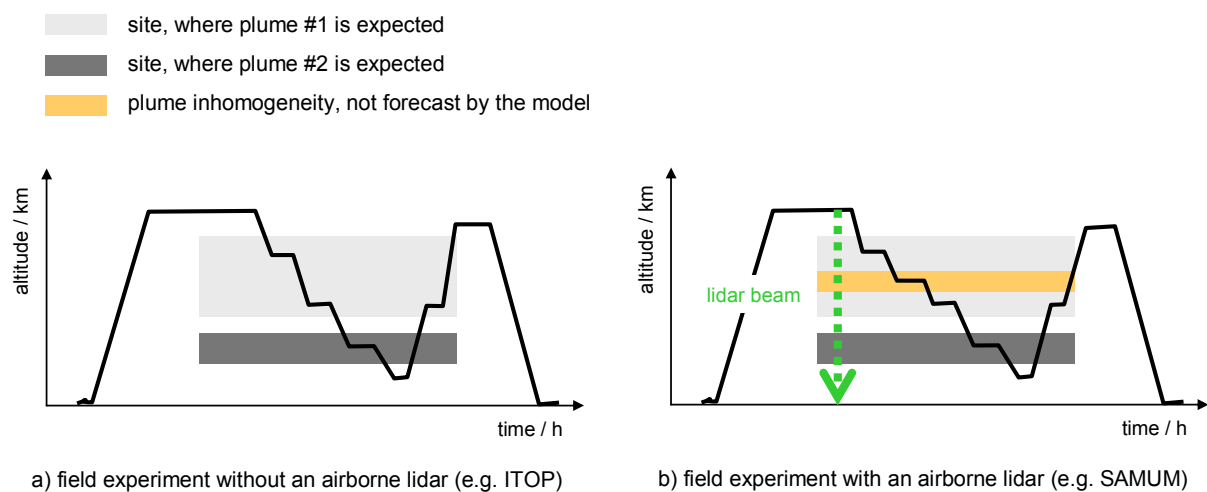


**Figure 36.** Flight strategy for airborne aerosol measurements. The left panel shows the flight route planned on the basis of model forecasts. The right panel shows a flight mission, in which an airborne lidar acted as pathfinder to direct the aircraft into the representative areas.

## 3.2.2 The ITOP study – Forest fire aerosol

### 3.2.2.1 ITOP – an overview

The Intercontinental Transport of Ozone and Precursors (ITOP) study took place in July/August 2004 and involved researchers and several research aircraft from France, Germany, and the UK. ITOP is part of the international ICARTT (International Consortium for Atmospheric Research on Transport and Transformation, <http://www.esrl.noaa.gov/csd/ICARTT/>) program with its main emphasis on the outflow of pollutants from the US east coast across the Atlantic Ocean. One of the primary aims of the ITOP field experiment in summer 2004 was to gather the necessary data to better understand intercontinental transport of aerosols from biogenic and anthropogenic origins, the transformation of aerosols during transport and possible interactions of these transported aerosols with atmospheric dynamics. For that purpose coordinated flights were conducted along the East coast of North America, the Azores and Western Europe with multiple aircraft.

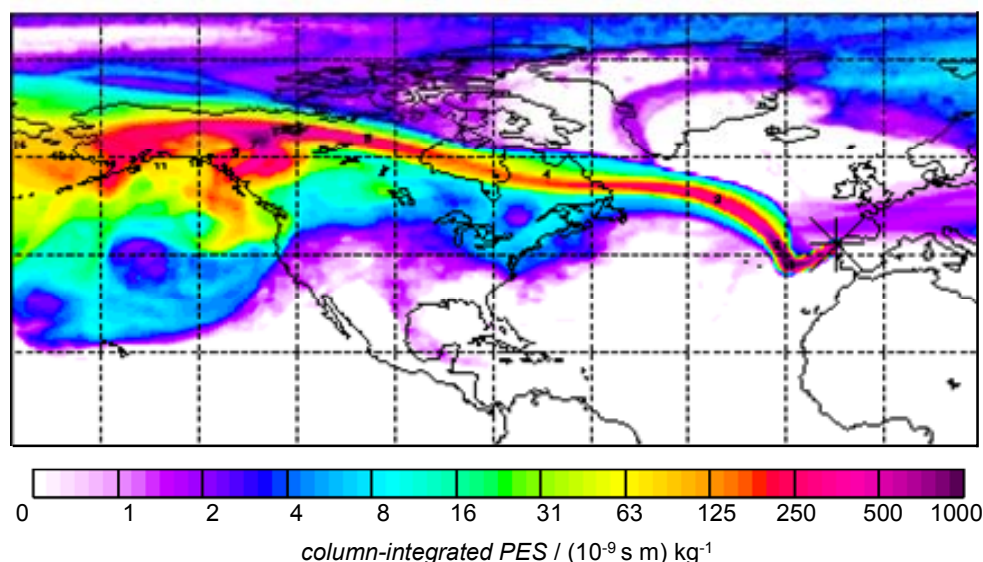


**Figure 37.** Retroplume results from the FLEXPART backward simulation for the ITOP flight on 22 July 2004 illustrating the source region of the air mass which had been sampled by the Falcon.

From July through August 2004 an unusual persistent high pressure system was centred over Alaska. The warm and dry conditions favoured a large number of thunderstorms and excessive lightning that ignited many wildfires in western Canada and Alaska (*Fuelberg et al.*, 2007). In general, the Canadian fire season lasts from April through October with the maximum area burned between June and August. Large forest fires (> 200 ha) represent 3.1% of the total number of Canadian fires, but they account for 97% of the total area burned (*Stocks et al.*, 2002). On average, an area of ~2 million ha burns annually in these large fires. The 2004 wildfire season set a new record in Alaska and Canada: about 2.7 million ha burned in Alaska, 8 times more than the 10-year average (*Turquety et al.*, 2007), and another 3.1 million ha burned in Canada (*Stohl et al.*, 2006). The strongest fire activity within the 2004 Alaskan/Canadian wildfire season occurred in July, coinciding with the ITOP core phase. Satellite images and trajectory calculations revealed that the forest fire plumes from Alaska and Canada were later transported to Europe, and influenced the aerosol and trace gas

composition over Europe. The 2004 North American wildfires released approximately the same amount of CO ( $30 \text{ Tg} \pm 5 \text{ Tg CO}$ ), as the anthropogenic emissions ( $\sim 25 \text{ Tg CO}$ ) in the continental US from June to August (Pfister *et al.*, 2005). The long-range transport of forest fire plumes enhanced European ground-level ozone and CO burden by up to 10% from June through August 2004 (Pfister *et al.*, 2006). The source region of the fires is illustrated in Figure 37 by the column-integrated potential emission sensitivity (*PES*) function (Stohl *et al.*, 2003) from a FLEXPART backward simulation (see Section 3.2.2.3, p. 59ff). The value of the *PES* function (in units of  $\text{s kg}^{-1}$ ) in a particular grid cell is proportional to the residence time of the particles in that cell. It is a measure for the simulated mixing ratio at the receptor that a source of unit strength in the respective cell would produce. The column-integrated *PES* (in units of  $\text{s m kg}^{-1}$ ) illustrates the pathway of a polluted airmass.

During the ITOP core period between 19 July and 3 August 2004, the German Falcon 20-E5 research aircraft operated from the airport of Creil ( $49^{\circ}15.6'N$ ,  $2^{\circ}31'E$ ) north of Paris in France. The Falcon performed research flights along the European west coast and probed aerosol layers at different altitudes from the boundary layer up to the upper free troposphere at about 11 km ASL. Figure 38 shows a map of the ITOP operation domain. The flight tracks are indicated by a black line, and the diamonds mark the sites in which forest fire plumes were encountered.

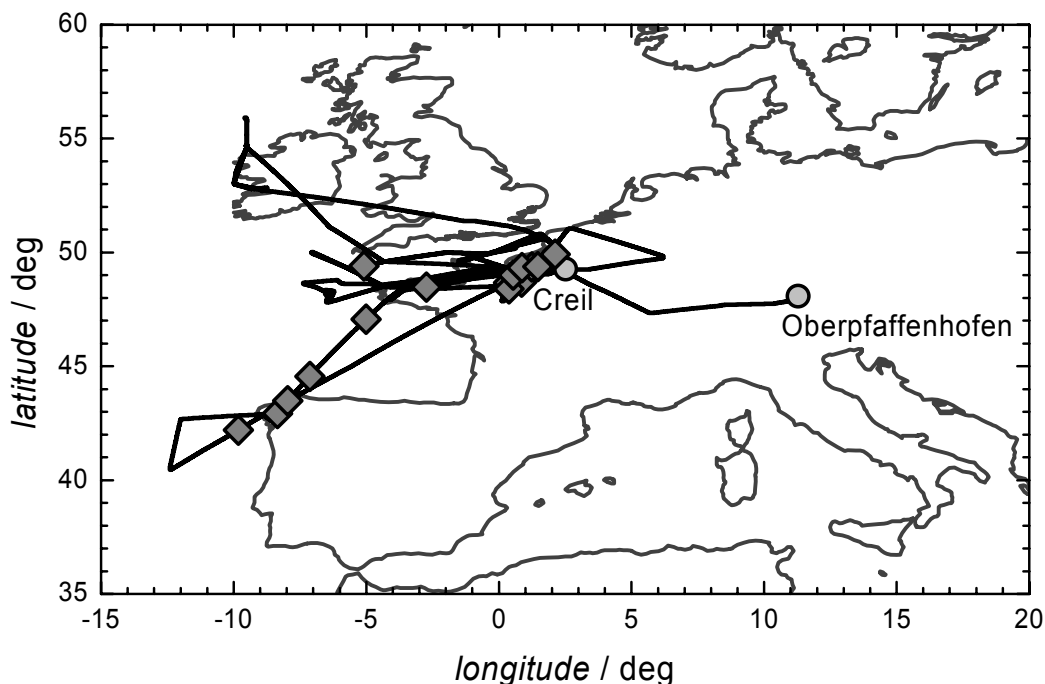


**Figure 38.** Map of ITOP operation domain and the Falcon operation base Creil (France). The diamonds indicate forest fire plume encounters, and the black lines show the flight tracks for all ITOP flights.

Table 5 summarises the times and routes of all flights performed during the ITOP core period. In seven of ten flights, forest fire plumes from Canada and Alaska were encountered at altitudes between 3 and 9 km ASL. Sometimes the forest fire plumes were mixed with anthropogenic pollution of different origins. More detail on the identification of the forest fire plumes and the determination of the plume composition is given in Section 3.2.2.3 (p. 59ff).

**Table 5.** Forest fire (FF) plumes probed during ITOP 2004. The forest fire plumes were partly mixed with anthropogenic pollution of different origins. The plume altitude was inferred from in-situ measurements.

Mission ID	Date (2004)	Time / UT	Route	Plume composition	Plume altitude / km ASL
040719a	19 July	09:23 – 10:47	Transfer Oberpfaffenhofen → Creil	no plume encounter	--
040722a	22 July	09:40 – 10:57	Creil → Santiago (Spain)	pure FF, mixed FF	4 – 9
040722b	22 July	15:05 – 17:03	Santiago (Spain) → Creil	pure FF, mixed FF	3 – 7
040723a	23 July	12:11 – 16:02	Creil → Channel → Creil	pure FF, mixed FF	3 – 6
040725a	25 July	13:37 – 16:40	Creil → Shannon (Ireland)	mixed FF	3 – 5
040725b	25 July	17:42 – 19:53	Shannon (Ireland) → Creil	pure FF, mixed FF	3 – 5
040726a	26 July	15:07 – 18:50	Creil → Channel → Creil	pure FF, mixed FF	3 – 4
040730a	30 July	15:00 – 18:35	Creil → Gulf of Biscay → Creil	pure FF, mixed FF	3 – 8
040731a	31 July	12:07 – 13:55	Creil → Northern France → Creil	no plume encounter	--
040803a	3 August	14:24 – 17:25	Transfer Creil → Oberpfaffenhofen	no plume encounter	--

### 3.2.2.2 Falcon instrumentation during ITOP

For ITOP, the Falcon aircraft was equipped with a comprehensive set of instruments for the in-situ measurement of aerosol microphysical and optical properties, and trace gas mixing ratios. The DLR aerosol in-situ instrument package represents state-of-the-art methods as introduced in Section 3.1 (p. 31ff). The aerosol in-situ instrumentation for ITOP consisted of six CPCs operated at different cut-off diameters (Figure 39). Three of the CPCs were connected to the non-heated sampling line, whereas three were combined with a TD (250°C). Two CPCs were combined with DS containing three screens. These screens shift the minimum threshold<sup>13</sup> diameter to 80 nm at FT conditions of approximately 300 hPa (Feldpausch *et al.*, 2006). This configuration allows the determination of the non-volatile components in three size ranges: *NUC* ( $4 < D_{p,50\%} < 14$  nm), *AIT* ( $14 < D_{p,50\%} < \sim 80$  nm) and *ACC* ( $D_{p,50\%} > \sim 80$  nm).

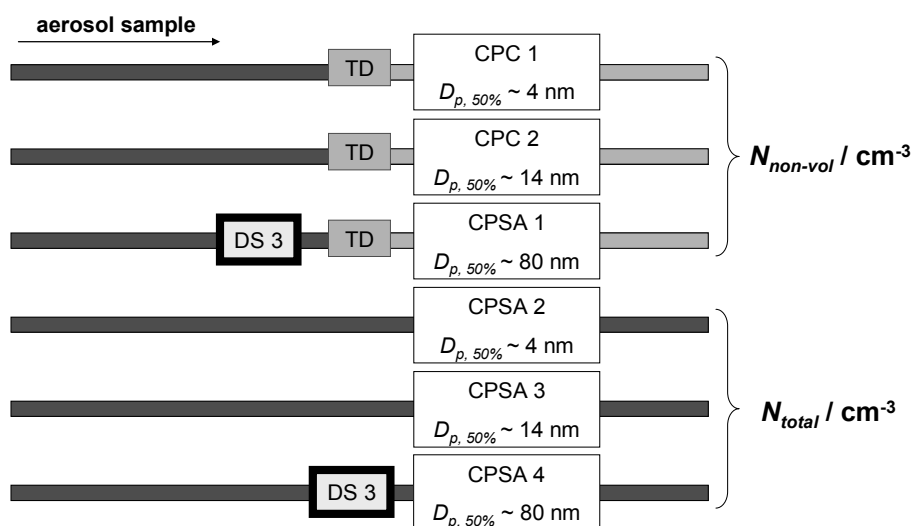


**Figure 39.** CPC configuration during ITOP 2004. Three of the CPCs were connected to the thermal denuder (TD). Two counters were combined with diffusion screen separators containing three screens (DS 3) each, which shifted the lower cut-off diameter to larger particle sizes. The CPSA is merely a combination of four CPCs, operated at different cut-off diameters.

<sup>13</sup> This threshold diameter varies with pressure.

In addition to the CPCs, a DMA was operated in a stepping mode at diameters 0.015, 0.023, 0.035, 0.053, 0.08, 0.12 and 0.2  $\mu\text{m}$  in the unheated branch of the sampling line. The in-situ aerosol instrumentation was completed by two optical particle counters type PCASP-100X and FSSP-300 and a 1- $\lambda$ -PSAP. During ITOP, the DMA and the PSAP were connected to the isokinetic sampling line, while the CPCs were connected to the backward-facing inlet (see 3.1.8, p. 44). With this aerosol in-situ instrumentation during ITOP, the entire size range of the total number of particles from smallest nucleation mode particles ( $D_p < 0.01 \mu\text{m}$ ) to coarse mode particles in the far super-micron range ( $D_p \gg 1 \mu\text{m}$ ), including the optically active background Aitken and accumulation mode particles ( $0.05 \mu\text{m} < D_p < \sim 2 \mu\text{m}$ ), was covered. The size distribution of non-volatile particles was measured in coarser size resolution as defined by the TD/CPC setup.

The Falcon standard instrumentation provided data for atmospheric parameters like temperature, pressure, relative humidity and 3D-wind velocity. In addition to the aerosol and Falcon standard measurements, a variety of gas tracers suitable to identify polluted air as NO/NO<sub>y</sub>, CO, O<sub>3</sub>, CO<sub>2</sub> and SO<sub>2</sub> were measured. Furthermore, H<sub>2</sub>O mixing ratios were recorded. Trace gas data relevant for this study are H<sub>2</sub>O and CO mixing ratios. The ITOP in-situ instrumentation is summarised in Table 7.

### 3.2.2.3 Identification of forest fire plumes with excess CO data and FLEXPART<sup>14</sup>

Previous investigations (e.g. Crutzen *et al.*, 1979; Kasischke and Penner, 2004; Pfister *et al.*, 2006) have shown that carbon monoxide (CO) is distinctly enhanced within forest fire plumes. CO is a long-lived tracer that is not removed by wet deposition processes and therefore suitable for the identification of anthropogenic or biomass burning plumes. To use CO as a tracer in the measurement data, the CO enhancements over background conditions have to be determined. The so-called “excess-CO” ( $\Delta\text{CO}$ ) was derived from measured CO mixing ratios for all ITOP flights. For every flight a minimum CO profile was constructed as a representation of background conditions by estimating the minimum CO mixing ratio for outside-plume conditions. Then  $\Delta\text{CO}$  was calculated as the difference between the measured CO and the minimum CO profile. Since the airmasses were quite different from day to day, a minimum CO profile had to be estimated for every flight. The minimum CO mixing ratios were in the range between 70 and 90 nmol mol<sup>-1</sup> for free tropospheric conditions. On some days, air with subtropical origins reached the operation area. These sub-tropical airmasses were characterised by very low minimum CO mixing ratios (50-60 nmol mol<sup>-1</sup>).

To distinguish forest fire CO emissions from anthropogenic emissions in an air sample with enhanced CO values, trajectory calculations are necessary. The sources (anthropogenic, biomass burning) which contributed to a certain plume were assessed with the Lagrangian particle dispersion model FLEXPART. Figure 40 is taken from Stohl *et al.* (2003) and summarises the basic steps of the FLEXPART forward and backward simulations. Forward simulations with FLEXPART are useful to understand transport processes or to provide plume forecasts and direct the research aircraft into the plumes. Backward simulations are a useful tool for a detailed analysis of the plume’s source regions. In any case, the model

<sup>14</sup> The excess CO data and the FLEXPART trajectories were provided by Dr. Heidi Huntrieser (DLR) and Dr. Andreas Stohl (NILU), respectively.

releases so-called tracer particles representing anthropogenic emissions from North America, Europe and Asia as well as tracers from forest fire emissions. The emission strength is derived from the EDGAR emission inventory (*Olivier and Berdowski, 2001*) for anthropogenic emissions with the base year 1999. As fire emissions are very variable from year to year, the forest fire emission strength was gained from daily MODIS fire hot spots detection and daily fire reports. All tracers behave passively in FLEXPART which means that no chemical processes are simulated. For the ITOP analyses, FLEXPART was driven by wind fields from the ECMWF. In addition to advection, the particles experienced parameterised turbulence and convection during transport. As long as linear processes are considered, a Lagrangian particle dispersion model can be run backward in time (*Stohl et al., 2003*). The Falcon flight track can be taken as starting point to determine the source of the investigated airmasses. For that purpose a large number of particles is released at a point located at the flight track (the receptor point in Figure 40) and transported in time. The multiplication with the actual source strengths is done after the model run. This allows the consideration of different emission scenarios without having to rerun FLEXPART for each scenario. The particle ensemble produced by the backward simulation is referred to as “retroplume” (see Figure 37, p. 56). The computation of retroplumes allows the characterisation of the origins of every air sample encountered during a flight.

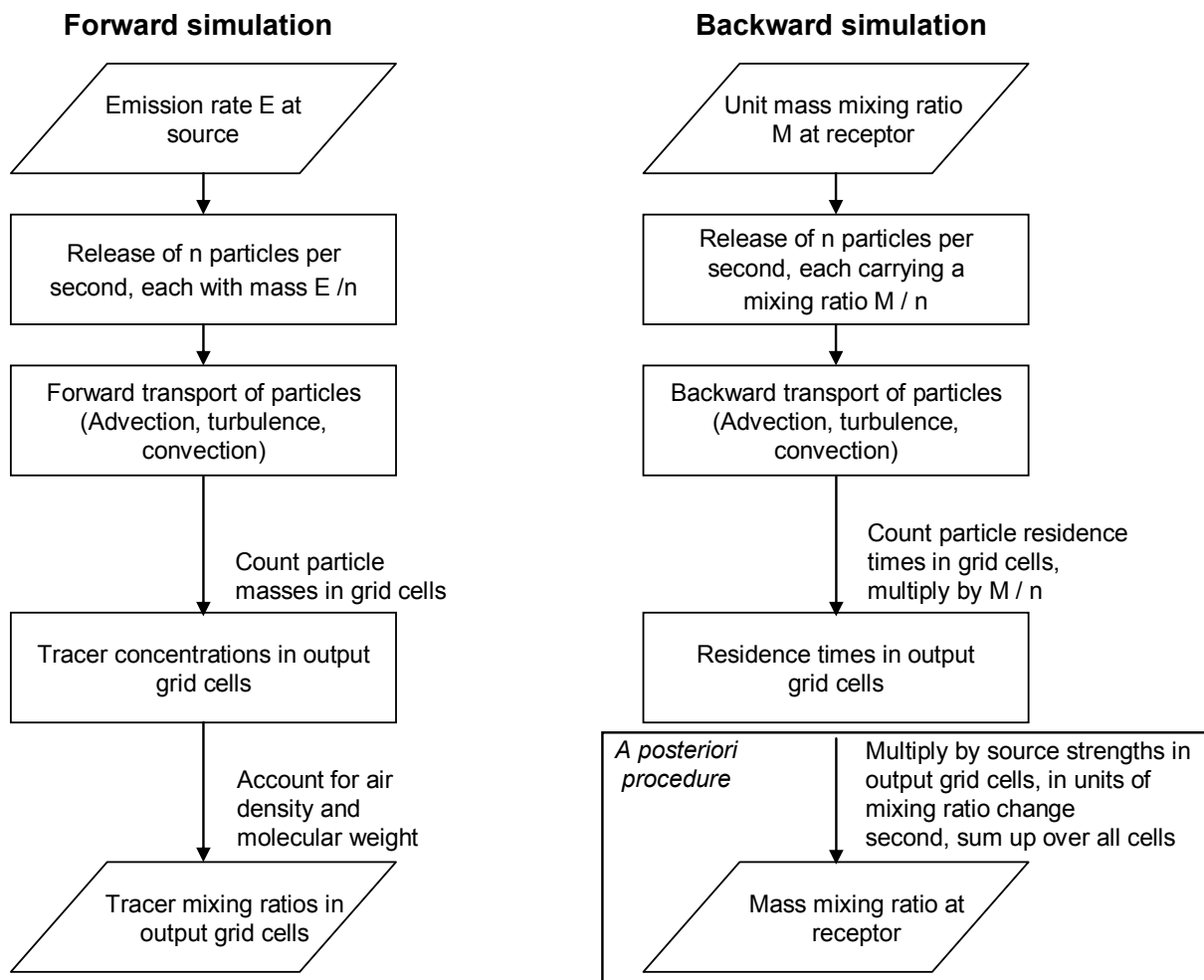


**Figure 40.** Flow chart summarising the basic steps in forward and backward model simulations with FLEXPART (adopted from *Stohl et al., 2003*).

To make sure that the FLEXPART represents the air mass transport correctly, the model predicted CO enhancements and the measured ones were compared for all flights. Figure 41 shows such an intercomparison: The panel on the left refers to the ascent over Creil (France), and the panel on the right refers to the descent over the Atlantic south-west of Spain. The flight altitude is denoted by dashed lines, the solid black line depicts  $\Delta\text{CO}$ , and the bars show sections along the flight track, where FLEXPART expected CO enhancements. The height of the bars represents the total CO values as computed by the model. The light grey part refers to the forest fire contribution, whereas the dark grey part of the bar shows anthropogenic contributions. An investigation of all ITOP flights revealed that FLEXPART has significant skills in forecasting the transport of pollution plumes (see also *Stohl et al., 2007*). The forecasted horizontal location of the plumes is in very good agreement with the measurements, whereas the absolute values of the CO mixing ratio slightly differ from the measurements, possibly due to the emission inventory from the year 1999 being updated. Some of the anthropogenic emissions may have changed since 1999. Another factor contributing to the uncertainty in the forecast CO values is the type of vegetation and the amount of vegetation consumed in the fires, which may have been slightly under- and overestimated, respectively.

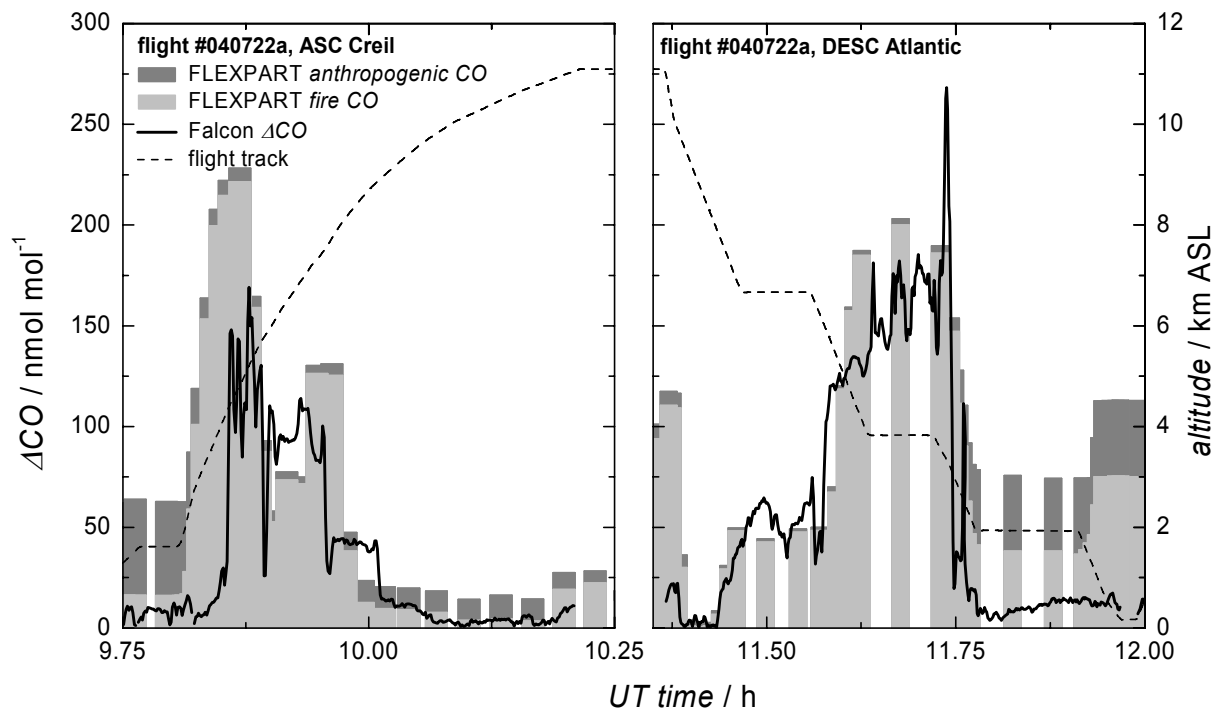


**Figure 41.** Comparison of FLEXPART CO tracer calculations and Falcon  $\Delta\text{CO}$  measurements for the ascent over Creil and the descent over the Atlantic south-west of Spain on 22 July 2004. The dashed line denotes the flight altitude, the solid black line depicts  $\Delta\text{CO}$ , and the bars show places along the flight track, where FLEXPART expected CO enhancements.

The plumes were classified by calculating the ratio of forest fire CO tracers compared to the total number of CO tracers (anthropogenic + forest fire) at every point of the flight track. Plumes were classified as “pure” forest fire plumes, when the FLEXPART forest fire CO fraction exceeded 80%. Pure forest fire plumes were probed in 6 of 10 flights. Measurements in mixed plumes (forest fire + anthropogenic pollution) were performed in 7 of 9 flights. According to FLEXPART, the age of the plumes ranged between 4 and 13 days. The

classification (forest fire plumes, anthropogenic pollution or mixed plumes), which resulted from  $\Delta CO$  measurements and the FLEXPART analyses, is corroborated by aerosol microphysical properties like particle size distribution (see Figure 54 and Figure 55, p. 86ff).

### 3.2.3 The SAMUM study – Desert dust aerosol

#### 3.2.3.1 SAMUM – an overview

The Saharan Mineral Dust Experiment (SAMUM, <http://www.tropos.de/samum/>) is dedicated to the understanding of the microphysical and optical properties of desert dust, and the impact of desert dust on the global climate system. A first field experiment focussing on the properties of pure dust over the source region and during transport to Western Europe took place in southern Morocco during May/June 2006. The mixing of desert dust aerosol with biomass burning aerosol, as well as the long-range transport of dust, are the objectives of a second SAMUM field experiment planned for January/February 2008 on the Cape Verde islands. SAMUM is a joint project of several German research institutes, in cooperation with the Mohammed I. University (Oujda, Morocco). SAMUM is funded by the German Research Foundation (DFG), and further supported by the European Space Agency and by the European EUFAR project DARPO (Desert Dust and Biomass Burning Aerosols over Portugal). Since no fires occurred in Portugal during the SAMUM intensive observation period, only pure dust plumes and dust plumes mixed with anthropogenic pollution were investigated.



**Figure 42.** The SAMUM ground sites at Ouarzazate and Zagora. The image was created by the MISR instrument during an overpass of the TERRA satellite on 19 May 2006 (courtesy: R. Kahn, NASA/JPL).

During the SAMUM field phase two aircraft were mainly cruising between the two ground stations Ouarzazate (OZT; 30°56.5'N, 6°54.4'W, 1150 m ASL) and Zagora (ZGA; 30°21'N, 5°52'W, 820 m ASL) airport (Figure 42). The Partenavia aircraft was measuring surface albedo and dust properties up to about 4 km altitude above ground level and was based at Ouarzazate. The Falcon aircraft operated from the International Airport Mohammed V in Casablanca (CASA 33°22'N, 7°35.5'W, 200 m ASL) and took measurements between

18 May and 7 June 2006. The ground station at Ouarzazate was equipped with several instruments like the IfT lidar and sun photometers. Radiosonde soundings were performed there as well. At Zagora, aerosol samples for chemical analyses were collected and a sun photometer recorded the aerosol optical depth. The measurements conducted during SAMUM address the full range of local microphysical, optical and chemical dust properties. Dust properties are derived from airborne, ground-based and space-borne sensors, and combined with laboratory studies and model simulations from advanced weather and climate models.

Three large-scale dust events extending from southern Morocco to Portugal occurred during the intensive observation period of SAMUM. The dust events were probed extensively, including horizontal and vertical dust plume structures. The dust events ranging from 16-22 May, 24-28 May and 31 May – 5 June 2006 are referred to as **Episode I**, **II** and **III**, respectively. The dust source regions within the three dust episodes were determined as part of the diploma thesis by *Rasp* (2007), based on Lagranto trajectory calculations, ECMWF surface wind analyses, and weather observations. Figure 43 summarises the dust source regions for the three dust events. The flight tracks for all flights performed during SAMUM are marked by a black line. The three dust episodes were well separated by phases without dust. At the time of every dust episode, several research flights close to the source and to Portugal were conducted. During the flight missions, the High Spectral Resolution Lidar HSRL acted as a path finder for the in-situ measurements (see also Section 3.2.1, p. 54). According to the vertical structure seen by the HSRL, the altitudes for the constant-level sequences were selected when the aircraft was well above the dust layer. Table 6 summarises all flight missions.

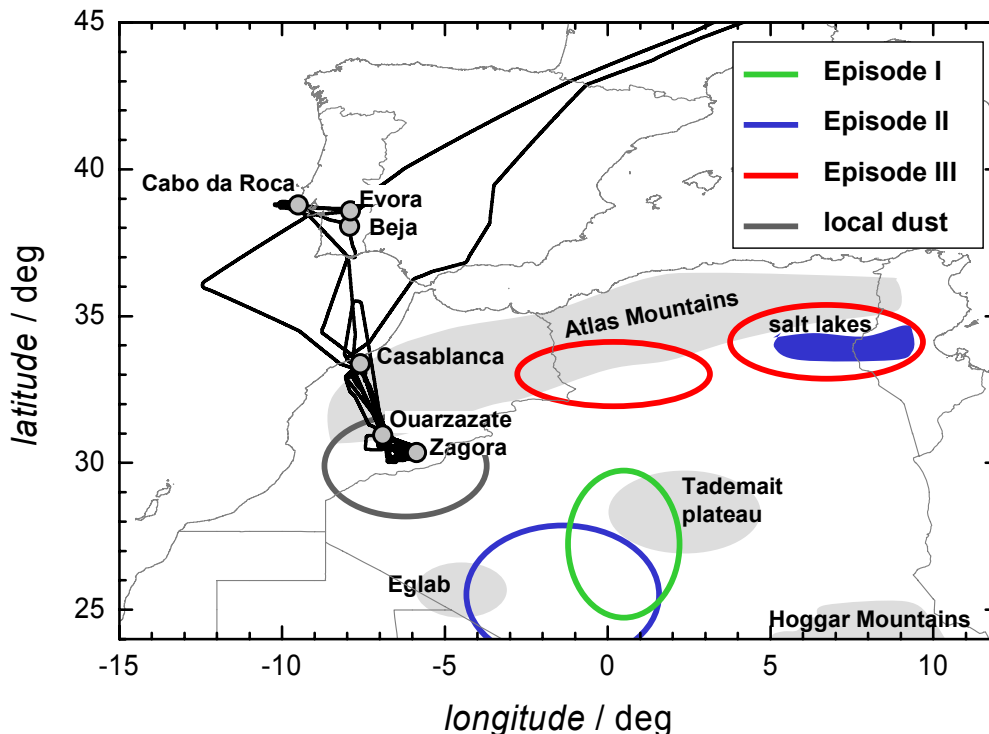


**Figure 43.** Map of Northern Africa and Western Europe with the location of the SAMUM ground sites Ouarzazate and Zagora, the Falcon operation base at Casablanca and the measurement sites at Portugal indicated. The black lines show the flight tracks for all flights performed during SAMUM. The dust source regions (*Rasp*, 2007) for **Episode I**, **II** and **III** are marked by circles.

During **Episode I**, a strong dust event took place. The dust plumes were extending from Morocco to Portugal. Within this episode, the dust was probed several times (flights #060518b-#060522c) over Cabo da Roca (38°47'N, 9°30'W), Evora (38°31.4'N, 7°54'W) in Portugal, close to the Moroccan coast and over Casablanca. Over Portugal on 18 May, only the northern edge of a thin (about 800 m vertical extent) dust plume was found at altitudes between 3.6 and 4.4 km ASL. On 19 May, the dust was probed close to the Sahara during the overpass of the TERRA and ENVISAT satellites with the MISR and MERIS instruments, respectively. On 20 May, the very distinct dust layer was still present over Morocco. Hence the flight pattern of the day before was repeated. In contrast to the 19 May, when almost no clouds were present, the dust layer on 20 May was partially topped by convective cumulus clouds. The highest *AODs* in **Episode I** occurred on 20 May and decreased towards the end of the episode on 22 May. The flights on 22 May (#060522a-c) were designed to probe the aerosol very close to the surface in the Dra valley near to Zagora. The lowest leg flown was at 500 m above ground.

**Table 6.** Research flights conducted during SAMUM. Besides day, time and type of the flight missions, also the flight routes are indicated. OP: Oberpfaffenhofen, CASA: Casablanca, OZT: Ouarzazate, ZGA: Zagora.

Mission ID	Date (2006)	Time / UT	Route	Flight mission
060518a	18 May	07:01 – 10:15	OP → Beja (Portugal)	transfer flight
060518b		11:33 – 13:50	Beja → Beja	long-range transport to Europe
060518c		14:44 – 15:04	Beja → Faro (Portugal)	long-range transport to Europe
060518d		15:55 – 16:50	Faro → CASA (Morocco)	long-range transport to Europe
060519a	19 May	10:35 – 12:10	CASA → OZT	closure OZT, MERIS (10:50), MISR (11:11)
060519b		14:35 – 15:10	OZT → CASA	dust
060520a	20 May	10:34 – 13:50	CASA → OZT → ZGA → CASA	convective dust layer, closure OZT & ZGA
060522a	22 May	15:04 – 16:09	CASA → OZT	dust
060522b		17:18 – 18:15	OZT → ZGA → OZT	low-level dust
060522c		21:23 – 22:01	OZT → CASA	dust
060527a	27 May	09:15 – 12:36	CASA → Beja → Evora → CASA	long-range transport to Portugal
060528a	28 May	10:13 – 13:35	CASA → ZGA → OZT → CASA	closure ZGA & OZT, MISR (11:05), MERIS (11:08)
060603a	3 June	01:36 – 04:49	CASA → ZGA → OZT → CASA	night flight
060603b		07:06 – 09:09	CASA → ZGA → OZT	early morning flight, closure ZGA & OZT, dust, MERIS (11:19)
060603c		11:04 – 11:42	OZT → CASA	
060604a	4 June	09:18 – 12:34	CASA → OZT → ZGA → CASA	closure OZT & ZGA, MERIS (10:48), MISR (11:11)
060607a	7 June	10:08 – 10:38	CASA → Spain → OP	long-range transport to Europe

Between 24 and 28 May the second dust event (**Episode II**) took place. The dust plumes extended from Morocco to Portugal. During this episode, dust layers were probed several times successfully in the far field (#070527a), close to the Atlantic coast of Morocco and near the source regions (#070628a).

The last dust event (**Episode III**) within the intensive observation period of SAMUM started in the evening of 31 May and reached its maximum strength on 3/4 June. Within **Episode III**, four research flights were conducted, including a night flight (#060603a), and an early morning flight (#060603b). During the night flight, the edge of a Saharan dust layer leaving the African continent was nicely detected. Furthermore, the dust layer close to the source was probed before sunrise, before convection became active. On 4 June, another satellite validation flight was performed. The dust layer of flight #060604a showed a clear horizontal and vertical gradient, providing another test case for MISR validation. During the

return flight (#060607a) from Morocco to Oberpfaffenhofen on 7 June, a dust plume extended from Morocco to the Pyrenees. The Falcon sampled the dust in-situ on constant-level sequences over the Atlantic, thereafter the remaining distance was performed at 11 km delivering a lidar cross-section from Spain to Oberpfaffenhofen.

The three dust events within the SAMUM observation period gave the opportunity for numerous measurements in dust layers. In total 4 aged dust layers and 49 pure dust layers were investigated, 37 of which were south of the Atlas Mountains. Altogether 73 size distributions of different aerosol types, including pure dust, aged dust, mixed plumes containing local pollution and dust aerosol, marine aerosol and local pollution aerosol were determined (see Section 4.2, p. 93ff).

The dust mobilisation was different within the three Episodes. In **Episode II** and **III**, the dust was frequently mobilised by density currents in the Atlas region, which caused strong turbulent winds along their leading edges (*Knippertz et al.*, 2007). According to *Knippertz et al.* (2007) dust mobilisation by density currents was identified on 7 May, 13 May, 25 May, 31 May, and between 2 and 5 June 2006.

### 3.2.3.2 SAMUM instrumentation

The SAMUM payload on board the Falcon combined a nadir-looking High Spectral Resolution Lidar (HSRL, *Esselborn*, 2007) with extensive aerosol microphysics and chemistry in-situ instruments. The SAMUM in-situ aerosol instrumentation comprehended a set of CPCs operated on different cut-off diameters ( $D_{p,50\%} = 4, 10$  and  $\sim 80$  nm), a DMA and several optical particle counters type Grimm 1.109, PCASP-100X, FSSP-300 and FSSP-100 (see Section 3.1, p. 31ff). The DMA was operated at ambient pressure in a stepping mode at diameters 0.015, 0.03, 0.05, 0.08, 0.12 and 0.16  $\mu\text{m}$ . Similar to the CPC configuration shown in Figure 39 (p. 58), the CPCs were partially equipped with DS, and three CPCs were connected to a TD (250°C). In contrast to ITOP, all instruments inside the cabin of the Falcon were connected to the isokinetic inlet (Section 3.1.8, p. 44) during SAMUM.

New features in the instrumentation compared to ITOP were the successfully employed HSRL for the separation of molecule and aerosol extinction, the sampling of particles for chemical analyses, and a multi-wavelength PSAP (3- $\lambda$ -PSAP) for the measurement of aerosol absorption in the red (660 nm), green (530 nm) and blue (467 nm) spectral ranges. The 3- $\lambda$ -PSAP was operated in cooperation with A. Virkkula from the Finnish Meteorological Service. It delivers data on the spectral dependence of the aerosol absorption coefficient, which is an essential input for radiative transfer calculations. The 3- $\lambda$ -PSAP data were used to determine the complex refractive index of desert dust, urban pollution aerosol and marine aerosol particles (more details on that are given in *Rasp*, 2007). The non-volatile aerosol component in the sub-2.5  $\mu\text{m}$  range was measured with a new configuration consisting of three CPCs and a new optical particle counter, type Grimm 1.109. These instruments were operated in combination with a TD, which heated the aerosol to 250°C. The information on the aerosol non-volatile size distribution complements the chemical analyses of filter samples collected during the flights. Again, the Falcon standard instrumentation provided data for atmospheric parameters like temperature, pressure, relative humidity and 3D-wind velocity. The SAMUM instrumentation is summarised in Table 7.

### 3.2.4 Differences between ITOP and SAMUM

ITOP and SAMUM were two completely different and independent field experiments, with ITOP focussing on forest fire aerosol after long-range transport and SAMUM mainly focussing on desert dust aerosol close to the Sahara. The different aerosol types required different instrumentation to sample the desired data set. Whereas the ITOP instrumentation consisted of in-situ trace gas and aerosol instruments, the SAMUM instrumentation involved an aerosol lidar (HSRL) and an extended set of aerosol in-situ instruments as explained in the previous sections. The differences between the ITOP and the SAMUM instrumentation are summarised in Table 7.

**Table 7.** Instrumentation on board the Falcon aircraft during ITOP 2004 and SAMUM 2006. The first column displays the name of the instrument, the second column the measured property. The cross in the third and fourth column marks if an instrument was employed during ITOP and SAMUM, respectively. A dash indicates that a particular instrument was not operated.

Instrumentation	Property	ITOP	SAMUM
<b>Aerosol in-situ instruments</b>			
CPC/CPSA	size distribution of ultrafine particles ( $0.004 < D_p < 0.080 \mu\text{m}$ )	x	x
DMA	size distribution Aitken mode ( $0.01 < D_p < 0.2 \mu\text{m}$ )	x	x
TD (250°C) + (DS) + CPC	non-volatile fraction in three size ranges ( <i>NUC</i> , <i>AIT</i> , <i>ACC</i> )	x	x
TD (250°C) + OPC	non-volatile size distribution	--	x
PCASP-100X-100X	dry state accumulation mode ( $0.1 \mu\text{m} < D_p < 3.0 \mu\text{m}$ )	x	x
FSSP-300	ambient state accumulation + coarse mode ( $0.1 < D_p < 20 \mu\text{m}$ )	x	x
FSSP-100	ambient state accumulation + coarse mode ( $1 < D_p < 100 \mu\text{m}$ )	--	x
1- $\lambda$ -PSAP	absorption coefficient at $\lambda = 567 \text{ nm}$	x	--
3- $\lambda$ -PSAP	absorption coefficient at $\lambda = 467$ , $\lambda = 530$ and $\lambda = 660 \text{ nm}$	--	x
Filter sampling	chemical composition and shape of sub- $2.5 \mu\text{m}$ particles	--	x
<b>Lidar instrument</b>			
High Spectral Resolution Lidar (HSRL)	backscatter at $\lambda = 532$ , $\lambda = 925$ and $\lambda = 1064 \text{ nm}$	--	x
	extinction coefficient at $\lambda = 532 \text{ nm}$	--	x
	lidar ratio at $\lambda = 532 \text{ nm}$	--	x
	AOD at $\lambda = 532$ and $1064 \text{ nm}$	--	x
	depolarisation at $\lambda = 532$ and $\lambda = 1064 \text{ nm}$	--	x
	water vapour at $\lambda = 925 \text{ nm}$	--	x
<b>Trace gas instrumentation</b>			
Chemiluminescence detector	NO / NO <sub>y</sub>	x	--
VUV fluorescence	CO	x	--
UV absorption	O <sub>3</sub>	x	--
IR absorption	CO <sub>2</sub>	x	--
Tunable Diode Laser Spectrometer	H <sub>2</sub> O	x	--
Ion Trap Chemical Ionisation MS	SO <sub>2</sub>	x	--
<b>Meteorological data</b>			
Falcon standard instrumentation	<i>T</i> , <i>p</i> , <i>RH</i> (BL, FT), 3D-wind velocity	x	x

The ITOP forest fire plumes were identified from the measurements by means of excess CO measurements and FLEXPART trajectory calculations (see Section 3.2.2.3, p. 59ff). Since the HSRL acted as pathfinder to direct the aircraft into the SAMUM dust plumes, the identification of dust encounters was much easier than the identification of forest fire plumes, and did not require the involvement of tracer measurements and trajectory calculations. Trajectories were only calculated to identify the source regions of the various dust encounters.

For the analysis of the SAMUM data a newly developed inversion algorithm (*Fiebig et al.*, 2005) was employed, which allowed the combined analysis of multiple instruments. The inversion algorithm was not available for the analysis of the ITOP data (Table 8). For that reason the data of each instrument were inverted separately and combined afterwards. To ensure that the analyses performed with and without the inversion algorithm yield the same results, which ensures comparability of data from both field experiments, the inversion algorithm has been validated based on a few SAMUM cases (see Section 3.3.4, p. 74ff).

The combination of the 3- $\lambda$ -PSAP data and the inversion algorithm was used to determine the complex refractive index of the particles for every SAMUM constant level sequence (*Rasp*, 2007). The refractive index provided the basis for the inversion of the data from the optical spectrometers (see Section 3.3.3, p. 68ff). In contrast, the ITOP data of the optical spectrometers were inverted using refractive indices typical for a particular aerosol type. As shown later (see Figure 46, p. 72, and Section 3.3.3), the PCASP-100X is not very sensitive to variations in the refractive index for the size range where forest fire particles usually occur. Therefore, uncertainties introduced in the analysis of the ITOP OPC data due to assumptions on the refractive index do not influence the results of ITOP.

**Table 8.** Data analysis methods used for the ITOP and SAMUM data. The inversion algorithm was only available for the analysis of the SAMUM data.

Data analysis procedure	Data analysis method	ITOP	SAMUM
conventional data analysis	separate data inversion for every single instrument	x	x
inversion algorithm	combined inversion of three CPCs and PCASP-100X (CPC+PCASP), TD, three CPCs and Grimm OPC (TD+CPC+GRIMM); separate analysis of FSSP-300	--	x

### 3.3 Data analysis

The characterisation of a specific aerosol type is a comprehensive task. To determine the particle concentration which changes in space and time is not sufficient. To characterise an aerosol requires, the determination of the number concentration as a function of particle diameter, the chemical composition, the state of mixing and the morphology of the particles. All those properties are related to formation and transformation processes (see Section 2, p. 17ff).

#### 3.3.1 Volumetric units and aerosol modes

The use of volumetric units throughout this work requires explanation. If number or mass concentrations, aerosol absorption coefficients and particle size distribution refer to standard temperature and pressure conditions STP (273.15 K, 1013.25 hPa), they are given as particles per standard  $\text{cm}^{-3}$  ( $\text{scm}^{-3}$ ),  $\mu\text{g}$  per standard  $\text{m}^3$  ( $\mu\text{g sm}^{-3}$ ), absorption per standard Mm ( $\text{sMm}^{-1}$ ,  $10^{-6} \text{ sm}^{-1}$ ). Since pressure and temperature vary during the measurement, it is important to define a standard set (STP) of conditions that enables comparisons between sets of data recorded under different temperature and pressure conditions. The STP concentration data correspond to mixing ratios, which are independent of ambient pressure and temperature during the measurement. If the concentration data are not explicitly given in STP, they refer to ambient conditions. In the presented tables (e.g. Table 10, Table 12, and Table 14) the

factor  $f_{STP}$  necessary for the conversion from STP to ambient conditions is given. Optical properties are calculated from ambient microphysical properties.

Based on the instrument and the inlet characteristics, the aerosol population is described in several sub-ranges: nucleation mode particles (*NUC*) with  $D_p < 14$  nm, Aitken mode particles (*AIT*) with  $14 \text{ nm} < D_p < 100$  nm, and accumulation mode particles (*ACC*) with  $0.1 \text{ }\mu\text{m} < D_p < 3.0 \text{ }\mu\text{m}$ . *COA* refers to coarse mode particles with  $D_p > 3 \text{ }\mu\text{m}$ . The inlet features during ITOP (cut-off; see Section 3.1.8, p. 44) justify the definition of  $N_{AIT} = N$  (CPC,  $D_{p,50\%} = 14$  nm) and  $N_{ACC} = N$  (PCASP-100X), since the instruments have only a limited overlap with respect to detection diameters. The classification of *NUC*, *AIT* and *ACC* played a major role only during ITOP, where the non-volatile size fraction was determined only in these size ranges.

### 3.3.2 Time series of microphysical aerosol properties and data reduction

Time series of *NUC*, *AIT* and *ACC* particle number concentrations (e.g. Figure 44) were determined from CPC and PCASP-100X data. Time series of *COA* (e.g. dust) particle concentrations are determined from FSSP-300 data. All instruments report 1 Hz data. However, the time series were calculated for a time resolution of 5 s to avoid instrument response time effects. Time series of *ACC* and *COA* mode aerosol volume were calculated from PCASP-100X and FSSP-300 data under the assumption of spherical particle shape and a preliminary (see Section 3.3.3) refractive index of  $m = 1.53 + 0i$  (ammonium sulphate). *PM2.5* time series were inferred from the aerosol volume by assuming unit particle density of  $1000 \text{ kg m}^{-3}$  for forest fire encounters and a particle density of  $2600 \text{ kg m}^{-3}$  (Hinds, 1999) for desert dust encounters.

For this study, data were reduced to relevant periods and interesting sequences, e.g. forest fire and desert dust encounters. Then, the data were averaged over homogeneous sequences, and size distributions were calculated. Figure 44 illustrates time series of forest fire (top panel) and desert dust (bottom panel) aerosol properties within a forest fire (dust) plume. In both panels, the flight altitude is indicated by a grey line. The grey shaded areas mark the sequences in which the data were averaged to derive size distributions. From Figure 44 a general feature of ITOP and SAMUM time series is obvious: the SAMUM time series are much more homogeneous than the ITOP time series. This point is taken into account in the data analysis. Whereas for SAMUM in almost all cases averaging over one constant level sequence (about 5-10 minutes) provided representative data, the ITOP data had to be averaged over much shorter time sequences in order not to smooth the structures within the layer too strong.

### 3.3.3 Size distribution data

Particle size distributions were derived from a combined analysis of CPC, DMA, PCASP-100X and FSSP-300 data. Figure 45 summarises the size range which is covered by various measurement techniques together with an idealised aerosol size distribution (grey line). The CPCs were operated at different lower cut-off diameters (see Figure 39, p. 58). The DMA was operated in a stepping mode, and it was kept for 10 s at each diameter, which gives a total measurement cycle of about one minute for one size distribution. To avoid relaxation

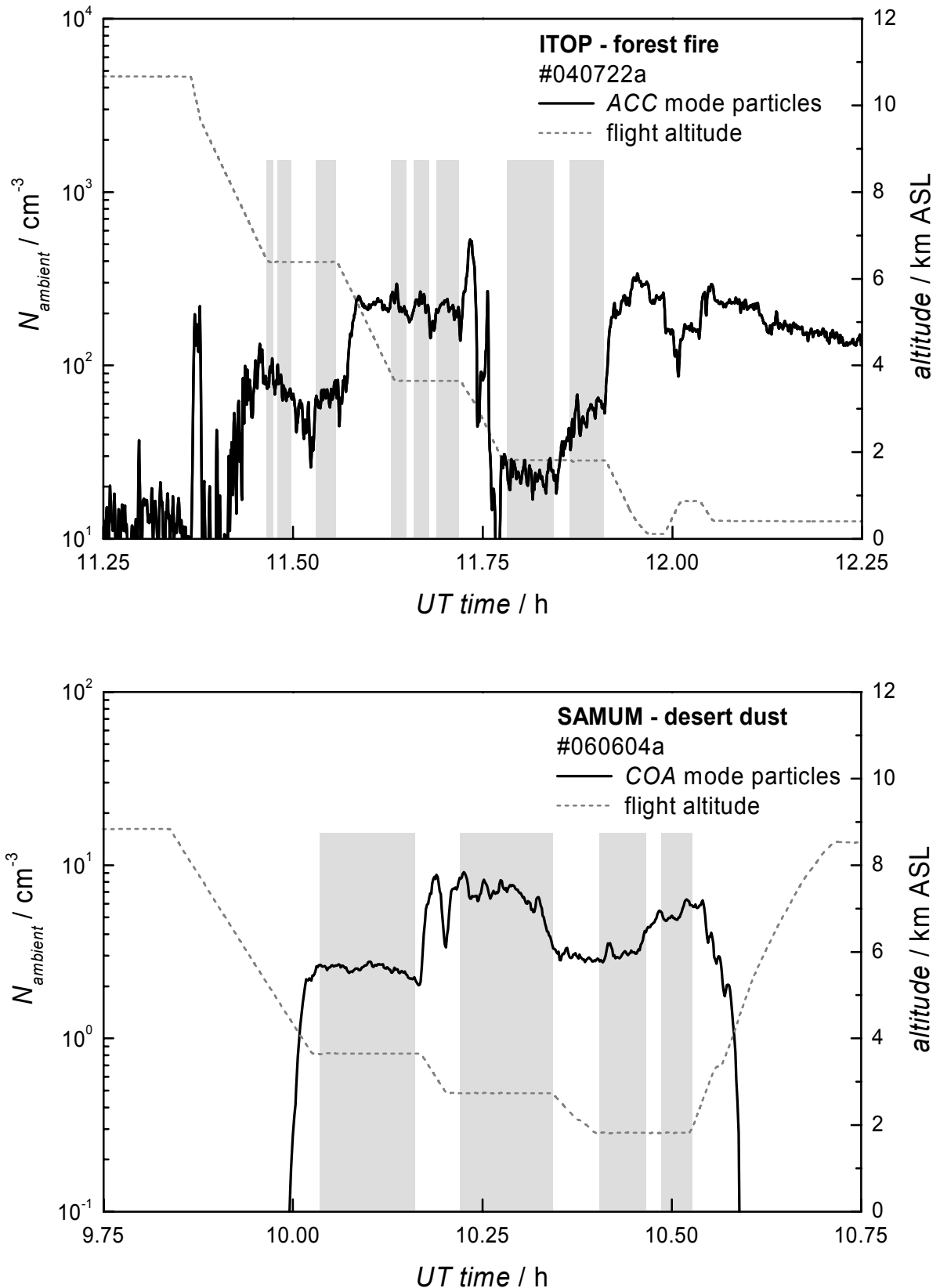


**Figure 44.** Time series of ACC mode particles for the ITOP (forest fire, top panel) research flight on 22 July 2004 and COA mode particles for the SAMUM (desert dust, bottom panel) research flight on 4 June 2006. The flight altitude is marked by the dashed grey line and the grey shaded areas indicate the averaging periods.

effects during the variation of the preset DMA diameter, the first 5 s of data at each diameter were not used for the analysis. The data inversion procedure used is based on the algorithm described by *Reischl* (1991). As the analysis schemes for the ITOP and the SAMUM size distribution data are slightly different, they are described separately for both data sets in the following paragraphs.

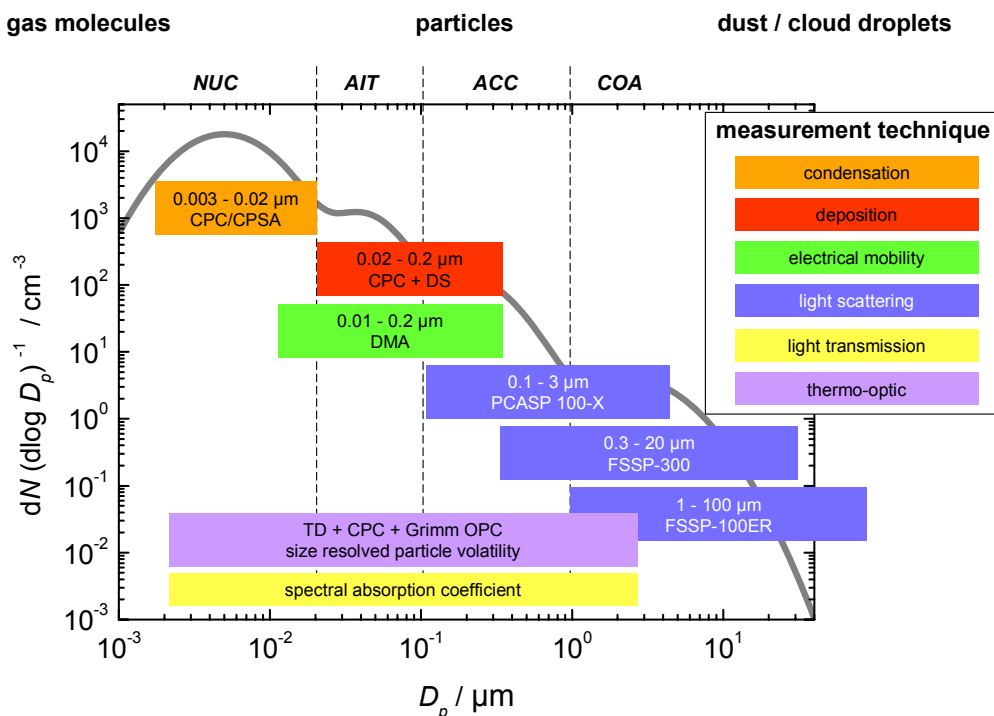


**Figure 45.** Schematic of size ranges covered by the in-situ measurement techniques of the DLR Falcon instrumentation. CPC: Condensation Particle Counter, CPSA: Condensation Particle Size Analyser, DS: Diffusion Screen, DMA: Differential Mobility Analyser, PCASP-100X: Passive Cavity Aerosol Spectrometer Probe, FSSP: Forward Scattering Spectrometer Probe, TD: thermal denuder, Grimm OPC: Grimm Optical Particle Counter.

### ITOP size distribution data

The DMA was the central instrument in the analysis of the ITOP data to derive the size distribution below  $0.2 \mu\text{m}$ . As forest fire particles dominate the Aitken and the accumulation mode, the CPC, DMA and PCASP-100X instruments were sufficient to determine the complete forest fire size distribution (see for example Figure 54, p. 86). The FSSP-300 was mainly used to identify in-cloud sequences in the ITOP data. Sequences were labelled in-cloud, when the number concentration in the FSSP-300 cloud/dust mode ( $D_p > 3 \mu\text{m}$ ) exceeded  $1 \text{ cm}^{-3}$ . The size distributions outside of forest fire plumes were calculated from PCASP-100X data (operation wavelength  $\lambda = 632 \text{ nm}$ ) using a refractive index of  $m = 1.53 + 0.0i$  (ammonium sulphate) for tropospheric airmasses, and  $m = 1.40 + 0.0i$  (sulphuric acid) for the tropopause region outside the forest fire smoke plumes. Inside forest fire plumes, complex refractive indices composed of a scattering component with  $m = 1.53 + 0.0i$  (*Haywood et al.*, 2003b) and an absorbing component with  $m = 2.00 + 0.63i$  (*Ackerman and Toon*, 1981) were considered reasonable assumptions. Refractive indices for different BC volume concentrations were inferred with the volume-weighting of refractive indices method (*Ackerman and Toon*, 1981; *Ouimette and Flagan*, 1982; *Chýlek et al.*, 1988) (see Equation

2.15, p. 28). An aerosol containing 5% (10%) of BC by volume is then described by a complex refractive index of  $m = 1.553 + 0.032i$  ( $m = 1.577 + 0.063i$ ). Both refractive indices were used for the PCASP-100X size distribution inversion of data from forest fire encounters.

### **SAMUM size distribution data**

The SAMUM size distributions were derived from the combined analysis of CPC and PCASP-100X<sup>15</sup>, TD, CPC and Grimm OPC<sup>16</sup>, and FSSP-300 data with a newly developed inversion algorithm<sup>17</sup> (Fiebig *et al.*, 2005). During SAMUM, sizing below 100 nm was based on CPC and DS-CPC combinations, whereas the DMA was used as backup instrument with lower time resolution (~60s) than the DS-CPC combination (1s). During SAMUM, the DMA was used to check the validity of the inverted CPC+PCASP-100X size distributions (see Section 3.3.4, p. 74ff). The FSSP-300 was the central instrument for the determination of the coarse mode particles. To distinguish the in-cloud sequences from the dust sequences in the SAMUM data, additionally the relative humidity (*RH*) was considered. Sequences with *RH* > 90% were labelled in-cloud. The SAMUM size distributions in desert dust, urban, and mixed plume probes were inverted using the refractive indices derived from the 3- $\lambda$ -PSAP measurements (see Section 3.3.6, p. 77ff) for the particular averaging period. Again, for the tropopause region outside of dust plumes, a refractive index of  $m = 1.40 + 0.0i$  was used. Desert dust size distributions were derived from PCASP-100X and FSSP-300 under the assumption of spherical shape, although dust particles have non-spherical shape. However, the derived dust size distributions are representative for the true dust size distribution, since both instruments are recording the forward scattered light. The forward scattered light is least sensitive to particle asphericity (Mishchenko *et al.*, 1997). A very recent study on the measurement of mineral aerosol size distributions with laser particle sizing instruments (recording the scattered light at various angles close to the forward direction) concluded that size distributions derived from optical probes using Mie theory are a useful estimate for the true desert dust size distribution (Veihelmann *et al.*, 2006).

### **Assessment of uncertainties in the size distribution due to assumptions on the refractive index**

To assess the errors introduced in the data analysis by uncertainties in the refractive index, the sensitivity of the size distribution from the PCASP-100X and the FSSP-300 was tested for several refractive indices, which covered the uncertainties in the refractive index. Results of the sensitivity study are shown in Figure 46. The size distribution of non-absorbing particles appears to be rather insensitive to the variation of the real part of the refractive index for both instruments (not shown). The size distribution of the PCASP-100X is even insensitive to the variation of the imaginary part of the refractive index for particles  $D_p < 0.6 \mu\text{m}$  (Figure 46, top panel), while for larger particles with increasing imaginary part the size distribution changes. In contrast, the size distribution derived from the FSSP-300 (Figure 46, bottom panel) is more sensitive to the variation of the imaginary part of the refractive index: an increasing absorption shifts the size distribution towards larger particle sizes.

<sup>15</sup> Henceforth, the notation CPC+PCASP refers to the combined data inversion with the inversion algorithm.

<sup>16</sup> The notation TD+CPC+Grimm OPC also refers to the combined data inversion with the inversion algorithm.

<sup>17</sup> In the following referred to as inversion algorithm.

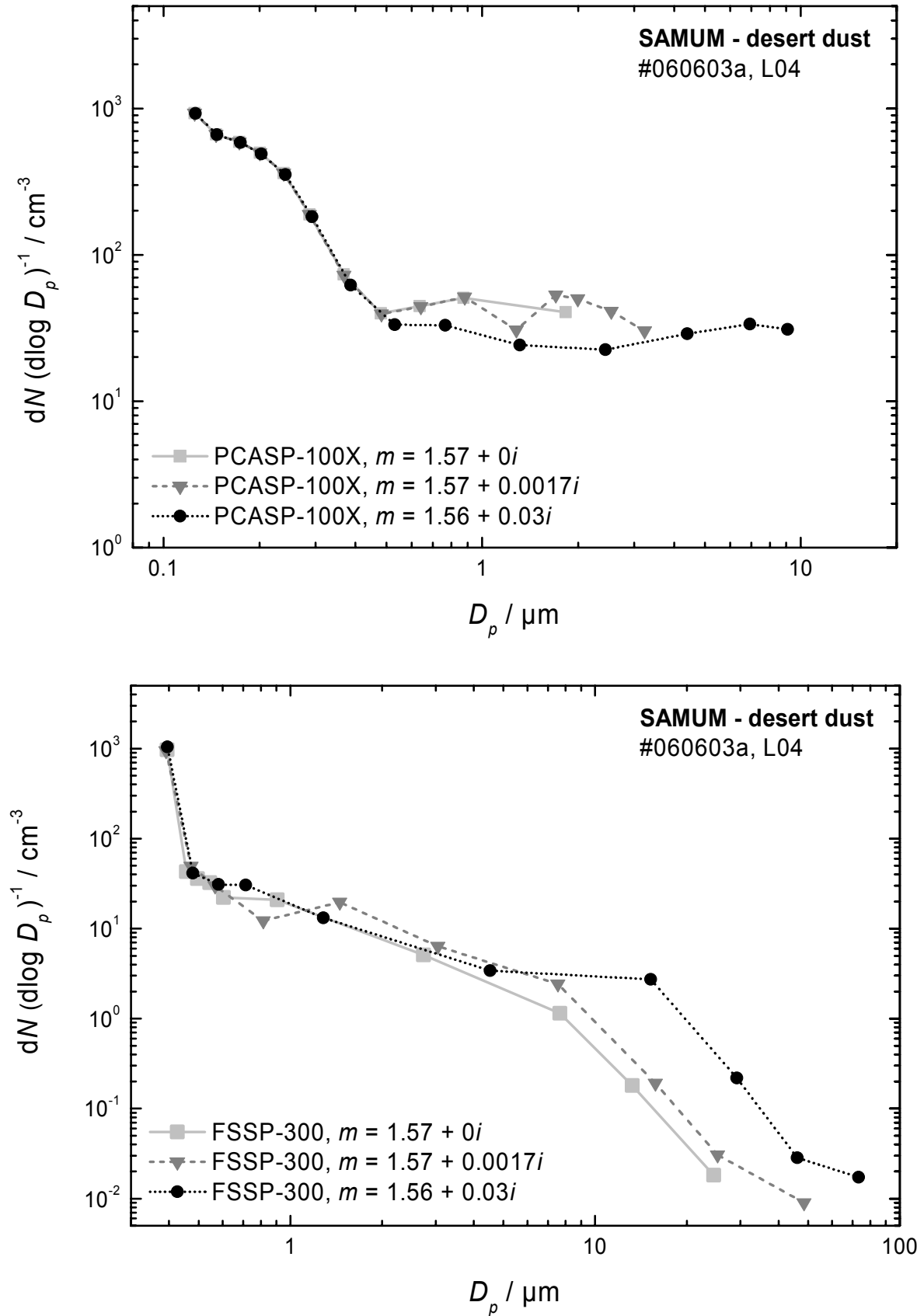


**Figure 46.** Sensitivity of particle size distribution derived from the PCASP-100X (top panel) and the FSSP-300 (bottom panel) to the chosen refractive index.

During ITOP the refractive index was not well known, but the less sensitive PCSAP-100X instrument was sufficient to derive the forest fire size distributions. Therefore, the error introduced in the derived forest fire aerosol size distributions can be neglected. During SAMUM, the FSSP-300 was very important due to the large sizes of the dust particles. However, the refractive index was better known, since it was inferred from the 3- $\lambda$ -PSAP measurements for every dust sequence. As shown in *Rasp* (2007), the imaginary part of the refractive index derived from the 3- $\lambda$ -PSAP measurements corresponds within 50% with chemical analyses (see also Section 3.3.6, p. 77ff). The influence of these uncertainties in the imaginary part of the refractive index on the derived size distributions can be quantified as follows: the particle size distribution for a particular dust sequence is calculated for different imaginary parts of the refractive index. Then, from the inferred size distribution the effective diameter  $D_{eff}$  is computed. To estimate the upper limit of these errors, a dust size distribution which extended to  $D_p \sim 40 \mu\text{m}$  was taken, and the imaginary part of the refractive index was varied by  $\pm 10\%$ ,  $\pm 20\%$  and  $\pm 50\%$ . For all cases the  $D_{eff}$  was calculated. A variation of  $\pm 10\%$  ( $\pm 20\%$ ,  $\pm 50\%$ ) in the imaginary part of the refractive index yielded a change in  $D_{eff}$  of 3-4% (3-5%, 5-8%). These results suggest that the uncertainty introduced in the derived size distributions can be regarded as minor.

### Parameterisation of size distributions

To describe particle size distributions in optical models, it is required to formulate a mathematical expression for the measurements with a few adjustable parameters. As pointed out in Section 2.2.1 (p. 19ff), a popular parameterisation is the log-normal distribution. In this study, the obtained size distributions were parameterised by fitting multi-modal log-normal distributions. Mode  $X_i$  is represented as a Gaussian distribution of  $\log D_p$ , which is centred at the count median diameter  $CMD$  with geometric standard deviation  $GSD$  of  $\log D_p$  (see Equation 2.2, p. 21). The log-normal distribution is completely described by three parameters: the particle concentration  $N$ ,  $CMD$  and  $GSD$ . It turned out that four modes are needed for an adequate representation of the observed dust size distributions, whereas three modes were sufficient for the representation of the forest fire size distributions.

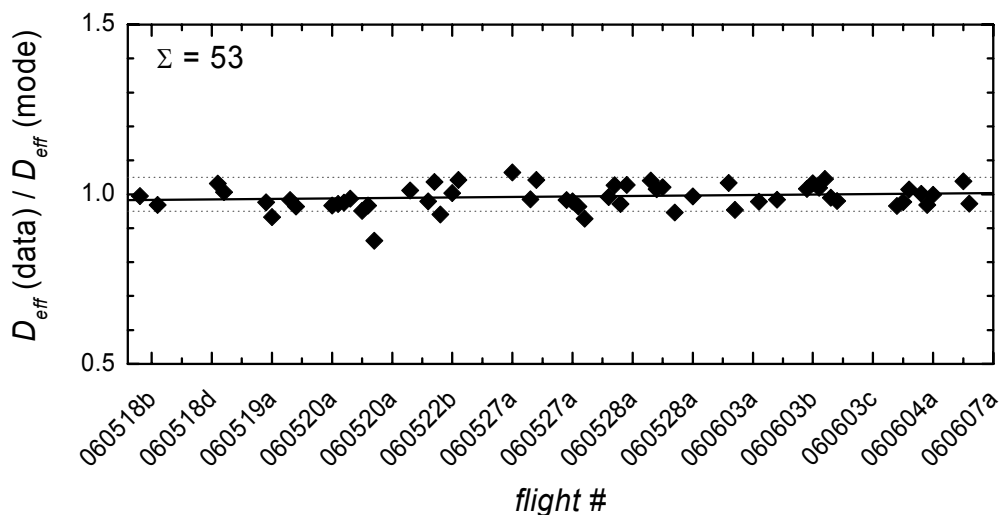


**Figure 47.** Quality control of the parameterised size distributions. The black symbols show the ratio of  $D_{eff}$  calculated from the data and from the parameterisation. The regression line is shown in black, and the dotted grey lines denote 5% deviation from perfect match.

Large errors can be introduced in the calculation of optical parameters, if the parameterisations do not exactly fit the measured size distribution. To avoid errors due to inadequate parameterisation a quality control criterion was developed. The quality of the parameterisations was controlled by comparing effective diameter calculated directly from the inverted data  $D_{eff}(\text{data})$  and from the parameterisation  $D_{eff}(\text{mode})$  using the Hatch-Choate conversion equations (*Hatch and Choate*, 1929) (see Equation 2.3, p.22). The parameterisations were regarded as adequate when the deviation between  $D_{eff}(\text{data})$  and  $D_{eff}(\text{mode})$  was smaller than 7.5%. Figure 47 summarizes the ratio  $D_{eff}(\text{data})/D_{eff}(\text{mode})$  (black symbols) for all 53 parameterised SAMUM size distributions. The regression line is shown in black, while the grey dotted lines indicate 5% deviation from the perfect match. In 91% of the cases the deviation between parameterisation and data was smaller than 5% and in 60% it was even smaller than 3%.

### 3.3.4 Validation of the inversion algorithm

The various measurement techniques described in Section 3.1 (p. 31ff) do not directly measure particle size distributions. To derive particle size distributions, the raw data of each instrument need to be inverted. This can be done separately for each instrument by applying the transfer equations for every instrument (described in detail in Section 3.1) or by an algorithm that combines simultaneously the information of several instruments and extracts the particle size distribution for the instrument combination. The inversion algorithm, which is described in detail in *Fiebig et al.* (2005), is capable of combining data from different instruments for the same aerosol into one particle size distribution without assuming a shape of the size distribution, covering four orders of magnitude in particle concentration, not needing an initial guess, and providing the uncertainty of the inversion result. Since for the analysis of the ITOP data the inversion algorithm was not yet available, the size distributions were derived for each instrument separately and subsequently combined to a size distribution (“conventional analysis”). The SAMUM data were inverted using the inversion algorithm.

So far, no validation of the inversion algorithm against the conventional data analysis procedure has been published. Hence, the inversion algorithm is here validated for the first time for atmospheric aerosols against the independent conventional data analysis procedure. The results for one case are displayed in Figure 48. The red, orange and brown symbols are deduced with the conventional method from DMA, PCASP-100X and FSSP-300 measurements, respectively. The PCASP-100X and FSSP-300 data were inverted using a refractive index of  $m = 1.57 + 0.0017i$ . The error bars represent the standard deviation of atmospheric particle concentration within the averaging interval, and are therefore dependent on the atmospheric variability of particle concentrations. The dark grey and black lines show the size distribution derived with the inversion algorithm. According to *Fiebig et al.* (2005), the inversion algorithm retrieves the size distribution with an uncertainty of less than 8%. The grey shaded area in Figure 48 indicates the uncertainty of the inversion result, based on the Monte-Carlo method, which is implemented in the inversion algorithm. The uncertainty is dominated by the atmospheric variability of the particle concentrations. Due to decreasing information, the uncertainty increases on both ends of the instrument spectrum. This may explain the larger deviation between inversion and conventional data analysis for diameters of  $\sim 0.02 \mu\text{m}$ . Generally, the size distributions of both methods are in excellent agreement for the

dust layer L04 on 3 June 2006. Also further intercomparisons between the conventional method and the inversion algorithm for other cases show excellent agreement.

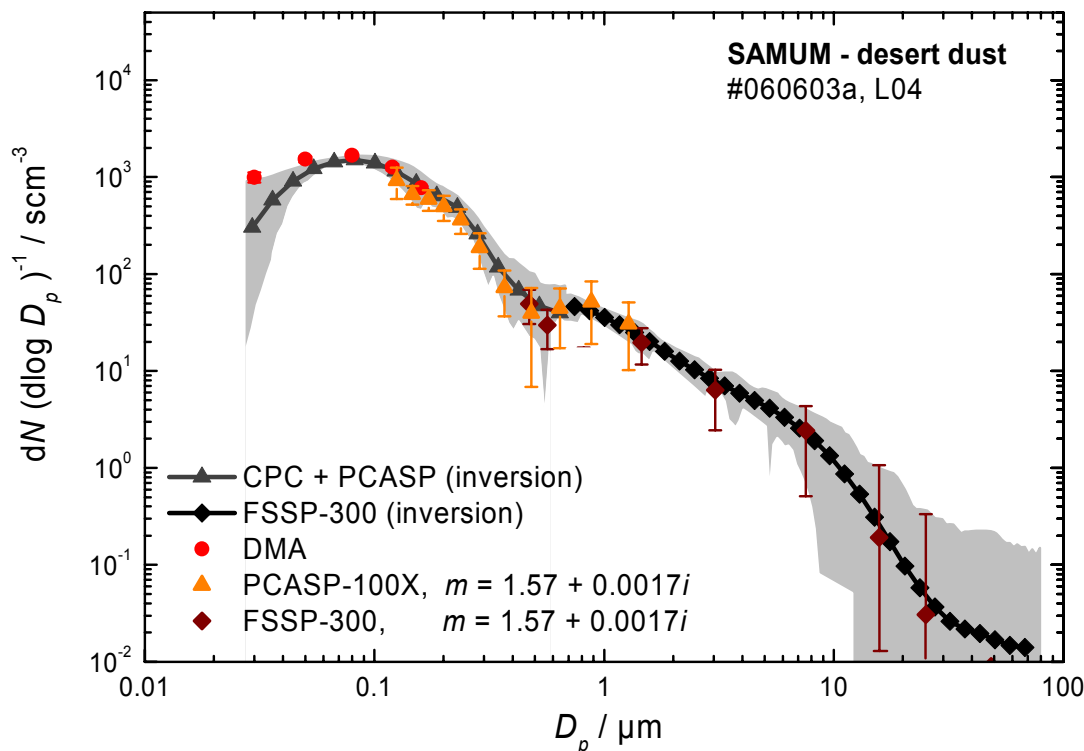


**Figure 48.** Size distribution deduced with the conventional method (red, orange and brown symbols), and size distribution from the inversion algorithm (lines) for the dust layer L04 on 3 June 2006. Particle number concentrations  $N$  refer to STP conditions.

### 3.3.5 Volatility analyses – aerosol mixing state

It is very important to investigate the aerosol mixing state, because it provides information on transformation and ageing processes acting on an aerosol population. The global characterisation of the mixing state is quite difficult, as most of the existing measurements are bulk measurements, which deliver no information on the chemical composition of the aerosol (Mishchenko *et al.*, 2004). Single particle analysis of aerosol samples can provide information on the mixing state, but these measurements are very time consuming, so that only a limited number of samples can be analysed. Another possibility to get information on the mixing state is the combination of particle sizing instruments with a thermal denuder TD (Clarke, 1991). This combination allows the determination of the volatile and non-volatile particle fractions with a high resolution in time and space. The heating temperature of the TD used during ITOP and SAMUM was set to 250°C for separating volatile components of sulphuric acid-like and ammonium sulphated-like behaviour from non-volatile or refractory components like BC, sea salt, dust and crustal material (e.g. Engler *et al.*, 2006). During ITOP, the non-volatile particle fraction was determined for three size ranges by three pairs of CPCs set to different lower cut-off diameters with one CPC of each pair connected to a TD. The three size ranges were *NUC* ( $4 < D_{p,50\%} < 14$  nm), *AIT* ( $14 < D_{p,50\%} < \sim 80$  nm) and *ACC* ( $D_{p,50\%} > \sim 80$  nm). For the SAMUM campaign the volatility measurements were extended. Additional to the three

pairs of CPCs, the Grimm OPC was connected to the TD. With this configuration the derivation of the non-volatile size distribution for particles  $D_p < \sim 2.5 \mu\text{m}$  was possible.

It is enlightening to compare the total and the non-volatile aerosol fraction to draw conclusions on the aerosol mixing state. Figure 49 illustrates how the aerosol mixing state is inferred from the volatility measurements in this work. Figure 49a depicts a scatter plot of the non-volatile number concentration and the total particle number concentration in a particular size range (e.g. in the *AIT* mode). An internally mixed aerosol composed of non-volatile components and coated particles with a non-volatile core would group on the 1:1 line in such a graph. Aerosols appearing below the 1:1 line are externally mixed, and include totally volatile particles. The further the particle population is shifted from the 1:1 line, the more totally volatile particles are contained in the aerosol population. Volatility analyses limited to a few ranges allow only a qualitative distinction between internal and external mixture. To investigate possible coatings on the particle, the total and the non-volatile size distributions have to be compared. Figure 49b-d shows intercomparisons of the total aerosol size distribution (blue line) and the non-volatile size distribution (brown line). In an internally mixed and coated aerosol (Figure 49b), the total and the non-volatile size distribution would have the same shape, but the maxima of the non-volatile size distribution would be shifted to smaller particle sizes. One would expect such a mixing state for an aged aerosol. In an externally mixed aerosol that contains a number of totally volatile particles, the shape of the total and the non-volatile size distribution would differ (Figure 49c). Such behaviour can be observed for example in fresh ship emissions. In an internally mixed aerosol without coatings, the total and the non-volatile size distribution would be identical (Figure 49d). Pure dust particles from fresh dust emissions are expected to have no coatings.

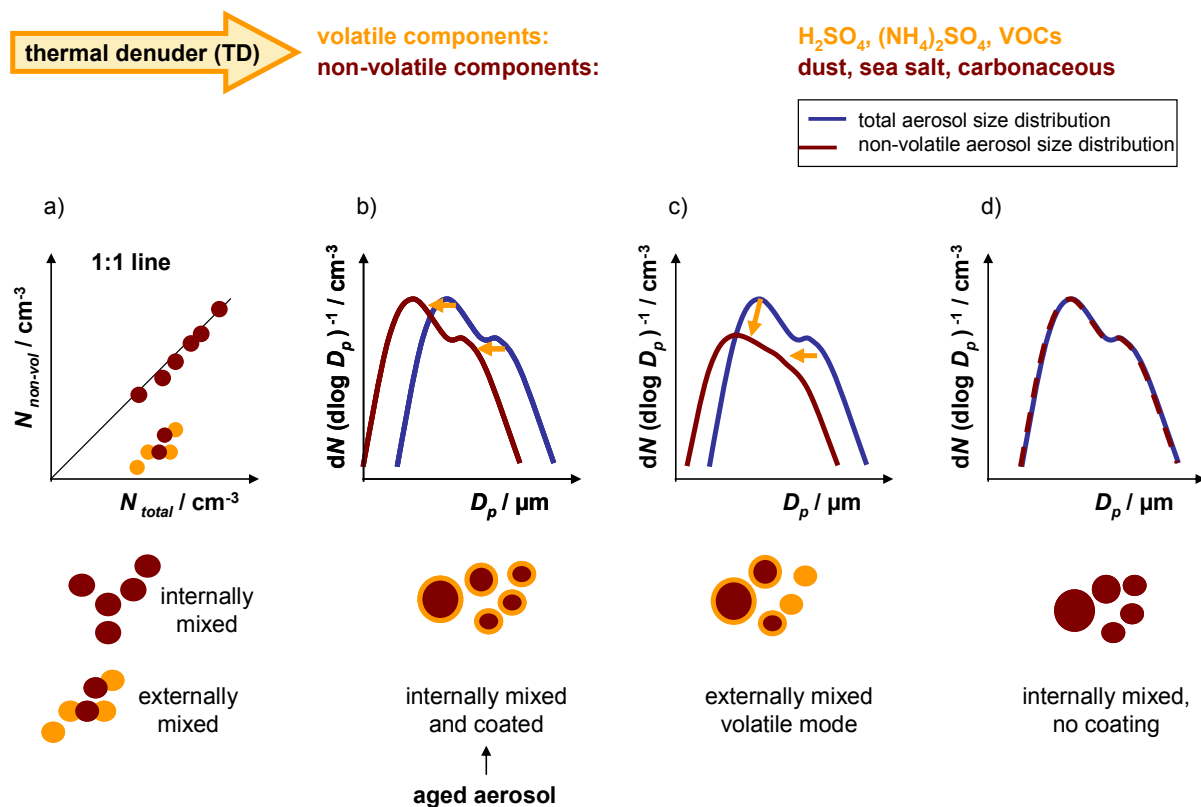


**Figure 49.** Schematic illustrating the derivation of the aerosol mixing state on the basis of volatility analyses.

### 3.3.6 Absorption data

During the ITOP field experiment, a Particle Soot Absorption Photometer (PSAP, see Section 3.1.6, p. 42ff) measuring at one wavelength was used, while during SAMUM a 3- $\lambda$ -PSAP was employed. The data from the PSAP were used to derive absorption coefficients  $\sigma_{ap}$  and BC mass concentrations. Former experience with the PSAP (*Petzold et al.*, 2002) evinced that only data on constant flight levels out of clouds are reliable. Out-of cloud sequences exclude measurement artefacts due to humidity-effects impacting on the filter transmission function (*Arnott et al.*, 2003). Reduction of PSAP data to constant-level sequences avoids measurement artefacts due to pressure changes in the sampling line which occur during ascent and descent of the aircraft and impact on the filter transmission function.

The 1- $\lambda$ -PSAP raw data from ITOP were smoothed using a 20 s moving average. The 20 s averaging time was found to smooth the scattered data sufficiently while keeping the time-resolution at a reasonable level. Based on the experience of earlier airborne applications of the PSAP (*Petzold et al.*, 2002), the detection limit of the method was determined to be  $0.1 \text{ Mm}^{-1}$ . The aerosol absorption coefficient  $\sigma_{ap}(\lambda = 550)$  was converted to an equivalent BC mass concentration by applying a mass-specific absorption cross-section of  $8 \text{ m}^2 \text{ g}^{-1}$  (*Bond and Bergstrom*, 2006). The 3- $\lambda$ -PSAP data from SAMUM were analysed using the inversion algorithm and the aerosol optical model (see Section 3.3.7). The absorption data were used to infer refractive indices from the spectral dependency of the absorption coefficient. The analysis of the absorption data is subject of a diploma thesis by *Rasp* (2007). As the refractive indices inferred from the 3- $\lambda$ -PSAP entered the analysis of size distribution data, the method by which refractive indices were derived is summarised in Figure 50 and explained briefly in the following.

In a first step, a realistic chemical composition is assumed. The aerosol was assumed to consist of one merely scattering component like quartz ( $\text{SiO}_2$ ) or ammonium sulphate ( $(\text{NH}_4)_2\text{SO}_4$ ), one light absorbing component with a weak spectral dependence of the absorption coefficient like BC or kaolinite ( $\text{Al}_2\text{Si}_2\text{O}_5(\text{OH})_4$ ), and one light absorbing component with a strong spectral dependence of the absorption coefficient like haematite ( $\text{Fe}_2\text{O}_3$ ). The assumptions on the chemical components were based on chemical analyses of filter samples by the Environmental Mineralogy Group of the Darmstadt University of Technology (*Kandler*, 2007, personal communication) which revealed that  $\text{SiO}_2$ ,  $\text{Al}_2\text{Si}_2\text{O}_5(\text{OH})_4$ ,  $\text{Fe}_2\text{O}_3$ , and  $(\text{NH}_4)_2\text{SO}_4$  are contributing significantly to the composition of desert dust. From the chemical composition the refractive index was inferred from an effective medium mixing rule (*Ackerman and Toon*, 1981; *Ouimette and Flagan*, 1982; *Chýlek et al.*, 1988). Applying this mixing rule, the real and imaginary part of the refractive index can be calculated as a linear combination of the refractive indices of the individual components  $l$  weighted by their volume fraction  $f_l$  (Figure 50). In a second step, a combined size distribution is calculated from CPC and PCASP-100X data. The size distribution and the refractive index served as input data for the aerosol optical model that computes the PSAP response. If the measured PSAP response is not matched by the computed one, the chemical composition is slightly varied. All steps are repeated until the calculated PSAP response fits the measured one. The graph on the right-hand side in Figure 50 illustrates the iterative inversion procedure of PSAP data. The measured PSAP signal is shown in black, the range of uncertainty is grey shaded, the dashed blue lines show the calculated response for different chemical compositions and the orange line shows the best match of measurements and

calculations. Since the PSAP measurements are conducted in the cabin of the aircraft, the characteristic of the aerosol inlet determines the maximum particle size collected on the PSAP filter.

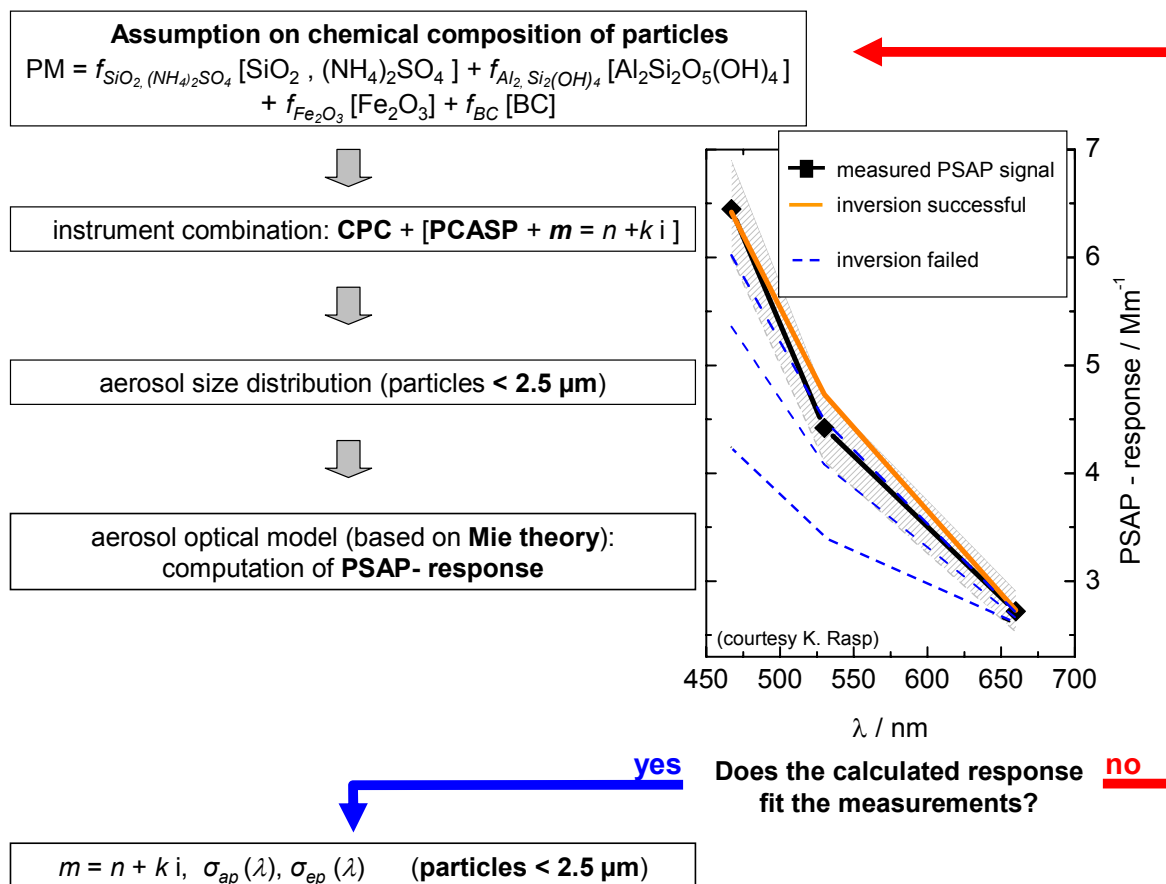


**Figure 50.** Schematic illustrating the derivation of refractive indices from 3- $\lambda$ -PSAP data by an iterative process (Rasp, 2007).

The described method allows the determination of the refractive index from absorption measurements. The derived refractive index was compared with chemical analyses from the University of Darmstadt for the SAMUM flight on 19 May 2006. Both methods corresponded within 50% (Rasp, 2007). Considering that the refractive indices of dust published in the literature vary by one order of magnitude, the agreement between the PSAP-derived refractive index and the chemical analyses is quite good.

### 3.3.7 Aerosol optical model

To perform radiative transfer calculations necessary for the interpretation of the data, several optical properties, namely, the light-scattering  $\sigma_{sp}$  and absorption coefficient  $\sigma_{ap}$ , the light-extinction coefficient  $\sigma_{ep}$ , the single-scattering albedo  $\omega_0$  and the asymmetry parameter  $g$  of the aerosol in the forest fire and desert dust plumes are required. These properties are a function of the wavelength. Spectral aerosol optical properties are calculated from size distribution, absorption measurements and volatility analyses with aid of an aerosol optical model. The *aerosol optical model* is based on two Mie codes, the *Bohren and Huffman* (1983) Mie code for the treatment of spherical particles and the *Toon and Ackerman* (1981) Mie code

for the treatment of coated spheres. The spherical particles are described by a single refractive index, while the coated spheres are described by two refractive indices, one for the core and one for the coating. Both models were combined by *Fiebig* (2007, personal communication) and embedded in a software routine written in C++ language, which was available for this investigation. This aerosol optical model includes a look-up table of common spectral refractive indices available in the literature. Spectral aerosol optical properties can be calculated from about 200 nm up to 20  $\mu\text{m}$ . The aerosol optical model is capable of treating internally and externally mixed aerosol modes and coated spheres within the same aerosol. Additionally, the model has a feature that allows the size-dependent specification of the chemical particle composition and the aerosol mixing state. This feature is necessary for example, if several chemical components are only present in a sub-size range of the total aerosol size range as it is observed in forest fire aerosols (see Section 4.1.3, p. 88ff). Input data of the aerosol optical model are the integral particle concentration of each log-normal mode ( $N_{mode\ j}$ ), the median diameter ( $CMD_{mode\ j}$ ) and the geometric standard deviation ( $GSD_{mode\ j}$ ), the volume fractions of chemical components within one mode and the mixing state. All parameters can be specified for each mode separately.

### 3.3.8 Heating rates

For the interpretation of experimental data, radiative transfer calculations with the libRadtran software package were performed<sup>18</sup>. The libRadtran software package, including some examples of use, is described in more detail in *Mayer and Kylling* (2005). The main tool of libRadtran is the UVSPEC radiative transfer model (*Mayer et al.*, 1997), which can be used for the computation of heating rates.

Heating rates were calculated from 0 to 12 km altitude in the spectral interval 200 nm – 100  $\mu\text{m}$ . The model input parameters were solar zenith angle, vertical profiles of atmospheric pressure, temperature and humidity, and trace gases, as well as aerosol optical properties, and surface albedo. For the calculations performed in this work, it was assumed that no reasonable clouds were present. Atmospheric profiles for pressure, temperature and humidity, trace gas mixing ratios of CO<sub>2</sub> and O<sub>3</sub> were averaged in bins of 50 m. Above the maximal flight altitude the profiles were completed with data from the ECMWF operational analysis. The aerosol extinction profile at 532 nm is taken from the lidar measurements in the case of desert dust, while for the forest fire case an extinction profile was derived from the from aerosol size distribution and absorption data. Spectral extinction  $\sigma_{ep}$ , single-scattering albedo  $\omega_0$ , and asymmetry factor  $g$  was derived from Mie calculations with the aerosol optical model (Section 3.3.7). The spectral refractive index was derived by an iterative process as described in Section 3.3.6. The surface is assumed to have the spectral albedo of ocean water (ITOP, Atlantic) or grass land (SAMUM, Casablanca). The radiative transfer calculation was performed with a discrete ordinate solver with 6 streams. The absorption is accounted for by a correlated-k parameterisation of *Fu and Liou* (1992).

### 3.3.9 Combination of data

Two hypotheses, the self-stabilising and the sealed ageing effect (see Section 1.3, p. 11) will be investigated in this work. The assessment of these hypotheses requires the

---

<sup>18</sup> The calculated heating rates were provided by Ulrich Hamann (DLR).

combination of measurement data and model calculations. The flow-chart in Figure 51 summarises how the numerous data are combined to assess radiatively-driven processes in forest fire and desert dust plumes.

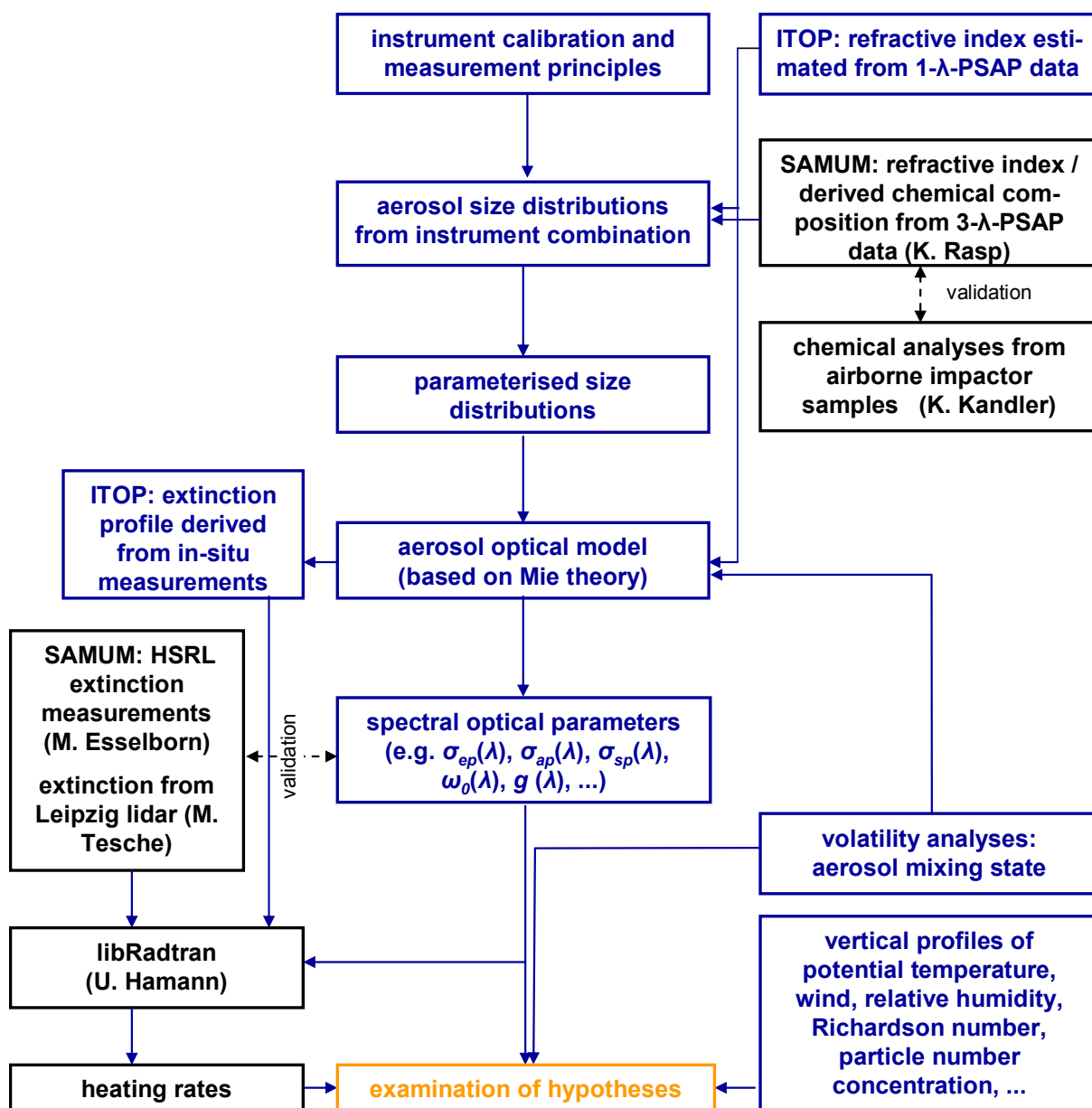


**Figure 51.** Flow-chart illustrating the data analysis procedure.

Particle size distributions are derived from measurements with multiple instruments. The size distributions are parameterised by fitting 3-4 log-normal distributions to the data. The quality of the parameterisations is evaluated by comparing effective diameter inferred from the inverted size distribution data and from the parameterisation. The size distribution data and the refractive index information serve as input for the aerosol optical model (based on Mie-theory) for the calculation of aerosol optical properties. The calculated aerosol optical properties are compared with other independent measurements of the optical properties like extinction coefficient from the HSRL (Esselborn, 2007) and the IFT-lidar (Tesche, 2007;

*Müller, 2007, personal communication*) to study the validity of the results. The optical properties are further compared with values published in the literature. The aerosol optical properties serve as basis for the radiative transfer calculations with libRadtran which were conducted by U. Haman. The heating rates are necessary to investigate the self-stabilising of the forest fire and desert dust plumes. The mixing state of the aerosol is derived from volatility analyses and gives insight into the ageing process of the aerosol during atmospheric transport. Vertical profiles of meteorological data like potential temperature, wind and humidity are used to explore the characteristic structures within lofted aerosol plumes. The information on meteorological parameters is used to show the impact of absorbing aerosol layers on atmospheric stability. Trajectory calculations are necessary to identify the sources of aerosol plumes and to estimate the age of the aerosol layers.



---

## **4 Properties of forest fire and desert dust plumes**

---

In this chapter the measured microphysical and optical properties of forest fire and desert dust aerosols are presented. In contrast to forest fire layers, where Falcon data only exist for aged aerosol layers (age: 4-13 days), dust layers were investigated close to the source (Sahara) and over Portugal (age: about 2 days). The findings will be discussed in Chapter 5, where explanations for the observed aerosol properties and the observed temperature structure are evaluated.

### **4.1 Forest fire aerosol (ITOP)**

This section investigates the frequency of forest fire plume transport to Europe in July 2004 (Section 4.1.1) and presents a case study of the most intensive forest fire plumes, investigated during ITOP (Section 4.1.2). Section 4.1.3 follows with the optical properties of the forest fire plumes on 22-23 July 2004, and Section 4.1.4 summarises the properties of other forest fire plumes during ITOP.

#### **4.1.1 Transport of forest fire plumes to Europe**

In July 2004, the European aerosol and trace gas composition was highly influenced by the long-range transport of forest fire plumes from Northern America. The CO mixing ratio was significantly increased in the altitude range between 3 and 9 km within the ITOP core phase between 19 July and 3 August 2004. The CO enhancement was mainly attributed to the frequent long-range transport of forest fire plumes from Northern America to Europe. The meteorological situation in Europe from 16 to 23 July 2004 was characterised by a low pressure system over the North Atlantic (a summary of daily large scale synoptic patterns is given in *Gerstengarbe and Werner, 2005*). Associated with this low pressure system the flow pattern over Western Europe was from the west-south-west. From 24 to 28 July 2004 a trough over Northern and Central Europe led to a west-north-westerly flow, advecting air masses from North America to Europe. The plumes arrived in Europe at 3-9 km altitude after a transport time of roughly one week (4-13 days). By the end of July a high pressure system started to build up over Central Europe and stopped the transport of forest fire plumes to Central Europe. This high pressure system persisted beyond the ITOP core phase until mid of August 2004.

Some insight into the frequency of forest fire plume transport across the Atlantic in July 2004 is gained from an examination of column integrated FLEXPART forest fire CO tracer simulations over Europe. The domain examined covers the region from 20° W to 10° E and from 35° N to 60° N corresponding to about 3300 km in the meridional direction and to 1900 km in the zonal direction. According to FLEXPART, forest fire plumes were present at least on 20 days over Europe in July 2004. For this analysis, only cases with the column integrated forest fire CO tracer concentrations larger than 120 mg m<sup>-2</sup> in an area larger than 100 km by 100 km were considered. This threshold value was chosen in order to not overestimate the forest fire contributions. Therefore the number of days with forest fire contributions can be seen as a minimum number. FLEXPART showed that the most intensive and strongest transport of forest fire plumes to Europe took place between 20 and 26 July, with a maximum on 22-23 July 2004. In this period the Falcon probed the layers several times.

#### 4.1.2 Case study 22 July 2004

Two research flights from Creil (France) to Santiago (Spain) and back were taking place on 22 July 2004 (see Table 5, p. 58). During these flights a forest fire plume emitted from strong boreal fires in Alaska (see Figure 37, p. 56) was probed several times at altitudes between 3 and 8 km ASL. Figure 52 summarises the flight track (light grey line) of the two flights on 22 July 2004.

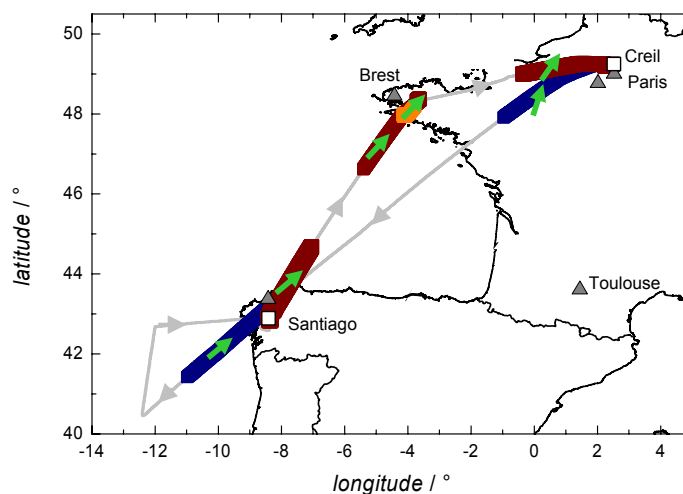
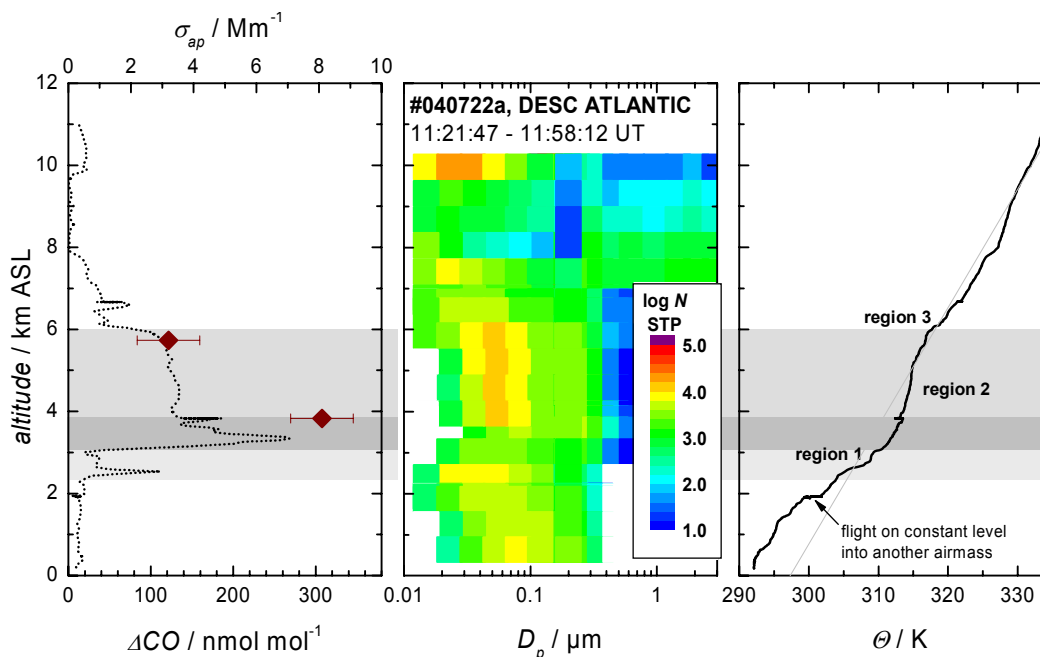


**Figure 52.** Map of the two ITOP flights on 22 July 2004. The light grey line shows the flight track with the flight direction indicated by grey arrows. The blue (brown/orange) lines mark the vertical profile measurements in the vicinity of Creil and Santiago during flight #040722a (#060522b). Forest fire layers have been encountered during all vertical profiles.

The blue lines mark the vertical profile measurements in the vicinity of Creil (France) and Santiago (Spain) during flight #040722a. The brown and orange lines mark vertical profile measurements during flight #040722b. Forest fire layers have been encountered during all profiles. The green arrows indicate the main wind direction. The wind blew from south-westerly directions (224-231°) and was rather constant with altitude above 2 km ASL. The flight path between Santiago and Brest was approximately parallel to the isentropes so that no appreciable temperature gradients have been crossed. Considering the wind speed and the time difference between the descent/ascent over Santiago and the descent over Brest (brown

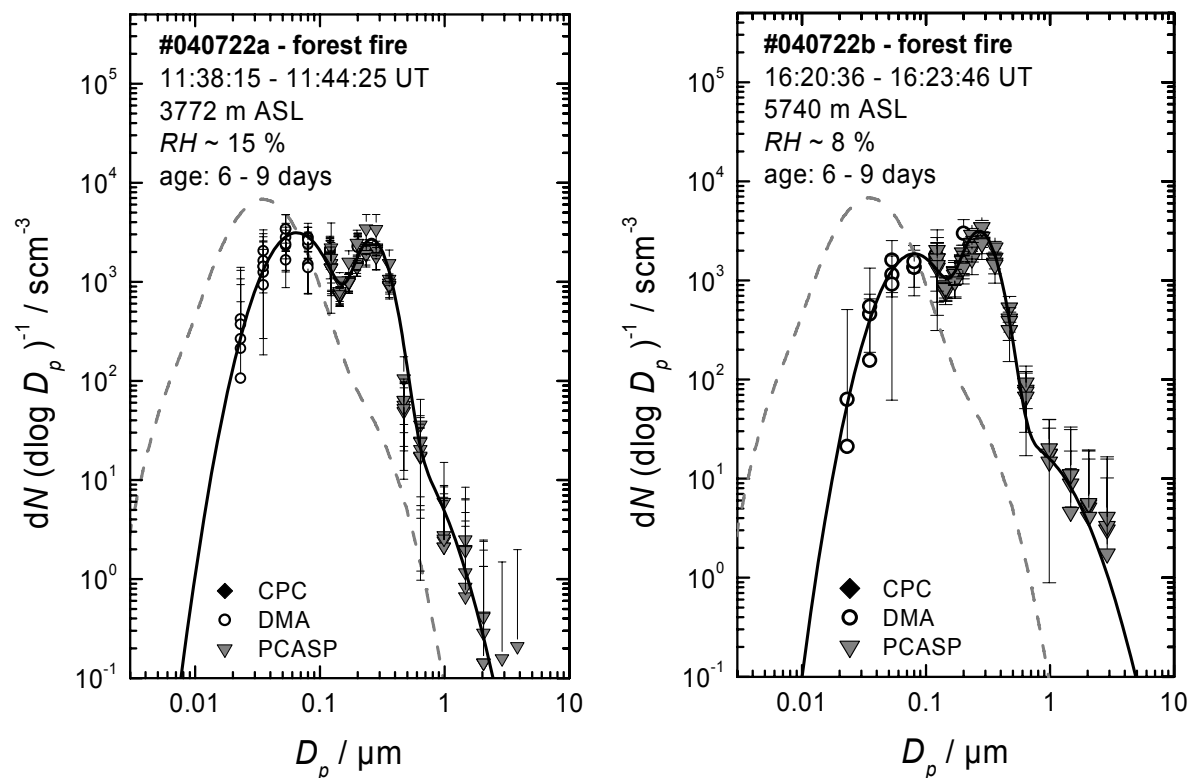
line in Figure 52), the forest fire plume that was first probed during the descent and ascent over Santiago was again probed during the descent and ascent south-west of Brest. The microphysical and chemical properties measured during the descent (blue line in Figure 52) and ascent in the vicinity of Santiago (brown line in Figure 52) were similar, although the altitude of the lower boundary of the forest fire layer was a little bit higher and deeper during the ascent.

Figure 53 presents one example of the complex structure of a vertical aerosol profile encountered during the flight #040722a. The graph shows a vertical profile of  $\Delta CO$  (left panel, dotted line), the absorption coefficient  $\sigma_{ap}$  derived on the constant-level sequences (left panel, brown symbols), a vertical profile of the aerosol size distribution inferred from DMA and PCASP-100X data (mid panel) and a vertical profile of the potential temperature. The measurements were taken above the Atlantic Ocean south-west of Santiago (blue line in Figure 52). The clean marine boundary layer reaches up to about 500 m ASL. From 2.3 km to approximately 6 km altitude, a layered structure is clearly visible, which can be attributed to the presence of forest fire aerosol. According to FLEXPART analyses, the lowest layer contains a mixture of forest fire aerosol and anthropogenic pollution from North America, the mean and upper layers contain pure forest fire aerosol. The polluted layers are characterised by enhanced  $\Delta CO$  values and enhanced aerosol absorption coefficients. The  $\Delta CO$  reaches a maximum of  $268 \text{ nmol mol}^{-1}$  at an altitude of 3.3 km ASL. The plume probed on 22 July was the densest with the highest aerosol absorption. Absorption coefficients ranged between 3 and about  $8 \text{ Mm}^{-1}$ , which is in the order of the polluted urban outflow of the Paris area. The maximum  $\sigma_{ap}$  of  $8.1 \text{ Mm}^{-1}$  was found at 3.8 km ASL (Figure 53, left panel).



**Figure 53.** Profiles of excess CO (left panel, dotted line) and aerosol absorption coefficient  $\sigma_{ep}$  (left panel, brown symbols), particle size distribution for STP conditions (mid panel) and potential temperature (right panel) for the profile over the Atlantic south of Santiago on 22 July 2004. The particle number concentration in the mid panel is colour coded (unit:  $\text{cm}^{-3}$ ). The shaded area illustrates the multi-layer structure (see text). FLEXPART analyses suggested that the lowest layer was a mixture of forest fire and anthropogenic aerosol, while the upper layers contained pure forest fire aerosol.

The size distribution in the left panel of Figure 54 corresponds to the measurements depicted in Figure 53, and the size distribution in the right panel of Figure 54 was taken during the descent south-west of Brest (Figure 52). Since the airmasses were very dry ( $< 30\%$  in most cases), no hygroscopic shift was applied to the size distributions. FLEXPART analyses indicated a plume age of 6-9 days. The forest fire size distributions are dominated by a strong accumulation mode with a  $CMD$  between  $0.2$  and  $0.3 \mu\text{m}$ , while the nucleation mode is entirely depleted. The absence of the nucleation mode is one of the key characteristics of aged forest fire layers.



**Figure 54.** Composite size distributions in forest fire plumes after transport times of more than one week determined from data of CPC (black squares), DMA (open circles) and the PCASP-100X (grey triangles). The size distribution in the left panel was measured during the descent over the Atlantic Ocean south-west of Santiago, while the size distribution in the right panel was measured during the descent close to Brest. Mission ID, time (UT), altitude, relative humidity RH and the plume age are given in the top left corner of each plot. The solid lines represent the 3-modal log-normal size distributions fitted to the measured data. The dashed grey lines illustrate a size distribution representative for the clean free troposphere measured on the same day. The error bars indicate the standard deviation of the particle concentration within the averaging interval.

Another important property of forest fire aerosols, the mixing state, can be assessed by means of volatility analyses as already explained in Section 3.3.5 (p. 75ff). Figure 55 shows scatter plots of the non-volatile and the total aerosol number concentration in the Aitken and accumulation mode size range for all forest fire encounters on 22 July 2004. Forest fire particles cluster along the 1:1 line with respect to  $N_{non-vol}$  versus  $N_{total}$  for both, Aitken (left panel) and accumulation mode (right panel). The non-volatile fraction in the Aitken mode  $f_{non-vol AIT}$  ranges between 80 and 95%, while the non-volatile fraction in the accumulation mode  $f_{non-vol ACC}$  is on average 95-100%. Almost all particles inside the aged forest fire layers

contain a non-volatile core and are entirely internally mixed. The smaller non-volatile fraction in the Aitken mode indicates that BC is mainly contained in the accumulation mode. In contrast, the Aitken mode contains particles with a certain volume fraction of BC and some totally volatile particles without BC.

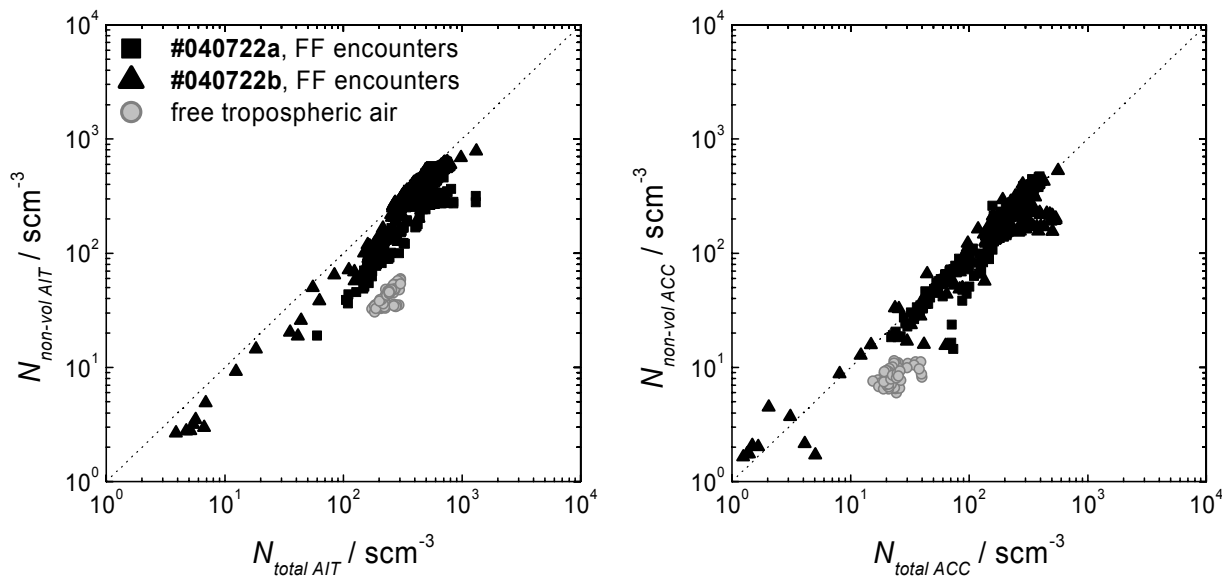


**Figure 55.** Mixing state of pure forest fire aerosol (FF; black symbols) sampled on 22 July 2004. The forest fire aerosol is internally mixed with non-volatile cores. Free troposphere data outside of smoke plumes (grey symbols) show a different behaviour.

Beside the microphysical properties, the forest fire plumes of the 22 July 2004 show a potential temperature<sup>19</sup> structure (Figure 53, right panel) which will prove to be characteristic for all forest fire plumes encountered: outside the forest fire layers potential temperature decreases on average by about  $3.5 \text{ K km}^{-1}$  (dashed line in the right panel of Figure 53). Inside the forest fire layer the potential temperature shows a typical structure with high stability at the lower and upper boundary of the aerosol layer and weak to almost neutral stability inside the layer. The lapse rate at the bottom and at the top of the aerosol layer is  $11.4$  and  $5.5 \text{ K km}^{-1}$ , respectively, while the lapse rate within the layer is  $2.5 \text{ K km}^{-1}$ . Assuming the standard atmosphere lapse rate of  $3.5 \text{ K km}^{-1}$ , the air within the forest fire layer is about  $4 \text{ K}$  warmer than expected. Similar structures of the vertical lapse rate were also found during the profile measurements over Creil and Brest. The potential temperature gradient within the forest fire layers can be grouped in three regions with different potential temperature gradient (Figure 53, right panel): the lower (region 1) and the upper part (region 3) with a large static stability, and the intermediate part (region 2) with neutrally to weakly stable stratification. Table 9 summarises the potential temperature gradient in the three regions of different static stability for forest fire layers on 22 July 2004, including an average lapse rate for the whole profile. Moreover, the altitude of the lower and upper plume boundary and the layer depth is shown. The lapse rate at the lower boundary of the layer is larger than  $5.6 \text{ K km}^{-1}$  in all cases and decreases to values between  $1.2$  and  $3.1 \text{ K km}^{-1}$  within the layer. The lapse rate at the

<sup>19</sup> The potential temperature is the temperature a parcel of air would have if it were adiabatically lowered (or raised) to a pressure of  $1000 \text{ hPa}$ . It is closely related to buoyancy. If the potential temperature increases with height, the profile is stably stratified, since a displaced air parcel will tend to return to its initial level.

upper boundary of the forest fire plumes ranges from 2.9 to 9.2 K km<sup>-1</sup>. Outside the plumes, lapse rates of 2.8 to 4.4 K km<sup>-1</sup> are found. In the case of the ascent over Brest only the lapse rates in region 1 and 2 could be determined, since the aircraft did not reach the top of the layer. Furthermore, the lapse rate in the forest fire layer over Creil (descent) exhibits only two regions of different potential temperature. It can be seen from Table 9 that in the course of the day, the stability inside the layer decreased and the inversion on top of the layer diminished.

**Table 9.** Forest fire layer structure on 22 July 2004. During the ascent over Brest only the lapse rate in region 1 and 2 could be determined, since the aircraft did not reach the top of the layer. The forest fire layer over Creil exhibited only two regions of different potential temperature.

Mission ID	Time of in-situ measurement / UT	Site	Lower boundary of forest fire layer / m ASL	Upper boundary of forest fire layer / m ASL	Forest fire layer depth / m	$d\theta dz^{-1} / K km^{-1}$ (region 1)	$d\theta dz^{-1} / K km^{-1}$ (region 2)	$d\theta dz^{-1} / K km^{-1}$ (region 3)	$d\theta dz^{-1} / K km^{-1}$ (profile average)
040722a	09:40 – 10:13	ASC Creil	4186	7671	3485	5.6	3.1	9.2	3.5
040722a	11:22 – 11:58	DESC Atlantic	2415	6197	3782	11.4	2.5	5.5	4.1
040722b	15:05 – 15:28	ASC Santiago	2592	6968	4376	10.9	1.2	5.8	3.5
040722b	15:45 – 16:06	DESC Brest	3735	6633	2898	10.0	1.5	6.7	3.7
040722b	16:11 – 16:17	ASC Brest	3581	n.d.	n.d.	7.9	1.5	n.d.	4.4
040722b	16:38 – 17:03	DESC Creil	2572	3608	1036	5.8	--	2.9	2.8

### 4.1.3 Optical properties of the aged forest fire plume on 22 July 2004

Optical properties of the forest fire plume on 22 July 2004 were calculated with the aerosol optical model (Section 3.3.7, p.78ff) on the basis of volatility analyses, size distribution and absorption measurements. The vertical profile of the size distribution (Figure 53, p. 85, mid panel) suggests that the forest fire plume can be divided into two sub-layers, each characterised by distinctive microphysical properties. The absorption measurements revealed absorption coefficients of 8.1 Mm<sup>-1</sup> and 3.5 Mm<sup>-1</sup> in the lower and upper sub-layer, respectively (Figure 53, left panel). BC contributed about 10% (3.5%) to the total aerosol volume in the lower (upper) sub-layer (Petzold *et al.*, 2007). The volatility analyses revealed 93% (80%) in the Aitken and nearly 100% (100%) non-volatile particles in the accumulation mode, i.e. all particles in the accumulation mode have a non-volatile core, while the Aitken mode contains both, totally volatile particles and particles with a non-volatile core. These analyses suggest that the non-volatile BC is only present in a limited size range if compared to the total size distribution (Figure 56). This BC size distribution does not necessarily peak at the same diameter as the overall size distribution. The size distribution of BC within the forest fire aerosol can be derived under consideration of the results of the volatility analysis together with the absorption measurements. First of all, the chemical composition of the particles, which is expressed by a complex refractive index, has to be estimated based on the measurements. A complex refractive index composed of a scattering component with  $m = 1.53 + 0.0i$  (Haywood *et al.*, 2003b) and an absorbing component with  $m = 2.00 + 0.63i$  (Ackerman and Toon, 1981) was considered as a reasonable assumption. Since the aerosol in the lower (upper) sub-layer contained 10% (3.5%) of BC by volume, the Aitken and the accumulation mode in the BC size distribution were described by a complex refractive index

of  $m = 1.577 + 0.063i$  ( $m = 1.546 + 0.022i$ ) (see also Equation 2.15, p. 28). The coarse mode was assumed to consist only of a scattering component with  $m = 1.53 + 0.0i$ , as BC particles are usually smaller. The volatility analyses showed 7% (20%) totally volatile particles in the Aitken mode. Therefore, the integral particle number concentration of the BC size distribution in the Aitken mode was assumed to be 93% (80%) of the total particle number concentration in the Aitken mode. In a next step the BC size distribution in the accumulation mode was slightly shifted to smaller particles until the calculated absorption coefficient reproduced the measured absorption coefficient. Figure 56 shows the resulting size-dependent composition of the forest fire aerosol.

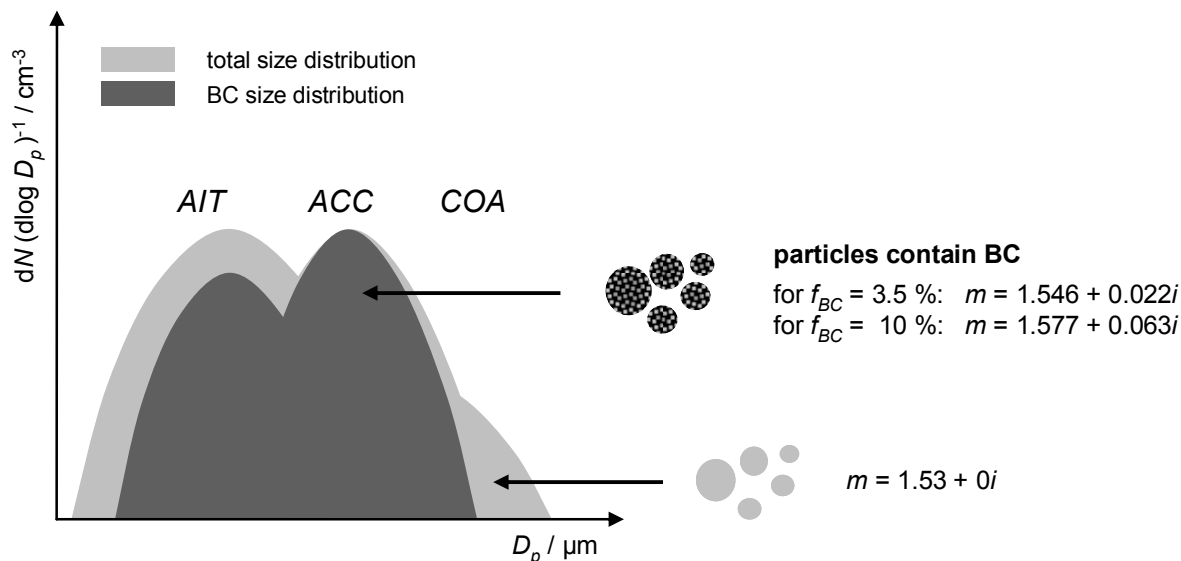


**Figure 56.** Sketch of the total size distribution and the BC size distribution observed in the ITOP forest fire aerosol. BC is only contained within the BC size distribution (dark grey shaded). In the Aitken mode some particles consist of purely scattering material and some particles contain an internal mixture of BC and purely scattering material. In the accumulation mode nearly all particles contain a certain fraction  $f_{BC}$  of BC. The particles in the coarse mode are again composed of purely scattering material.

Using this information on the mixture and size-dependent BC content, the aerosol optical model can be used to calculate the aerosol optical properties for the aerosol composition shown in Figure 56. Considering the information on the vertical plume extent from the in-situ measurements and assuming that the optical properties are constant with altitude in the lower and upper sub-layer, the *AOD* of the forest fire plume can be retrieved. This retrieval yielded an *AOD* of  $0.15 \pm 0.02$  for the forest fire layer on 22 July 2004. To check the plausibility of these calculations, similar calculations were conducted for the forest fire layer on 23 July 2003 that was also observed by the SARTA lidar at Palaiseau south of Paris. The retrieval yielded an *AOD* of  $0.13 \pm 0.02$  for the forest fire plume on 23 July 2004. This is in the range of the *AOD* (0.1-0.15) observed by the SARTA lidar on that day (*Real et al.*, 2007). The optical calculations yielded a single-scattering albedo of 0.85 (0.92) at 550 nm for the lower (upper) part of the forest fire layer. These values are consistent with the range of single-scattering albedo values of 0.83-0.9 indicated by *Reid et al.* (2005b) for boreal forest fires plumes.

**Table 10.** Microphysical properties of aged forest fire aerosol after long-range transport across the Atlantic Ocean. For comparison the properties of a size distribution in the free troposphere (FT) are also given. Size distributions were derived on constant altitude sequences out of cloud. The aerosol type was classified according to FLEXPART analyses and ACO measurements, and the plume age was estimated from FLEXPART trajectories. Besides start and stop time for each averaging interval, the altitude of the measurements, the relative humidity (RH) and the water vapour mixing ratio in the plume is given.  $N_j$ ,  $CMD_j$  and  $GSD_j$  result from log-normal fitting and denote the particle number concentration in mode  $X_j$ , the count median diameter and  $GSD$  is the geometric standard deviation. All mode parameters are given for STP conditions and can be converted to ambient conditions by multiplication with  $f_{STP}$ .  $F_{NUC}$  is the ratio of  $[N(CPC, D_{p,50\%} = 4) - N(CPC, D_{p,50\%} = 14)]/N(CPC, D_{p,50\%} = 4)$ .  $f_{non-vol AIT/ACC}$  is the ratio of the non-volatile and the total number concentration in the Aitken/accumulation mode. The effective diameter  $D_{eff}$  was calculated from parameterised size distributions via the Hatch-Choate conversion equations.

Mission ID	Type	Start Time / UT	Stop Time / UT	Altitude / m ASL	RH / %	Water vapour mixing ratio / g kg <sup>-1</sup>	$f_{STP}$	$N_{mode 1}$	$CMD_{mode 1} / \mu m$	$GSD_{mode 1}$	$N_{mode 2}$	$CMD_{mode 2} / \mu m$	$GSD_{mode 2}$	$N_{mode 3}$	$CMD_{mode 3} / \mu m$	$GSD_{mode 3}$	$f_{NUC} / \%$	$f_{non-vol AIT} / \%$	$f_{non-vol ACC} / \%$	ACO / nmol mol <sup>-1</sup>	Plume age / days	$D_{eff}(\text{mode}) / \mu m$
040722a	99 ± 1 % FF	11:36:15	11:38:25	4331	34	2.0	0.601	3200	0.064	1.57	590	0.25	1.31	15	0.33	1.80	0	83	100	78	6-9	0.27
040722a	98 ± 1 % FF	11:38:15	11:44:25	3772	15	1.1	0.634	1600	0.065	1.60	750	0.26	1.30	15	0.35	1.80	0	93	100	167	6-9	0.31
040722a	94 ± 6 % FF	11:44:15	11:45:25	2960	3	0.3	0.687	1400	0.060	1.70	400	0.26	1.30	15	0.32	1.80	0	82	100	131	6-9	0.30
040722b	97 ± 1 % FF	15:53:36	15:55:46	4983	39	1.4	0.568	1800	0.065	1.60	900	0.26	1.30	12	0.45	1.80	0	81	100	133	6-9	0.33
040722b	96 ± 1 % FF	16:20:36	16:23:46	5740	8	0.2	0.523	950	0.080	1.60	900	0.27	1.31	15	0.60	1.90	0	96	100	174	6-9	0.48
040723a	82 ± 7 % FF	12:58:29	13:05:39	4897	48	1.9	0.572	900	0.090	1.40	800	0.30	1.30	16	0.60	1.90	0	96	81	146	7-10	0.50
040723a	87 ± 7 % FF	15:45:29	15:47:39	3286	n.d.	n.d.	0.677	1050	0.091	1.38	990	0.29	1.32	23	0.62	1.85	0	84	100	119	7-10	0.52
040725b	99 ± 1 % FF	19:40:05	19:41:15	2229	45	3.8	0.760	890	0.078	1.56	350	0.26	1.31	6	0.47	1.75	0	83	100	92	6-9	0.32
040726a	97 ± 3 % FF	16:26:22	16:27:32	2484	13	1.3	0.716	1800	0.065	1.64	500	0.27	1.32	14	0.47	1.82	0	98	100	74	10-13	0.37
040730a	93 ± 2 % FF	15:13:44	15:16:54	7649	41	0.5	0.428	4600	0.039	1.69	290	0.20	1.39	11	0.37	1.52	5	56	20	58	4-6	0.21
040730a	89 ± 1 % FF	15:21:45	15:25:54	7652	92	1.2	0.427	2100	0.063	1.71	400	0.23	1.38	11	0.37	1.52	8	74	79	86	4-6	0.25
040730a	93 ± 3 % FF	15:48:45	15:49:54	4557	24	1.3	0.586	1900	0.065	1.90	240	0.22	1.35	3	0.33	1.52	0	79	100	48	4-6	0.23
040730a	84 ± 7 % FF	18:16:45	18:17:55	6437	14	0.3	0.485	1300	0.085	1.90	850	0.23	1.39	1.5	0.90	1.70	3	80	100	119	4-6	0.33
040722a	FT	11:19:15	11:20:22	11088	n.d.	n.d.	0.289	360	0.009	1.50	3800	0.035	1.67	35	0.16	1.65	34	30	63	0	--	0.10

#### 4.1.4 Properties of other forest fire plumes during ITOP

During the 16-day period of ITOP (19 July – 3 August 2004), forest fire plumes were sampled on 22, 23, 25, 26 and 30 July 2004. The transport analyses of FLEXPART suggested that the aerosol plumes were also emitted from strong boreal forest fires in Alaska and Canada. Table 10 compiles data of the analysed constant-level sequences of forest fire encounters (FF). For comparison, the properties of measurements representative for unpolluted, free tropospheric air (FT) are also shown. In addition to the microphysical properties, the plume age and the percentage of CO tracers originating from forest fires in the FLEXPART calculations is indicated in Table 10. FLEXPART tracer analyses (forest fire fraction > 80%; see also Section 3.2.2.3, p. 59ff) suggest that almost pure forest fire aerosol was sampled in most cases. The measurements show enhanced CO mixing ratios within all forest fire plumes. On average a value of  $\Delta CO = 110 \pm 40 \text{ nmol mol}^{-1}$  was found in the forest fire plumes. The highest  $\Delta CO$  value of  $283 \text{ nmol mol}^{-1}$  was detected during flight #040722b.

In general, the pure forest fire layers show several characteristic aerosol properties. The aerosol light absorption coefficient  $\sigma_{ap}$  and the BC concentrations inside the probed layers increase the background value by more than two orders of magnitude (*Petzold et al.*, 2007). A detailed investigation of the non-volatile particle fraction within the Aitken mode  $f_{non-vol AIT}$  and the accumulation mode  $f_{non-vol ACC}$  for all forest fire encounters during ITOP yielded that in the accumulation mode nearly 100% of the particles and in the Aitken mode even more than 80% of the particles contain a non-volatile core (Table 10). In contrast to that, the undisturbed background aerosol contains a considerable fraction of entirely volatile particles, even in the accumulation mode. A key feature of all forest fire aerosol size distributions is an almost complete depletion of the nucleation mode particles, a small Aitken mode and an enhanced accumulation mode compared to the free tropospheric background aerosol outside of forest fire layers (Figure 54, p. 86; Figure 57, p. 92).

The size distributions displayed in Figure 57 represent different plume ages. According to FLEXPART, the plume investigated on 26 July (left panel) had an age of 10-13 days, while the plume investigated on 30 July was younger with an approximated age of 4-6 days after emission. Differences between the younger and the older plume are obvious: the younger plume exhibits some nucleation mode particles ( $f_{NUC} < 10\%$ ); the Aitken mode in the younger plume is broader and the *CMD* of the Aitken and accumulation mode is shifted to smaller particle sizes compared to the older plume (Table 10). The differences between the older and the younger forest fire plumes were investigated in more detail by means of the effective diameter  $D_{eff}$  (Table 10), which was calculated from the parameterised size distributions.  $D_{eff}$  ranges between 0.21 and 0.52  $\mu\text{m}$  and increases with increasing transport time such that the lower values are found after 4-6 days of transport, while after about 10 days  $D_{eff}$  is about 0.52  $\mu\text{m}$ . These values of  $D_{eff}$  measured during ITOP are in agreement with values of  $0.50 \pm 0.14 \mu\text{m}$  (*Fiebig et al.*, 2002; *Wandinger et al.*, 2002) reported for forest fire plumes after about one week of transport during the LACE 98 field experiment.

All forest fire layers encountered during ITOP were characterised by a comparably low relative humidity (< 50%). In about half of the cases, the relative humidity was even lower than 15%. The water vapour mixing ratio dropped from more than 5  $\text{g kg}^{-1}$  underneath the forest fire layers to very low values (0.5-1.5  $\text{g kg}^{-1}$ ) within the forest fire plumes. This feature was obvious in almost all forest fire plumes. The characteristic lapse rate, which was shown

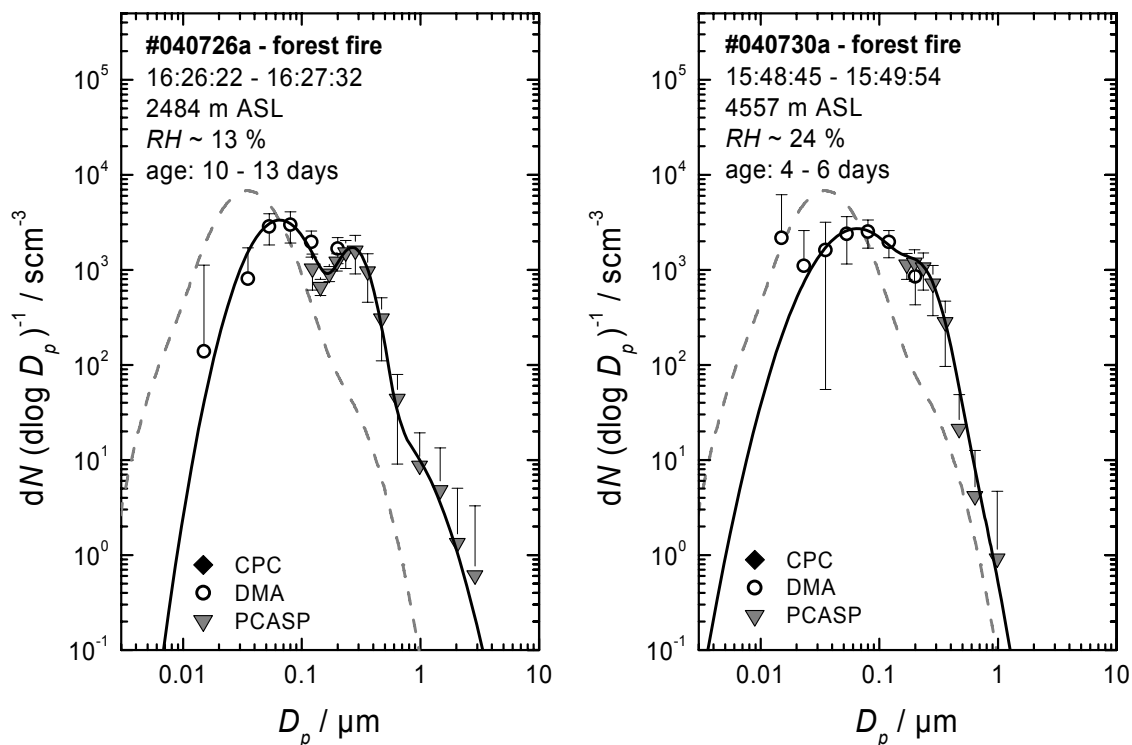


**Figure 57.** Same illustration as in Figure 54, but for forest fire plumes of different ages. The plume measured on 26 July 2004 had an age of about 10-13 days (left panel), while the plume investigated on 30 July 2004 was younger with an age of about 4-6 days (right panel).

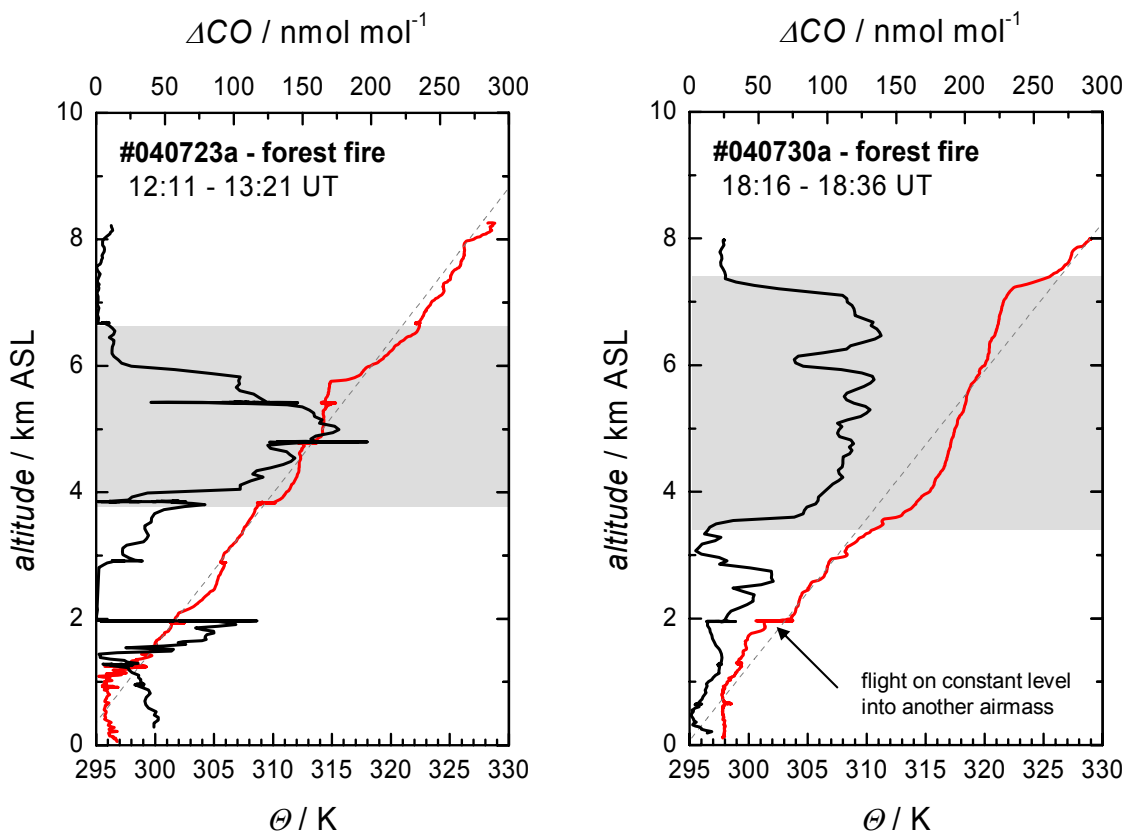


**Figure 58.** Vertical profiles of potential temperature  $\theta$  (red line) and  $\Delta\text{CO}$  (black line) measured over Creil during the ITOP flights on 23 and 30 July 2004. The grey shaded area marks the vertical dimension of the forest fire plumes. The dashed line indicates the average lapse rate.

in detail for the forest fire plumes on 22 July 2004, was also evident in the other cases: the average lapse rate was  $8.6 \text{ K km}^{-1}$ ,  $1.9 \text{ K km}^{-1}$  and  $6.0 \text{ K km}^{-1}$  in region 1, 2 and 3, respectively. For comparison, averaged of the whole atmospheric profile from the surface up to the upper troposphere, a lapse rate of  $3.7 \pm 0.6 \text{ K km}^{-1}$  was found. This fits very well with the lapse rate of  $3.5 \text{ K km}^{-1}$  assumed in the standard atmosphere. Two more examples of potential temperature profiles are shown in Figure 58 (red lines). The black line shows  $\Delta CO$  measurements. As mentioned earlier, the CO enhancement can either be caused by biomass burning plumes or by anthropogenic pollution. According to FLEXPART analyses, forest fire plumes were only present in the grey shaded altitude ranges. Besides forest fire plumes, anthropogenic pollution was present in both cases. In both forest fire plumes, the characteristic potential temperature is visible.

## **4.2 Desert dust aerosol (SAMUM)**

To understand the physical processes in lofted, aged desert dust layers it is necessary to understand the dust aerosol released close to the source. One important issue addressed in this section is the vertical structure of dust layers, which can not be detected by satellite remote sensing and from sun photometry. Another important scientific question addressed here concerns the complete dust size distribution. How will it look like, especially at elevated altitudes, and how variable are dust microphysical and optical properties, even for a confined source region like the north-western Saharan desert? This section is organised as follows: first, the microphysical and optical properties of fresh desert dust layers including the dust layer structure close to the Sahara are presented (Section 4.2.1) and then the properties of aged dust layers close to the Moroccan coast (Section 4.2.2) and over Portugal (Section 4.2.3) are shown. The optical properties of dust and an extinction closure follow in Section 4.2.4.

### **4.2.1 Properties of dust aerosol layers south of the Atlas Mountains**

Dust layers over Ouarzazate (OZT) and Zagora (ZGA) at the Saharan border were found to extend from the surface to altitudes of about 4-6 km ASL. The internal structure of the dust layers varied from well mixed to stratified. In all cases the dust layers exhibited very sharp upper edges. Table 11 (p. 98) summarises times of vertical in-situ profiles at Ouarzazate and Zagora, the altitude of the upper boundary of the dust layers and the dust layer structure.

It is obvious that stratified layers were observed in the early and late morning, while during afternoon and evening flights well-mixed dust layers were present. Stratified layers were observed, when the boundary layer was not yet completely developed and in the case of advection of dust plumes. The upper boundary of the well-mixed dust layers coincided with the top of the boundary layer. Figure 59 shows two cases, the well-mixed dust layer at Ouarzazate on 19 May and the stratified dust layer at Ouarzazate on 4 June 2006. In the former case the boundary layer is well developed with potential temperature  $\theta$  being almost constant ( $\theta = 315.2 \pm 0.5 \text{ K}$ ) and wind being variable from the surface up to an altitude of about 5 km (Figure 59a, mid panel). The particle number concentrations are almost constant from the surface to the top of the dust layer (Figure 59a, left panel), which can be attributed to turbulence within the boundary layer. The dust layer is topped by a strong inversion: within 235 m potential temperature increases by about 3 K, and particle number concentrations drop

by 1-2 orders of magnitude. The HSRL cross-section (Figure 59a, right panel) illustrates the homogenous dust layer. At the upper boundary of the dust layer a wave-like structure is visible.

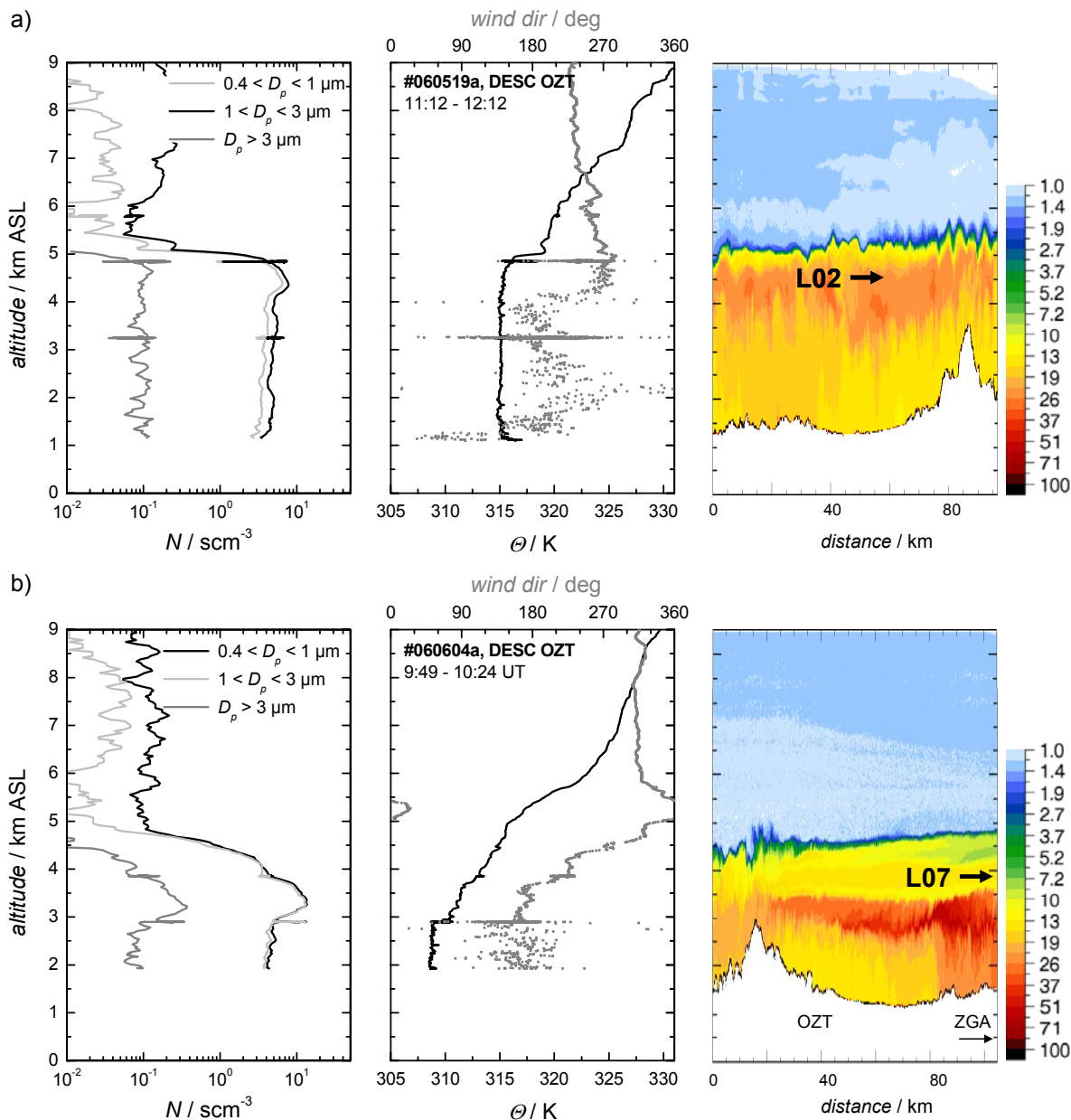


**Figure 59.** Vertical structure of (a) the well-mixed dust layer on 19 May 2006 and (b) the 2-3-layer-structure dust layer on 4 June 2006. Both profiles were measured at Ouarzazate. The left panels show profiles of particle number concentration for STP conditions in the size range of  $0.4 < D_p < 1 \mu\text{m}$  (black line),  $1 < D_p < 3 \mu\text{m}$  (light grey line) and  $D_p > 3 \mu\text{m}$  (grey line). The mid panels show potential temperature (black line) and wind direction (grey symbols). In the right panels (courtesy: M. Esselborn, DLR) the dust layer structure is illustrated by HSRL backscatter ratio at 1064 nm (colour coded). The black arrows mark where the size distributions L02 and L07 shown in Figure 61 were measured.

On 4 June, a 3-layer structure over Ouarzazate and a 2-layer structure over Zagora is visible in the lidar signal (Figure 59b, right panel). The different layers over Ouarzazate coincide with different potential temperature gradients and wind signals (Figure 59b, mid

panel). While the well-mixed boundary layer ( $\theta = 308.8 \pm 0.2$  K) reaches up to about 3 km ASL, the layer above is characterised by a stable stratification. Between 3 and 4 km ASL advection of dust is taking place and the upper part of the dust layer is probably the residuum of the lofted boundary layer from the day before. The advection of dust in an altitude of about 3 km was also documented by the IFT-lidar at Ouarzazate (not shown).

Well-mixed dust layers without major vertical gradients in the concentration of large particles were characteristic for SAMUM. Figure 60 shows averaged vertical profiles of aerosol number concentrations measured during SAMUM. Note the sharp upper boundary of the dust layers. In contrast to the expected vertical gradient in the number concentration of large particles, no enhancement of large particles close to the surface and no depletion of large particles close to the top of the dust layer was observed. This is the result of turbulent mixing within the boundary layer. Above the main dust layer dust filaments were observed on most days, and wave-like structures were present at the top of the dust layer.

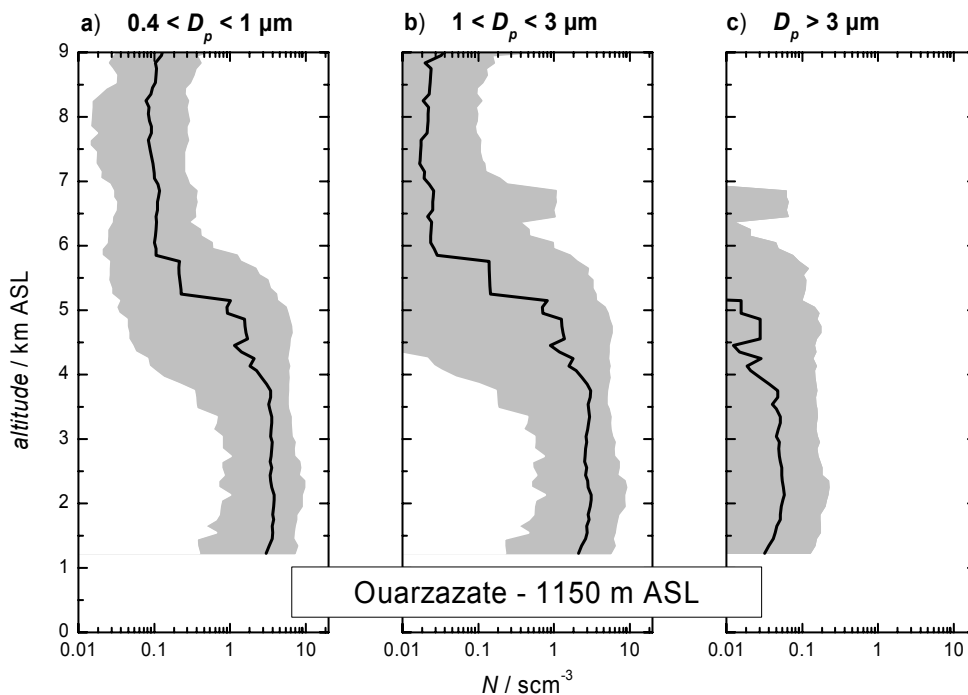


**Figure 60.** Average vertical profiles of aerosol number concentration for STP conditions measured during SAMUM: median number concentrations (black line) of particles with diameters  $D_p$  (a)  $0.4 < D_p < 1 \mu\text{m}$ , (b)  $1 < D_p < 3 \mu\text{m}$  and (c)  $D_p > 3 \mu\text{m}$ . The grey shaded area represents the range within 10- and 90-percentile values.

Figure 61 shows two examples of dust size distributions, one measured over Ouarzazate at 4898 m ASL on 19 May (L02, left panel) close to the top of the dust layer and one measured over Zagora at 3703 m ASL on 4 June 2006 (L07, right panel). The measurements correspond to the vertical profiles in Figure 59. The black symbols depict the non-volatile size distribution, while the grey symbols show the total aerosol size distribution. The error bars indicate the standard deviation of the atmospheric particle concentration within the averaging interval. The parameterisation of the size distribution is marked by the dashed line. The size distributions of both dust layers exhibit similar microphysical properties. Comparing the non-volatile (black symbols) and the total aerosol size distribution (grey symbols) two ranges with different mixing states and therefore different particle morphology are striking: in the size

range beyond  $0.5 \mu\text{m}$ , the non-volatile and the total size distribution are coinciding, while for particles smaller than  $0.5 \mu\text{m}$  this is not the case. Though the non-volatile size distribution has the same shape and similar particle number concentrations (within 10% deviation) as the total size distribution, the peak of the size distribution is shifted towards smaller particle diameters. This feature suggests that particles smaller  $0.5 \mu\text{m}$  have a non-volatile core with a volatile coating (see also Figure 49, p.76). According to the results of the volatility analyses, the dust size distribution can be separated into two zones. Zone 1 (below  $0.5 \mu\text{m}$ ) is composed of internally mixed and coated particles and zone 2 (above  $0.5 \mu\text{m}$ ) is composed of internally mixed particles without coating.

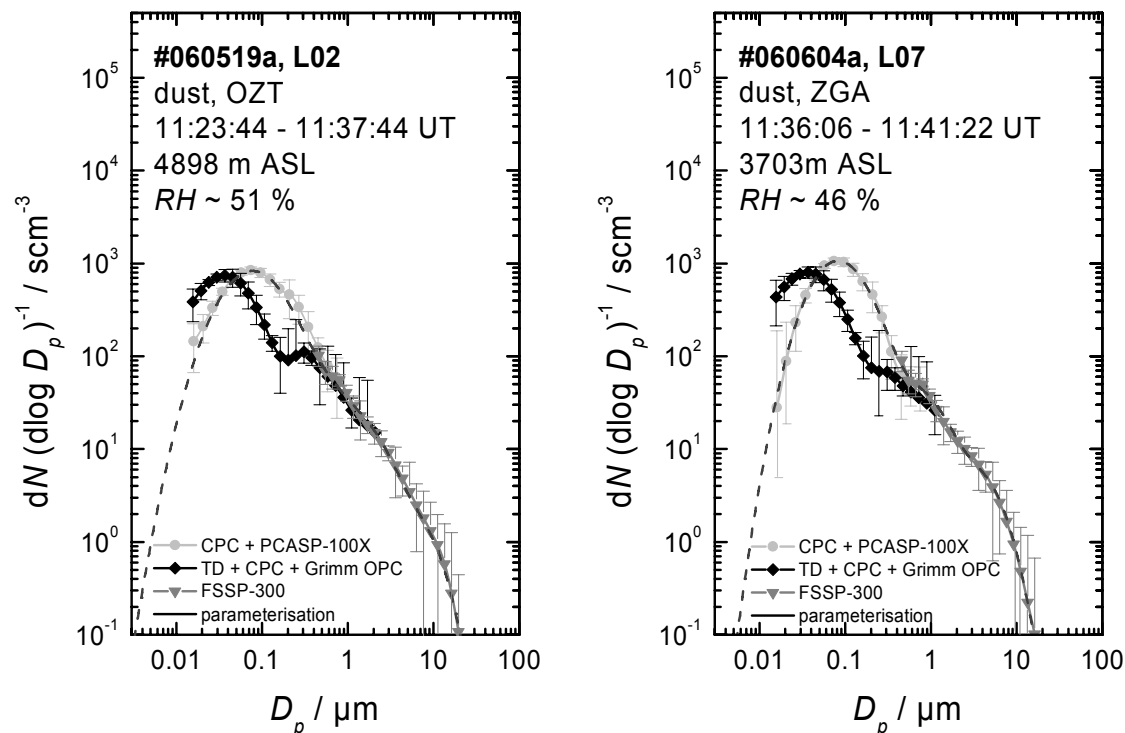


**Figure 61.** Composite size distribution of desert dust from CPC, PCASP-100X, Grimm OPC and FSSP-300 for L02 on 19 May over Ouzarazate (left panel) and L07 on 4 June 2006 (right panel). The black line shows the non-volatile size distribution from the combined analysis of the Grimm instrument and heated CPCs, the light grey line shows the size distribution derived from the combined analysis of CPC and PCASP-100X data, and the grey line shows data from the FSSP-300. The parameterisation is indicated by the dashed line. Particle number concentrations refer to STP conditions.

This feature of two zones with different mixing states is obvious in all dust size distributions measured during SAMUM. Figure 62 displays a selection of size distributions measured during different SAMUM flights, including examples for a clean tropospheric size distribution (#060519a, L00), a mixture of dust and urban pollution (#060528a, L14), and urban pollution and marine aerosol (#060527a, L13). The urban pollution aerosol (e.g. #060527a, L13) and the free tropospheric aerosol (#060519a, L00) differ clearly from the dust aerosol. The pollution aerosol exhibits a large number of small ( $D_p < 0.1 \mu\text{m}$ ), totally volatile particles. The number concentration of the sub- $0.1 \mu\text{m}$  particles in the pollution aerosol is even increased by 1-2 orders of magnitudes compared to the dust aerosol. In the free tropospheric aerosol, the concentration of non-volatile particles is below the detection limit of the Grimm OPC, and coarse mode particles are missing.

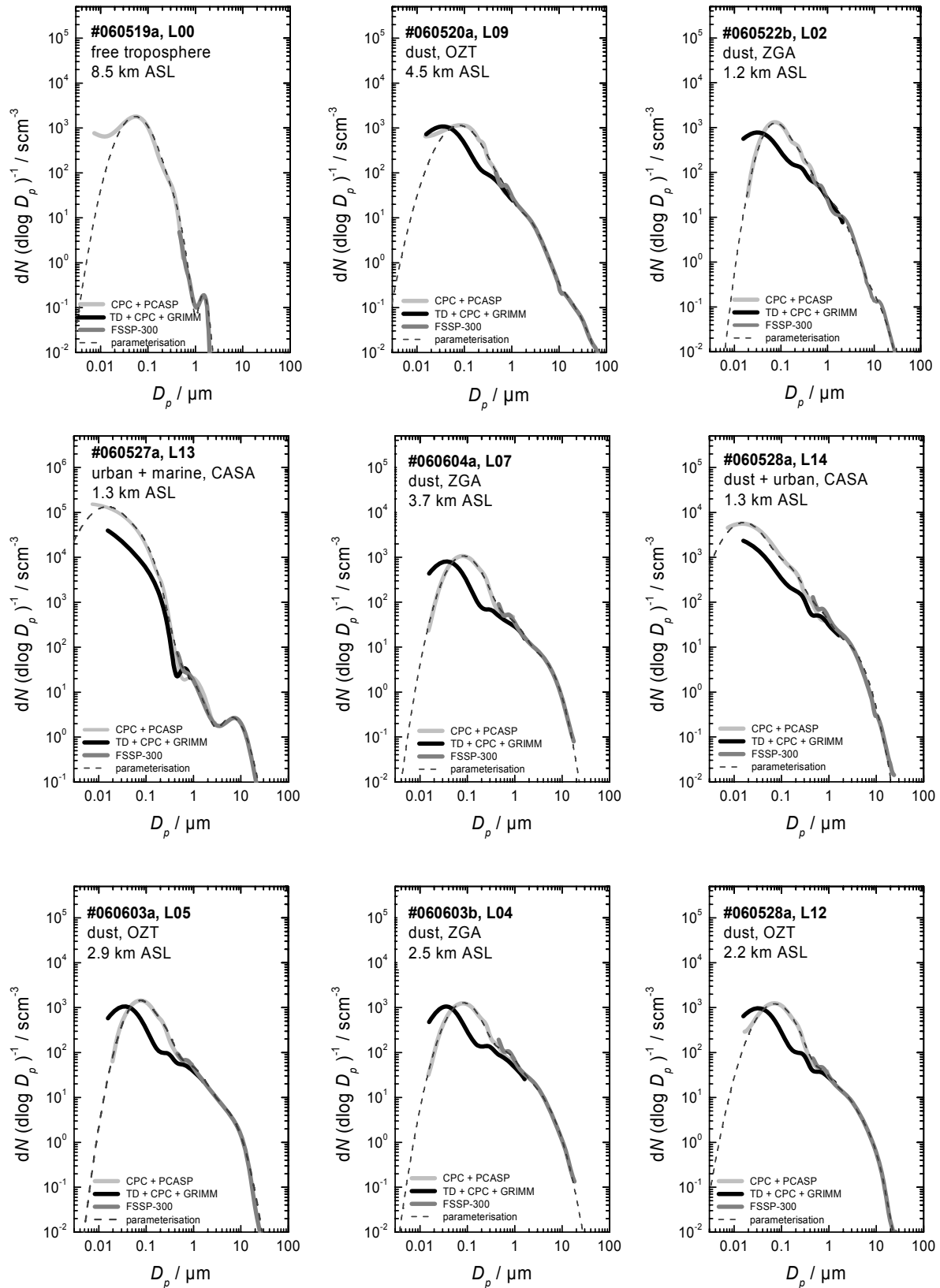


**Figure 62:** Examples of size distributions measured during different SAMUM flights, including dust aerosol and examples for a clean tropospheric size distribution (#060519a, L00), a mixture of dust and urban pollution (#060528a, L14), and a mixture of urban pollution and marine aerosol (#060527a, L13). For clarity, no error bars are shown. The dust aerosol shows a characteristic structure with two zones of different mixing states (see text). In the pollution case (#060527a, L13), the number concentration of small particles ( $D_p < 0.1 \mu\text{m}$ ) is increased by two orders of magnitude.

**Table II.** Dust layer structure over Ouarzazate (OZT) and Zagora (ZGA). OZT and ZGA are situated 1150 m and about 820 m above sea level (ASL), respectively. The atmosphere over ZGA was only probed during selected flights. Cases without vertical profiles over ZGA are indicated by "n.d.".

Mission ID	Time of in-situ measurement OZT / UT	Upper boundary dust layer OZT / m ASL	Dust layer structure OZT	Time of in-situ measurement ZGA / UT	Upper boundary dust layer ZGA	Dust layer structure ZGA
060519a	11:12 – 12:12	5130	well-mixed	n.d.	n.d.	n.d.
060519b	14:35 – 14:42	6900	well-mixed	n.d.	n.d.	n.d.
060520a	12:33 – 13:27	5500 – 5560	well-mixed	11:29 – 12:28	5980	well-mixed
060522a	15:30 – 16:04	6620	well-mixed	n.d.	n.d.	n.d.
060522b	17:18 – 17:24	low-level	well-mixed	17:25 – 18:00	low-level	well-mixed
	18:01 – 18:15	low-level	well-mixed	n.d.	n.d.	n.d.
060522c	17:24 – 21:33	4650	well-mixed	n.d.	n.d.	n.d.
060528a	12:19 – 12:55	4500 – 4700	well-mixed	11:12 – 12:15	4020 – 4040	2-layer structure
060603a	03:18 – 04:09	4420 – 4470	2-3-layer structure	high level	~4500	2-3-layer structure
060603b	08:59 – 09:09	~4000	2-layer structure	08:02 – 08:58	4400	2-layer structure
060603c	11:04 – 11:18	4480	well-mixed	n.d.	n.d.	n.d.
060604a	09:49 – 10:43	4680 – 4840	3-layer structure	11:24 – 12:04	4720 – 4820	2-layer structure

The schematic in Figure 63 summarises the microphysical properties found in all dust samples during SAMUM. In all cases two zones in the size distribution with different particle morphology are evident. The inversion of the 3- $\lambda$ -PSAP data (*Rasp*, 2007) yielded a mean refractive index of  $m = 1.531 + 0i$  for zone 1 and a mean refractive index of  $m = (1.555 \pm 0.0053) + (0.0032 \pm 0.0012)i$  for zone 2 at the HSRL wavelength of 532 nm. To derive a refractive index with the PSAP-method (see Section 3.3.6, p.77ff), the particles in zone 1 were assumed to consist of a quartz core coated with ammonium sulphate, while particles in zone 2 were assumed to consist of an internal mixture of quartz, haematite and kaolinite.

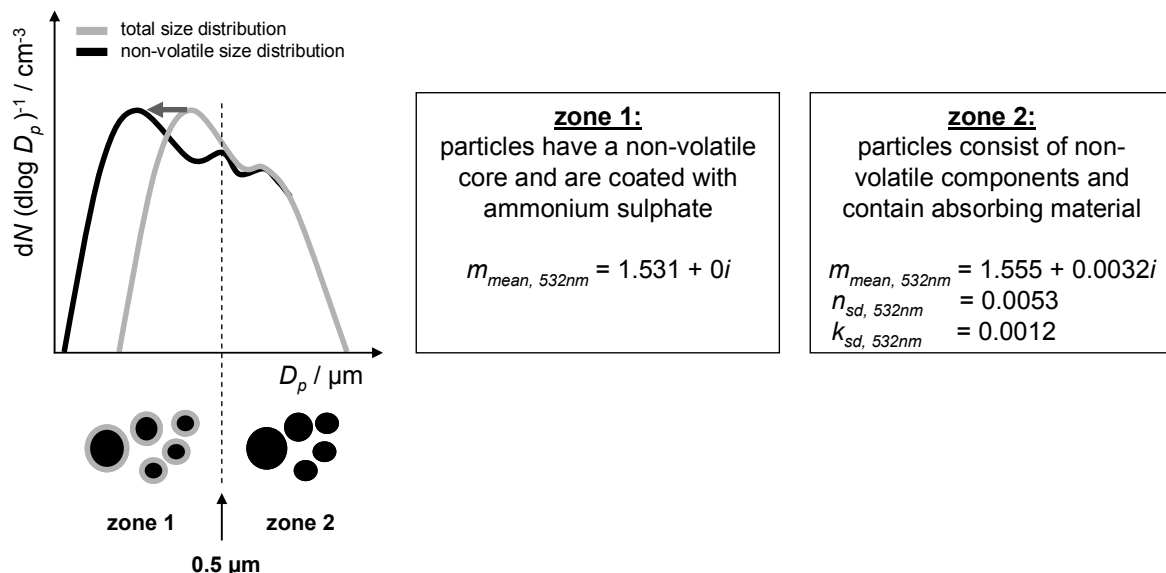


**Figure 63.** Schematic summarising the microphysical aerosol properties found in the dust layers investigated during SAMUM.

Chemical analyses of filter samples (*Kandler*, 2007, personal communication) confirmed that the assumed chemical constituents are contributing significantly to the composition of the

desert dust. Since the refractive index was derived only for particles smaller 2.5  $\mu\text{m}$ , the analysis of the size distribution data and the calculation of optical properties from the size distribution data have been performed under the assumption that the refractive index for particles larger than 2.5  $\mu\text{m}$  is the same as for particles in the size range 0.5-2.5  $\mu\text{m}$ .

Figure 64 shows scanning electron microscope images of particles found in zone 1 (left panel) and zone 2 (right panel). The images confirm the particle morphology inferred from the volatility analyses. The left panel shows ammonium sulphate and dust particles around 350 nm, which correspond to zone 1, while the right panel illustrates dust particles up to sizes of 20  $\mu\text{m}$  which correspond to zone 2. As a result of the chemical composition, the particles in zone 1 are closer to spherical shape than the particles in zone 2.

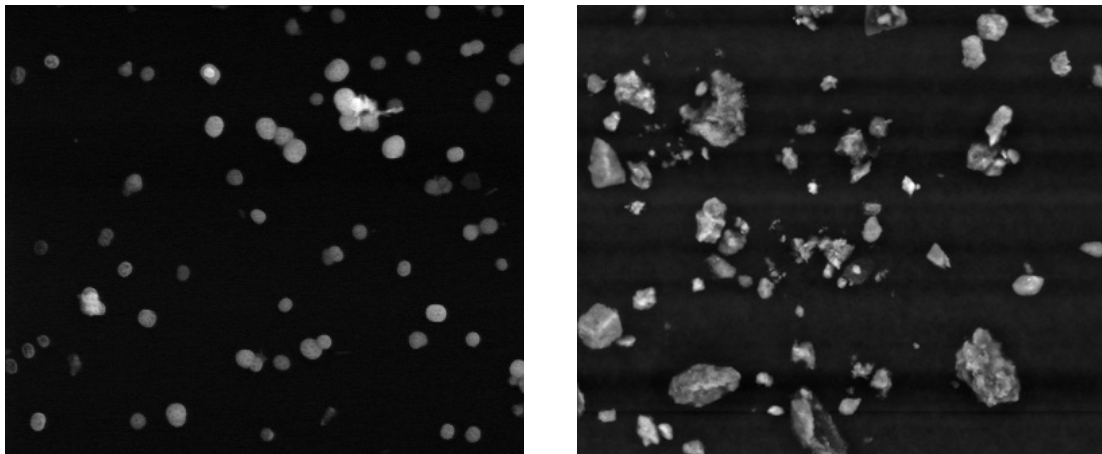


**Figure 64.** Secondary electron image of ammonium sulphate and dust particles (left panel) found in desert dust samples around 350 nm and backscatter electron image (right panel) of dust particles up to sizes of 20  $\mu\text{m}$  (courtesy: K. Kandler, Environmental Mineralogy Group of the Darmstadt University of Technology).

Table 12 compiles the microphysical properties of the pure dust layers including the flight mission ID and layer ID, start and stop time of averaging sequences, altitude of the measurement, and relative humidity during the time of measurement. The parameters of the multi-modal log-normal size distribution fits are given for STP conditions. They can be converted to ambient conditions by multiplication of the particle number concentration with  $f_{STP}$  (see Section 3.3.1, p. 67). The  $PM_{2.5}$  and total mass ( $TSP$ ) concentrations refer to spherical particles of a density of 2600  $\text{kg m}^{-3}$  (Hess *et al.*, 1998b). On average  $PM_{2.5}$  contributes only  $7 \pm 5\%$  to the total mass; the aerosol mass is dominated by the coarse mode particles. The ratio  $PM_{2.5}/TSP$  ( $f_{PM_{2.5}/TSP}$ ) is dependent on the height of the sampled dust layer. While  $PM_{2.5}$  contributes about 3-4% to the total mass at 5 km altitude ASL, the contribution increases to 10-15% close to the surface, indicating a contribution of local pollution at lower levels. For particles smaller 2.5  $\mu\text{m}$ , the non-volatile volume fraction ( $f_{non-vol 2.5}$ ) ranges around  $78 \pm 9\%$ .

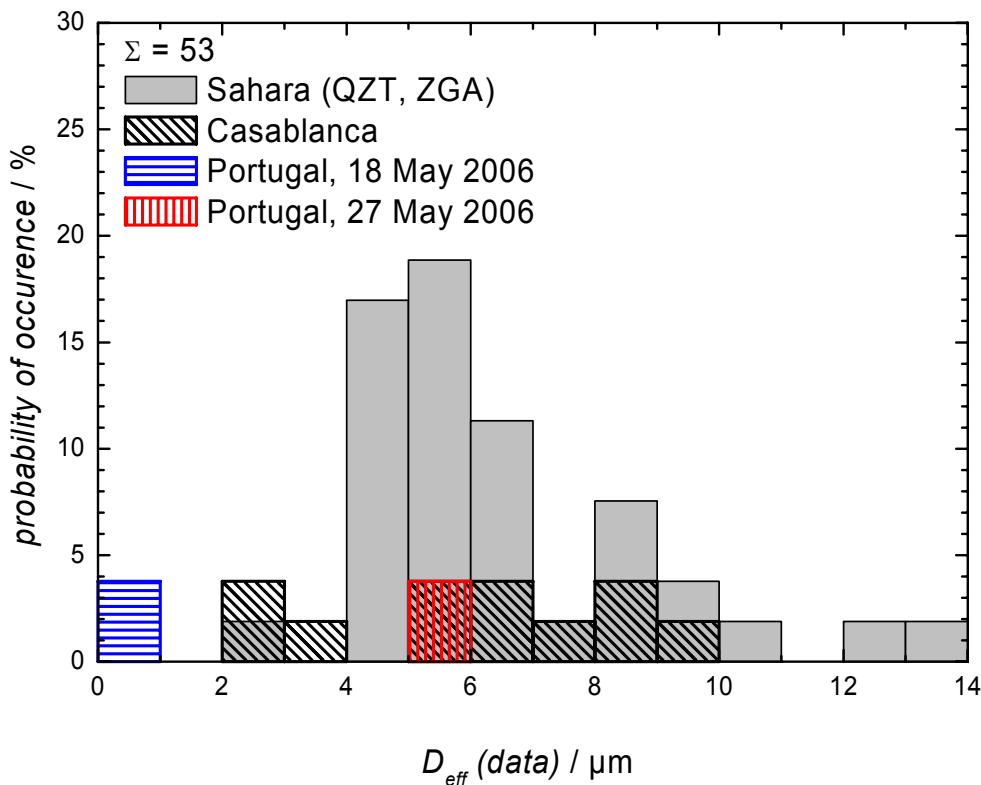
The geometric standard deviation  $GSD$  of the dust mode ( $GSD_{mode 4}$  in Table 12) ranges between 1.42 and 2.33 with an average value of  $1.73 \pm 0.18$ . The count median diameter  $CMD_{mode 4}$  of the dust mode varies between 2.3 and 9.5  $\mu\text{m}$  with an average  $CMD_{mode 4}$  of  $5.66 \pm 1.48 \mu\text{m}$ . The associated average effective diameter  $D_{eff}$  is  $6.5 \pm 2.5 \mu\text{m}$ . However, the

Table 12. continued.

Mission ID	Layer ID	Site	Start Time / UT	Stop Time/ UT	Altitude / m ASL	RH / %	$f_{STP}$	$N_{mode 1}$	$CMD_{mode 1} / \mu m$	$GSD_{mode 1}$	$N_{mode 2}$	$CMD_{mode 2} / \mu m$	$GSD_{mode 2}$	$N_{mode 3}$	$CMD_{mode 3} / \mu m$	$GSD_{mode 3}$	$N_{mode 4}$	$CMD_{mode 4} / \mu m$	$GSD_{mode 4}$	TSP (data) / $\mu g m^{-3}$	PM <sub>2.5</sub> (data) / $\mu g m^{-3}$	$f_{PM2.5/TSP} / \%$	$f_{non-vol 2.5} / \%$	$D_{eff}(\text{data}) / \mu m$	$D_{eff}(\text{data}) / D_{eff}(\text{mode})$
060528a	L04	ZGA	11:41:07	11:46:01	1914	32	0.748	900	0.069	2.05	18	0.55	1.50	14	1.40	1.90	0.30	6.50	1.60	688	72.2	10.5	71.6	4.8	1.03
060528a	L05	ZGA	11:46:01	11:48:02	1912	26	0.747	980	0.074	2.05	9.5	0.62	1.45	10	1.30	1.92	0.34	7.95	1.42	625	52.6	8.4	82.0	5.1	0.97
060528a	L06	ZGA	11:51:47	11:54:52	1280	22	0.786	950	0.069	2.05	18	0.55	1.50	11	1.40	1.85	0.20	6.50	1.60	470	60.3	12.8	76.8	4.2	1.03
060528a	L10	OZT	12:42:42	12:49:47	3870	61	0.630	880	0.077	2.07	11	0.69	1.50	11	1.35	2.05	0.59	6.55	1.65	1153	59.8	5.2	69.4	6.9	1.04
060528a	L11	OZT	12:52:02	12:54:02	2907	37	0.684	900	0.077	2.05	9	0.67	1.45	13	1.25	2.10	0.28	6.50	1.75	867	57.0	6.6	72.4	6.1	1.01
060528a	L12	OZT	12:55:57	12:59:07	2194	29	0.728	950	0.072	2.05	9	0.67	1.45	13	1.25	2.10	0.24	6.25	1.45	591	56.5	9.6	79.6	4.6	1.02
060603a	L04	OZT	03:39:53	03:44:53	3798	81	0.633	880	0.077	1.70	100	0.20	1.50	33	0.65	2.10	2.00	4.40	1.75	1194	62.6	5.2	75.6	6.5	1.03
060603a	L05	OZT	03:46:41	03:56:45	2855	49	0.689	880	0.075	1.75	100	0.22	1.50	45	0.65	2.10	2.50	4.40	1.70	1113	77.0	6.9	78.0	5.5	0.95
060603b	L03	ZGA	08:16:58	08:27:52	3814	74	0.632	900	0.083	1.80	15	0.55	1.70	7.4	1.40	2.11	0.50	6.50	1.51	819	45.2	5.5	69.2	6.0	1.02
060603b	L04	ZGA	08:31:07	08:39:55	2534	39	0.710	890	0.083	1.90	50	0.55	1.69	19.5	1.35	2.10	0.95	4.40	1.68	1267	116.9	9.2	58.1	5.1	1.03
060603b	L05	ZGA	08:44:07	08:50:31	1195	28	0.799	1100	0.072	1.80	100	0.40	1.73	22	1.35	1.95	0.30	6.51	1.54	884	126.4	14.3	65.4	4.0	1.02
060603b	L06	ZGA	08:55:16	08:58:31	3816	76	0.633	750	0.077	1.85	100	0.20	1.50	18	0.65	2.10	2.50	2.30	1.55	181	47.6	26.2	76.6	2.5	1.04
060603b	L07	OZT	09:01:43	09:03:04	2487	44	0.713	800	0.075	1.75	120	0.22	1.50	33	0.60	2.30	1.50	5.00	1.60	899	57.2	6.4	68.2	5.4	0.99
060603b	L08	OZT	09:04:16	09:05:04	2356	48	0.723	880	0.073	1.80	100	0.20	1.50	40	0.60	2.10	3.80	3.70	1.85	1498	70.9	4.7	74.0	6.7	0.98
060604a	L03	OZT	10:02:18	10:10:02	3854	39	0.629	560	0.075	1.80	75	0.22	1.48	39	0.49	2.38	1.38	4.38	1.69	714	54.5	7.6	82.3	5.2	0.97
060604a	L04	OZT	10:12:26	10:20:22	2895	58	0.691	800	0.073	2.00	70	0.20	1.50	75	0.62	2.19	4.50	3.66	1.74	1558	138.9	8.9	82.3	5.1	0.98
060604a	L05	OZT	10:24:14	10:31:22	1928	44	0.753	4600	0.010	2.96	330	0.13	1.70	41	0.59	2.09	3.00	3.20	1.74	701	75.4	10.8	99.2	4.4	1.01
060604a	L07	ZGA	11:36:06	11:41:22	3703	46	0.639	670	0.077	1.85	90	0.16	1.70	35	0.60	2.06	2.40	3.78	1.68	704	57.9	8.2	70.2	4.8	1.00
060604a	L08	ZGA	11:45:38	11:50:02	1938	37	0.752	840	0.072	1.85	90	0.16	1.65	35	0.53	2.30	1.00	4.67	1.58	512	51.1	10.0	73.3	4.3	0.97
060604a	L09	ZGA	11:53:10	11:54:50	1288	26	0.793	850	0.072	1.80	90	0.16	1.65	50	0.50	2.10	2.35	3.28	1.74	559	64.4	11.5	78.2	4.2	1.00

**Table 12.** Microphysical properties of pure dust aerosol over Quarzazate (OZT) and Zagora (ZGA). Size distributions were derived on constant altitude sequences out of cloud. Besides start and stop time for each averaging interval, the altitude of the measurements, and the relative humidity (RH) are given.  $N_j$ ,  $CMD_j$ , and  $GSD_j$  result from log-normal fitting and denote the particle number concentration in mode  $j$ , the count median diameter, and the geometric standard deviation. All mode parameters are given for STP conditions and can be converted to ambient conditions by multiplication with  $f_{STP}$ . The  $PM_{2.5}$  mass concentration ( $D_p < 2.5 \mu\text{m}$ ) and the total mass (TSP) concentration refer to spherical particles of a density of  $2600 \text{ kg m}^{-3}$ .  $f_{PM_{2.5}/TSP}$  is the ratio of  $PM_{2.5}$  and TSP, and  $f_{non-vol 2.5}$  is the non-volatile volume fraction in the sub-2.5  $\mu\text{m}$  size range. The effective diameter  $D_{eff}(\text{data})$  was calculated from the measurements, while  $D_{eff}(\text{mode})$  was derived from the parameterised size distributions via the Hatch-Choate conversion equations. The ratio  $D_{eff}(\text{data})/D_{eff}(\text{mode})$  is a quality control criterion for parameterisations of the size distributions (see Figure 47, p. 73).

Mission ID	Layer ID	Site	Start Time / UT	Stop Time/ UT	Altitude / m ASL	RH / %	$f_{STP}$	$N_{mode 1}$	$CMD_{mode 1} / \mu\text{m}$	$GSD_{mode 1}$	$N_{mode 2}$	$CMD_{mode 2} / \mu\text{m}$	$GSD_{mode 2}$	$N_{mode 3}$	$CMD_{mode 3} / \mu\text{m}$	$GSD_{mode 3}$	$N_{mode 4}$	$CMD_{mode 4} / \mu\text{m}$	$GSD_{mode 4}$	TSP (data) / $\mu\text{g m}^{-3}$	$PM_{2.5}(\text{data}) / \mu\text{g m}^{-3}$	$f_{PM_{2.5}/TSP} / \%$	$f_{non-vol 2.5} / \%$	$D_{eff}(\text{data}) / \mu\text{m}$	$D_{eff}(\text{data}) / D_{eff}(\text{mode})$
060519a	L02	OZT	11:23:44	11:37:44	4853	51	0.574	670	0.077	2.10	30	0.44	1.90	11	1.40	1.90	0.70	6.50	1.66	1189	68.9	5.8	83.4	6.5	0.98
060519a	L03	OZT	11:44:02	12:06:28	3246	26	0.662	900	0.079	2.30	10	0.55	1.50	8.3	1.40	1.90	0.58	6.50	1.74	1026	52.2	5.1	81.3	6.8	0.93
060520a	L02	ZGA	11:38:16	11:48:36	5169	64	0.556	620	0.077	1.90	75	0.24	1.60	32	0.78	1.95	2.00	6.20	1.76	2800	72.5	2.6	80.9	9.9	0.97
060520a	L03	ZGA	11:48:36	11:51:01	5170	66	0.556	590	0.074	1.93	80	0.32	1.70	27	1.18	1.94	1.80	6.21	1.95	5065	110.4	2.2	63.3	12.2	0.97
060520a	L04	ZGA	11:55:32	12:10:36	3242	27	0.662	800	0.076	1.90	75	0.20	1.55	16	0.66	1.97	1.00	4.75	1.92	1016	31.6	3.1	84.3	8.8	0.98
060520a	L05	ZGA	12:10:36	12:18:32	3242	25	0.661	700	0.075	1.90	85	0.20	1.90	14	0.90	2.15	0.50	5.65	1.72	697	47.0	6.7	78.3	5.9	0.99
060520a	L07	OZT	12:41:48	12:50:12	5176	75	0.556	900	0.077	2.30	15	0.55	1.50	14	1.25	1.90	1.10	6.50	1.75	1908	74.7	3.9	79.6	8.2	0.95
060520a	L08	OZT	12:54:36	13:09:36	3247	26	0.659	1000	0.071	2.40	15	0.55	1.50	10	1.40	1.95	0.40	6.50	1.75	856	58.1	6.8	77.0	5.9	0.97
060520a	L09	OZT	13:11:44	13:14:08	4536	56	0.589	950	0.078	2.15	15	0.55	1.50	9	1.40	1.95	0.15	9.50	2.10	2006	54.6	2.7	95.9	13.7	0.86
060522a	L04	OZT	15:53:15	15:57:17	3188	22	0.655	700	0.077	1.70	120	0.22	1.60	14	0.80	2.00	1.05	5.90	1.75	1336	38.0	2.8	69.1	8.6	0.98
060522a	L05	OZT	15:58:15	16:00:39	2858	19	0.674	750	0.075	1.75	120	0.22	1.60	14	0.80	2.00	0.90	5.90	1.75	1137	32.4	2.8	80.8	8.6	1.04
060522a	L06	OZT	16:01:51	16:04:27	2525	16	0.693	720	0.076	1.65	100	0.23	1.60	14	0.80	2.00	1.15	5.90	1.80	1439	33.3	2.3	95.2	9.4	0.94
060522b	L01	OZT	17:21:36	17:31:06	2870	20	0.674	700	0.073	1.70	125	0.21	1.67	15	0.82	2.05	0.13	7.15	1.98	650	35.1	5.4	90.9	7.8	1.00
060522b	L02	ZGA	17:34:48	17:53:42	1220	9	0.772	700	0.075	1.67	125	0.22	1.67	19	0.82	2.00	0.13	6.55	1.77	369	47.1	12.6	79.9	4.4	1.04
060522b	L03	ZGA	17:56:26	18:06:16	2875	20	0.674	700	0.073	1.70	125	0.21	1.67	13	0.82	2.05	0.09	7.15	2.33	881	33.3	9.8	97.4	11.0	0.73
060528a	L03	ZGA	11:26:37	11:35:32	3206	26	0.668	950	0.072	1.90	7.5	0.60	1.50	4.7	1.44	2.12	0.26	6.40	1.47	459	27.3	6.0	83.8	5.3	0.99



**Figure 65.** Frequency distribution of effective diameters  $D_{eff}$  found in dust layers south of the Atlas Mountains. For comparison the frequency distribution of  $D_{eff}$  found in dust layers north of the Atlas including aged dust over Evora are shown.

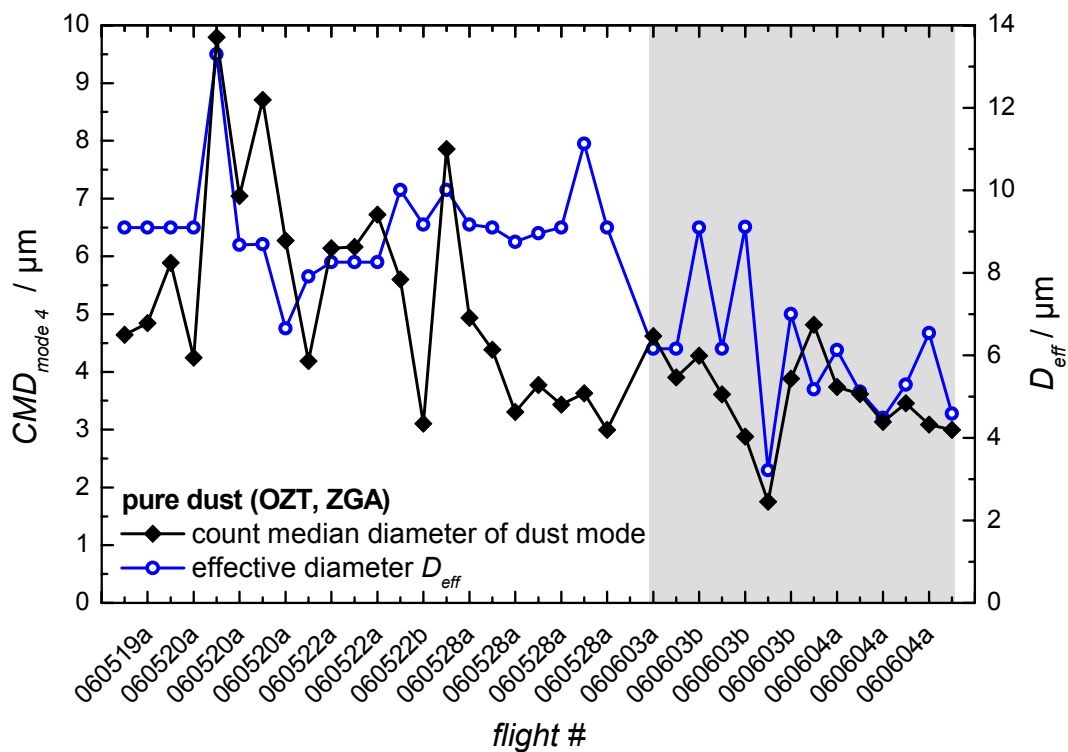


**Figure 66.** Time series of effective diameter  $D_{eff}$  and count median diameter of the dust mode  $CMD_{mode\ 4}$  for the 37 pure dust sequences south of the Atlas Mountains. Data are taken from Table 12. Periods in which density currents frequently occurred are grey shaded.

probability of occurrence for different  $D_{eff}$  shown in Figure 65 suggests that it may be inadequate to use an average effective diameter for a typical dust size distribution: the  $D_{eff}$  south of the Atlas Mountains can be separated into two ranges, one with  $D_{eff}$  around 4-7  $\mu\text{m}$  and a second range with  $D_{eff}$  between 7-10  $\mu\text{m}$  and more than half of all effective diameter values fall in the range of 4-7  $\mu\text{m}$ . More than 75% of all  $D_{eff}$  values are smaller than 8  $\mu\text{m}$ . Time series of  $D_{eff}$  and count median diameter of the dust mode  $CMD_{mode\ 4}$  (Figure 66) suggest that the two ranges of different  $D_{eff}$  can be attributed to the different dust episodes with their different dust mobilisation mechanisms (see also Section 3.2.3.1, p. 65). The very high  $D_{eff}$  occurred preferably in **Episode I**. Smaller  $D_{eff}$  occurred, when the dust was mobilised by density currents. During flight #060603b, higher and lower  $D_{eff}$  were observed. On that day, the dust layer evinced a two layer structure with different dust origins (*Rasp*, 2007) and different dust mobilisation mechanisms. In general, no dependency of  $D_{eff}$  on the altitude was observed. Figure 65 also shows that the  $D_{eff}$  over Casablanca is within the spread of the  $D_{eff}$  south of the Atlas, with a slight tendency towards decreasing  $D_{eff}$ .

A comprehensive comparison of the measured size distributions with already published information is difficult, since the literature on dust size distribution measurements is very sparse. Different measurement techniques resulting in different equivalent diameters (see Figure 8, p. 20) make a comparison even more difficult. In addition, the microphysical dust properties may differ for various source regions and distances from the dust source region (*Sokolik et al.*, 1998). Furthermore, most of the existing measurements are ground-based measurements (e.g. *Schütz and Jaenicke*, 1974; *Schütz and Jaenicke*, 1978; *d'Almeida and Schütz*, 1983) while the data presented here cover the whole dust column. As pointed out in the Introduction (p. 7ff) during recent field experiments focussing on dust (e.g. *Reid et al.*, 2003a), problems with the airborne optical particle counters in the super-micron size range occurred. Large differences were found between different particle sizing methods causing inherent uncertainties in the dust size distribution measurements (*Reid et al.*, 2003a). Similar to most other studies presenting airborne dust measurements, *Clarke et al.* (2004) also reported particle size distributions of Asian dust only for particle diameters smaller  $\sim 10\ \mu\text{m}$ . Therefore, the data presented in this study, are quite unique as the whole size range up to particle sizes of  $\sim 100\ \mu\text{m}$  was covered by the Falcon aerosol in-situ instrumentation.

Several other authors inferred dust properties from satellite measurements or sun photometry: for example, *Dubovik et al.* (2002) retrieved dust volume distributions from data of the AERONET (Aerosol Robotic Network; <http://aeronet.gsfc.nasa.gov/>) network of ground-based radiometers. Their retrieval yielded coarse mode volume median diameter  $D_{Vc}$  of 3.8-5.0  $\mu\text{m}$ . Another widely used data set on optical properties of aerosols and clouds (OPAC) that also provides information on mineral dust was published by *Hess et al.* (1998b). The dust properties in OPAC are based on older descriptions (e.g. *Shettle and Fenn*, 1979; *d'Almeida et al.*, 1991) with slight modifications that can be found by *Koepke et al.* (1997). In OPAC, a volume median diameter  $D_{Vc}$  for the coarse mode of mineral dust of 22  $\mu\text{m}$  is given. From the SAMUM size distributions,  $D_{Vc}$  of the coarse mode (mode 4 in Table 12) was calculated via the Hatch-Choate conversion equations (Equation 2.3, p. 22) and compared with other existing information. The results of the comparison are shown in Figure 67. A more detailed overview over commonly cited coarse mode particle mass/volume distributions is listed in Table 1 in *Reid et al.* (2003a). The authors point out that the results

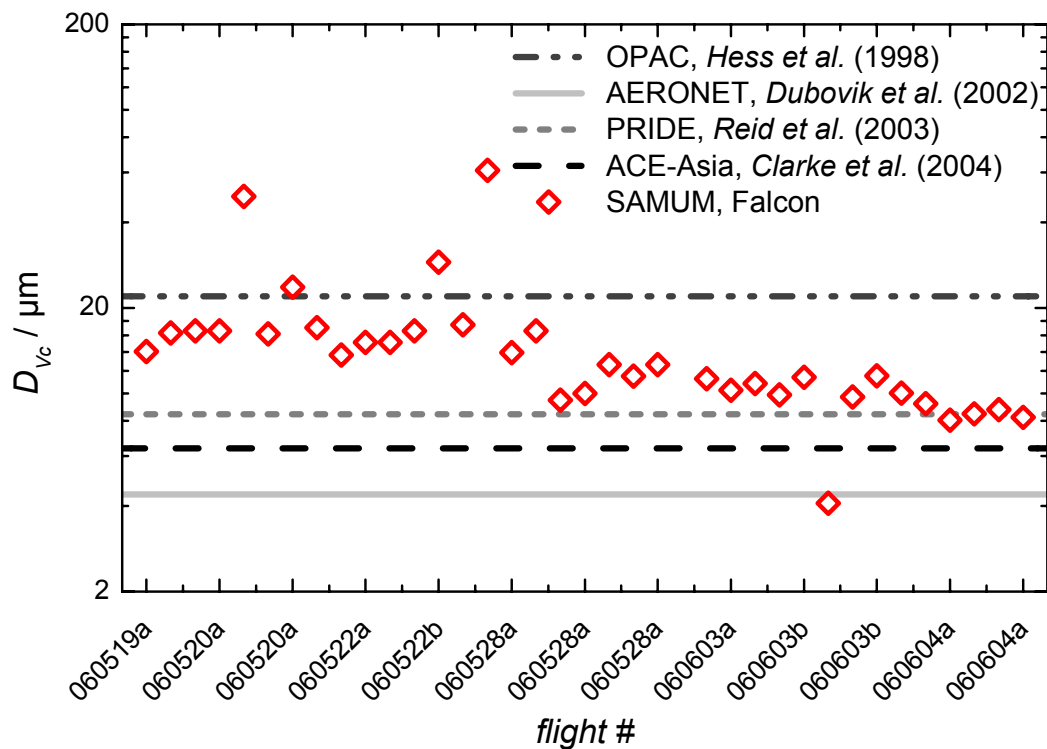


**Figure 67.** Intercomparison of coarse mode volume median diameter  $D_{vc}$  derived by different methods. Data are taken from Hess et al. (1998b), Dubovik et al. (2002), Reid et al. (2003a), Clarke et al. (2004), and from this study. Except the data from Clarke et al., all measurements refer to African dust.

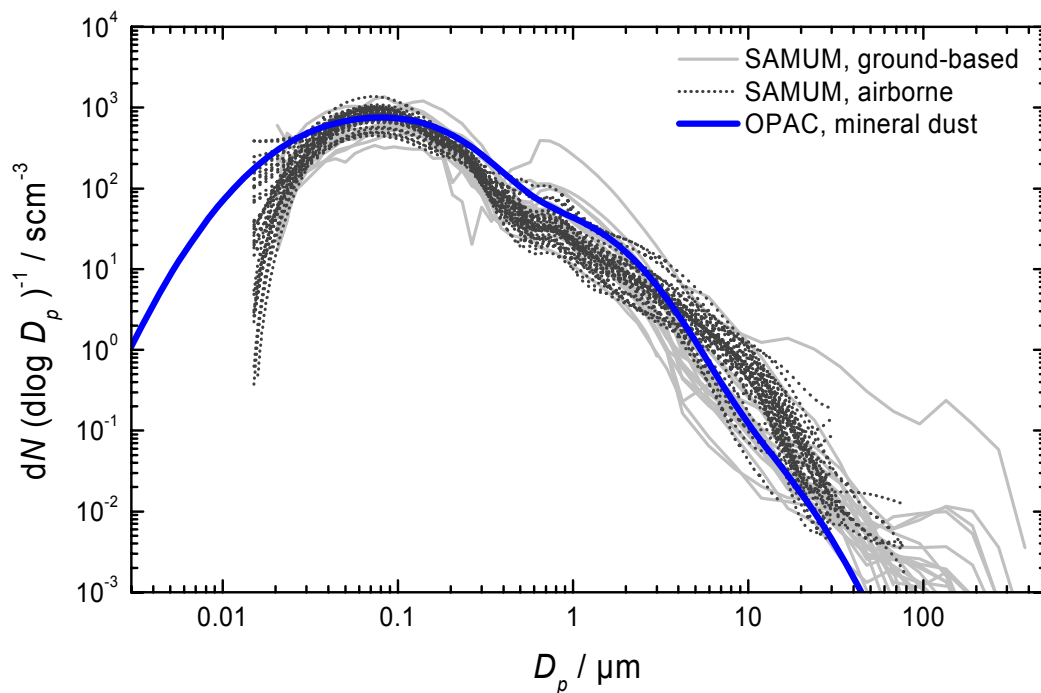


**Figure 68.** Intercomparison of SAMUM dust size distributions measured on board the Falcon (dotted grey lines), ground-based measurements (grey lines) performed at Zagora (courtesy: L. Schütz, University of Mainz; K. Kandler, Darmstadt University of Technology; A. Schladitz and T. Müller, IfT), and OPAC values (Hess et al., 1998b) for mineral dust (blue line).

derived with optical inversion methods (e.g. AERONET in Figure 67) and with aerodynamic<sup>20</sup> methods group into the same size range ( $D_{Vc} \sim 3-7 \mu\text{m}$ ), while the results based on optical counter methods are higher ( $D_{Vc} > 9 \mu\text{m}$ ). Reid *et al.* (2003a) attributed these differences to shortcomings of the optical particle counters. They further reported large differences between the measurements of their FSSP-100 and their PCASP during PRIDE, where their FSSP-100 showed concentrations consistently a factor 2.2 higher than their PCASP. During SAMUM, the particle number concentrations measured with the FSSP-300 and the PCASP were in close agreement in the overlap region of both instruments ( $< 5\%$  deviation; see also Figure 61, p. 96; Figure 62, p. 97). The SAMUM data yield an average  $D_{Vc}$  of  $15.5 \pm 10.9 \mu\text{m}$ , and the airborne measurements are in good agreement with ground-based size distribution measurements. Furthermore, the measured extinction coefficient can be reproduced with the size distribution measurements (see Figure 77, p. 116), indicating that the size distribution measurements very well cover the complete dust size distribution.

Figure 68 shows an intercomparison of airborne size distribution measurements with ground-based methods performed at Zagora during SAMUM. The size distributions at the ground were inferred from aerodynamic methods (courtesy: L. Schütz, University of Mainz; K. Kandler, Darmstadt University of Technology; A. Schladitz and T. Müller, IfT). The ground-based measurements represent the aerosol in the boundary layer below 5 m altitude. Figure 68 indicates close correspondence between the ground-based and the airborne measurements. A more detailed comparison of ground-based and airborne measurements for single days revealed good agreement between both methods. In contrast to the airborne measurements, the ground-based measurements show a further mode with a maximum around  $100 \mu\text{m}$ . This is probably the saltation mode, which is only present close to the ground, as the large particles settle rather quickly due to gravity.

#### **4.2.2 Desert dust layers at the boundary between source and long-range transport regime**

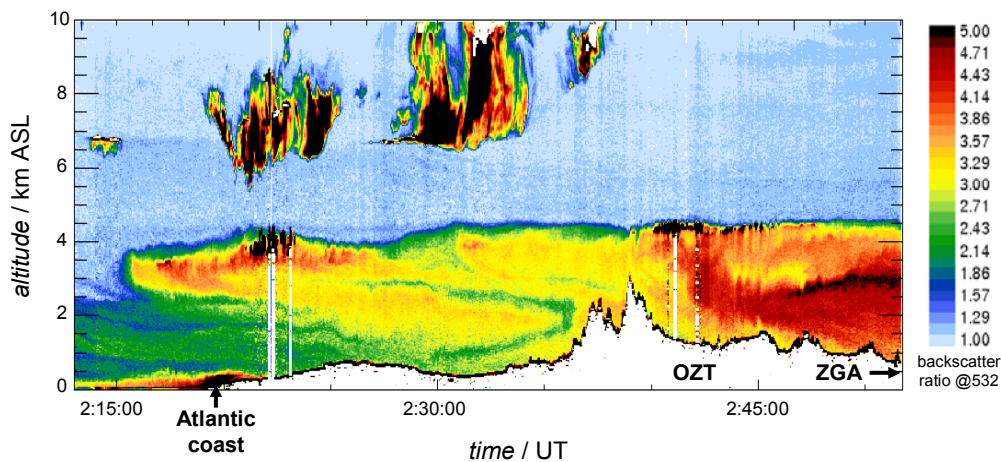
West, north-west, and north of the Atlas Mountains the dust enters the long-range transport regime. The formation of lofted dust plumes was documented for example on 3 June 2006 (Figure 69). The dust plume which extended from the surface up to about 4.5 km altitude close to the Sahara was lofted across the Atlas Mountains by meso-scale dynamic processes<sup>21</sup>. North-west of the Atlas Mountains the dust layer interacted with the sea-breeze that came in from the north north-east. A lofted dust plume had formed, and was exported from the African continent.

Over Casablanca (CASA), situated at the Atlantic coast of Morocco, only lofted dust plumes were observed. The atmosphere over Casablanca always exhibited a typical structure with quite a polluted boundary layer at the surface and a lofted dust layer in the altitude range between 1 and 6 km ASL. Sometimes the boundary layer and the lofted dust layer were

<sup>20</sup> Aerodynamic methods size particles based on their mass-to-drag characteristics. The two most common aerodynamic methods are cascade impactors and aerodynamic particle sizers (APS). More detailed information on these instruments can be found, for example, in Hinds (1999).

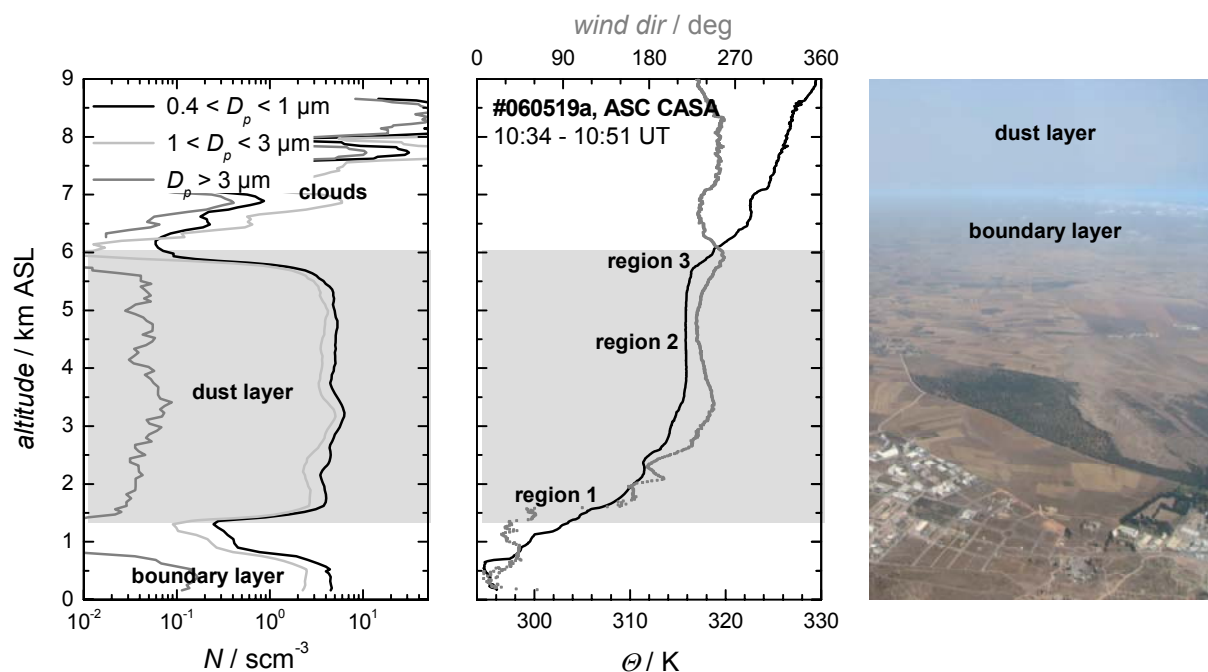
<sup>21</sup> A detailed investigation of the processes that lead to the formation of the lofted plumes is beyond the scope of this work. It would require model calculations to study all possible processes involved in the formation of lofted dust plumes.

separated by a thin layer of very clean air. The dust layers were characterised by a very sharp lower and upper boundary, within several 200-300 m the particle concentration changed by more than one order of magnitude.



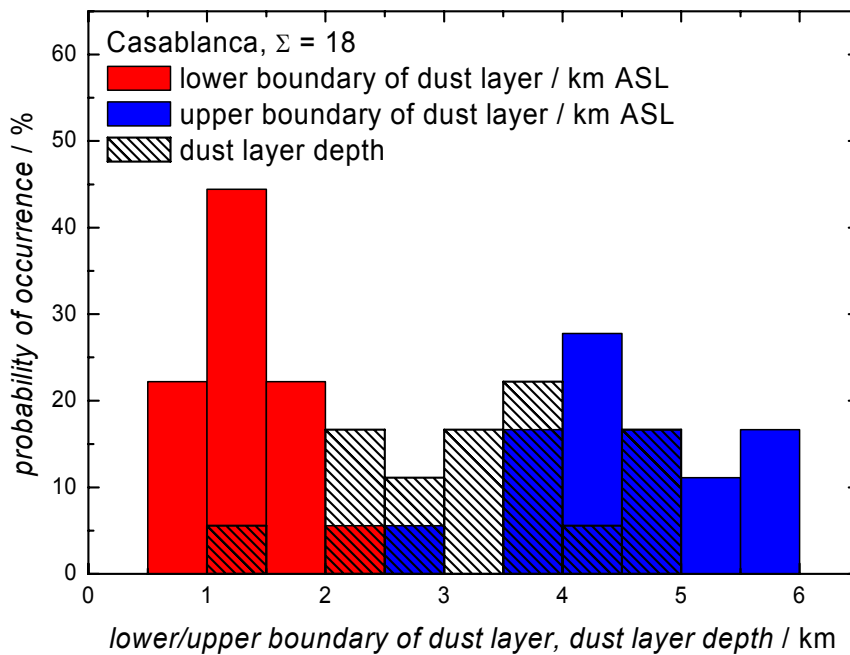
**Figure 69.** North-west – south-east HSRL cross-section (courtesy: M. Esselborn, DLR) illustrating the formation of lofted dust layers. The measurements were taken during the night flight on 3 June 2006. The shown cross-section corresponds to a horizontal distance of about 600 km. The Atlantic coast, Ouarzazate (OZT) and Zagora (ZGA) are marked in the graph.

Figure 70 shows the vertical structure of the atmosphere during the ascent over Casablanca on 19 May 2006. The polluted boundary layer, the dust layer and the clean layer in between are also visible on a photograph taken during the ascent over Casablanca (Figure 70, right panel).



**Figure 70.** Vertical structure of the atmosphere during the ascent over Casablanca (CASA) on 19 May 2006. The left panel shows vertical profiles of particles in the size range of  $0.4 < D_p < 1 \mu\text{m}$  (black line),  $1 < D_p < 3 \mu\text{m}$  (light grey line) and  $D_p > 3 \mu\text{m}$  (grey line). The mid panel shows vertical profiles of potential temperature (black line) and wind direction (grey symbols). The dust layer is also visible on a photograph taken during the ascent over Casablanca (right panel).

On other days, a similar structure was observed over Casablanca. In Table 15, the structure of the lofted dust plumes over Casablanca are listed for the period between 18 May and 7 June 2006. On average the lower boundary of the dust layer was located at  $1320 \pm 420$  m ASL. Small lower limits tended to occur during the night flight #060603a and early day flights. The mean upper boundary was found at  $4660 \pm 910$  m. The low upper boundary of 2745 m was found during the ascent on 4 June, which marked the leading edge of a dust front approaching from the Sahara. High upper dust layer boundaries of  $> 5800$  m tended to occur in the afternoon. On average the dust layers had a depth of  $3350 \pm 1030$  m. Figure 71 summarises the probability of occurrence for the lower (red) and upper (blue) dust layer limits and the dust layer depth (black).



**Figure 71.** Frequency distributions of lower and upper boundaries of the dust layer, and dust layer depth over Casablanca.

The potential temperature profile from 19 May (Figure 70, mid panel) shows a structure that was always observed in lofted dust layers. Three regions of different potential temperature gradient can be identified in the dust layer: the lower (region 1) and the upper part (region 3) of the dust layer exhibit a large gradient in potential temperature and are therefore very stable stratified, while the intermediate part (region 2) of the dust layer is (almost) neutrally stratified. The lapse rates found in the different regions are summarised in Table 15. In addition to that, the lapse rate found outside the dust layers is indicated. In the desert dust plumes an average lapse rate of  $9.8 \text{ K km}^{-1}$ ,  $1.0 \text{ K km}^{-1}$  and  $7.0 \text{ K km}^{-1}$  was observed in region 1, 2 and 3, respectively. Outside the plumes, potential temperature increased on average by  $3.3 \pm 0.5 \text{ K km}^{-1}$ . The lapse rate at the bottom of the dust layer exceeded in all cases the average lapse rate found outside the desert dust plumes by at least a factor of 2. The lapse rate within the dust plumes was always smaller than the average lapse rate for the whole vertical profile. The lapse rate at the top of the dust layer was in most cases larger than the average lapse rate. In two cases (#060522a, ASC; #060603a, DESC), a 2-layer dust structure was observed over Casablanca. In both cases, each of the sub-layers was characterised by three regions of different potential temperature. Furthermore,

**Table 13.** Microphysical properties of pure dust layers over Casablanca (CASA). For label see Table 12.

Mission ID	Layer ID	Site	Start Time / UT	Stop Time / UT	Altitude / m ASL	RH / %	$f_{STP}$	$N_{mode 1}$	$CMD_{mode 1} / \mu m$	$GSD_{mode 1}$	$N_{mode 2}$	$CMD_{mode 2} / \mu m$	$GSD_{mode 2}$	$N_{mode 3}$	$CMD_{mode 3} / \mu m$	$GSD_{mode 3}$	$N_{mode 4}$	$CMD_{mode 4} / \mu m$	$GSD_{mode 4}$	TSP (data) / $\mu g m^{-3}$	PM2.5 (data) / $\mu g m^{-3}$	$f_{PM2.5/TSP} / \%$	$f_{non-vol 2.5} / \%$	$D_{eff} (data) / \mu m$	$D_{eff}(data) / D_{eff}(mode)$
060518d	L02	CASA	16:24:40	16:27:26	4189	51	0.608	500	0.095	2.20	50	0.22	1.50	28	0.90	2.10	1.55	4.90	1.74	1346	81	6.1	64.5	6.5	1.03
060518d	L03	CASA	16:29:46	16:35:24	3226	28	0.662	620	0.075	1.95	70	0.22	1.50	28	0.60	2.30	0.83	6.10	1.78	1423	48	3.4	70	8.7	1.01
060519b	L02	CASA	14:51:52	14:53:46	4568	46	0.590	500	0.110	1.90	55	0.20	1.55	25	0.72	2.30	1.20	5.80	1.65	1300	60	4.6	66.1	6.8	0.98
060519b	L03	CASA	14:54:45	14:57:16	4251	44	0.607	650	0.087	2.20	40	0.20	1.45	32	0.60	2.30	1.85	5.80	1.78	2250	62	3.2	71.5	9.2	0.96
060522a	L01	CASA	15:09:27	15:10:23	3819	27	0.627	800	0.073	1.90	6	0.66	1.60	2	1.40	2.15	0.23	8.70	1.50	610	17	2.8	89.6	8.0	1.01
060527a	L10	CASA	12:18:14	12:21:09	4169	74	0.676	950	0.073	1.80	30	0.35	1.45	50	0.73	2.47	--	--	--	1104	109	9.9	70	5.0	0.98
060527a	L11	CASA	12:23:44	12:26:39	3217	42	0.736	1250	0.073	2.00	30	0.49	1.52	62	1.00	2.37	--	--	--	2536	201	7.9	54.1	5.8	0.98
060603a	L09	CASA	04:29:41	04:32:41	3829	81	0.632	1350	0.067	2.15	80	0.20	1.45	15	0.70	2.00	2.30	4.80	1.83	1900	40	2.1	71.4	8.7	0.98
060603a	L12	CASA	04:43:41	04:45:41	926	32	0.833	1180	0.073	1.85	90	0.18	1.50	7.6	0.64	2.18	0.31	5.53	1.42	179	18	10	67.9	3.1	0.98
060607a	L01	CASA	10:13:30	10:17:54	2588	38	0.705	620	0.084	1.73	45	0.22	1.48	19	0.51	2.29	0.04	6.52	1.42	121	30	25	72.1	2.5	1.04
060607a	L02	CASA	10:20:42	10:25:46	3880	36	0.628	700	0.077	1.80	45	0.22	1.48	15	0.51	2.29	0.03	6.45	1.59	94	20	21.9	76.6	2.3	0.97

**Table 14.** Microphysical properties of aged dust over Portugal. For label see Table 12.

060518b	L03	CDR	12:16:42	12:18:57	3891	1	0.635	700	0.057	2.00	80	0.20	1.35	1.40	0.68	1.60	0.16	2.29	1.54	11	5	51.6	49	0.6	0.99
060518b	L06	EVO	13:14:50	13:15:46	3899	--	0.631	520	0.08	1.90	40	0.22	1.30	1.40	0.58	1.60	0.18	2.32	1.50	9	5	52.9	48.3	0.6	0.97
060527a	L04	EVO	10:46:04	10:51:09	3245	67	0.678	680	0.067	2.10	7.5	0.60	1.53	6.50	1.20	2.00	0.38	6.59	1.55	513	34	6.5	63.4	5.8	0.98
060527a	L05	EVO	10:53:54	10:57:44	2300	52	0.742	900	0.055	2.20	4.6	0.67	1.42	5.40	1.20	2.00	0.28	6.55	1.52	393	26	6.6	72.1	5.5	1.04

the microphysical dust properties in both sub-layers were slightly different. The analysis of the wind speed and wind direction indicated that the two sub-layers were advected from slightly different sources. As every sub-layer exhibited the three regions of static stability, the lapse rates for every sub-layer are given in Table 15. Figure 72 shows vertical profiles of potential temperature for 9 ascents/descents over Casablanca. The grey dashed line in each panel indicates the average lapse rate, and the grey shaded area marks the vertical dimension of the dust plumes.

**Table 15.** Structure of lofted dust layers over Casablanca (CASA). On 4 June 2006, the lapse rate at the lower boundary of the dust layer over Casablanca could not be determined as the aircraft left the dust layer and flew into another airmass during a constant level sequence at about 960 m ASL.

Mission ID	Time of in-situ measurement / UT	Casablanca	Lower boundary of dust layer / m ASL	Upper boundary of dust layer / m ASL	Dust layer depth / m	$d\theta/dz$ / K km <sup>-1</sup> (region 1)	$d\theta/dz$ / K km <sup>-1</sup> (region 2)	$d\theta/dz$ / K km <sup>-1</sup> (region 3)	$d\theta/dz$ / K km <sup>-1</sup> (profile average)
060518d	16:15 – 16:50	DESC	845	5360	4515	16.3	0.5	6.8	3.8
060519a	10:35 – 10:51	ASC	1420	5810	4390	10.1	0.3	7.8	3.3
060519b	14:44 – 15:10	DESC	1040	6000	4960	16.6	1.0	5.3	3.8
060520a	10:34 – 10:52	ASC	1280	5240	3960	8.3	1.8	3.5	3.0
060520a	13:29 – 13:50	DESC	1290	5920	4630	13.0	1.1	3.1	3.6
060522a	15:04 – 15:30	ASC, low	2020	5930	3910	5.9	0.7	5.4	3.5
060522a		ASC, high				5.4	1.1	7.1	
060522c	21:41 – 22:01	DESC	1450	3560	2110	21.1	4.5	14.7	4.6
060527a	09:15 – 09:43	ASC	1210	4255	3045	8.2	0.9	3.7	3.3
060527a	11:47 – 12:36	DESC	1650	4130	2480	6.8	0.4	3.5	2.9
060528a	10:13 – 10:36	ASC	800	4740	3940	6.7	1.7	7.2	2.9
060528a	13:11 – 13:35	DESC	960	4840	3880	11.4	1.3	18.7	3.0
060603a	01:36 – 02:07	ASC	1470	3980	2510	7.3	1.2	7.1	3.1
060603a	04:20 – 04:49	DESC, low	1000	4300	3300	9.5	1.7	5.8	3.9
		DESC, high				5.8	0.7	7.2	
060603b	07:06 – 07:30	ASC	600	3720	3120	8.7	1.9	15.5	3.4
060603c	11:21 – 11:42	DESC	1970	4400	2430	5.2	2.4	9.8	3.1
060604a	09:18 – 09:39	ASC	1550	2745	1195	8.8	0.1	8.8	3.2
060604a	12:12 – 12:34	DESC	unclear	4360	n.d.	unclear	1.7	6.1	2.8
060607a	10:08 – 10:45	ASC	1900	4525	2625	5.8	0.7	5.4	2.9

The microphysical properties found in the dust layers over Casablanca were very similar to those found over Ouarzazate and Zagora. Again, the size distribution showed 2 zones with different mixing states (see Figure 63, p. 98). In zone 1 (below 0.5  $\mu\text{m}$ ) the particles have a non-volatile core with a volatile coating, while in zone 2 (above 0.5  $\mu\text{m}$ ) the particles consist of an internal mixture of non-volatile components. Table 13 compiles the microphysical properties of the dust layers over Casablanca. The table is organised in the same manner as Table 12. The  $PM_{2.5}$  and  $TSP$  mass concentrations refer to spherical particles of a density of 2600 kg m<sup>-3</sup>. On average  $PM_{2.5}$  contributes 9% to the total mass. In contrast to the dust layers over Ouarzazate and Zagora, the ratio  $PM_{2.5}/TSP$  does not show a height dependency. For particles smaller 2.5  $\mu\text{m}$  the non-volatile volume fraction  $f_{non-vol, 2.5}$  ranges around  $70 \pm 9\%$ . This is still within the standard deviation of the mean non-volatile fraction over the source, but with a tendency to increased volatile components. The mean  $D_{eff}$  in the dust over Casablanca was  $6.0 \pm 2.6 \mu\text{m}$ . Compared to the dust over the source, the  $D_{eff}$  over Casablanca is on average about 8% lower than that over Ouarzazate and Zagora (see also Figure 65, p. 102).

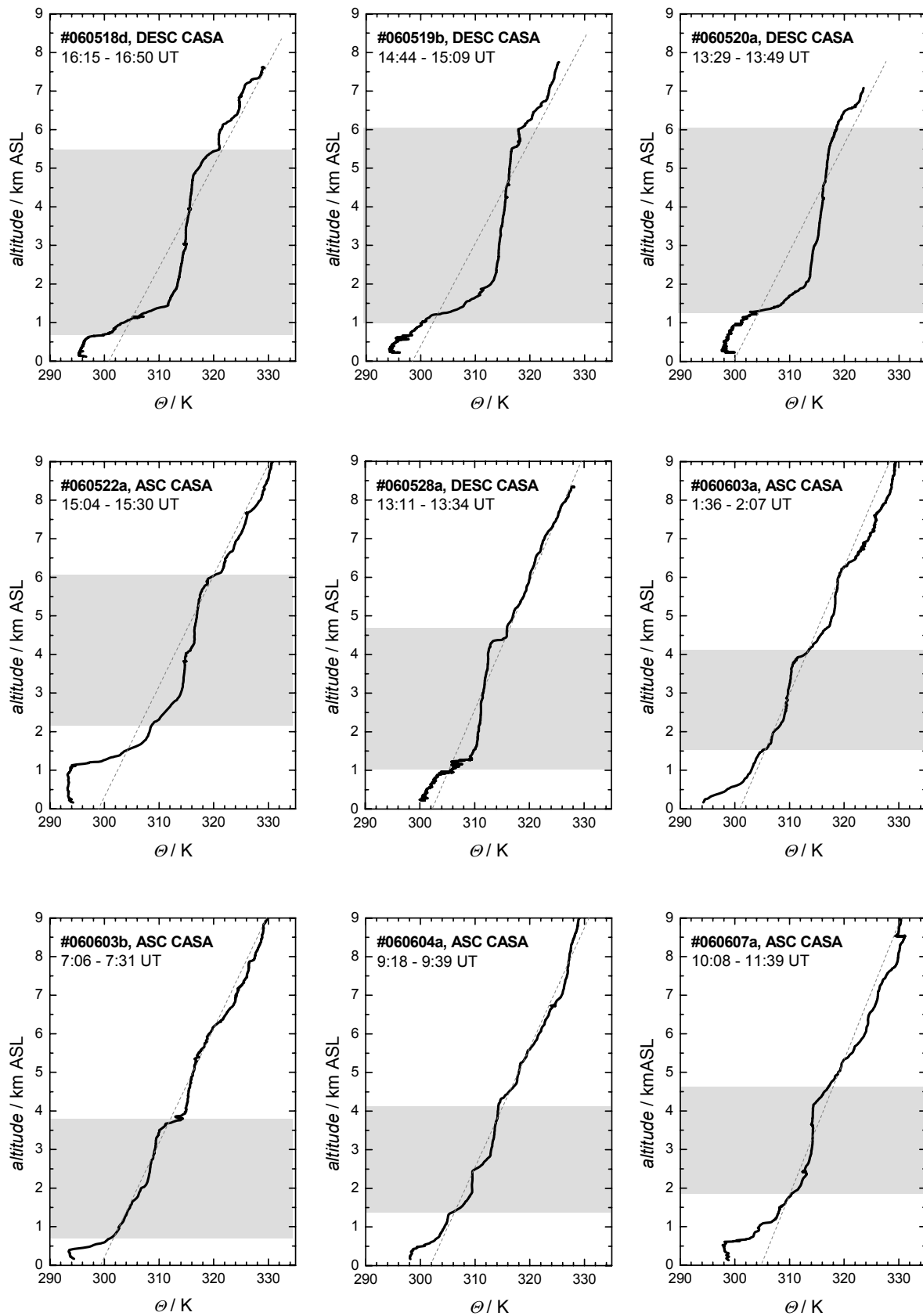


**Figure 72.** Vertical profiles of potential temperature found over Casablanca in the period 18 May-7 June 2006. The vertical dimension of the dust plume is indicated by the grey shaded area. In case #060522a and #060603a, the dust plume showed a 2-layer structure. The sub-layers were advected from slightly different source regions.

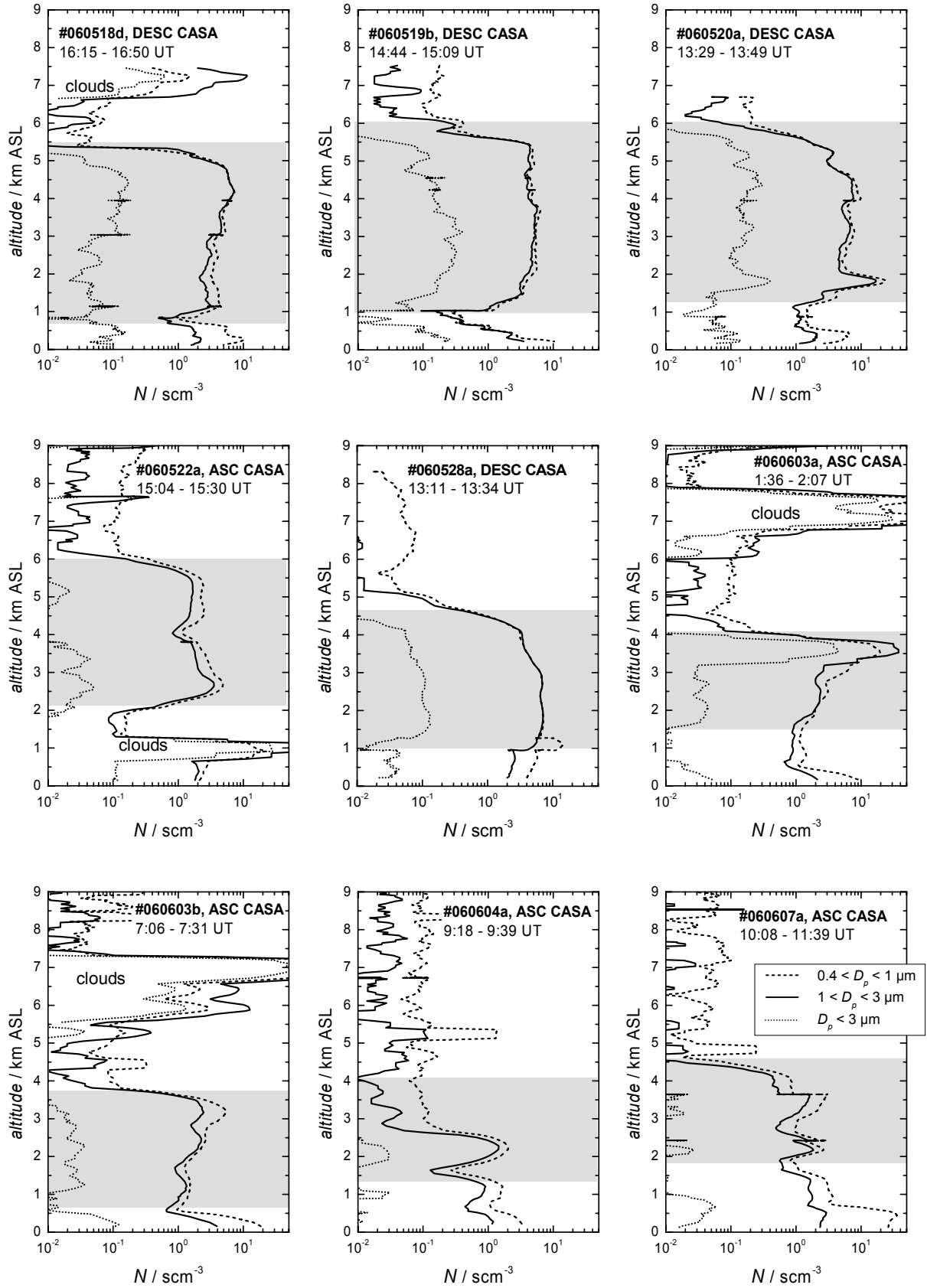


**Figure 73.** Vertical profiles of particle number concentration measured with the FSSP-300 over Casablanca. The panels correspond to the vertical profiles of potential temperature shown in Figure 72. The dashed, solid and dotted lines show particles in the size range of  $0.4 < D_p < 1 \mu\text{m}$ ,  $1 < D_p < 3 \mu\text{m}$  and  $D_p > 3 \mu\text{m}$ , respectively.

### 4.2.3 Properties of aged dust layers

Aged dust layers were measured on 18 and 27 May 2006 at Evora (EVO) and Cabo da Roca (CdR) in Portugal. Trajectory calculations did not clear resolve the dust plume of the 18 May, therefore its age could only be estimated from the model. One reason may be that the dust plume of the 18 May was very thin with a depth of about 800 m, which is probably not resolved by the trajectory model. The estimated age of this plume is 3-10 days. In contrast, the dust layer of the 27 May had a depth of about 2700 m and extended from ~1600 to 4290 m ASL. The layer of the 27 May was very inhomogeneous and showed wave-like structures. Trajectory calculations revealed an age of 2 days for the dust plume over Portugal on 27 May 2006.

Figure 74 illustrates the dust layer structure on 18 May over Portugal. The left panel shows particle number concentrations, the mid panel potential temperature (black line) and wind direction (grey symbols). In the right panel the dust layer structure is illustrated by HSRL backscatter ratio at 1064 nm (colour coded).

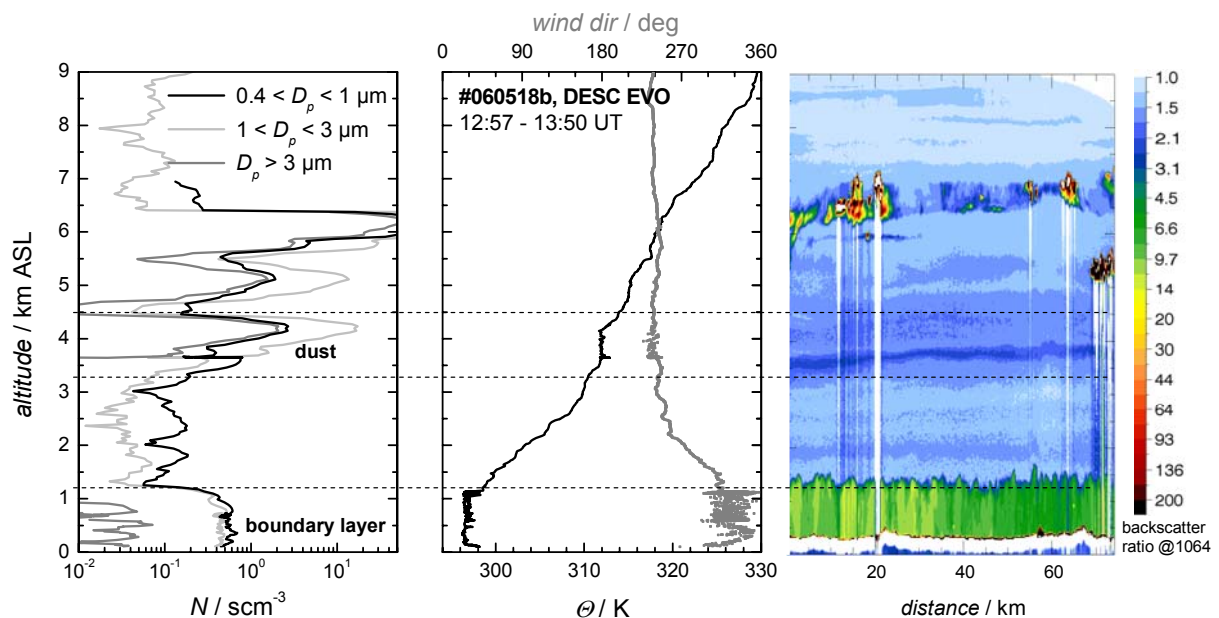


**Figure 74.** Dust layer over Evora (Portugal) on 18 May 2006. The left panel shows vertical profiles of particles in the size range of  $0.4 < D_p < 1 \mu\text{m}$  (black line),  $1 < D_p < 3 \mu\text{m}$  (light grey line) and  $D_p > 3 \mu\text{m}$  (grey line). The mid panel shows potential temperature (black line) and wind direction (grey symbols). In the right panel (courtesy: M. Esselborn, DLR) the dust layer structure is illustrated by HSRL backscatter ratio at 1064 nm (colour coded).

The polluted boundary layer reaches up to an altitude of 1.2 km ASL and is dominated by high particle concentrations. The boundary layer is neutrally stratified and the wind is variable. From 3650 to 4460 m altitude, a layer with enhanced particle number concentrations of particles in the size range  $D_p > 3 \mu\text{m}$  is observed which can be attributed to dust from the Sahara. The structure of the potential temperature in the layer is similar to that observed in lofted dust layers over Casablanca: large lapse rates at the bottom ( $5.0 \text{ K km}^{-1}$ ) and at the top ( $8.5 \text{ K km}^{-1}$ ) of the layer and a neutrally stratified layer ( $312.0 \pm 0.1 \text{ K}$ ) of about 400 m depth in between. The size distribution of flight #060518a shows with two zones of different mixing states (not shown) a similar structure than that observed over Ouarzazate, Zagora and

Casablanca, although the large particles are depleted. The  $D_{eff}$  decreased to  $0.6 \mu\text{m}$  (Table 14), the smallest value observed during SAMUM (see also Figure 65, p. 102). The age of the dust layer (3-10 days), which was the oldest investigated during SAMUM, may explain the observed  $D_{eff}$ : parts of the large particles may have settled due to gravity. The non-volatile fraction of particles smaller  $2.5 \mu\text{m}$  has decreased to 52% compared to  $78\% \pm 9\%$  over Ouarzazate and Zagora. This decrease in  $f_{non-vol\ 2.5}$  may also be the result of ageing/dilution processes during transport (see Section 5.2, p. 132ff).

The size distributions measured over Evora on 27 May 2006 show the typical features found in dust layers close to the Sahara. Figure 75 (left panel) shows size distributions measured at two altitudes over Evora on 27 May 2006. The solid lines refer to measurements at 3245 m ASL, while the dashed lines refer to the measurements at 2300 m ASL. Again, the size distributions exhibit two zones of different mixing states. In the size range beyond  $0.5 \mu\text{m}$  (zone 2) both size distributions are indistinguishable, while in the smaller size range there are some differences between the measurements at 3245 and 2300 m ASL: the non-volatile fraction  $f_{non-vol\ 2.5}$  has slightly decreased during transport and is 63% in the upper part (L04) and 72% in the lower part (L05) of the plume (Table 13). After 2 days of transport  $D_{eff}$  ( $6.5$  and  $6.6 \mu\text{m}$ ) is still within the range of  $D_{eff}$  found over Ouarzazate and Zagora (see also Figure 65, p. 102). There are still particles of  $20\text{-}30 \mu\text{m}$  size over Evora. The right panel of Figure 75 depicts parameterisations of size distributions recorded at 3 km altitude (grey lines). Those recorded over Evora are marked by a blue and red line. The size distributions over Evora on 27 May are within the spread of the size distributions found close to the Sahara. However, they belong to the size distributions with lower particle concentrations in the super-micron range. The size distribution found on 28 May (L03, black line in the right panel of Figure 75) is almost identical with the Evora measurements.

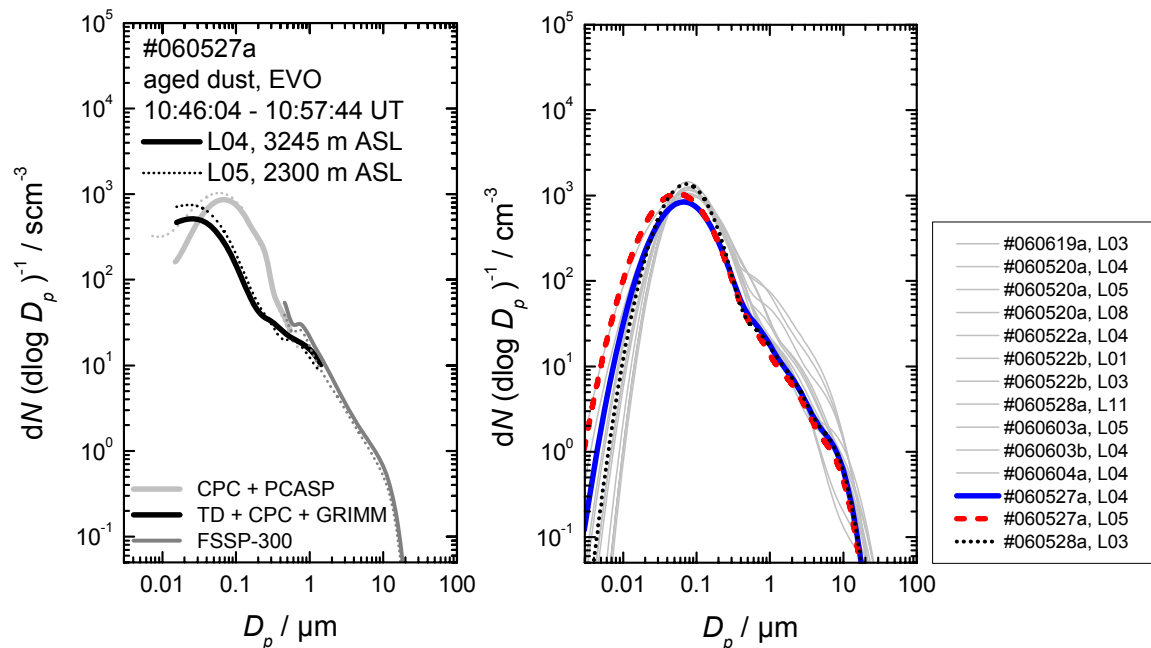


**Figure 75.** Composite size distribution (grey lines) determined in desert dust layers over Evora (left panel), including non-volatile size distribution (black lines). The dashed lines show measurements at 3245 m ASL, while the solid lines show measurements at 2300 m. The right panel depicts a comparison of parameterised size distributions recorded over Evora (blue and red line) and measurements over Ouarzazate and Zagora at 3 km altitude.

#### 4.2.4 Optical properties of dust layers

The microphysical dust properties described in the preceding sections (parameterised size distribution, refractive index, and aerosol mixing state) entered the aerosol optical model (see Section 3.3.7, p. 78ff) to calculate spectral aerosol optical properties required for the computation of heating rates. The aerosol optical model requires assumption of spherical particles, which dust particles are not in general (see Figure 64, p. 99). Possible implications of the assumption of spherical particles on the derived heating rates are evaluated in this section. Although desert dust particles have a non-spherical shape it is expected that the difference in extinction coefficient  $\sigma_{ep}$  calculated under the assumption of spherical particle shape and the direct extinction measurements with the HSRL in most cases does not exceed several percent. However, one expects significant spherical/non-spherical differences in angle-dependent quantities like scattering phase function, especially at side-scattering and backscattering angles (*Mishchenko et al.*, 1997). For strongly absorbing aerosol components, such as hematite, the phase function and the asymmetry parameter is much less dependent on particle shape as a result of the quenching of internal resonances inside the particle (*Kahnert et al.*, 2007).

Figure 76 depicts two examples of vertical profiles of HSRL extinction measurements (grey lines) and calculated extinction coefficient  $\sigma_{ep}$  (black symbols). In the left and right panel HSRL extinction measurements at 532 nm and calculated extinction at 532 nm are compared for the 3 June and the 4 June 2006, respectively. Extinction coefficients  $\sigma_{ep}$  calculated from particle size distributions and refractive index data reproduce in all cases the values from direct measurements and reflect the vertical structure of the dust layer, although the calculated  $\sigma_{ep}$  slightly overestimate the values from the direct measurements. The calculated extinction coefficient at 355 nm was also compared with measurements of the IfT-lidar. Altogether, calculated  $\sigma_{ep}$  (in-situ) and measured  $\sigma_{ep}$  (HSRL, IfT-lidar) were compared for 19 cases. The optical closure between calculated extinction coefficients and HSRL/IfT-lidar measurements, respectively, has been achieved successfully as shown in Figure 77. The data of the lidar/in-situ intercomparison are summarised in Table 16. In 53% of the cases, the deviation between HSRL measurements and the in-situ calculations was  $<15\%$ . For extinction coefficients larger  $0.05 \text{ km}^{-1}$ , the HSRL-in-situ difference was between 3 and 26%. Considering the time off-set of about one hour between the HSRL and the in-situ measurements, both methods are in good agreement. The largest deviations between HSRL extinction coefficient and calculated extinction coefficient occurred on 27 May 2006, when the dust layer showed a lot of structure and was very inhomogeneous. For this case, good agreement can not be expected. The deviation between lidar and in-situ measurement was larger close to the top of the dust layer than well within the dust layer. One factor causing the larger difference at the top of the dust layer is that the lidars average over a particular vertical distance (HSRL, extinction coefficient:  $dz \sim 250 \text{ m}$ ; IfT-lidar:  $dz \sim 300 \text{ m}$ ), therefore slightly smoothing the sharp upper edge of the dust layer. Furthermore, the uncertainty in the derived refractive index and aspherical effects can contribute a few percent to the overestimation.

The extinction calculated under the assumption of spherical particles was compared to non-spherical calculations conducted at the University of Munich. The effect of non-sphericity on calculated extinction coefficients was smaller than  $-5\%$  (*J. Gasteiger*, personal communication), that is,  $\sigma_{ep}$  was slightly smaller for aspherical than for spherical calculations. In general, the Mie model seems to be applicable to the calculation of extinction coefficients

of desert dust. The good agreement between calculation and measurements at 355 nm and 532 nm enabled the computation of  $\sigma_{ep}$  for other wavelengths in the spectral range between 200 nm and 20  $\mu\text{m}$ . The calculation of  $\sigma_{ep}$  for other wavelengths revealed that  $\sigma_{ep}$  is almost independent of the wavelength. However, effects of particle asphericity were clearly visible in the particle backscatter closure (not shown). The Mie model underestimated the lidar ratio by a factor of 2-3.

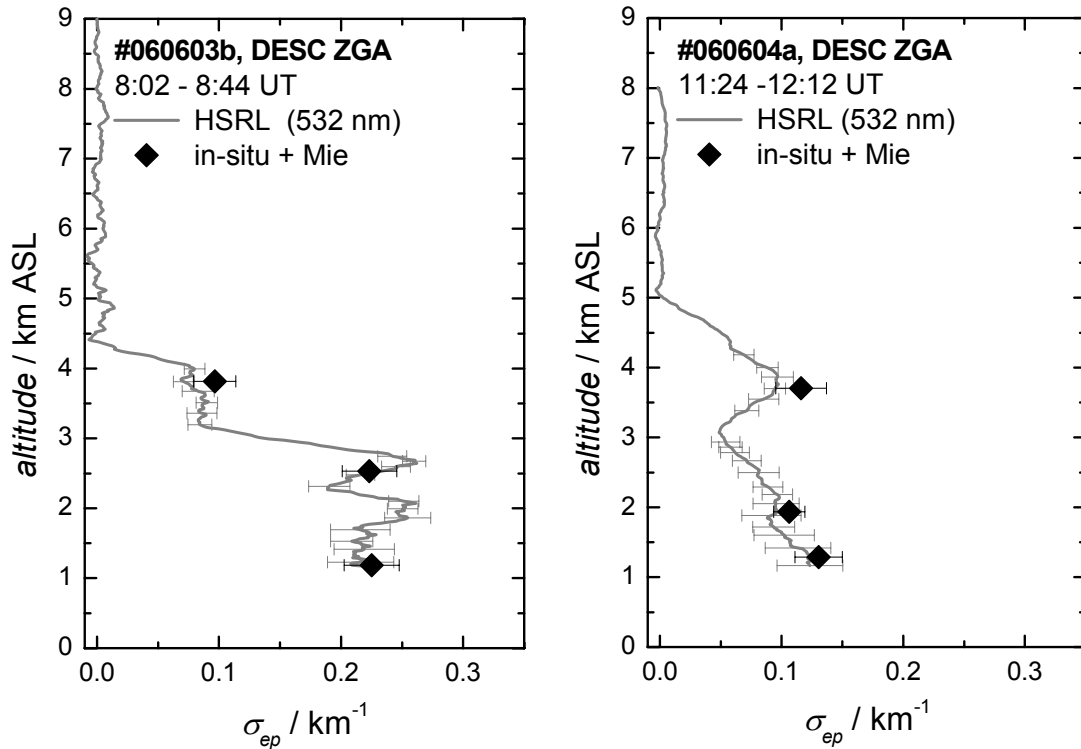


**Figure 76.** Vertical profiles of lidar extinction measurements (grey lines) and extinction coefficient calculated from in-situ measurements on the basis of Mie theory (black symbols). The left and right panel show an intercomparison of HSRL extinction measurements at 532 nm and calculated extinction at 532 nm for the 3 and 4 June 2006, respectively.

*Kahnert et al.* (2007) investigated the error of Mie simulations introduced in mineral aerosol radiative forcing calculations on the basis of spherical and aspherical calculations at two wavelengths in the visible spectrum. They performed the radiative transfer calculations with libRadtran, the same model as used in this study. They pointed out that the single-scattering albedo  $\omega_0$  is quite insensitive to particle shape of non-spherical aerosols. Therefore,  $\omega_0$  determined by Mie calculations provides an accurate estimate for the true value of  $\omega_0$  for non-spherical particles. In this study, radiative transfer calculations have been performed for several dust plumes: in the dust layers over Ouarzazate and Casablanca on 19 May 2006,  $\omega_0$  ranged between 0.82 and 0.83 at 550 nm; in the plumes over Evora on 27 May 2006 and over Casablanca on 28 May 2006, the optical calculations showed in each case  $\omega_0 = 0.88$  at 550 nm. *Rasp* (2007) investigated the spread of  $\omega_0$  within the three SAMUM dust episodes and found values of  $0.83 \pm 0.04$  (**Episode I**),  $0.89 \pm 0.02$  (**Episode II**) and  $0.92 \pm 0.02$  (**Episode III**) at a wavelength of 550 nm. The values of  $\omega_0$  found in this study are in good agreement with the OPAC database (*Hess et al.*, 1998a), where a value of 0.89 is given at 550 nm for mineral dust. Transforming the values of  $\omega_0$  for dust given in *Dubovik et al.* (2002) to 550 nm results in values of 0.93-0.95 for  $\omega_0$ .

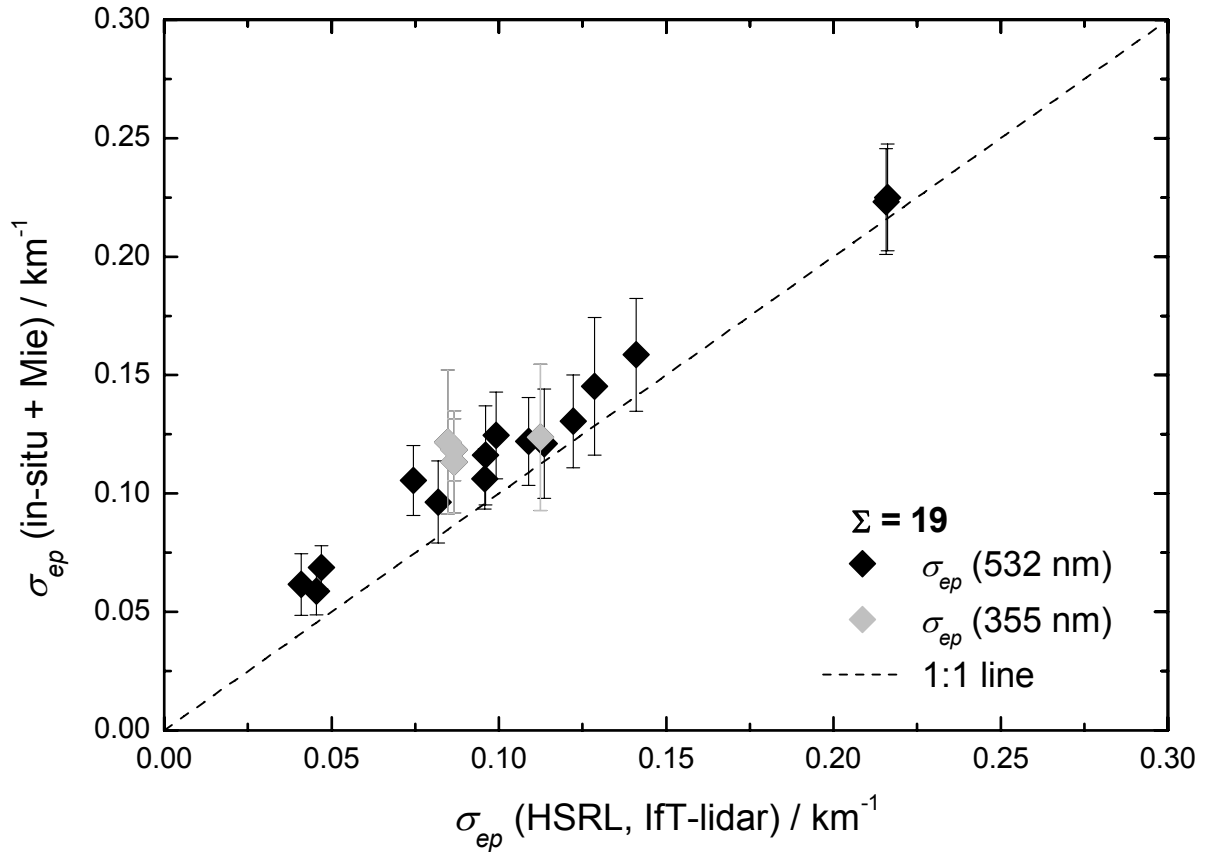


**Figure 77.** Closure of extinction coefficient calculated from in-situ measurements and measured with the HSRL (532 nm) and the lft-lidar (355 nm).

**Table 16.** Extinction coefficient of dust for lidar/in-situ intercomparison levels. The HSRL and the in-situ extinction coefficient  $\sigma_{ep}$  are compared at 532 nm. At 355 nm the calculated  $\sigma_{ep}$  is compared with measurements of the lft-lidar. The seventh column shows the difference  $\sigma_{ep}(\text{in-situ}) - \sigma_{ep}(\text{lidar})$  and in the eighth column the relative deviation  $\sigma_{ep}(\text{in-situ})/\sigma_{ep}(\text{lidar})$  between both methods is presented.

Mission ID	Layer ID	Site	$\lambda / \text{nm}$	$\sigma_{ep} / \text{km}^{-1}$			
				Lidar	In-situ	$\Delta \sigma_{ep}$	Rel. $\Delta \sigma_{ep} / \%$
060519a	L02	OZT	532	0.10887	0.12196	0.01309	1.12
060519a	L03	OZT	532	0.11360	0.12105	0.00745	1.07
060527a	L04	EVO, P	532	0.04702	0.06883	0.02181	1.46
060527a	L05	EVO, P	532	0.04548	0.05872	0.01324	1.29
060528a	L03	ZGA	532	0.04097	0.06157	0.02060	1.50
060528a	L04	ZGA	532	0.09922	0.12456	0.02534	1.26
060528a	L18	CASA	532	0.14100	0.15860	0.01760	1.12
060603b	L03	ZGA	532	0.08192	0.09642	0.01450	1.18
060603b	L04	ZGA	532	0.21576	0.22324	0.00748	1.03
060603b	L05	ZGA	532	0.21615	0.22502	0.00887	1.04
060604a	L03	OZT	532	0.07445	0.10546	0.03101	1.42
060604a	L05	OZT	532	0.12866	0.14529	0.01663	1.13
060604a	L07	ZGA	532	0.09598	0.11613	0.02015	1.21
060604a	L08	ZGA	532	0.09574	0.10624	0.01050	1.11
060604a	L09	ZGA	532	0.12221	0.13050	0.00829	1.07
060519a	L02	OZT	355	0.08469	0.12168	0.03699	1.44
060519a	L03	OZT	355	0.11239	0.12372	0.01133	1.10
060528a	L11	OZT	355	0.08663	0.11848	0.03185	1.37
060528a	L12	OZT	355	0.08663	0.11335	0.02672	1.31

The calculation of the heating rates requires besides the spectral extinction coefficient  $\sigma_{ep}$  and the single-scattering albedo  $\omega_0$ , the calculation of the asymmetry parameter. As spectral extinction coefficient and  $\omega_0$  seem to be well reproduced by Mie calculations (see above), the only relevant error source resulting from the assumption of spherical particles is introduced by the asymmetry parameter. *Kahnert et al.* (2007) concluded their study that the use of spherical particles can introduce errors up to several 10 percent in the simulated aerosol radiative forcing at the TOA and at the surface. In this study however, the calculation of heating rates is not used to derive a value for the dust forcing at the TOA and at the surface, respectively. Rather, the vertical gradient of the heating rate is used to interpret the characteristic potential temperature structure observed at the bottom and at the top of forest fire and desert dust plumes in the experimental data. Therefore, the uncertainty introduced into the calculation of heating rates by the assumption of spherical particle shape does not influence the results of this study.



---

## 5 Discussion and Conclusions

---

In the preceding chapter the microphysical and optical particle properties observed in lofted forest fire layers during ITOP 2004 and desert dust layers during SAMUM 2006 were described in detail. It has been shown that lofted forest fire and desert dust plumes exhibit a characteristic potential temperature structure with high static stability at the bottom and at the top of the lofted plume. Furthermore, characteristic aerosol properties were observed in the plumes. This chapter aims to explain the experimental data and the observed features.

Lofted aerosol layers can be generated by several mechanisms. These mechanisms are not discussed in detail here, but a summary of the most important ones is given below. Air from lower levels is connected to the free troposphere by sloping isentropic surfaces, since to a first approximation airstreams are moving on isentropic surfaces (*Browning and Roberts, 1994; Bethan et al., 1998; Cooper et al., 2001*). Lofted aerosol layers can arise for example, when continental aerosol plumes are advected from land to sea over cool oceanic air, where they are forced to rise above the marine boundary layer (e.g. *Angevine et al., 1996*). In this way, aerosol burdened air from near the surface may reach higher altitudes and enter the free troposphere, while the near-surface air remains clean (*Ansmann et al., 2001*). *Léon et al. (2001)* suggested that aerosol plumes can be lofted above the boundary layer and entrained into the regional-scale flow by an interaction of the sea-breeze circulation with the regional-scale air flow. As a consequence, part of the continental boundary layer aerosols may be transported over thousands of kilometres without washout processes (*Ansmann et al., 2001*). During SAMUM, the formation of a lofted dust layer by lifting of the plume across the Atlas Mountains and the subsequent interaction with the sea-breeze circulation was documented on 3 June 2006 (see Figure 69, p. 106). Uplifting of aerosol laden air in so-called warm conveyor belts ahead of cold fronts provides another effective mechanism for the rapid transport of pollutants from the surface to the middle and upper troposphere (e.g. *Owen et al., 2006*). Pollution export from Northern America often involves the uplifting of plumes by warm conveyor belts (e.g. *Stohl et al., 2007*). Several recent studies revealed that pyro-convection can inject forest fire emissions well above the boundary layer, even into the upper troposphere/lower stratosphere (*Fromm et al., 2000; 2005; 2006; Jost et al., 2004*). The injection of smoke plumes from forest fires at high altitudes into the atmosphere increases the plume's lifetime compared to injection in the boundary layer (*Trentmann et al., 2006*). The injection height of the forest fire plumes is an area of considerable uncertainty; it varies with the severity of the fire and the prevailing meteorological conditions (e.g. *Turquety et al., 2007*).

Lofted aerosol layers containing forest fire or desert dust particles are not a rare atmospheric phenomenon. *Müller* (2007) investigated the frequency of lofted aerosol layers transported to Leipzig on the basis of lidar observations in the years 1997-2004. He found that lofted aerosol layers from anthropogenic and biogenic origins occurred in at least 30% of the regular annual measurements. In spring and summer lofted aerosol plumes occurred even in about 60% of the regular measurements. *Müller* (2007) pointed out that the maximum in spring and summer coincides with the forest fire season in boreal areas that starts in spring and reaches its maximum intensity in summer. Most layers over Leipzig were found in the altitude range between 2 and 6 km. For comparison, the ITOP forest fire plumes were found in 3-9 km altitude, while during SAMUM desert dust plumes were found in 1-6 km altitude. The frequent presence of lofted aerosol layers in the atmosphere raises several scientific questions: why are these layers present in the atmosphere so frequent? Is there a mechanism that stabilises the plume itself, therefore extending its lifetime? How influences a self-stabilising mechanism the aerosol ageing in the plume?

## **5.1 Hypothesis I – Self-stabilising effect**

The first hypothesis (see p. 12) stated in this work is that the processes in the aerosol layer caused by the heating of the absorbing particles together with large-scale subsidence lead to a stabilisation of the aerosol plume itself and help to explain the characteristic lapse rate (Section 4.1.4, p. 91ff; Section 4.2.2, p. 105ff) and aerosol properties observed in the plume.

### **5.1.1 Heating rates**

In the preceding sections the static stability in forest fire and desert dust plumes was investigated in detail (Figure 53, p. 85; Figure 58, p. 92; Figure 70, p. 106; Figure 72, p. 110). Figure 78 summarises the probability of occurrence of a particular lapse rate in each of the three regions of different static stability for 25 atmospheric profiles. The inversions at the top and at the bottom of the aerosol layer appear to trap the particles within the layer. From these observations the question arises whether the absorption of the trapped forest fire and desert dust particles contributes to the development and maintenance of the characteristic lapse rate and acts to strengthen the atmospheric stability at the bottom of the aerosol layer. In the following, a mechanism that explains the observed temperature profile in the lofted plumes is discussed.

One possibility to explore the characteristic lapse rate within an aerosol layer is to use the aerosol properties to calculate the heating rates with a radiative transfer model. While heating rates in the order of several  $\text{K day}^{-1}$  are able to alter the vertical temperature gradient of the atmosphere very rapidly, smaller heating rates can also influence the vertical temperature gradient, especially when the aerosol layer, which causes the heating, is long-lived. The vertical gradient of the net heating rate is an important parameter in the dynamics of a radiatively heated plume (*Lilly*, 1968;1988; *Herring and Hobbs*, 1994). A heating rate that decreases with height tends to destabilise the atmosphere, while a heating rate that increases with height tends to stabilise the atmosphere.

Most studies dealing with the dynamics of radiatively heated plumes are modelling studies, e.g. *Lilly* (1988) explored the radiatively-driven dynamics in upper tropospheric cirrus outflow plumes from deep convection. The cirrus outflow was characterised by strong

infrared (IR) heating and a heating rate that decreased very rapidly with height. The strong vertical gradient in the heating rate produces what Lilly calls a “radiative-convective mixed layer”. The radiative-convective mixed layer develops a distinctive potential temperature profile. Figure 79 (adopted from *Lilly, 1988*) sketches the hypothetical development of the potential temperature profile of an elevated layer with a strong negative vertical gradient of the net heating rate within the layer.

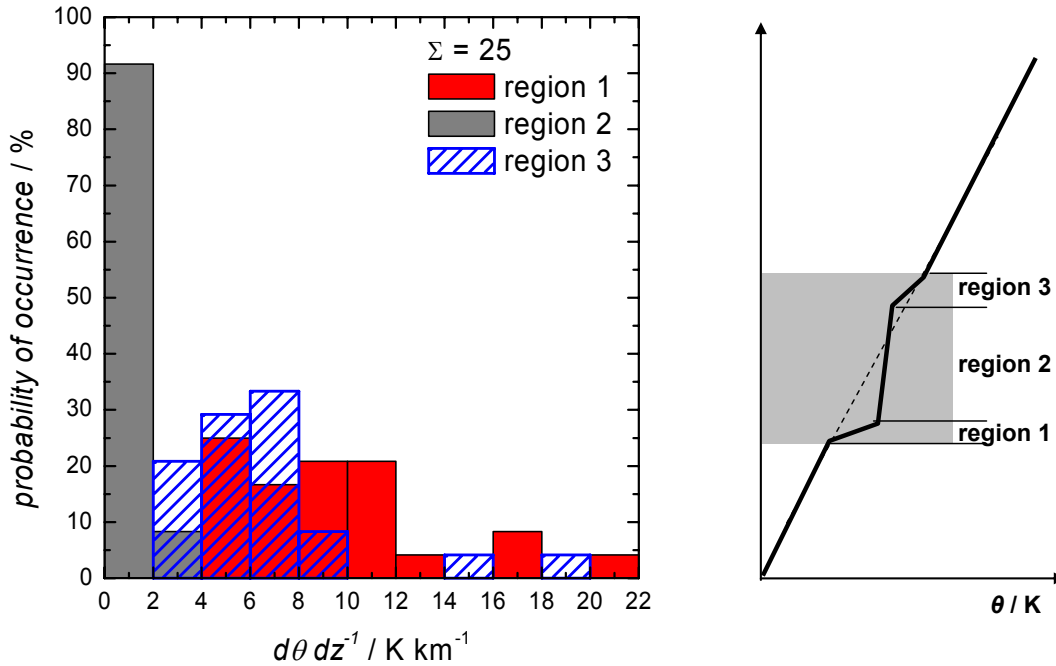


**Figure 78.** Probability of occurrence of potential temperature gradients (left panel) at the lower (red) and upper boundaries (blue) of lofted forest fire and desert dust layers and within the aerosol layer (grey). The right panel illustrates the position of the three regions of different static stability in the lofted aerosol layer. The aerosol layer is marked by the grey shaded area.

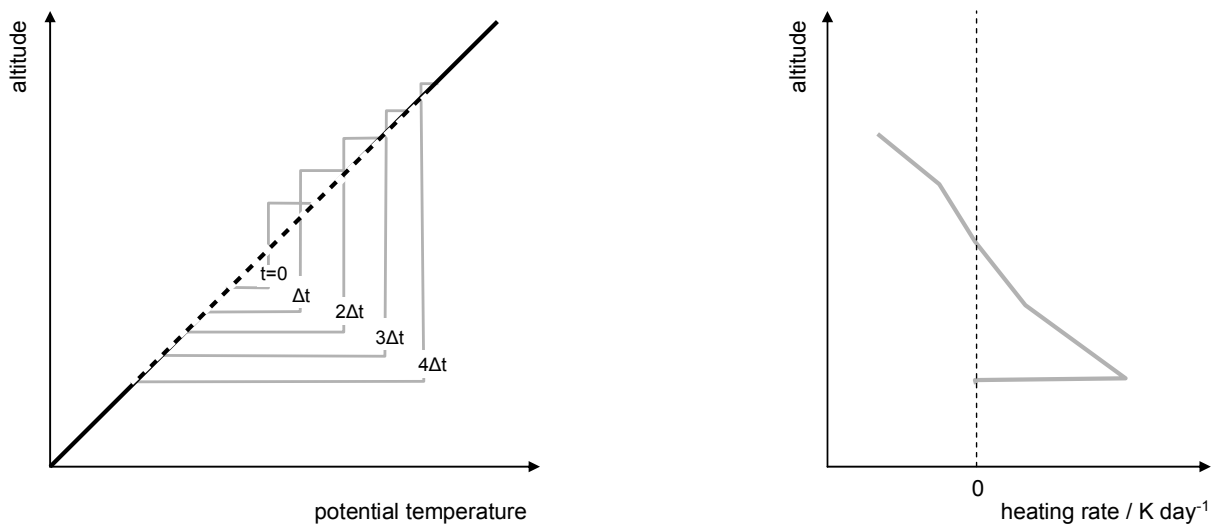


**Figure 79.** Development of the potential temperature profile in a radiative-convective mixed layer (left panel). The mixing is driven by a net heating rate that decreases with height (right panel) (adopted from *Lilly, 1988*).

The negative vertical gradient of the net heating rate decreases the stability until the layer mixes vertically. As the heating continues, the temperature in the layer becomes higher and the mixed layer becomes deeper with time. The temperature jump at the bottom increases, while that at the top decreases. As long as the aerosol layer is topped by a stable stratified layer, mixing is suppressed. If the heating continues long enough, the inversion at the top of the layer will vanish, thus removing the barrier for entrainment at the top of the layer. If no processes like large-scale subsidence are counteracting the turbulent encroachment, the mixed layer can grow very rapidly in depth (Turner, 1973; Carson, 1973). Herring and Hobbs (1994) applied Lilly's (1988) approach to the radiative heating within plumes from the Kuwait oil fires. They describe the development of a radiative-convective mixed layer without any significant temperature inversion at the top of the layer. The missing inversion allowed the entrainment of air into the plume top causing a deepening of the plume. In addition, the plume as a whole was lifted at a rate of  $\sim 0.1 \text{ m s}^{-1}$  during the first few hours of plume evolution.

Similar to the proposed potential temperature gradient of a radiative-convective mixed layer, the potential temperature profiles of the ITOP and SAMUM plumes exhibit three regions of different lapse rates (e.g. Figure 72, p. 110). However, the lapse rate at the top of the forest fire and desert dust plumes is in most cases larger than the average lapse rate found outside the plumes and neutral stratification inside the plume is detected only in 3 of 25 profiles investigated (Figure 78). Although, the plumes investigated do not show exactly the potential temperature profile proposed for a radiatively-driven convective mixed layer, the calculation of the heating rates is helpful in understanding the lapse rate within the forest fire and desert dust plumes.

Figure 80 and Figure 81 show vertical profiles of IR, solar and net heating rates for two typical cases, the lofted forest fire layer over the Atlantic south-west of Spain on 22 July 2004 and the dust layer over Casablanca on 19 May 2006. Both cases show daily mean heating rates. The heating rates have been calculated with libRadtran (Section 3.3.8, p. 79) under the assumption that no clouds were present. For the forest fire layer no vertical measurement of the extinction was available, therefore an extinction profile has been derived from the calculation of optical properties within the forest fire layer (see Section 4.1.3, p. 88ff). Further input parameters like asymmetry parameter and single-scattering albedo have also been taken from the optical calculations. During SAMUM 2006, the aerosol extinction was measured directly with the HSRL and the heating rates in the dust layer were calculated from these measurements. Asymmetry parameter and single-scattering albedo were calculated from the size distribution measurements with the aerosol optical model (see Section 4.2.4, p. 114ff). For the calculation of the heating rates, also profiles of temperature, humidity, and trace gas mixing ratio profiles of  $\text{CO}_2$  and  $\text{O}_3$  are required. As these quantities are not independent of the existing aerosol plume, the vertical profiles of the net heating rates with and without aerosols are expected to be in phase. In both cases, the solar heating dominates over the IR cooling. In the forest fire plume, the strongest heating with  $\sim 0.2 \text{ K day}^{-1}$  occurs around 3.7 km altitude. It coincides with the maximum deviation (about 4 K) of the potential temperature from the average potential temperature profile (Figure 82, left panel). The heating rates found in the forest fire plume are in accordance with findings by Treffeisen *et al.* (2007): they investigated the radiative impact of two Eastern European biomass burning plumes transported to the Arctic and found a heating of about  $0.1\text{-}0.55 \text{ K day}^{-1}$  at an altitude of about

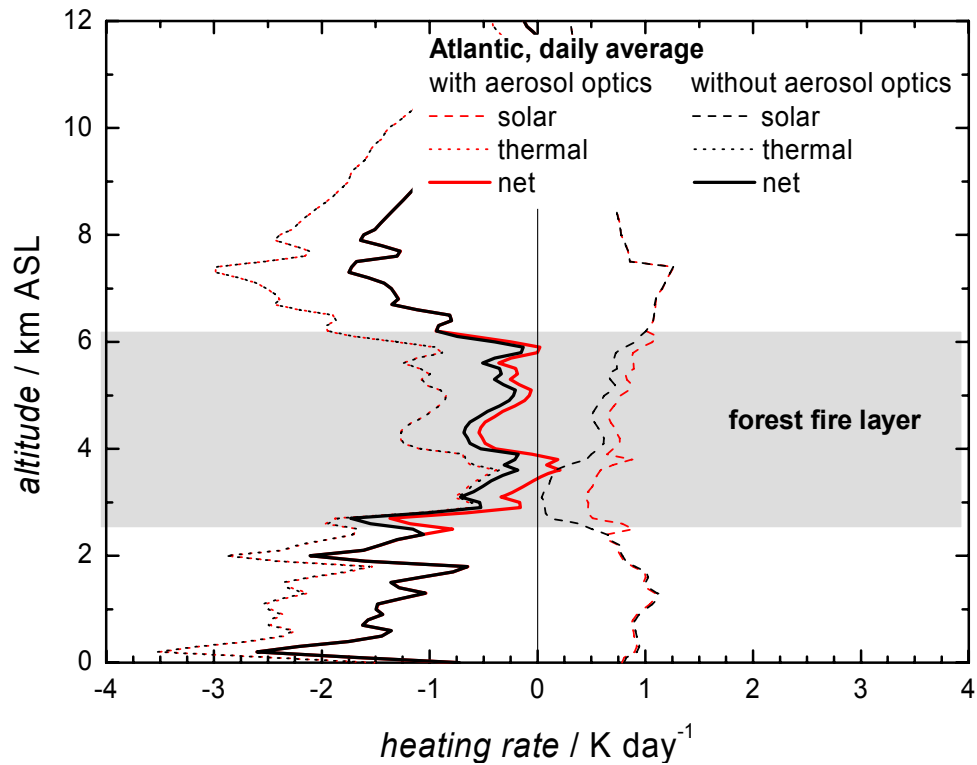


**Figure 80.** Vertical profiles of daily averaged infrared (IR, dotted lines), solar (dashed lines) and net (solid lines) heating rates for the lofted forest fire layer on 22 July 2004. The black curves refer to calculations without aerosol, while the red curves refer to calculations with aerosol particles. The vertical extent of the aerosol layer is marked by the grey shaded area. It was assumed that aerosols are only present in the forest fire layer. See text.

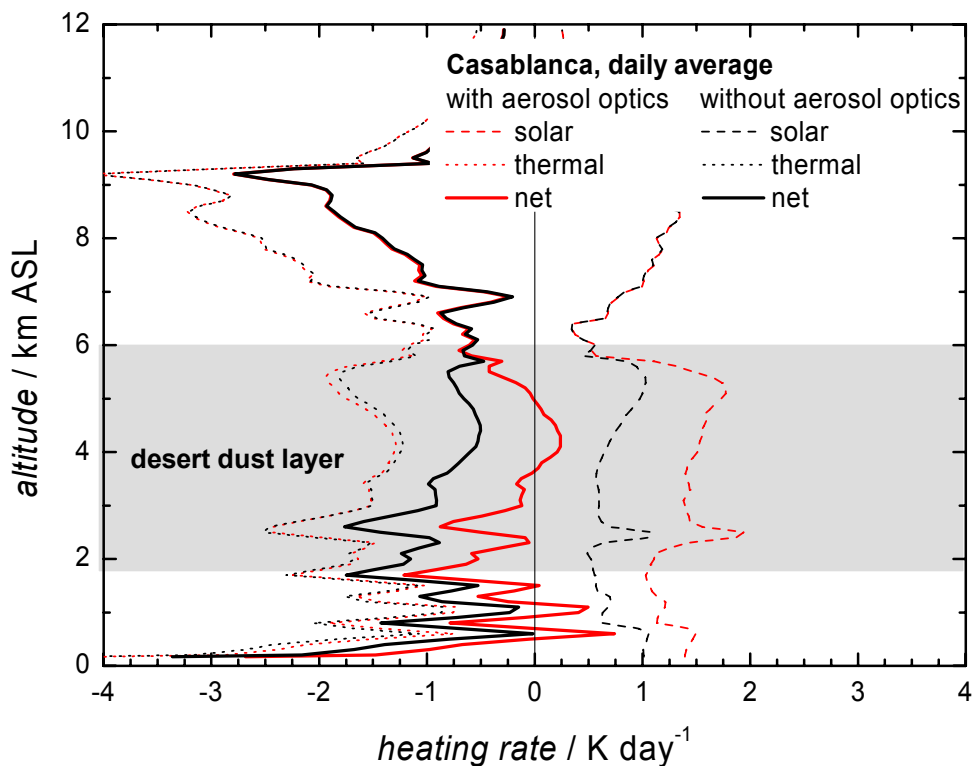


**Figure 81.** Same illustration as in Figure 80, but for the lofted dust layer measured east of Casablanca on 19 May 2006. In this case, the measured aerosol extinction profile entered libRadtran.

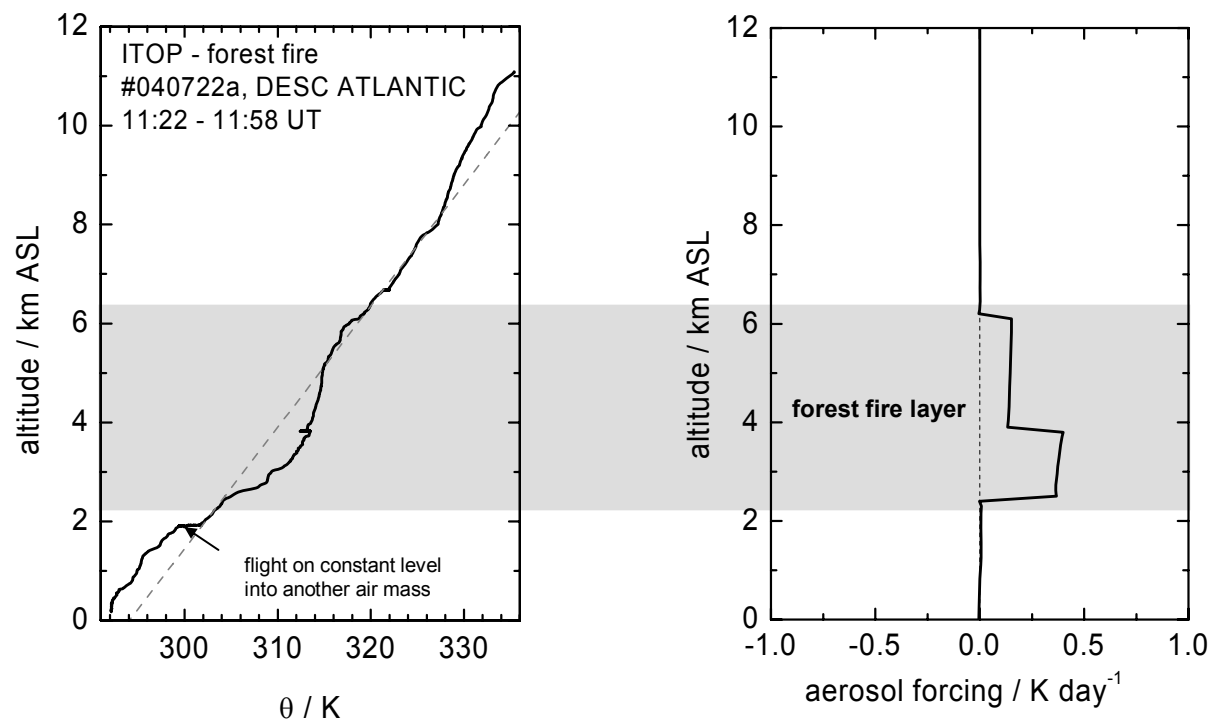


**Figure 82.** Potential temperature profile (left panel) and daily averaged aerosol forcing for the forest fire layer on 22 July 2004. The dashed grey line in the left panel indicates the average potential temperature profile. The aerosol forcing refers to the difference between the daily averaged heating rate with and without aerosols.

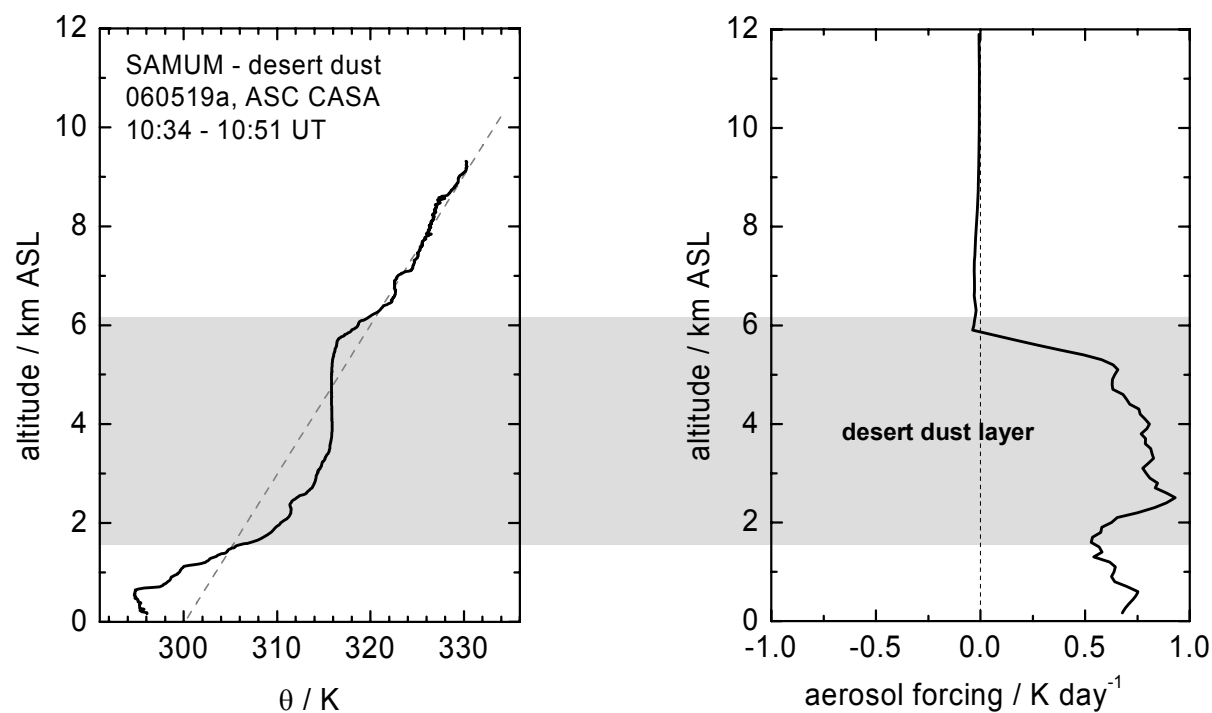


**Figure 83.** Same illustration as in Figure 82, but for the lofted dust layer measured east of Casablanca on 19 May 2006.

1-2 km. In the case of the desert dust plume (Figure 81), the strongest heating with  $0.24 \text{ K day}^{-1}$  occurs in the altitude range between 3.9 and 4.5 km, and it again coincides with the maximum deviation of the potential temperature from the average profile. For comparison, *Alpert et al.* (1998) estimated that an average dust event heats the lower atmosphere (1.5-3.5 km altitude) by  $\sim 0.2 \text{ K day}^{-1}$ .

The right panels of Figure 82 and Figure 83 illustrate vertical profiles of the net aerosol forcing. The net aerosol forcing refers to the difference between the daily mean net heating rates with and without aerosol optics. The presence of absorbing aerosol particles causes a net forcing of  $0.1\text{-}0.4 \text{ K day}^{-1}$  in the forest fire layer, and a forcing of  $0.6\text{-}1.0 \text{ K day}^{-1}$  in the desert dust layer. The vertical gradient of the heating rate increases in the lower part of both layers. This behaviour tends to intensify the atmospheric stability at the bottom of the plumes with time. The aerosol plumes are getting more and more isolated from the underlying airmass.

In the case of the forest fire layer on 22 July 2004, the highest absorption coefficients (see Figure 53, p. 85) and the largest heating rates are found in the lower part of the layer. In contrast, in the desert dust layer on 19 May 2006, the largest heating rate is found in the middle/upper part of the plume. Based on the hypothesis stated in Section 1.3, the vertical aerosol profiles of aerosol properties and the heating rates suggest that entrainment of ambient air has already taken place in the case of the forest fire plume. This is in accordance with numerical simulations of an ITOP forest fire plume by *Real et al.* (2007). They simulated the plume dilution and found that the forest fire plume mixed with upper tropospheric and free tropospheric airmasses during transport. The entrainment has diluted the particle concentration in the upper part of the plume causing there a smaller absorption coefficient. In contrast to the forest fire plume, in the case of the dust plume no mixing has been taken place so far. One reason for that can be that the dust plume is younger (about 1-2 days) than the forest fire plume (about 6-9 days). Therefore the time, in which the aerosol plume is heated is much longer for the forest fire plume than for the desert dust plume. This increases the probability for entrainment of background air into the plume for the forest fire case. Additionally, the large-scale subsidence on the 19 May 2006 has increased the inversion at the top of the dust layer, acting as barrier to mixing.

The vertical profiles of net heating rates help to explain the observed stratification in forest fire and desert dust plumes. Due to a smaller content of absorbing particles, the heating rates found in the investigated forest fire (desert dust) plumes are much smaller than the heating rates of  $94 \text{ K day}^{-1}$  and  $56 \text{ K day}^{-1}$  in the plumes close to the Kuwait oil fires described by *Herring and Hobbs* (1994) or the heating found in the cirrus outflow by *Lilly* (1988). However, even if the process is much slower in the forest fire and desert dust plumes than in the plumes from the Kuwait oil fires, the atmospheric stability at the bottom of the forest fire and desert dust layers is gradually increased. Since the plumes are travelling through a region which is influenced by the presence of a subtropical high pressure system, the probability for increasing the stability at the plume top by large-scale subsidence is high. Therefore, the heating of the absorbing particles and any large-scale subsidence act to strengthen the inversion that is trapping the absorbing particles and prolong the lifetime of the layer.

The static stability at the lower and upper boundary of the plumes, and the mixing in the plumes is investigated in more detail in the next section.

### 5.1.2 Static stability

A method to explore the stratification and the mixing of the plumes with ambient air in more detail is to use an indicator for static stability and to assess the static stability at the lower and upper boundary of the aerosol layer. The static stability impacts on the turbulent mixing of the atmosphere, hence influencing the mixing of the aerosol plume with ambient air. Static instability ( $d\theta/dz < 0$ ) causes vertical mixing. In contrast, within a stable stratified atmosphere ( $d\theta/dz > 0$ ) turbulent mixing is suppressed. However, vertical mixing may also occur in a stable stratified atmosphere by breaking gravity waves causing turbulence locally. The advantage of a dynamic stability indicator over potential temperature is that it also takes into account the wind speed, since sufficiently large wind shear may drive turbulent mixing. This is the first study to our knowledge in which a dynamic stability indicator is applied to forest fire and desert dust layers to assess the stability and mixing in the plumes.

One parameter indicating conditions favourable for dynamic instability is the dimensionless Richardson number  $Ri$ , defined as follows

$$Ri = \frac{g \cdot \frac{d\Theta}{dz}}{\Theta \cdot \left(\frac{du}{dz}\right)^2} \quad (5.1)$$

where  $g$  is the acceleration of gravity,  $\theta$  is the potential temperature, and  $du/dz$  is the vertical shear of the horizontal wind speed.  $Ri$  is the ratio of the buoyant suppression of turbulence by a stable temperature gradient and the generation of turbulence by wind shear. Thus turbulence can develop only for  $Ri < 1.0$ . Linear stability theory yielded that the onset of turbulence normally does not occur above a value of 0.25 (Turner, 1973). Therefore the critical value for the occurrence of turbulence is usually taken as  $Ri = 0.25$ .

$Ri$  was calculated from temperature and wind measurements performed on board the Falcon for the ITOP and SAMUM measurements with a vertical resolution of approximately 15 m. Two examples of vertical profiles of  $Ri$  are illustrated in the left panels of Figure 84 and Figure 85, respectively. Figure 84 shows  $Ri$  for the lofted forest fire layer found over the Atlantic south-west of Santiago/Spain on 22 July 2004 and Figure 85 depicts  $Ri$  in the lofted dust layer over Casablanca on 19 May 2006. As indicator for the forest fire (desert dust) aerosol, the non-volatile fraction of the Aitken mode (coarse mode number concentration) profiles was used (right panels in Figure 84 and Figure 85). The grey shaded area indicates the vertical dimension of the aerosol layer in each case. The black solid line marks  $Ri = 1$ , while the black dashed line indicates  $Ri = 0.25$ . Very high stability is evident at the bottom and at the top of the aerosol layers in both cases. In the case of the forest fire layer the  $Ri$  is exceeding 30 between approximately 2.0 and 3.4 km ASL, reaching a maximum value of 75 at 2.5 km altitude. Within the aerosol layer,  $Ri$  is smaller than 1 for example around 5.0 km altitude. This indicates conditions favourable for dynamic instability. Beyond 6.0 km altitude the forest fire layer is capped by a layer of large  $Ri$  ( $> 20$ ). The stability is larger at the bottom of the layer ( $Ri_{max}=75$ ) than at the top of the layer ( $Ri_{max}=28$ ). Similar observations are made in the desert dust layer over Casablanca, although the magnitude of  $Ri$  is nearly similar at the bottom and at the top of the layer.  $Ri$  exceeds 30 at the bottom and at the top of the layer, reaching a maximum of 37 at the bottom and 42 at the top, respectively. Between 3.9 and

4.4 km, the  $Ri$  indicates conditions favourable for turbulent mixing. The presence of turbulent mixing in this altitude range is corroborated by the potential temperature profile, which shows neutral stratification in this altitude range.

The vertical profiles of  $Ri$  were explored for 9 (15) ascents and descents in which lofted forest fire (desert dust) layers were observed. Figure 86 shows nine more vertical profiles of  $Ri$  for forest fire and desert dust plumes. The structure is at least in seven cases very similar to that depicted in Figure 84 and Figure 85, since the aerosol plumes are enclosed by layers of high  $Ri$ , and evince sections of  $Ri$  below the critical value inside the plumes. On 23 July 2004, the structure of the atmosphere was very complex, since below the forest fire layer two layers with a mixture of long-range transported anthropogenic pollution and forest fire aerosol and pure anthropogenic pollution were present (see also left panel in Figure 58, p. 92). In about 67% of the investigated forest fire and 47% of the investigated desert dust layers  $Ri$  was higher at the bottom of the plume than at the top. In 11% (33%) of the forest fire (desert dust) layers the magnitude of  $Ri$  at the bottom and at the top of the layer was similar ( $\pm 10\%$ ) and in 22% (20%) of the forest fire (desert dust) layers  $Ri$  at the top exceed  $Ri$  at the bottom. In the forest fire plumes, a larger  $Ri$  at the top compared to the bottom tended to occur in the “younger” forest fire plumes (e.g. #040730a). In comparison to the forest fire layers, a higher percentage of dust layers exhibited similar or even larger values of  $Ri$  at the top than at the bottom of the layer. One reason for this might be that the dust layers are “younger” (mainly 2 days) than the forest fire layers (4-13 days). Due to the self-stabilisation the inversion at the bottom strengthens with the extended atmospheric residence time, while the layers are destabilised at the top. The analyses of the magnitude of the  $Ri$  at the bottom and at the top of the aerosol plumes corroborate the self-stabilisation hypothesis.

According to these stability analyses of the layers, the aerosol inside the layers can be regarded as isolated (“sealed”) at the lower boundary. The upper boundary of the layer is permeable. Dilution – if no large-scale frontal system is disturbing the aerosol layer – acts from the top to bottom, since the radiative heating is stabilising the lower part and destabilising the upper part of the plume. If the heating within the layer continues long enough, the inversion at the top will vanish and entrainment is taking place from above. The turbulent encroachment can be counteracted by large-scale subsidence, which was observed for example on 19 May 2006.

The analysis of the forest fire plume on 22 July 2004 (Section 4.1.2, p. 84ff) indicated a decreasing stability at the top of the forest fire layer during the course of the day. This is in accordance with the calculated heating rate in the plume. Furthermore, the observed absorption coefficient was higher in the lower part ( $8.1 \text{ M m}^{-1}$ ) than in the upper part of the layer ( $3.1 \text{ M m}^{-1}$ ). Assuming that the aerosol properties were initially homogeneously distributed, these observations indicate that some entrainment has diluted the layer from above. This hypothesis is in accordance with findings by *Fiebig et al.* (2003) in an aged forest fire layer during LACE 98. They investigated a forest fire plume which had been transported from Canada to Germany and found that plume dilution was inhibited in the lower part of the plume. The entrainment of air from the top of the plume is corroborated by the distribution of aerosol properties in the plume (e.g. stronger absorption in the lower part of the forest fire plume, Figure 53, p. 85; some nucleation mode particles in the forest fire plume top, Figure 89, p. 133; decreased  $f_{non-vol 2.5}$  in the dust layer top, Figure 90, p. 134; Table 13 and Table 14, p. 108) which will be discussed in Section 5.2.1.

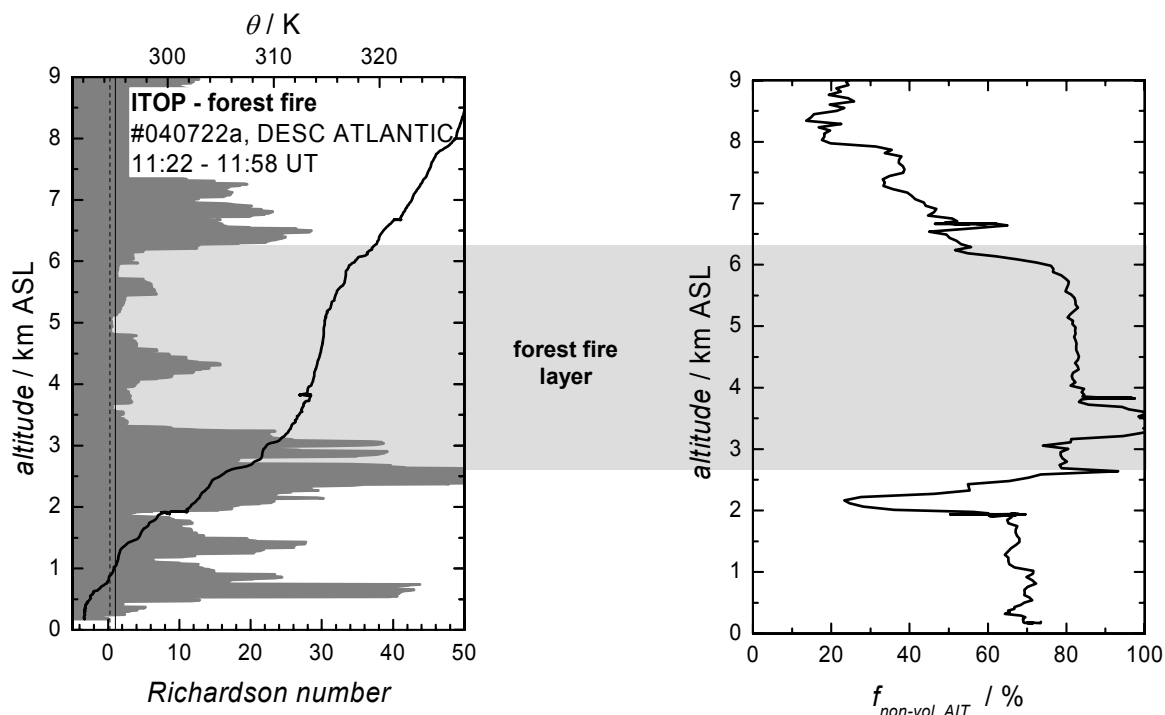


**Figure 84.** The left panel shows a vertical profile of the Richardson number ( $Ri$ , dark grey shaded) and potential temperature (black line), while the right panel depicts the non-volatile fraction of the Aitken mode particle concentration  $f_{non-vol, AIT}$  measured over the Atlantic south-west of Santiago (Spain) on 22 July 2004. The grey shaded area indicates the vertical dimension of the forest fire layer. The solid black line in the left panel marks  $Ri = 1$ , while the dashed black line marks  $Ri = 0.25$ .

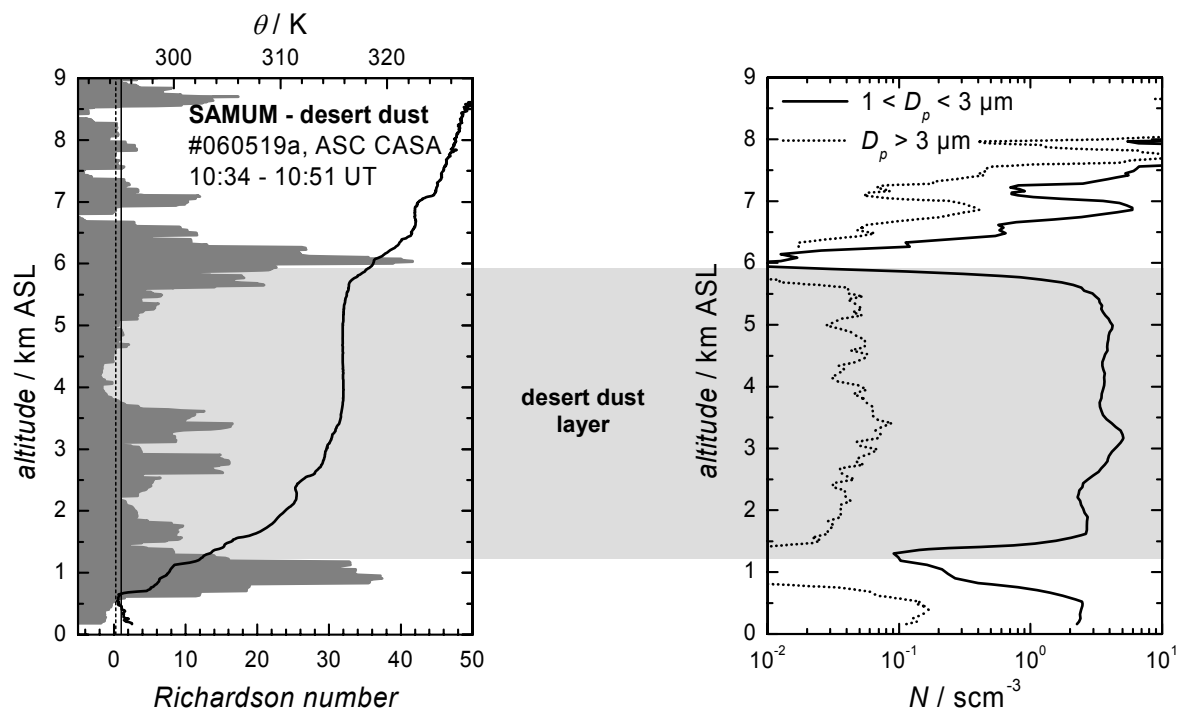


**Figure 85.** Same illustration as in Figure 84, but the profile was measured east of Casablanca/Morocco on 19 May 2006. Instead of  $f_{non-vol, AIT}$ , the particle concentration in the size range  $1 < D_p < 3 \mu m$  and  $D_p > 3 \mu m$  is shown. The grey shaded area indicates the vertical dimension of the desert dust layer.

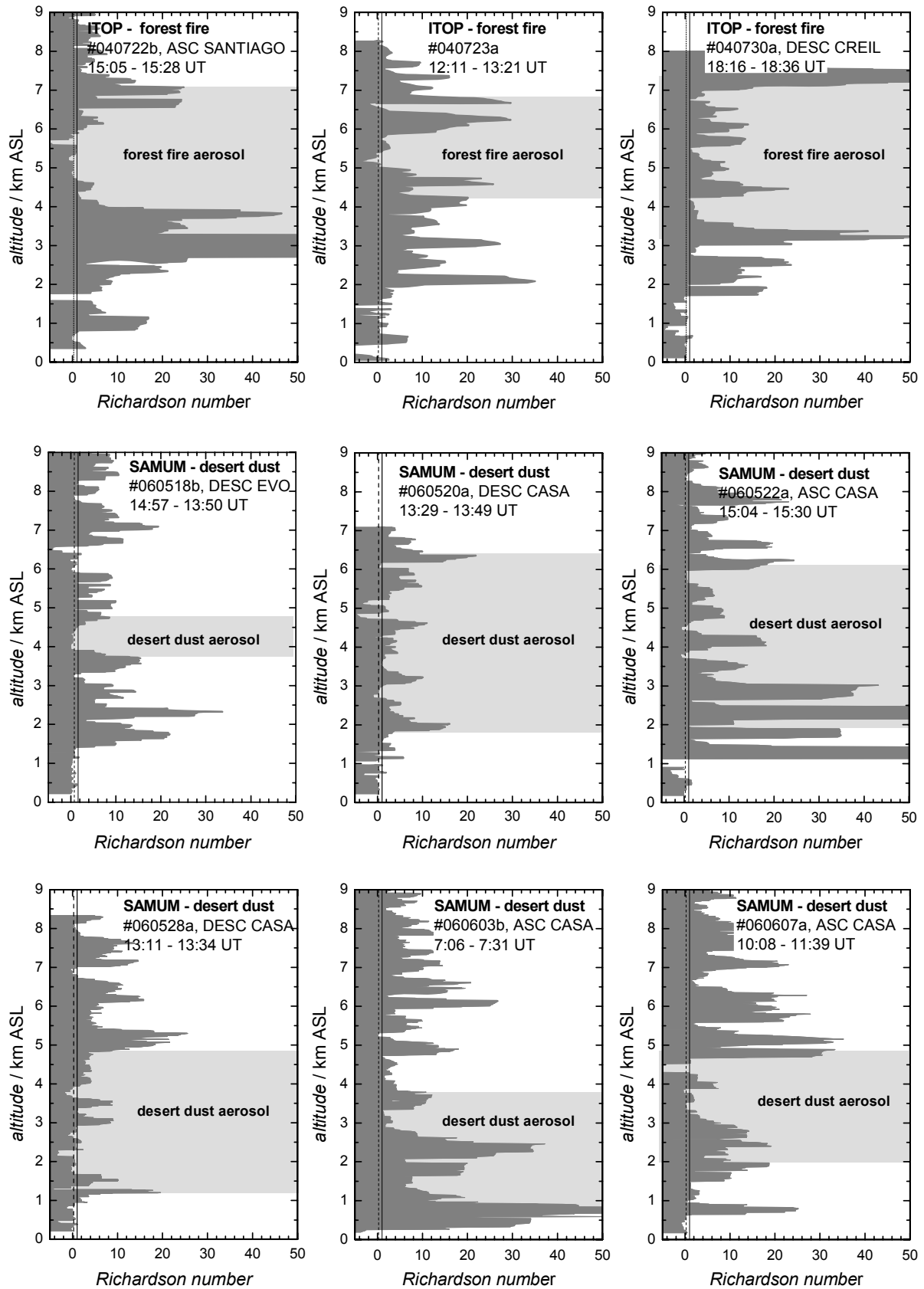


**Figure 86.** Vertical profiles of Richardson number for three ITOP and six SAMUM cases. In all cases the same vertical resolution was used. The grey shaded area indicates the vertical dimension of the aerosol layer. The solid black line in the left panel marks  $Ri = 1$ , while the dashed black line marks  $Ri = 0.25$ .

The described processes in the aerosol layer tend to stabilise the layer itself and to increase its lifetime. The inversion at the bottom of the layer is increased due to the interaction of the absorbing particles with the solar radiation, thus inhibiting the dilution of the layer from below. The heating in the layer destabilises the layer top, causing mixing of the plume top with free tropospheric background air thereby diluting the particle concentration in the upper part of the plume. Large scale-subsidence can counteract the turbulent encroachment. As the air descends, it is warmed adiabatically and typically a subsidence inversion will form. This inversion is a barrier to mixing. The changed aerosol distribution in the plume leads to a changed heating distribution with the maximum heating being in the lower part of the plume. This described stabilisation mechanism gives rise to the “sealed ageing” effect and the development of the aerosol within an almost “closed” system.

### 5.1.3 Wave breaking and mixing

The interior of the forest fire (desert dust) layer is characterised by low static stability and a  $Ri$  that falls below the critical value at some ranges. This indicates that turbulent mixing or wave breaking is taking place or already has taken place within the aerosol plumes. The high static stability at the bottom of the aerosol layer can facilitate the formation of waves (e.g. *Hauf and Clark, 1989*). Since the lofted forest fire (desert dust) plumes investigated in this work were found in the altitude range between approximately 3 and 9 km (1 and 6 km) ASL, slightly above the continental/marine boundary layer (Figure 53, p. 85; Figure 58, p. 92; Figure 72, p. 110), waves can be triggered for example by thermals or convection within the boundary layer (e.g. *Hauf and Clark, 1989*).

Wave breaking was not observed in the two cases (22 July 2004 and 19 May 2006) shown in Figure 84 and Figure 85, but in the aged dust layer over Portugal on 18 May 2006. Moreover, the aged dust layer over Portugal on 27 May 2006 evinced wave-like structures too (Figure 87). These two cases are discussed in more detail below.

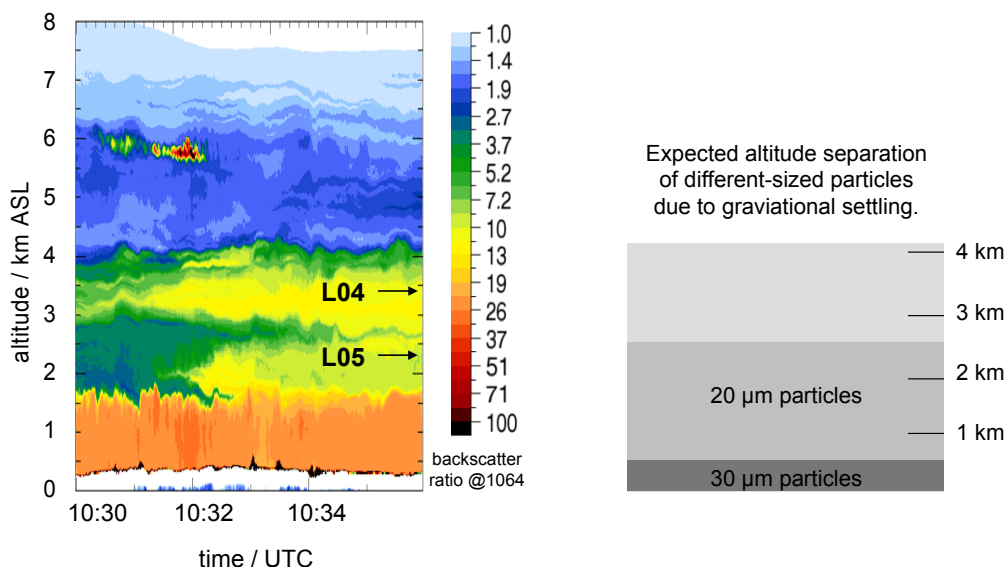


**Figure 87.** The dust layer over Evora on 27 May 2006. The HSRL backscatter ratio at 1064 nm (left panel) illustrates the wave-like structure in the dust layer. The arrows denoted with L04 and L05 mark the altitude in which the size distribution L04 and L05 were measured. The right panel sketches the expected separation of particles with different diameters due to gravitational settling during transport.

The dust layer of the 18 May 2006 showed a well-mixed layer of about 400 m depth (Figure 74, p. 112) and was enclosed by strong inversions. The analysis of the vertical  $Ri$  profile revealed values of 16 and 9 at the bottom and at the top of the plume, and values below the critical  $Ri$  within the well-mixed layer, indicating turbulence created by breaking waves. The examination of the vertical profile of horizontal wind speeds corroborates this hypothesis: within the dust layer the horizontal wind speed is variable, an evidence for the existence of turbulence. Furthermore, the vertical profile of the horizontal wind speed shows oscillations, which are characteristic for the presence of waves (Figure 88). During the second flight mission over Evora (Portugal) on 27 May 2006 the results of breaking waves may have been observed. Figure 87, (left panel) shows a HSRL cross-section of the atmosphere over Evora on that day. Wave like structures are evident in the HSRL cross-section. The black arrows indicate the altitudes in which the size distributions L04 and L05 (Figure 75, p. 113) were measured.

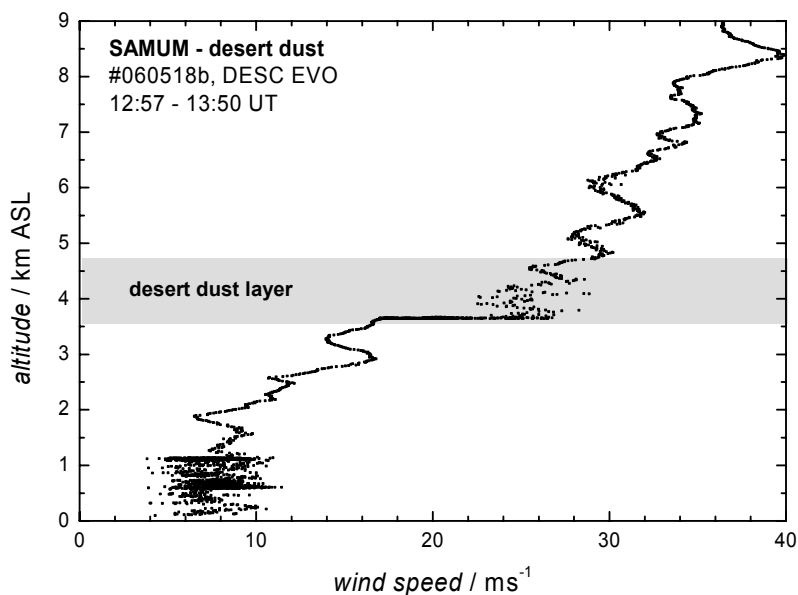


**Figure 88.** Vertical profile of horizontal wind speed over Evora on 18 May 2006. The grey shaded area indicates the vertical extent of the dust layer. The wind profile was recorded at the same time as the measurements shown in Figure 74.

As pointed out in Section 4.2.3, the size distributions L04 and L05 were almost identical in the size range  $D_p > \sim 0.5 \mu\text{m}$ . Moreover, the size distributions L04 and L05 were very similar to the size distributions found in about the same altitude close to the Sahara (Figure 75, p. 113, right panel), since particles of 20-30  $\mu\text{m}$  size were still detected. The measurements on 27 May are within the variance of the measurements close to the Sahara, although there is a tendency towards decreasing particle diameters due to settling. Assuming that the particles were initially homogeneously distributed in the dust layer as it was observed over the Sahara (see Figure 59, p. 94), a separation of particles sizes with altitude due to gravitational settling is expected during transport to Portugal. Larger particles are expected to settle faster than smaller particles do. Applying the theory of gravitational settling (see Equation 2.1) for non-spherical particles (shape factor 1.25), for example, particles with  $D_p \geq 30 \mu\text{m}$  should occur only in the lower 0.4 km, and particles with  $D_p \geq 20 \mu\text{m}$  should occur only below 2.5 km ASL after 2 days of transport from the Sahara. The expected separation of different-sized particles with altitude is sketched in the right panel of Figure 87. According to

gravitational settling, the size distribution measured at 3245 m (L04) ASL is expected to be different from the size distribution measured at 2300 m ASL (L05). However, as noted earlier, both size distributions are identical in the size range beyond 0.5  $\mu\text{m}$  (Figure 75, left panel). The wave-like structures obvious in the HSRL cross-section (Figure 87, left panel) indicate the presence of waves. If those waves had broken at some time, the related turbulence could have mixed the large particles into higher altitudes. In fact, a stability analysis of the  $Ri$  shows values  $< 1$  around 2.5 km and below 2.3 km altitude. Unfortunately, the lowest altitude in which in-situ measurements were taken was 2.1 km, so that no Falcon in-situ data are available in the lower part of the dust layer and underneath.

The presence of some large particles after transport is in accordance with findings by *Maring et al.* (2003a). They investigated the desert dust aerosol size distribution change during transport across the Atlantic and found that the normalized dust size distribution of particles smaller than 7.3  $\mu\text{m}$  over the Canary Islands and Puerto Rico were indistinguishable. They employed a simple empirical model setting the vertical velocity of dust equal to the Stokes gravitational settling. Assuming an upward velocity of  $\sim 0.33 \text{ cm s}^{-1}$  they could explain the presence of larger particles. They concluded that some atmospheric process(es) may partially counteract the gravitational settling, but they could not specify the responsible process(es). They hypothesised that buoyancy caused by solar heating of the dust and/or turbulence in the Saharan air layer could be important.

In this thesis it has been shown that at least in one or two cases turbulence created by breaking waves was observed within the dust layer over Portugal. It is suggested that this turbulence may have mixed larger particles into higher altitudes, therefore partly counteracting the gravitational settling.

## **5.2 Hypothesis II – Sealed ageing effect**

The second hypothesis stated in this work is a consequence of the self-stabilising effect: the lower boundary of the forest fire/desert dust layers is “sealed”, while the upper boundary of the layer is permeable. As a result the aerosol layer can be considered as being isolated from the underlying air mass and the aerosol is processed within an almost “closed” system.

### **5.2.1 Nucleation and Aitken mode**

The aged aerosol found in the lofted forest fire layers during ITOP 2004 was characterised by a missing nucleation mode and a depleted Aitken mode. Figure 89 depicts nine vertical profiles of particle size distributions on five days between 19 July and 31 July 2004. In seven profiles, forest fire layers were detected, on 19 July (Figure 89, first graph) and on 31 July (Figure 89, last graph) no forest fire plumes were observed. The forest fire plumes are marked by red circles. It is striking that the nucleation mode is completely missing in the lower part of the plumes and that the Aitken mode is depleted in any forest fire layer. A completely missing nucleation mode outside a forest fire plume is observed only during flight #040722a over the Atlantic in the unpolluted marine boundary layer due to missing sources for ultra-fine particles. The feature of a missing nucleation mode and a small Aitken mode in a long-range transported forest fire plume was not only observed during ITOP. In a recent study, *Treffeisen et al.* (2007) showed a suppression of nucleation and small Aitken mode particles within a smoke plume measured at Ny-Ålesund in May 2006.

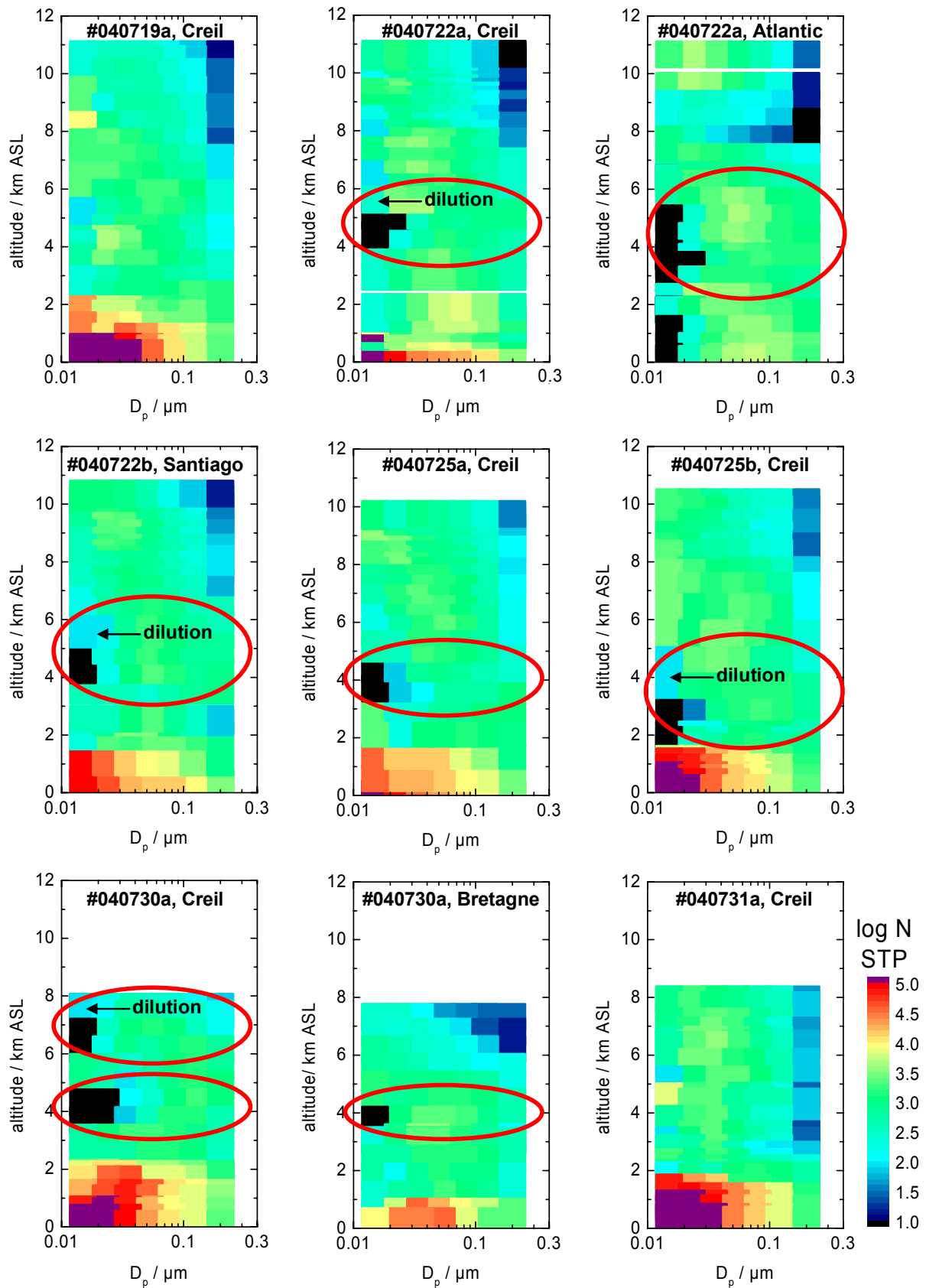


**Figure 89.** Vertical profiles of particle size distributions for STP conditions recorded on five days between 19 July and 31 July 2004. The particle number concentration  $N$  (unit:  $\text{scm}^{-3}$ ) is colour coded. In each plot the same scales were used. Forest fire layers are marked by red circles. On 19 and 31 July no forest fire layers were observed.

The profiles in Figure 89 additionally illustrate that entrainment – if present – takes place from the top to the bottom of the layer: on some days (e.g. #060522a, Creil), some nucleation mode particles, characteristic for free tropospheric air, are evident in the upper part of the forest fire plumes. This implies that some ambient air has entrained into the upper part of the plume and has diluted the plume top layer, in accordance with the self-stabilisation hypothesis.

In contrast to the forest fire layers which had ages of 4-13 days, the investigated desert dust layers had only ages of about 2 days, and in the case of the dust plume over Portugal on 18 May 2006, the age could not exactly be determined, but it was estimated to be 3-10 days. As both, the fresh pure dust layers and the aged plumes did not show nucleation mode particles (Figure 62, p. 97), another quantity has to be used to investigate the sealed ageing effect in the lofted dust plumes. The non-volatile fraction in the sub- $2.5\ \mu\text{m}$  range ( $f_{non-vol\ 2.5}$ ) may act as indicator to investigate the entrainment/non-entrainment of condensable gases or free tropospheric background aerosol into the layer. A decrease in  $f_{non-vol\ 2.5}$  during transport would indicate that some condensable gases or free tropospheric background aerosol have entrained into the layer. The direction of the entrainment into the layer (from the top or the bottom) can be assessed by investigating  $f_{non-vol\ 2.5}$  in the plume as a function of the distance from the plume top. The open diamonds in Figure 90 show  $f_{non-vol\ 2.5}$  in the plumes over Casablanca and Portugal as a function of the distance from the dust plume top. The black line in Figure 90 represents the average  $f_{non-vol\ 2.5}$  over the Sahara (see Table 12, p.101), and the grey shaded area marks the standard deviation of  $f_{non-vol\ 2.5}$  over the Sahara. Part of the values of  $f_{non-vol\ 2.5}$  found at Casablanca and Portugal are within the variance of the values of  $f_{non-vol\ 2.5}$  found at Ouarzazate and Zagora, especially those which are more than 1.5 km away from the plume top.

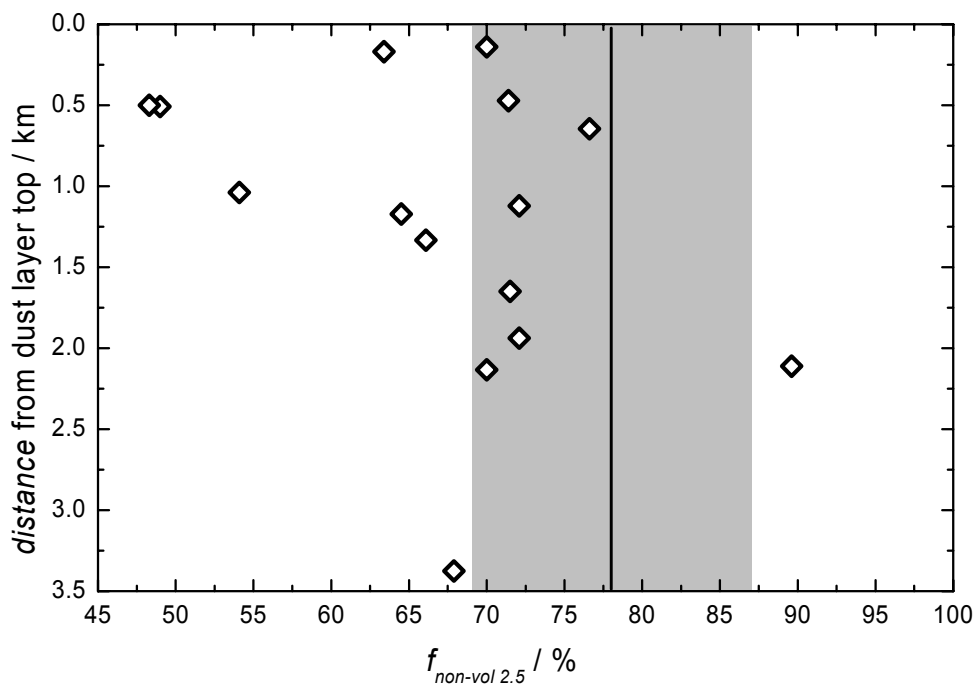


**Figure 90.** Non-volatile particle fraction in the sub- $2.5\ \mu\text{m}$  range ( $f_{non\ vol\ 2.5}$ ) within the plume as a function of the distance from the dust plume top (open diamonds) for dust layers over Casablanca and Portugal. The black line represents the average  $f_{non\ vol\ 2.5}$  over the Sahara (see Table 12, p.99), and the grey shaded area marks the standard deviation of  $f_{non\ vol\ 2.5}$  over the Sahara. See text.

Though, there is a tendency to a decreased non-volatile fraction. Generally, lower values of  $f_{non-vol\ 2.5}$  tend to occur in the upper part of the plumes close to the plume tops. A detailed investigation of the lower values of  $f_{non-vol\ 2.5}$  yielded that the lowest values of  $f_{non-vol\ 2.5}$  appeared at the top of the dust layer on 18 May 2006 over Portugal, which was the oldest investigated during SAMUM.

The findings of the missing nucleation mode and depleted Aitken mode in aged forest fire layers and the only slight decrease of  $f_{non-vol\ 2.5}$  in the aged dust layers indicate that the layers were prevented from rapid mixing with other airmasses and give rise to the sealed ageing hypothesis. The interpretation that the plumes are diluted from the top is supported by the findings shown in Figure 90 and Figure 89.

### 5.2.2 Accumulation mode

The aerosol processing within an almost “closed” system results in a characteristic development of the accumulation mode. This phenomenon can only be demonstrated for forest fire aerosol due the lack of data on aged (> 5 days) dust layers.

In general, the ageing of an aerosol up to 1-2 days is dominated by condensational growth, followed by coagulative growth. In a “closed system”, the suppressed entrainment of condensable gases from the surface inhibits particle nucleation and the formation of coated particles. Coagulation changes then the shape of the size distribution. *Fiebig et al.* (2003) applied the theory on particle ageing processes proposed in *Reid et al.* (1998) to reproduce the growth in the *CMD* of the accumulation mode in an aged (~6 days) forest fire layer. They calculated the change in accumulation mode parameters of the forest fire aerosol due to ageing by coagulation for various assumptions on initial conditions and dilution during transport. They could explain the observed size distribution by coagulation and concluded that the plume dilution was inhibited in the lower part of the plume, which is in accordance with the sealed ageing effect observed in this investigation during ITOP 2004 and SAMUM 2006.

After more than one week of transport, the size distribution differs significantly from the size distribution reported for fresh emissions from forest fires, and the modification of the size distribution is still active. *Dentener et al.* (2006) found a linear relation between the *CMD* and *GSD* of the accumulation mode for the ageing process of biomass aerosols. The data recorded during ITOP 2004 fit well into the picture of size distribution modification during atmospheric residence time. Figure 91 shows the correlation (dashed line) found by *Dentener et al.* (2006) together with data found during ITOP 2004 (brown symbols). In addition, data from *Fiebig et al.* (2003) and *Reid et al.* (2005a) for aged, and from *Martins et al.* (1996) for fresh forest fire aerosol are shown. The development of the accumulation mode in aged forest fire plumes can be explained under consideration of a sealed ageing effect: the absence of gaseous precursors inhibits particle nucleation. So self-coagulation is forced within the accumulation mode, which results in a narrowing of the size distribution, and an increase of the modal diameter in the accumulation mode. *Müller et al.* (2007) report similar observations in well-aged forest fire plumes. They observed an increase in effective diameters until an approximate plume age of 10-15 days. Afterwards, a steady state of the aerosol size distribution was reached.

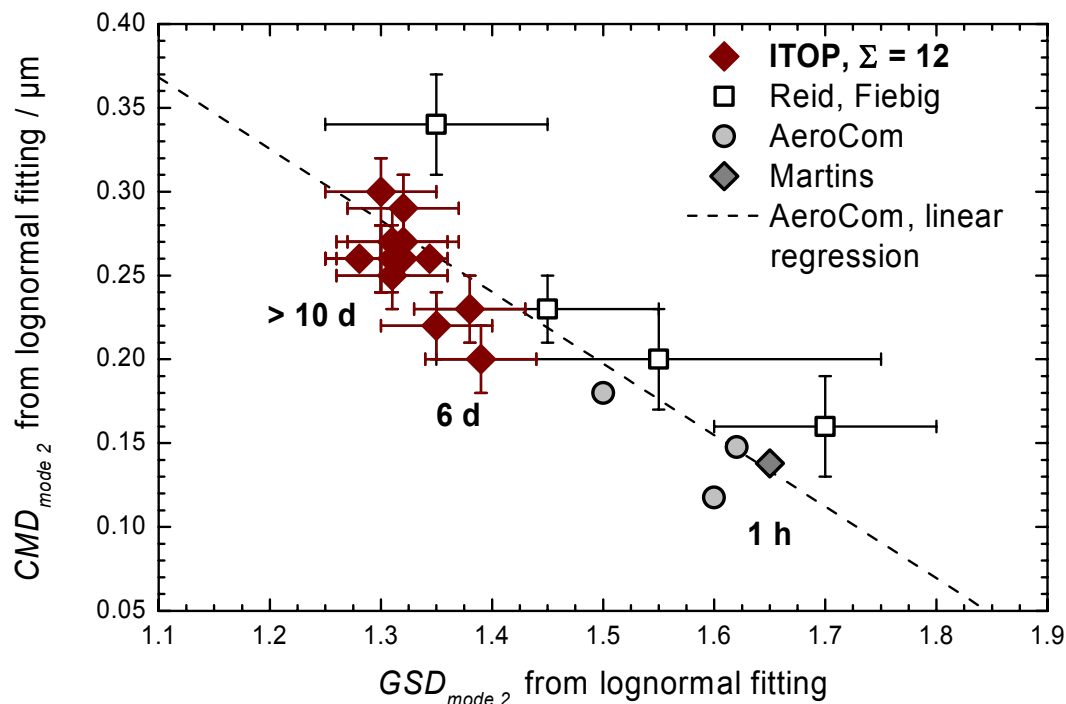


**Figure 91.** Count median diameter ( $CMD_{mode 2}$ ) of size distributions measured in boreal forest fires as a function of geometric standard deviation ( $GSD_{mode 2}$ ). The dashed line corresponds to the regression analysis for the AeroCom data set (Dentener et al., 2006). Further data are taken from Fiebig et al. (2003), Reid et al. (2005a) for aged and from Martins et al. (1996) for fresh forest fire aerosol. The brown symbols show data from the ITOP flights #040722a, #040722b, #040723a, #040725b, #040726a and #040730a.

The development of the nucleation, Aitken and accumulation mode during transport is the result of a sealed ageing effect. The sealed ageing is caused by the interaction of the absorbing particles with the solar radiation.

---

## 6 Summary and Outlook

---

In this study a large number of experimental data was analysed. The experimental data discussed in this work, originated from two major field experiments, the Intercontinental Transport of Ozone and Precursors (ITOP) study and the Saharan Mineral Dust Experiment (SAMUM) which were conducted in July/August 2004 and in May/June 2006, respectively. The data were used to investigate in detail the impact of plumes containing absorbing forest fire and desert dust aerosol particles on the atmospheric stability and the implications of a changed stability on the aerosol properties during long-range transport. For the first time at all, the well-known concept of the Richardson number  $Ri$  has been applied to assess the stability and mixing in forest fire and desert dust plumes. Also for the first time, the processes in forest fire and desert dust layers have been discussed from a common perspective. Based on the experimental data, two mechanisms, the **self-stabilising** and the **sealed ageing effect**, acting in both forest fire and desert dust aerosol layers were proposed to explain the characteristic vertical temperature structure as well as the aerosol properties observed in the lofted forest fire and desert dust plumes.

### 6.1 Summary of results

To investigate the existence of the two proposed mechanisms, a number of analyses had to be carried out with the experimental data of ITOP 2004 (forest fire) and SAMUM 2006 (desert dust), which are summarised below. High data quality of the experimental data was ensured by performing numerous calibration tests and sensitivity studies of the instrument response on assumptions that entered the data analysis.

#### **Identification of forest fire and dust sequences**

Altogether, 9 research flights were performed during ITOP and 17 during SAMUM. From these data, forest fire and desert dust encounters had to be identified. In the case of the ITOP measurements a combined approach of excess CO measurements, a tracer for forest fire and anthropogenic pollution, and FLEXPART back-trajectory calculations was used to identify forest fire sequences. The sequences were labelled as “pure forest fire”, when more than 80% of the filaments in the FLEXPART calculations originated from fires. In the case of the SAMUM measurements, the HSRL acted as pathfinder to direct the aircraft into the interesting dust layers so that the identification of dust sequences was much easier than that of the forest fire layers. Lofted forest fire and desert dust plumes were found on average at altitudes between 3-9 km and 1-6 km altitude, respectively. Lofted aerosol layers can arise for

example, when continental aerosol plumes are advected from land to sea over the marine boundary layer where they are forced to rise above the marine boundary layer. The formation of a lofted dust layer by this mechanism was documented on 3 June 2006. Other mechanisms for the formation of lofted aerosol plumes are pyro-convection and the uplift of pollution plumes by warm conveyor belts.

### **Size distributions**

Size distributions were calculated for about 90 encounters of forest fire, desert dust, mixed plumes, and of the free tropospheric background air. The size distributions were parameterised by multi-modal log-normal distributions. If the parameterisations do not reasonably fit the measured size distributions, large errors can be introduced in the calculation of optical parameters. Therefore, the quality of the parameterisations was controlled by comparing the effective diameter,  $D_{eff}$ , calculated directly from the inverted data and from the parameterisation using the Hatch-Choate conversion equations (see Equation 2.3, p. 22). In 91% of the SAMUM cases the deviation between parameterisation and data was smaller than 5%, and in 60% it was even smaller than 3%.

The analysis of the size distributions yielded typical properties for both, forest fire and desert dust plumes:

The forest fire plumes were characterised by the absence of a nucleation mode, a depleted Aitken mode and an enhanced accumulation mode. They further showed an average  $D_{eff}$  of  $0.34 \pm 0.1 \mu\text{m}$ , and  $D_{eff}$  increased with increasing atmospheric residence time as a result of ageing processes (coagulation). The modification of the forest fire size distribution fits well with a linear correlation between the *CMD* and *GSD* of the accumulation mode reported by *Dentener et al.* (2006) (Figure 91). Evidence for a top-down dilution was detected in the forest fire layers, because some nucleation mode particles, characteristic for free tropospheric air, were evident in the upper part of the some forest fire plumes.

The dust plumes investigated south of the Atlas revealed two main ranges of  $D_{eff}$ : the first range of  $D_{eff}$  peaked around  $5 \mu\text{m}$  and the second range of  $D_{eff}$  around  $8 \mu\text{m}$ . The different ranges of  $D_{eff}$  are probably the result of different dust mobilisation mechanisms. In total, an average  $D_{eff}$  of  $6.3 \pm 2.4 \mu\text{m}$  ( $6.5 \pm 2.5 \mu\text{m}$ ) was found in dust layers south and north (only south) of the Atlas Mountains. However, the two ranges of  $D_{eff}$  found during SAMUM suggest that it may be inadequate to use an average effective diameter for a typical dust size distribution. The  $D_{eff}$  found in the dust layer over Portugal on 27 May 2006 is within the variance of  $D_{eff}$  over the source, but there is a tendency to a decreased  $D_{eff}$  during transport due to ageing processes (gravitational settling of large particles). The smallest  $D_{eff}$  occurred in the dust layer over Portugal on 18 May 2006, which was the “oldest” dust layer (age: 3-10 days) investigated.

### **Mixing state**

In volatility analyses, information on the mixing state of the aerosol was gathered, which has to be known for the calculation of optical parameters. During ITOP, the non-volatile fraction was measured in three size regions, whereas during SAMUM the non-volatile size distribution was measured in the size range below  $2.5 \mu\text{m}$ .

The volatility analyses revealed that within forest fire plumes more than 80 % of the particles in the Aitken mode and approximately all particles in the accumulation mode have a solid core, which can be attributed to the presence of BC.

The volatility analyses of desert dust aerosol evinced two zones with different particle mixing states and refractive index (Figure 63): particles in zone 1 ( $D_p < 0.5 \mu\text{m}$ ) have a non-volatile core and are coated with ammonium sulphate, while particles in zone 2 ( $D_p > 0.5 \mu\text{m}$ ) consist of non-volatile components and contain absorbing material. Images from a scanning electron microscope confirm the particle morphology inferred from the volatility analyses. The non-volatile fraction of particles  $D_p \leq 2.5 \mu\text{m}$  ( $f_{non-vol\ 2.5}$ ) ranges around  $78 \pm 9\%$ ,  $70 \pm 9\%$ , and  $58 \pm 11\%$  over the Sahara, over Casablanca and over Portugal, respectively. The tendency to a decreased non-volatile fraction far away from the source is obvious. The lowest values of  $f_{non-vol\ 2.5}$  were mainly observed at the plume tops. This indicates that dilution – if present – is taking place from the top down to the bottom of the plume.

### **Optical properties**

The parameterised size distributions served together with the volatility analyses and absorption data as basis for the calculation of optical parameters, which are required for the calculation of heating rates. The validity of the calculated optical parameters was compared with lidar measurements, with values given in the literature, and in the case of dust particles with aspherical calculations.

In the case of the forest fire layer on 22 and 23 July 2004, the calculated *AOD* ( $0.15 \pm 0.02$  and  $0.13 \pm 0.02$ , respectively) was in a similar range as measured by the SARTA lidar ( $0.1-0.15$ ) in a forest fire plume south of Paris on 23 July 2004 (*Real et al.*, 2007). The derived single-scattering albedo of 0.85 (0.92) at 550 nm for the lower (upper) part of the forest fire layer is consistent with values of single-scattering albedo of 0.83-0.9 reported for boreal forest fires (*Reid et al.*, 2005b).

For the SAMUM measurements, the calculated extinction coefficient could be compared with direct measurements of the extinction coefficient (Figure 77). For 15 (4) cases the HSRL (IfT-lidar) measurements and the calculated extinction coefficients were compared. In 53% of the comparisons, the deviation between HSRL extinction coefficient and calculated extinction coefficient was smaller than 15%. The deviation between lidar and in-situ measurements was larger close to the plume top than well within the plume, which may be a consequence of the fact that the lidar data analysis averages over a particular vertical distance, therefore slightly smoothing the sharp upper edge of the dust layer. Considering the time off-set of about one hour between the HSRL and the in-situ measurements and the assumed spherical particle shape in the calculations, both methods are generally in good agreement.

### **Stability analyses**

Based on the observations in forest fire and desert dust plumes, two hypotheses were stated. The examination of the stated hypotheses required the calculation of vertical profiles of meteorological parameters, like potential temperature, humidity, wind direction and speed, and Richardson number *Ri*. All lofted forest fire (desert dust) plumes investigated in this work showed a potential temperature profile, which proved to be characteristic. Three regions of different static stability could be identified in the observations: the aerosol layers were

separated from the underlying airmass by a strong inversion. Within the aerosol plume more neutral to weakly stable conditions were observed, and the plumes were topped by a strong inversion. In forest fire (desert dust) plumes, an average lapse rate of  $8.6$  ( $9.8$ )  $\text{K km}^{-1}$ ,  $1.9$  ( $1.0$ )  $\text{K km}^{-1}$  and  $6.0$  ( $7.0$ )  $\text{K km}^{-1}$  was observed at the bottom, within and at the top of the layer, respectively. For comparison, outside the forest fire (desert dust) plumes, on average a lapse rate of  $3.7 \pm 0.6$  ( $3.3 \pm 0.5$ )  $\text{K km}^{-1}$  was measured. This fits very well with the lapse rate of  $3.5 \text{ K km}^{-1}$  assumed in the standard atmosphere. The inversion which capped the plume tended to be smaller than inversion at bottom of the plume. The static stability of the forest fire (desert dust) layers and the mixing was assessed in more detail, based on analyses of vertical  $Ri$  profiles. In about 67% (47%) of the forest fire (desert dust) layers,  $Ri$  was higher at the bottom of the layers than at the top, in about 11% (33%) of the forest fire (desert dust) layers showed similar ( $\pm 10\%$ )  $Ri$  at the bottom and at the top of the plume and in 22% (20%) of the forest fire (desert dust) layers  $Ri$  at the top exceeds  $Ri$  at the bottom. In the forest fire plumes, a larger  $Ri$  at the top compared to the bottom tended to occur in the “younger” forest fire plumes (e.g. #040730a). A higher percentage of dust layers compared to forest fire layers exhibited similar or even larger values of  $Ri$  at the top than at the bottom of the layer. One explanation for this might be that the dust layers are “younger” ( $< 5$  days) than the forest fire layers (4-13 days). Due to the proposed self-stabilisation, the inversion at the bottom is expected to strengthen with the extended atmospheric residence time.

### **Heating rates**

The characteristic lapse rate in the forest fire and desert dust plumes was evaluated with aid of radiative transfer calculations with libRadtran. The calculated optical properties and the direct extinction measurements served as basis for the computation of heating rates with libRadtran. For the forest fire plumes no vertical extinction measurements were available, therefore an extinction profile was derived from the optical calculations. In contrast, extinction was measured directly with the HSRL during SAMUM and the heating rates were calculated from these measurements. Asymmetry parameter and single-scattering albedo values were taken from the optical calculations. The daily mean heating rates in the forest fire (desert dust) plumes showed maximum values of  $\sim 0.2 \text{ K day}^{-1}$  ( $\sim 0.24 \text{ K day}^{-1}$ ). The calculation of heating rates yielded an increasing heating rate at the bottom of the plumes, while it decreased towards the plume top. This behaviour tends to increase the atmospheric stability in the lower part of the plumes and to decrease the stability in the upper part of the plumes and is in agreement with the stability analyses.

### **Self-stabilisation**

On the basis of experimental data and radiative transfer calculations it could be shown that the interaction of absorbing particles with the solar radiation drives several processes in the aerosol plumes: the aerosol absorption causes a heating which strengthens the inversion at the bottom of the aerosol layer, thus inhibiting the dilution from below and trapping the particles in the layer. In contrast, the heating destabilises the layer near the top. If the heating within the layer continues long enough, the temperature in the interface layer will exceed the temperature of the overlying air and entrainment is taking place from above. The presence of any large-scale subsidence counteracts the turbulent encroachment. In the regions where the lofted aerosol plumes were observed during ITOP and SAMUM, large-scale subsidence could

be accounted for by the presence of a subtropical high pressure system. As a consequence of the proposed self-stabilisation, the lifetime of the aerosol layer is extended and the layer can be transported over long distances.

The very stable stratification at the bottom of the plumes may facilitate the formation of waves. Breaking waves were observed during the measurements in a dust layer on 18 May 2007 over Portugal. The turbulence created by breaking waves might be an explanation for the presence of large particles with  $D_p \approx 20\text{-}30 \mu\text{m}$  over Portugal on 27 May 2007, which should have settled due to gravitation. It is suggested that the turbulence created by breaking waves may mix larger particles into higher altitudes, therefore partly counteracting the gravitational settling.

### ***Sealed ageing effect***

The self-stabilisation mechanism gives rise to the “sealed ageing” effect and the processing of the aerosol within an almost “closed” system. The experimental data revealed the absence of a nucleation mode and depleted Aitken mode in aged forest fire layers and a slight decrease of  $f_{non-vol\ 2.5}$  in the aged dust layers. The lower values of  $f_{non-vol\ 2.5}$  tended to occur in the upper part of the dust plumes close to the plume tops, indicating some dilution from the top. Generally, the observed aerosol properties indicated that the forest fire and desert dust layers were prevented from rapid mixing with other airmasses. Moreover, the development of the accumulation mode in aged forest fire plumes with time (increasing  $CMD$ , narrowing of the mode) can be explained with the sealed ageing effect: the sealing of the layer inhibits entrainment of condensable gases from below. As a result, there is a missing supply of nucleation/Aitken mode particles, which can coagulate to Aitken and accumulation mode particles. Therefore, self-coagulation is forced within the accumulation mode which leads to a narrowing of the size distribution with time (Figure 91). Moreover, the stratification of the plume inhibits/decelerates the formation of coated particles and has therefore an impact on the radiative effects of the forest fire and desert dust particles.

## **6.2 Open scientific questions**

The analyses performed in this work showed evidence for a self-stabilisation and a sealed ageing of forest fire and desert dust layers. From this work a number of scientific questions arise:

### ***Presence of large particles after several days of transport***

The investigated forest layers exhibited ages of 4-13 days, the investigated dust layers were mainly younger than 2 days due to the lack of data on older dust plumes. It would be interesting to investigate dust layers older than 2 days to see if the sealed ageing mechanism leads to a depleted Aitken mode and an enhanced accumulation mode as it has been observed in forest fire layers. Moreover, a larger number of measurements in aged dust layers is necessary to investigate the presence of large particles after several days of transport.

### ***Impact of dust feedback on boundary layer dynamics over the Sahara***

The dust layers over Ouarzazate and Zagora extended from the surface to altitudes of more than 5.5 km above ground level and in the afternoon the top of the dust layer coincided with the top of the well-mixed boundary layer. One question arising from the presence of these deep boundary layers is: Does the interaction of the dust feedback on boundary layer dynamics and cause a deeper boundary layer over the Sahara? A possible impact of desert dust on the boundary layer height could be investigated using the measured dust properties and the EULAG (Eulerian/LAGrangian) model.

### ***Impact of stabilisation on dynamical processes***

The presence of absorbing aerosol layers with their characteristic lapse rates in the lower troposphere has clearly a stabilising effect on the atmosphere. The lofted forest fire (desert dust) plumes investigated in this work were found in the altitude range between approximately 3-9 km (1-6 km) ASL. All layers investigated here showed large static stability at the lower boundary of the layer. The lower boundaries of the forest fire and desert dust plumes fall into an altitude range, which is important for dynamical processes like convection and the formation of thunderstorms. The ITOP and SAMUM data could be used to investigate the impact of the lofted forest fire and desert dust layers on the formation of thunderstorms and convection. Moreover, further impacts on atmospheric dynamics, caused by the presence of lofted forest fire and desert dust plumes could be investigated. These questions can not be addressed by experimental data only. It requires a modelling study, e.g. with a numerical weather prediction model, in which the changed static stability is implemented in the dynamic evolution of the atmosphere is investigated.

### ***Assessment of the proposed self-stabilisation mechanism with a numerical model***

The proposed self-stabilisation mechanism is a possible scenario to explain the observed temperature profile and the aerosol properties in the forest fire and desert dust plumes. The scenario has been formulated on the basis of the measurements. Therefore, it would be good to simulate the proposed mechanism with a numerical model. These simulations would allow the quantification of the details of the scenario such as the details of the entrainment process. Furthermore, the rate of subsidence necessary to suppress turbulent encroachment, and the lifetime of the plumes with and without the presence of large-scale subsidence could be quantified. These simulations are beyond the scope of this thesis.

### ***Mixing of biomass burning and desert dust aerosol***

Dust is exported across the Atlantic Ocean all over the year. Figure 1 illustrated that the main transport route on which dust is exported across the Atlantic coincides with the outflow of biomass burning aerosol from central Africa. Biomass burning aerosol has a strong accumulation mode ( $D_p < 1 \mu\text{m}$ ) and is an absorbing aerosol, while desert dust aerosol has a strong coarse mode ( $D_p \gg 1 \mu\text{m}$ ) and is an absorbing aerosol (Figure 92). What happens, when both aerosol types mix? Are both aerosol types really mixed or are they just layered?

Most of the arising questions can not yet be answered with the present data set and some of them need the involvement of numerical models. However, some of the questions will be

addressed by another field experiment, SAMUM II, which will take place in January/February 2008 on the Cape Verde islands. SAMUM II focuses on the mixing of biomass burning and desert dust aerosol and the transformation of desert dust during long-range transport across the Atlantic Ocean. The same, or even extended instrumentation is used as during SAMUM I. Therefore, a good comparability of the data can be expected.

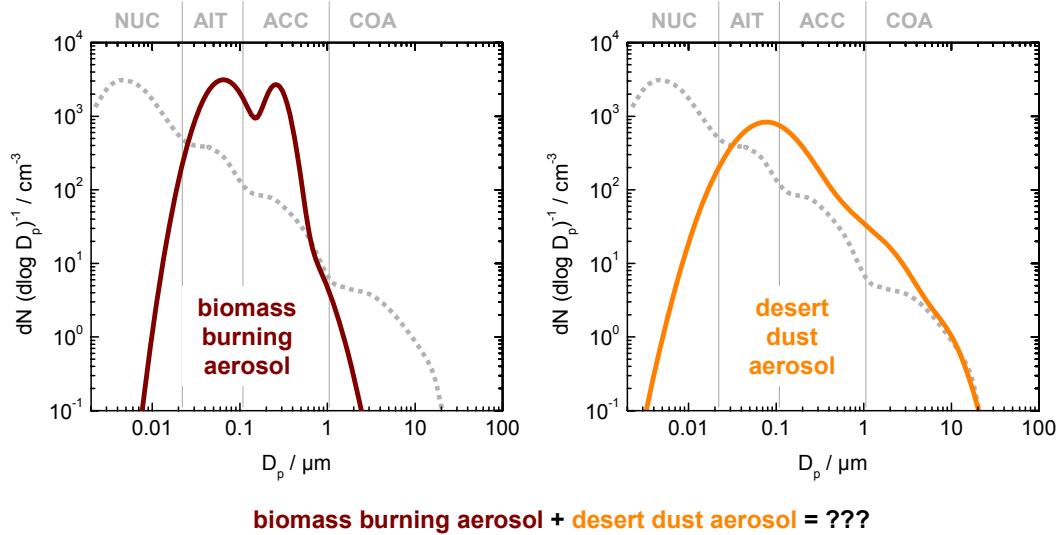


**Figure 92.** Characteristic size distribution (parameterisations are taken from this study) of an aged biomass burning aerosol (left panel) and a pure desert dust aerosol (right panel). How will the size distribution of a mixed biomass burning – desert dust aerosol look like?

The findings of this thesis demonstrate that it is very important to investigate both, the thermodynamic structure together with the aerosol properties. Therefore, the SAMUM II instrumentation will also include drop sonde measurements. The use of an airborne lidar together with extended aerosol in-situ instrumentation has been proven a successful measurement strategy to get representative data of aerosol plumes and to cover all details of the aerosol plume structure.



---

## Acknowledgements

---

This thesis is the result of the research work performed between September 2004 and October 2007 at the Institut für Physik der Atmosphäre (IPA) at the DLR (Deutsches Zentrum für Luft- und Raumfahrt). During this time I have been accompanied and supported by many people. Therefore, I would like to take this opportunity to thank numerous persons for their help and support throughout the last three years.

First of all I want to thank my supervisor Prof. Dr. Andreas Petzold<sup>22</sup> for giving me the opportunity to carry out this research, for his excellent guidance during the last three years, and for introducing me to the international aerosol community. Furthermore, I am very grateful to my co-supervisor Prof. Dr. Olaf Krüger<sup>23</sup> for his interest and support, and for several constructive discussions about this thesis. I wish to acknowledge Prof. Dr. Ulrich Schumann<sup>22</sup>, director of the IPA, for the opportunity to work at the institute, for supporting my work, and for giving valuable advice on this thesis. I am also very grateful to Dr. Hans Schlager<sup>22</sup>, head of the department, for his excellent support, and for providing the trace gas measurements.

My special thanks go to Dr. Heidi Huntrieser<sup>22</sup> for many inspiring discussions, for her perceptive critique of this thesis, and for providing the excess CO data. I am very grateful to Ulrich Hamann<sup>22</sup> for performing the radiative transfer calculations on the basis of the aerosol microphysical and optical properties, and for many fruitful discussions. I would like to thank Dr. Markus Fiebig<sup>24</sup> for providing the aerosol optical model/inversion algorithm and for helping me getting started with laboratory work and with the aerosol instruments. Many thanks due to Dr. Andreas Minikin<sup>22</sup> for his helpful comments on drafts of this work, for introducing me to the secrets of database systems, HTML and Origin programming. This thesis benefited much from the good and straightforward collaboration with Michael Esselborn<sup>22</sup> and Katharina Rasp<sup>22</sup>, who provided essential High Spectral Resolution Lidar data and refractive index data, respectively. Very helpful was the technical support by Hans Rüba<sup>22</sup>, Hans Sedlmeir<sup>22</sup>, Hans Krafczyk<sup>22</sup>, and the support of Jan Haßelbach<sup>22</sup> during instrument calibration and preparation for SAMUM. Thanks are due to Dr. Andreas Dörnbrack<sup>22</sup>, Dr. Waldemar Krebs<sup>22</sup>, and Dr. Hermann Mannstein<sup>22</sup> for preparing ECMWF charts and Meteosat scenes on which I based the weather forecasts during SAMUM.

---

<sup>22</sup> DLR

<sup>23</sup> Meteorological Institute, University of Munich

<sup>24</sup> DLR/Norwegian Institute for Air Research (NILU), Kjeller

Furthermore, I want to thank Dr. Andreas Dörnbrack<sup>22</sup> for helping with his expertise on atmospheric dynamics. I am very grateful to Prof. Dr. Roger Smith<sup>23</sup> for the invitation to the meteorological seminar, which resulted in several very fruitful discussions, and for help with English expressions. I thank Yvonne Fliecker<sup>22</sup> for her assistance with some of the sensitivity tests of the inversion algorithm.

The valuable contributions of lidar data by Matthias Tesche<sup>25</sup> and Dr. Detlef Müller<sup>25</sup>, chemical analysis data by Dr. Konrad Kandler<sup>26</sup>, ground-based dust data by Dr. Lothar Schütz<sup>27</sup>, Dr. Thomas Müller<sup>25</sup> and Alexander Schladitz<sup>25</sup>, FLEXPART trajectory calculations by Dr. Andreas Stohl<sup>28</sup>, LAGRANTO trajectory calculations by Thomas Hamburger<sup>22</sup> and Katharina Rasp<sup>22</sup>, dust optical properties from aspherical calculations by Josef Gasteiger<sup>23</sup>, LM-Muscat simulations of the dust event on 19 and 27 May 2006 by Dr. Ina Tegen<sup>25</sup> and Bernd Heinold<sup>25</sup>, the supply of ECHAM simulations by Christian Kurz and the supply of MISR scenes by Ralph Kahn<sup>29</sup> were very welcome.

I am grateful to the participants of the ITOP and SAMUM field experiments from DLR: Dr. Reinhold Busen, Dr. Volker Dreiling, Dr. Gerhard Ehret, Michael Esselborn, Philipp Feldpausch, Dr. Markus Fiebig, Heinz Finkenzeller, Dr. Andreas Fix, Christian Hinz, Dr. Heidi Huntrieser, Christoph Kiemle, Michael Lichtenstern, Wolfgang Meier, Dr. Andreas Petzold, Anke Roiger, Hans Rüba, Dr. Hans Schlager, Paul Stock, Gerd Uhlemann, Dr. Martin Wirth, Alexander Wolf, and Dr. Martin Zöger. A big “thank you” is due to the pilots Steffen Gemsa, Stefan Grillenbeck, Michael Großrubatscher and Roland Welser for the wonderful research flights. This thesis would be incomplete without special thanks to Özkan Bayro<sup>30</sup>, Winfried Beer<sup>22</sup>, Helmut Löffler<sup>22</sup> and Karl-Ernst Müller<sup>22</sup> for the excellent IT support.

Many thanks go to all my colleagues at the IPA for the good cooperation and the pleasant working atmosphere.

Finally, I want to thank my parents, my brother and Gernot for their constant support, their understanding, encouragement and their love when it was most required.

This work was mainly funded by the German Research Foundation (Deutsche Forschungsgemeinschaft) within the project SAMUM under Contract No. Pe 632/2-1. Significant contributions for Falcon operation from the European Space Agency and from the European EUFAR project DARPO are gratefully acknowledged.

---

<sup>25</sup> Institute for Tropospheric Research (IfT), Leipzig

<sup>26</sup> Environmental Mineralogy Group, Darmstadt University of Technology

<sup>27</sup> Institute for Atmospheric Physics, University of Mainz

<sup>28</sup> Norwegian Institute for Air Research (NILU), Kjeller

<sup>29</sup> Jet Propulsion Laboratory/Caltech, Pasadena, USA

<sup>30</sup> T-Systems

---

## List of abbreviations

---

Abbreviation	Definition
ACE	Aerosol Characterisation Experiment
AIT	Aitken mode
$\text{Al}_2\text{Si}_2\text{O}_5(\text{OH})_4$	kaolinite
AMMA	African Monsoon Multidisciplinary Analysis
ASC	ascent
ASL	above sea level
BC	black carbon
BL	boundary layer
CASA	Casablanca
$\text{CH}_4$	methane
CMD	count median diameter
CO	carbon monoxide
COA	coarse mode
CPC	Condensation Particle Counter
CPSA	Condensation Particle Size Analyser
DARPO	Desert Dust and Biomass Burning Aerosols over Portugal
DESC	descent
DLR	Deutsches Zentrum für Luft- und Raumfahrt
DMA	Differential Mobility Analyser
DMS	dimethyl sulphide
DS	Diffusion Screen Separator
ECMWF	European Centre for Medium-Range Weather Forecasts
EDGAR	Emission Database for Global Atmospheric Research
EUFAR	European Fleet for Airborne Research
EVO	Evora
$\text{Fe}_2\text{O}_3$	haematite
FF	forest fire
FSSP-100	Forward Scattering Spectrometer Probe, model 100
FSSP-300	Forward Scattering Spectrometer Probe, model 300
FT	free troposphere
FT	free troposphere
GSD	geometric standard deviation
$\text{H}_2\text{SO}_4$	sulphuric acid

---

<b>Abbreviation</b>	<b>Definition</b>
HSRL	High Spectral Resolution Lidar
ICARTT	International Consortium for Atmospheric Research on Transport and Transformation
ID	identifier
IFT	Institute for Tropospheric Research, Leipzig
IPCC	Intergovernmental Panel on Climate Change
IR	infrared
ITOP	Intercontinental Transport of Ozone and Precursors
LACE	Lindenberg Aerosol Characterisation Experiment
LAGRANTO	Lagrangian Analysis Tool
libRadtran	library for radiative transfer
Lij	layer ID of constant level sequence
MODIS	Moderate Resolution Imaging Spectroradiometer
n.d.	not determined
N <sub>2</sub> O	nitrous oxide
NASA	National Aeronautics and Space Administration
NH <sub>4</sub> ) <sub>2</sub> SO <sub>4</sub>	ammonium sulphate
NILU	Norwegian Institute for Air Research
NO	nitric oxide
NUC	nucleation mode
O <sub>3</sub>	ozone
OC	organic carbon
OP	Oberpfaffenhofen
OPC	Optical Particle Counter
OZT	Ouarzazate
PCASP-100X	Passive Cavity Aerosol Spectrometer Probe
PES	Potential Emission Sensitivity
PRIDE	Puerto Rico Dust Experiment
PSAP	Particle Soot Absorption Photometer
SAFARI	Southern African Regional Science Initiative
SAMUM	Saharan Mineral Dust Experiment
SHADE	Saharan Dust Experiment
SiO <sub>2</sub>	quartz
SO <sub>2</sub>	sulphur dioxide
STP	standard conditions (273.15 K, 1013.25 hPa)
TAS	true air speed
TD	Thermal Denuder
TOA	top of atmosphere
UT	Universal Time
ZGA	Zagora

---

## List of symbols

---

Symbol	Definition	Unit
$A$	PSAP sample spot area	$\text{cm}^{-2}$
$A_{meas}$	measured PSAP sample spot size	$\text{cm}^{-2}$
$AOD$	aerosol optical depth	dimensionless
$A_p$	cross-sectional area of a particle	$\text{m}^2$
$A_{PSAP}$	PSAP sample spot size indicated by the manufacturer	$\text{cm}^{-2}$
$C_{bound,i}$	scattering cross-section at the boundary between channel $i$ and channel $i+1$	$\text{m}^{-2}$
$C_c$	Cunningham factor	dimensionless
$C_{scat, instrument}$	instrument specific scattering cross-section	$\text{m}^{-2}$
$C_{scat/abs/ext}$	scattering/absorption/extinction cross-section	$\text{m}^{-2}$
$D_{aero}$	aerodynamic diameter	$\mu\text{m}$
$D_{eff}$	effective diameter	$\mu\text{m}$
$D_{eff}(data)$	effective diameter calculated from the measurements	$\mu\text{m}$
$D_{eff}(mode)$	effective diameter derived from the parameterised size distributions via the Hatch-Choate conversion equations	$\mu\text{m}$
$D_f$	single-fibre diameter	$\mu\text{m}$
$D_p$	particle diameter	$\mu\text{m}$
$D_{p,50\%}$	Kelvin diameter for 50% counting efficiency	$\mu\text{m}$
$(D_{qm})_p$	$p^{th}$ moment average of the $q^{th}$ moment distribution	
$D_{Stk}$	Stokes diameter	$\mu\text{m}$
$e$	charge of an electron	$1.6 \cdot 10^{-19} \text{ C}$
$E_D$	single-fibre efficiency for diffusion	dimensionless
$E_{DR}$	single-fibre efficiency for diffusion-interception interaction	dimensionless
$E_G$	single-fibre efficiency for settling	dimensionless
$E_I$	single-fibre efficiency for impaction	dimensionless
$E_q$	single-fibre efficiency for electrostatic attraction	dimensionless
$E_R$	single-fibre efficiency for interception	dimensionless
$E_\Sigma$	total single-fibre efficiency	dimensionless
$f_{flow}$	PSAP flow correction factor	dimensionless
$f_l$	volume fraction of chemical component	%

---

Symbol	Definition	Unit
$f_{non-vol\ 2.5}$	non-volatile volume fraction in the sub-2.5 $\mu\text{m}$ size range	%
$f_{non-vol\ ACC}$	fraction of non-volatile particles in the accumulation mode	%
$f_{non-vol\ AIT}$	fraction of non-volatile particles in the Aitken mode	%
$f_{NUC}$	fraction of nucleation mode particles	%
$f_{PM2.5/TSP}$	fine mode fraction	%
$f_{spot}$	PSAP spot size correction factor	dimensionless
$f_{STP}$	conversion factor between STP and ambient conditions	dimensionless
$g$	asymmetry parameter	dimensionless
$g_a$	acceleration of gravity	$\text{m s}^{-1}$
$I$	irradiance/intensity	$\text{W m}^{-2}$
$I_0$	incident irradiance/intensity	$\text{W m}^{-2}$
$I_t$	filter transmittance at time t	dimensionless
$k$	imaginary part of refractive index	dimensionless
$K_{1,2}$	PSAP correction factors	dimensionless
$m$	refractive index	dimensionless
$M_{fluid}$	molecular weight	$\text{g mol}^{-1}$
$n$	real part of refractive index	dimensionless
$N$	particle number concentration in the atmosphere	$\text{cm}^{-3}$
$n_e$	number of elementary units charges of charges $e$	dimensionless
$p$	pressure	hPa
$P$	overall filter penetration	dimensionless
$PM$	particulate mass	$\mu\text{g m}^{-3}$
$q_{aerosol/excess/sheath}$	monodisperse aerosol/sheath air/excess air flow through the DMA	$\text{cm}^3 \text{s}^{-1}$
$q_{default/calib}$	default/calibrated flow rate through the CPC	$\text{cm}^3 \text{s}^{-1}$
$Q_{scat/abs/ext}$	scattering/absorption/extinction efficiency	dimensionless
$R$	gas constant	$8.31 \text{ N m K}^{-1} \text{ mol}^{-1}$
$RH$	relative humidity	%
$Ri$	Richardson number	dimensionless
$S$	saturation ratio	dimensionless
$T$	temperature	K
$t_f$	thickness of the filter or mesh	mm
$t_{pulse}$	CPC pulse width	s
$TSP$	total suspended particulate mass	$\mu\text{g m}^{-3}$
$V$	volume of air	$\text{m}^{-3}$
$v_{TS}$	terminal settling velocity	$\text{m s}^{-1}$
$x$	size parameter for light scattering	dimensionless
$Z$	electrical mobility	$\text{m}^2 (\text{V s})^{-1}$
$\alpha(D_p, n_e = 1)$	fraction of single charged particles	dimensionless
$\alpha_s$	solidity volume fraction of the filter material	dimensionless
$\Delta CO$	excess CO	$\text{nmol mol}^{-1}$

<b>Symbol</b>	<b>Definition</b>	<b>Unit</b>
$\Delta F$	radiative forcing	$\text{W m}^{-2}$
$\eta$	viscosity	$\text{kg (m s)}^{-1}$
$\Theta$	potential temperature	K
$\theta_s$	scattering angle	°
$\lambda$	wavelength	nm
$\rho$	density of gas; density of particle	$\text{g cm}^{-3}$ ; $\text{kg m}^{-3}$
$\sigma_0$	uncorrected PSAP absorption coefficient	$\text{Mm}^{-1}$ ; $\text{km}^{-1}$
$\sigma_{adj}$	absorption coefficient calculated from the PSAP before scattering correction	$\text{Mm}^{-1}$ ; $\text{km}^{-1}$
$\sigma_{fluid}$	surface tension	$\text{N m}^{-1}$
$\sigma_{PSAPout}$	absorption coefficient calculated from the PSAP before flow, spot size, and scattering correction	$\text{Mm}^{-1}$ ; $\text{km}^{-1}$
$\sigma_{scat/abs/ext}$	total scattering/absorption/extinction coefficient, including contributions from gases and particles	$\text{Mm}^{-1}$ ; $\text{km}^{-1}$
$\sigma_{sgas/agas/egas}$	gas scattering/absorption/extinction coefficient	$\text{Mm}^{-1}$ ; $\text{km}^{-1}$
$\sigma_{sp/ap/ep}$	particle scattering/absorption/extinction coefficient	$\text{Mm}^{-1}$ ; $\text{km}^{-1}$
$\chi$	dynamic shape factor	dimensionless
$\omega_0$	single-scattering albedo	dimensionless



---

## References

---

- Ackerman, A. S., O. B. Toon, D. E. Stevens, A. J. Heymsfield, V. Ramanathan, and E. J. Welton, 2000: Reduction of Tropical Cloudiness by Soot. *Science*, **288**, 1042-1047.
- Ackerman, T. P., and O. B. Toon, 1981: Absorption of visible radiation in atmosphere containing mixtures of absorbing and nonabsorbing particles. *Appl. Opt.*, **20**, 3661-3668.
- Albrecht, B. A., 1989: Aerosols, Cloud Microphysics, and Fractional Cloudiness. *Science*, **245**, 1227-1230.
- Alpert, P., Y. J. Kaufman, Y. Shay-El, D. Tanre, A. Da Silva, S. Schubert, and J. H. Joseph, 1998: Quantification of dust-forced heating of the lower troposphere. *Nature*, **395**, 367-370.
- Andreae, M. O., 2007: Aerosols before pollution. *Science*, **315**, 50-51.
- Andreae, M. O., and A. Gelencsér, 2006: Black carbon or brown carbon? The nature of light-absorbing carbonaceous aerosols. *Atmos. Chem. Phys.*, **6**, 3131-3148.
- Andreae, M. O., D. Rosenfeld, P. Artaxo, A. A. Costa, G. P. Frank, K. M. Longo, and M. A. F. Silva-Dias, 2004: Smoking Rain Clouds over the Amazon. *Science*, **303**, 1337-1342.
- Angevine, W. M., M. Trainer, S. A. McKeen, and C. M. Berkowitz, 1996: Mesoscale meteorology of the New England coast, Gulf of Maine, and Nova Scotia: Overview. *J. Geophys. Res.*, **101**, 28893-28902.
- Ansmann, A., F. Wagner, D. Althausen, D. Müller, A. Herber, and U. Wandinger, 2001: European pollution outbreaks during ACE 2: Lofted aerosol plumes observed with Raman lidar at the Portuguese coast. *J. Geophys. Res.*, **106**, 20725-20734.
- Ansmann, A., I. Mattis, D. Müller, U. Wandinger, M. Radlach, D. Althausen, and R. Damoah, 2005: Ice formation in Saharan dust over central Europe observed with temperature/humidity/aerosol Raman lidar. *J. Geophys. Res.*, **110**, 1-12.
- Arakawa, E. T., P. S. Tuminello, B. N. Khare, M. E. Millham, S. Authier, and J. Pierce, 1997: *Measurement of Optical Properties of Small Particles*. Oak Ridge National Lab, 30 pp.
- Arnott, W. P., H. Moosmüller, P. J. Sheridan, J. A. Ogren, R. Raspert, W. V. Slaton, J. L. Hand, S. M. Kreidenweis, and J. L. J. Collett, 2003: Photoacoustic and filter-based ambient aerosol light absorption measurements: Instrument comparisons and the role of relative humidity. *J. Geophys. Res.*, **108**, 4034.
- Banse, D. F., K. Esfeld, M. Hermann, B. Sierau, and A. Wiedensohler, 2001: Particle counting efficiency of the TSI CPC 3762 for different operating parameters. *J. Aerosol Sci.*, **32**, 157-161.
- Bauer, S. E., M. I. Mishchenko, A. A. Lacis, S. Zhang, J. Perlwitz, and S. M. Metzger, 2007: Do sulfate and nitrate coatings on mineral dust have important effects on radiative properties and climate modeling? *J. Geophys. Res.*, **112**, D06307.
- Baumgardner, D., J. E. Dye, B. W. Gandrud, and R. G. Knollenberg, 1992: Interpretation of measurements made by the forward scattering spectrometer probe (FSSP-300) during the Airborne Arctic Stratospheric Expedition. *J. Geophys. Res.*, **97**, 8035-8046.

- Bethan, S., G. Vaughan, C. Gerbig, A. Volz-Thomas, H. Richer, and D. A. Tiddeman, 1998: Chemical air mass differences near fronts. *J. Geophys. Res.*, **103**, 13413-13434.
- Bohren, C. F., and D. R. Huffman, 1983: *Absorption and Scattering of Light by Small Particles*. John Wiley & Sons, Inc, 544 pp.
- Bond, T. C., and R. W. Bergstrom, 2006: Light Absorption by Carbonaceous Particles: An Investigative Review. *Aerosol Sci. Technol.*, **40**, 27-67.
- Bond, T. C., T. L. Anderson, and D. Campbell, 1999: Calibration and Intercomparison of Filter-Based Measurements of Visible Light Absorption by Aerosols. *Aerosol Sci. Technol.*, **30**, 582-600.
- Borrmann, S., B. Luo, and M. Mishchenko, 2000: Application of the T-matrix method to the measurement of aspherical (ellipsoidal) particles with forward scattering optical particle counters. *J. Aerosol Sci.*, **31**, 789-799.
- Brock, C. A., F. Schröder, B. Kärcher, A. Petzold, R. Busen, and M. Fiebig, 2000: Ultrafine particle size distributions measured in aircraft exhaust plumes. *J. Geophys. Res.*, **105**, 26555-26568.
- Browning, K. A., and N. M. Roberts, 1994: Structure of a frontal cyclone. *Q. J. R. Meteorol. Soc.*, **120**, 1535-1557.
- Burtscher, H., U. Baltensperger, N. Bukowiecki, P. Cohn, C. Hüglin, M. Mohr, U. Matter, S. Nyeki, V. Schmatloch, N. Streit, and E. Weingartner, 2001: Separation of volatile and non-volatile aerosol fractions by thermodesorption: Instrumental development and applications. *J. Aerosol Sci.*, **32**, 427-442.
- Butcher, S. S., and R. J. Charlson, 1972: *An introduction to air chemistry*. Academic Press, 240 pp.
- Carson, D. J., 1973: The development of a dry inversion-capped convectively unstable boundary layer. *Q. J. R. Meteorol. Soc.*, **99**, 450-467.
- Cheng, Y. S., and H. C. Yeh, 1980: Theory of a screen-type diffusion battery. *J. Aerosol Sci.*, **11**, 313-320.
- Chýlek, P., V. Srivastava, R. G. Pinnick, and R. T. Wang, 1988: Scattering of electromagnetic waves by composite spherical particles: experiment and effective medium approximations. *Appl. Opt.*, **27**, 2396.
- Clarke, A., C. McNaughton, V. Kapustin, Y. Shinozuka, S. Howell, J. Dibb, J. Zhou, B. Anderson, V. Brekhovskikh, H. Turner, and M. Pinkerton, 2007: Biomass burning and pollution aerosol over North America: Organic components and their influence on spectral optical properties and humidification response. *J. Geophys. Res.*, **112**, D12S18.
- Clarke, A. D., 1991: A thermo-optic technique for in situ analysis of size-resolved aerosol physicochemistry. *Atmos. Environ., Part A*, **25**, 635-644.
- Clarke, A. D., Y. Shinozuka, V. N. Kapustin, S. Howell, B. Huebert, S. Doherty, T. Anderson, D. Covert, J. Anderson, X. Hua, K. G. Moore, C. McNaughton, G. Carmichael, and R. Weber, 2004: Size distributions and mixtures of dust and black carbon aerosol in Asian outflow: Physicochemistry and optical properties. *J. Geophys. Res.*, **109**, D15S09.
- Colarco, P. R., O. B. Toon, J. S. Reid, J. M. Livingston, G. Russell, J. Redemann, B. Schmid, H. Maring, D. Savoie, E. J. Welton, J. R. Campbell, B. Holben, and R. Levy, 2003: Saharan dust transport to the Caribbean during PRIDE: 2. Transport, vertical profiles, and deposition in simulations of in situ and remote sensing observations. *J. Geophys. Res.*, **108**, 8590.
- Cooper, O. R., J. L. Moody, D. D. Parrish, M. Trainer, T. B. Ryerson, J. S. Holloway, G. Hübler, F. C. Fehsenfeld, S. J. Oltmans, and M. J. Evans, 2001: Trace gas signatures of the airstreams within North Atlantic cyclones: Case studies from the North Atlantic Regional Experiment (NARE'97) aircraft intensive. *J. Geophys. Res.*, **106**, 5437-5456.
- Crutzen, P. J., L. E. Heidt, J. P. Krasnec, W. H. Pollock, and W. Seiler, 1979: Biomass burning as a source of atmospheric gases CO, H<sub>2</sub>, N<sub>2</sub>O, NO, CH<sub>3</sub>Cl and COS. *Nature*, **282**, 253-256.
- d'Almeida, G. A., and L. Schütz, 1983: Number, Mass and Volume Distributions of Mineral Aerosol and Soils of the Sahara. *Journal of Applied Meteorology*, **22**, 233-243.
- d'Almeida, G. A., P. Koepke, and E. P. Shettle, 1991: *Atmospheric Aerosols: Global Climatology and Radiative Characteristics*. A. Deepak Publishing, 561 pp.

- Damoah, R., N. Spichtinger, C. Forster, P. James, I. Mattis, U. Wandinger, S. Beirle, T. Wagner, and A. Stohl, 2004: Around the world in 17 days - hemispheric-scale transport of forest fire smoke from Russia in May 2003. *Atmos. Chem. Phys.*, **4**, 1311-1321.
- de Reus, M., F. Dentener, A. Thomas, S. Borrmann, J. Stroem, and J. Lelieveld, 2000: Airborne observations of dust aerosol over the North Atlantic Ocean during ACE 2: Indications for heterogeneous ozone destruction. *J. Geophys. Res.*, **105**, 15263-15275.
- Dentener, F., S. Kinne, T. Bond, O. Boucher, J. Cofala, S. Generoso, P. Ginoux, S. Gong, J. J. Hoelzemann, A. Ito, L. Marelli, J. E. Penner, J.-P. Putaud, C. Textor, M. Schulz, G. R. van der Werf, and J. Wilson, 2006: Emissions of primary aerosol and precursor gases in the years 2000 and 1750 prescribed data-sets for AeroCom. *Atmos. Chem. Phys.*, **6**, 4321-4344.
- Dubovik, O., B. Holben, T. F. Eck, A. Smirnov, Y. J. Kaufman, M. D. King, Tanr, eacute, Didier, and I. Slutsker, 2002: Variability of Absorption and Optical Properties of Key Aerosol Types Observed in Worldwide Locations. *J. Atmos. Sci.*, **59**, 590-608.
- Dusek, U., G. P. Frank, L. Hildebrandt, J. Curtius, J. Schneider, S. Walter, D. Chand, F. Drewnick, S. Hings, D. Jung, S. Borrmann, and M. O. Andreae, 2006: Size Matters More Than Chemistry for Cloud-Nucleating Ability of Aerosol Particles. *Science*, **312**, 1375-1378.
- Engler, C., D. Rose, B. Wehner, A. Wiedensohler, E. Brüggemann, T. Gnauk, G. Spindler, T. Tuch, and W. Birmili, 2006: Size distributions of non-volatile particle residuals ( $D_p < 800$  nm) at a rural site in Germany and relation to air mass origin. *Atmos. Chem. Phys.*, **6**, 1021-1031.
- Esselborn, M., 2007: Measurement of atmospheric extinction by means of a High Spectral Resolution Lidar. Ph.D. thesis, Physik, Ludwig-Maximilians-Universität, in preparation pp.
- Feldpausch, P., M. Fiebig, L. Fritzsche, and A. Petzold, 2006: Measurement of ultrafine aerosol size distributions by a combination of diffusion screen separators and condensation particle counters. *J. Aerosol Sci.*, **37**, 577-597.
- Fiebig, M., 2001: Das troposphärische Aerosol in mittleren Breiten - Mikrophysik, Optik und Klimaantrieb am Beispiel der Feldstudie LACE 98. Ph.D. thesis, Physik, Ludwig-Maximilians-Universität, 244 pp.
- Fiebig, M., A. Stohl, M. Wendisch, S. Eckhardt, and A. Petzold, 2003: Dependence of solar radiative forcing of forest fire aerosol on ageing and state of mixture. *Atmos. Chem. Phys.*, **3**, 881-891.
- Fiebig, M., C. Stein, F. Schroder, P. Feldpausch, and A. Petzold, 2005: Inversion of data containing information on the aerosol particle size distribution using multiple instruments. *J. Aerosol Sci.*, **36**, 1353-1372.
- Fiebig, M., A. Petzold, U. Wandinger, M. Wendisch, C. Kiemle, A. Stifter, M. Ebert, T. Rother, and U. Leiterer, 2002: Optical closure for an aerosol column: Method, accuracy, and inferable properties applied to a biomass-burning aerosol and its radiative forcing. *J. Geophys. Res.*, **107**, 8130.
- Flannigan, M., K. Logan, B. Amiro, W. Skinner, and B. Stocks, 2005: Future Area Burned in Canada. *Climatic Change*, **72**, 1-16.
- Flannigan, M. D., B. J. Stocks, and B. M. Wotton, 2000: Climate change and forest fires. *The Science of The Total Environment*, **262**, 221-229.
- Forster, C., U. Wandinger, G. Wotawa, P. James, I. Mattis, D. Althausen, P. Simmonds, S. O'Doherty, S. G. Jennings, C. Kleefeld, J. Schneider, T. Trickl, S. Kreipl, H. Jäger, and A. Stohl, 2001: Transport of boreal forest fire emissions from Canada to Europe. *J. Geophys. Res.*, **106**, 22887-22906.
- Fritzsche, L., 2002: Untersuchung der thermischen Stabilität von künstlich generierten Aerosolen mit einer Kombination aus einem Differential Mobility Analyser und einem thermischen Partikeldiskriminator. Diploma thesis, Mathematik/Physik/Informatik, Fachhochschule Mittweida, 87 pp.
- Fromm, M., A. Tupper, D. Rosenfeld, R. Servranckx, and R. McRae, 2006: Violent pyro-convective storm devastates Australia's capital and pollutes the stratosphere. *Geophys. Res. Lett.*, **33**, 1-5.

- Fromm, M., R. Bevilacqua, R. Servranckx, J. Rosen, J. P. Thayer, J. Herman, and D. Larko, 2005: Pyro-cumulonimbus injection of smoke to the stratosphere: Observations and impact of a super blowup in northwestern Canada on 3-4 August 1998. *J. Geophys. Res.*, **110**, 1-16.
- Fromm, M., J. Alfred, K. Hoppel, J. Hornstein, R. Bevilacqua, E. Shettle, R. Servranckx, Z. Li, and B. Stocks, 2000: Observations of boreal forest fire smoke in the stratosphere by POAM III, SAGE II, and lidar in 1998. *Geophys. Res. Lett.*, **27**, 1407-1410.
- Fu, Q., and K. N. Liou, 1992: On the Correlated k-Distribution Method for Radiative Transfer in Nonhomogeneous Atmospheres. *J. Atmos. Sci.*, **49**, 2139-2156.
- Fuelberg, H. E., M. J. Porter, C. Kiley, J. J. Halland, and D. Morse, 2007: Meteorological conditions and anomalies during the Intercontinental Chemical Transport Experiment-North America. *J. Geophys. Res.*, **112**, D12S06.
- Gerstengarbe, F.-W., and P. C. Werner, 2005: *Katalog der Großwetterlagen Europas (1881-2004) nach Paul Hess und Helmut Brezowsky, 6. verbesserte und ergänzte Auflage*. Vol. 100, 148 pp.
- Gillett, N. P., A. J. Weaver, F. W. Zwiers, and M. D. Flannigan, 2004: Detecting the effect of climate change on Canadian forest fires. *Geophys. Res. Lett.*, **31**, 1-4.
- Grassl, H., 1975: Albedo reduction and radiative heating of clouds by absorbing aerosol particles *Beitr. Phys. der Atmos.*, **48**, 199-210.
- Grousset, F. E., P. Ginoux, A. Bory, and P. E. Biscaye, 2003: Case study of a Chinese dust plume reaching the French Alps. *Geophys. Res. Lett.*, **30**, 10-11.
- Hansen, J., M. Sato, and R. Ruedy, 1997: Radiative forcing and climate response. *J. Geophys. Res.*, **102**, 6831-6864.
- Hansen, J., M. Sato, L. Nazarenko, R. Ruedy, A. Lacis, D. Koch, I. Tegen, T. Hall, D. Shindell, B. Santer, P. Stone, T. Novakov, L. Thomason, R. Wang, Y. Wang, D. Jacob, S. Hollandsworth, L. Bishop, J. Logan, A. Thompson, R. Stolarski, J. Lean, R. Willson, S. Levitus, J. Antonov, N. Rayner, D. Parker, and J. Christy, 2002: Climate forcings in Goddard institute for space studies SI2000 simulations. *J. Geophys. Res.*, **107**, 4347.
- Hansen, J., M. Sato, R. Ruedy, L. Nazarenko, A. Lacis, G. A. Schmidt, G. Russell, I. Aleinov, M. Bauer, S. Bauer, N. Bell, B. Cairns, V. Canuto, M. Chandler, Y. Cheng, A. Del Genio, G. Faluvegi, E. Fleming, A. Friend, T. Hall, C. Jackman, M. Kelley, N. Kiang, D. Koch, J. Lean, J. Lerner, K. Lo, S. Menon, R. Miller, P. Minnis, T. Novakov, V. Oinas, J. Perlwitz, J. Perlwitz, D. Rind, A. Romanou, D. Shindell, P. Stone, S. Sun, N. Tausnev, D. Thresher, B. Wielicki, T. Wong, M. Yao, and S. Zhang, 2005: Efficacy of climate forcings. *J. Geophys. Res.*, **110**, 1-45.
- Hansen, J. E., 1971: Multiple scattering of polarized light in planetary atmospheres. Part II. Sunlight reflected by terrestrial water clouds. *J. Atmos. Sci.*, **28**, 1400-1426.
- Hatch, T., and S. P. Choate, 1929: Statistical description of the size properties of non uniform particulate substances. *Journal of the Franklin Institute*, **207**, 369-387.
- Hauf, T., and T. L. Clark, 1989: Three-dimensional numerical experiments on convectively forced internal gravity waves. *Q. J. R. Meteorol. Soc.*, **115**, 309-333.
- Haywood, J., and O. Boucher, 2000: Estimates of the direct and indirect radiative forcing due to tropospheric aerosols: A review. *Rev. Geophys.*, **38**, 513-543.
- Haywood, J., P. Francis, S. Osborne, M. Glew, N. Loeb, E. Highwood, D. Tanré, G. Myhre, P. Formenti, and E. Hirst, 2003a: Radiative properties and direct radiative effect of Saharan dust measured by the C-130 aircraft during SHADE: 1. Solar spectrum. *J. Geophys. Res.*, **108**, 8577.
- Haywood, J. M., S. R. Osborne, P. N. Francis, A. Keil, P. Formenti, M. O. Andreae, and P. H. Kaye, 2003b: The mean physical and optical properties of regional haze dominated by biomass burning aerosol measured from the C-130 aircraft during SAFARI 2000. *J. Geophys. Res.*, **108**, 8473.
- Haywood, J. M., R. P. Allan, I. Culverwell, T. Slingo, S. Milton, J. Edwards, and N. Clerbaux, 2005: Can desert dust explain the outgoing longwave radiation anomaly over the Sahara during July 2003? *J. Geophys. Res.*, **110**, 1-14.

- Heinold, B., J. Helmert, O. Hellmuth, R. Wolke, A. Ansmann, B. Marticorena, B. Laurent, and I. Tegen, 2007: Regional modeling of Saharan dust events using LM-MUSCAT: model description and case studies. *J. Geophys. Res.*, **112**, 1-21.
- Helmert, J., B. Heinold, I. Tegen, O. Hellmuth, and M. Wendisch, 2007: On the direct and semidirect effect of Saharan dust over Europe: a modelling study. *J. Geophys. Res.*, **112**, D13208.
- Herring, J. A., and P. V. Hobbs, 1994: Radiatively driven dynamics of the plume from 1991 Kuwait oil fires. *J. Geophys. Res.*, **99**, 18809-18826.
- Hess, M., P. Koepke, and I. Schult, 1998a: Optical Properties of Aerosols and Clouds: The Software Package OPAC. *Bulletin of the American Meteorological Society*, **79**, 831-844.
- , 1998b: Optical Properties of Aerosols and Clouds: The Software Package OPAC. *Bull. Am. Met. Soc.*, **79**, 831-844.
- Hinds, W. C., 1999: *Aerosol Technology: Properties, Behaviour and Measurement of Airborne Particles*. John Wiley & Sons, Inc., 483 pp.
- Horvath, H., 1996: Spectral extinction coefficients of rural aerosol in southern Italy—a case study of cause and effect of variability of atmospheric aerosol. *J. Aerosol Sci.*, **27**, 437-453.
- Huntrieser, H., and H. Schlager, 2004: Air Pollution Export from and Import to Europe: Experimental Evidence. *The Handbook of Environmental Chemistry*, A. Stohl, Ed., Springer-Verlag, Heidelberg, 69-98.
- Huntrieser, H., J. Heland, H. Schlager, C. Forster, A. Stohl, H. Aufmhoff, F. Arnold, H. E. Scheel, M. Campana, S. Gilge, R. Eixmann, and O. Cooper, 2005: Intercontinental Air Pollution Transport from North America to Europe: Experimental Evidence from Airborne Measurements and Surface Observations. *J. Geophys. Res.*, **110**, D01305.
- Husar, R. B., D. M. Tratt, B. A. Schichtel, S. R. Falke, F. Li, D. Jaffe, S. Gasso, T. Gill, N. S. Laulainen, F. Lu, M. C. Reheis, Y. Chun, D. Westphal, B. N. Holben, C. Gueymard, I. McKendry, N. Kuring, G. C. Feldman, C. McClain, R. J. Frouin, J. Merrill, D. DuBois, F. Vignola, T. Murayama, S. Nickovic, W. E. Wilson, K. Sassen, N. Sugimoto, and W. C. Malm, 2001: Asian dust events of April 1998. *J. Geophys. Res.*, **106**, 18317-18330.
- IPCC, 2001: *Climate Change 2001: The Scientific Basis*. Cambridge University Press, 944 pp.
- , 2007: *Climate Change 2007: The Scientific Basis*. Cambridge University Press, 940 pp.
- Jost, H. J., K. Drdla, A. Stohl, L. Pfister, M. Loewenstein, J. P. Lopez, P. K. Hudson, D. M. Murphy, D. J. Cziczo, M. Fromm, T. P. Bui, J. Dean-Day, C. Gerbig, M. J. Mahoney, E. C. Richard, N. Spichtinger, J. V. Pittman, E. M. Weinstock, C. W. Wilson, and I. Xueref, 2004: In-situ observations of mid-latitude forest fire plumes deep in the stratosphere. *Geophys. Res. Lett.*, **31**, 1-5.
- Kahnert, M., T. Nousiainen, and P. Räisänen, 2007: Mie simulations as an error source in mineral aerosol radiative forcing calculations. *Q. J. R. Meteorol. Soc.*, **133**, 299-307.
- Kasischke, E. S., and J. E. Penner, 2004: Improving global estimates of atmospheric emissions from biomass burning. *J. Geophys. Res.*, **109**, 1-9.
- Kinne, S., M. Schulz, C. Textor, S. Guibert, Y. Balkanski, S. E. Bauer, T. Berntsen, T. F. Berglen, O. Boucher, M. Chin, W. Collins, F. Dentener, T. Diehl, R. Easter, J. Feichter, D. Fillmore, S. Ghan, P. Ginoux, S. Gong, A. Grini, J. Hendricks, M. Herzog, L. Horowitz, I. Isaksen, T. Iversen, A. Kirkeva?g, S. Kloster, D. Koch, J. E. Kristjansson, M. Krol, A. Lauer, J. F. Lamarque, G. Lesins, X. Liu, U. Lohmann, V. Montanaro, G. Myhre, J. E. Penner, G. Pitari, S. Reddy, O. Seland, P. Stier, T. Takemura, and X. Tie, 2006: An AeroCom initial assessment - Optical properties in aerosol component modules of global models. *Atmos. Chem. Phys.*, **6**, 1815-1834.
- Knippertz, P., D. Deutscher, K. Kandler, T. Müller, O. Schulz, and L. Schütz, 2007: Dust mobilization due to density currents in the Atlas region: Observations from the SAMUM 2006 field campaign. *J. Geophys. Res.*, **112**, D21109.
- Knutson, E. O., 1999: History of Diffusion Batteries in Aerosol Measurements. *Aerosol Sci. Technol.*, **31**, 83-128.

- Knutson, E. O., and K. T. Whitby, 1975a: Accurate measurement of aerosol electric mobility moments. *J. Aerosol Sci.*, **6**, 453-460.
- , 1975b: Aerosol classification by electric mobility: apparatus, theory, and applications. *J. Aerosol Sci.*, **6**, 443-451.
- Koepke, P., M. Hess, I. Schult, and E. P. Shettle, 1997: Global Aerosol Data Set. MPI-Rep., 44 pp.
- Léon, J. F., P. Chazette, F. Dulac, J. Pelon, C. Flamant, M. Bonazzola, G. Foret, E. Alfaro, H. Cachier, G. Cautenet, E. Hamonou, A. Gaudichet, L. Gomes, J. L. Rajot, F. Lavenu, S. R. Inamdar, P. R. Sarode, and J. S. Kadadevarmath, 2001: Large-scale advection of continental aerosols during INDOEX. *J. Geophys. Res.*, **106**, 28427-28440.
- Levine, J. S., 1991: *Global Biomass Burning: Atmospheric, Climatic, and Biospheric Implications*. MIT Press ed., 599 pp.
- Lilly, D. K., 1968: Models of Cloud-Topped Mixed Layers under a Strong Inversion. *Q. J. R. Meteorol. Soc.*, **94**, 292-309.
- , 1988: Cirrus outflow dynamics. *J. Atmos. Sci., Boston. Vol. 45*, 1594-1605.
- Mahowald, N. M., A. R. Baker, G. Bergametti, N. Brooks, R. A. Duce, T. D. Jickells, N. Kubilay, J. M. Prospero, and I. Tegen, 2005: Atmospheric global dust cycle and iron inputs to the ocean. *Global Biogeochem. Cycles*, **19**, 1-15.
- Maring, H., D. L. Savoie, M. A. Izaguirre, L. Custals, and J. S. Reid, 2003a: Mineral dust aerosol size distribution change during atmospheric transport. *J. Geophys. Res.*, **108**, 8592.
- , 2003b: Vertical distributions of dust and sea-salt aerosols over Puerto Rico during PRIDE measured from a light aircraft. *J. Geophys. Res.*, **108**, 8587.
- Martins, J. V., P. Artaxo, P. V. Hobbs, C. Liou, H. Cachier, Y. Kaufman, and A. Plana-Fattori, 1996: *Particle size distributions, elemental compositions, carbon measurements, and optical properties of smoke from biomass burning in the Pacific Northwest of the United States*. MIT press, 717-732 pp.
- Mayer, B., and A. Kylling, 2005: Technical note: The libRadtran software package for radiative transfer calculations - description and examples of use *Atmos. Chem. Phys.*, **5**, 1855-1877.
- Mayer, B., G. Seckmeyer, and A. Kylling, 1997: Systematic long-term comparison of spectral UV measurements and UVSPEC modeling results. *J. Geophys. Res.*, **102**, 8755-8767.
- McFarquhar, G. M., and A. J. Heymsfield, 1998: The Definition and Significance of an Effective Radius for Ice Clouds. *J. Atmos. Sci.*, **55**, 2039-2052.
- Miller, R. L., I. Tegen, and J. Perlwitz, 2004: Surface radiative forcing by soil dust aerosols and the hydrologic cycle. *J. Geophys. Res.*, **109**, 1-24.
- Mishchenko, M. I., 1990: Extinction of light by randomly-oriented non-spherical grains. *Astrophys. Space Sci.*, **164**, 1-13.
- Mishchenko, M. I., L. D. Travis, R. A. Kahn, and R. A. West, 1997: Modeling phase functions for dustlike tropospheric aerosols using a shape mixture of randomly oriented polydisperse spheroids. *J. Geophys. Res.*, **102**, 16831-16848.
- Mishchenko, M. I., B. Cairns, J. E. Hansen, L. D. Travis, R. Burg, Y. J. Kaufman, J. Vanderlei Martins, and E. P. Shettle, 2004: Monitoring of aerosol forcing of climate from space: analysis of measurement requirements. *J. Quant. Spectrosc. Radiat. Transfer*, **88**, 149-161.
- Mollicone, D., H. D. Eva, and F. Achard, 2006: Ecology: Human role in Russian wild fires. *Nature*, **440**, 436-437.
- Moorthy, K. K., S. S. Babu, S. K. Satheesh, J. Srinivasan, and C. B. S. Dutt, 2007: Dust absorption over the "Great Indian Desert" inferred using ground-based and satellite remote sensing. *J. Geophys. Res.*, **112**, D09206.
- Moulin, C., and I. Chiapello, 2006: Impact of human-induced desertification on the intensification of Sahel dust emission and export over the last decades. *Geophys. Res. Lett.*, **33**, 1-5.

- Müller, D., 2007: Characterization of Free-Tropospheric Particles with Multiwavelength Raman Lidar: Geometrical, Optical, and Microphysical Properties of Aerosol Pollution from Europe, North Africa, South Asia, and North America, Physics, University of Leipzig, 208 pp.
- Müller, D., I. Mattis, A. Ansmann, U. Wandinger, C. Ritter, and D. Kaiser, 2007: Multiwavelength Raman lidar observations of particle growth during long-range transport of forest-fire smoke in the free troposphere. *Geophys. Res. Lett.*, **34**, L05803.
- Müller, D., I. Mattis, U. Wandinger, A. Ansmann, D. Althausen, O. Dubovik, S. Eckhardt, and A. Stohl, 2003: Saharan dust over a central European EARLINET-AERONET site: Combined observations with Raman lidar and Sun photometer. *J. Geophys. Res.*, **108**, 4345.
- Olivier, J. G. J., and J. J. M. Berdowski, 2001: *Global emission sources and sinks*. A.A. Balkema Publishers/Swets & Zeitlinger Publishers, 33-78 pp.
- Otto, S., M. de Reus, T. Trautmann, A. Thomase, M. Wendisch, and S. Borrmann, 2007: Atmospheric radiative effects of an in-situ measured Saharan dust plume and the role of large particles. *Atmos. Chem. Phys. Discuss.*, **7**, 7767-7817.
- Ouimette, J. R., and R. C. Flagan, 1982: The extinction coefficient of multicomponent aerosols. *Atmosph. Env.*, **16**, 2405-2419.
- Owen, R. C., O. R. Cooper, A. Stohl, and R. E. Honrath, 2006: An analysis of the mechanisms of North American pollutant transport to the central North Atlantic lower free troposphere. *J. Geophys. Res.*, **111**, 1-14.
- Pace, G., D. Meloni, and A. Di Sarra, 2005: Forest fire aerosol over the Mediterranean basin during summer 2003. *J. Geophys. Res.*, **110**, D21202.
- Pérez, C., S. Nickovic, G. Pejanovic, J. M. Baldasano, and E. Özsoy, 2006: Interactive dust-radiation modeling: A step to improve weather forecasts. *J. Geophys. Res.*, **111**, D16206.
- Perlwitz, J., I. Tegen, and R. L. Miller, 2001: Interactive soil dust aerosol model in the GISS GCM: 1. Sensitivity of the soil dust cycle to radiative properties of soil dust aerosols. *J. Geophys. Res.*, **106**, 18167-18192.
- Petzold, A., M. Fiebig, H. Flentje, A. Keil, U. Leiterer, F. Schröder, A. Stifter, M. Wendisch, and P. Wendling, 2002: Vertical variability of aerosol properties observed at a continental site during the Lindenberg Aerosol Characterization Experiment (LACE 98). *J. Geophys. Res.*, **107**, LAC 10-11-LAC 10-18.
- Petzold, A., B. Weinzierl, H. Huntrieser, A. Stohl, E. Real, J. Cozic, M. Fiebig, J. Hendricks, A. Lauer, K. Law, A. Roiger, H. Schlager, and E. Weingartner, 2007: Perturbation of the European free troposphere aerosol by North American forest fire plumes during the ICARTT-ITOP Experiment in summer 2004 *Atmos. Chem. Phys.*, **7**, 5105-5127.
- Pfister, G., P. G. Hess, L. K. Emmons, J. F. Lamarque, C. Wiedinmyer, D. P. Edwards, G. Pétron, J. C. Gille, and G. W. Sachse, 2005: Quantifying CO emissions from the 2004 Alaskan wildfires using MOPITT CO data. *Geophys. Res. Lett.*, **32**, 1-5.
- Pfister, G. G., L. K. Emmons, P. G. Hess, R. Honrath, J.-F. Lamarque, M. Val Martin, R. C. Owen, M. A. Avery, E. V. Browell, J. S. Holloway, P. Nedelec, R. Purvis, T. B. Ryerson, G. W. Sachse, and H. Schlager, 2006: Ozone production from the 2004 North American boreal fires. *J. Geophys. Res.*, **111**, D24S07.
- Pilewskie, P., 2007: Climate change: Aerosols heat up. *Nature*, **448**, 541-542.
- Pincus, R., and M. B. Baker, 1994: Effect of precipitation on the albedo susceptibility of clouds in the marine boundary layer. *Nature*, **372**, 250-252.
- Pinnick, R. G., and H. J. Auvermann, 1979: Response characteristics of Knollenberg light-scattering aerosol counters. *J. Aerosol Sci.*, 55-74.
- Prospero, J. M., P. Ginoux, O. Torres, S. E. Nicholson, and T. E. Gill, 2002: Environmental characterization of global sources of atmospheric soil dust identified with the NIMBUS 7 Total Ozone Mapping Spectrometer (TOMS) absorbing aerosol product. *Rev. Geophys.*, **40**, 1002.
- Radke, L. F., J. H. Lyons, P. V. Hobbs, and R. E. Weiss, 1990: Smokes from the burning of aviation fuel and their self-lofting by solar heating. *J. Geophys. Res.*, **95**, 14071-14076.

- Raes, F., T. Bates, F. McGovern, and M. Van Liedekerke, 2000a: The 2nd Aerosol Characterization Experiment (ACE-2): General overview and main results. *Tellus Ser. B*, **52**, 111-125.
- Raes, F., R. V. Dingenen, E. Vignati, J. Wilson, J.-P. Putaud, J. H. Seinfeld, and P. Adams, 2000b: Formation and cycling of aerosols in the global troposphere. *Atmosph. Env.*, **34**, 4215-4240.
- Ramanathan, V., P. J. Crutzen, J. T. Kiehl, and D. Rosenfeld, 2001: Aerosols, Climate, and the Hydrological Cycle. *Science*, **294**, 2119-2124.
- Ramanathan, V., M. V. Ramana, G. Roberts, D. Kim, C. Corrigan, C. Chung, and D. Winker, 2007: Warming trends in Asia amplified by brown cloud solar absorption. *Nature*, **448**, 575-578.
- Rasp, K., 2007: Spektrale Absorption und Brechungsindex von Saharastaub - Ergebnisse der SAMUM-I Messkampagne. Diploma thesis, Physik, Ludwig-Maximilians-Universität, 133 pp.
- Real, E., K. S. Law, B. Weinzierl, M. Fiebig, A. Petzold, O. Wild, J. Methven, F. Arnold, A. Stohl, H. Huntrieser, A. Roiger, H. Schlager, D. Stewart, M. Avery, G. Sachse, E. Browell, R. Ferrare, and D. Blake, 2007: Processes influencing ozone levels in Alaskan forest fire plumes during long-range transport over the North Atlantic. *J. Geophys. Res.*, **112**, 1-19.
- Reid, J. S., R. Koppmann, T. F. Eck, and D. P. Eleuterio, 2005a: A review of biomass burning emissions part II: intensive physical properties of biomass burning particles. *Atmos. Chem. Phys.*, **5**, 799-825.
- Reid, J. S., P. V. Hobbs, R. J. Ferek, D. R. Blake, J. Martins, M. R. Dunlap, and C. Liousse, 1998: Physical, chemical, and optical properties of regional hazes dominated by smoke in Brazil. *J. Geophys. Res.*, **103**, 32059-32080.
- Reid, J. S., T. F. Eck, S. A. Christopher, R. Koppmann, O. Dubovik, D. P. Eleuterio, B. N. Holben, E. A. Reid, and J. Zhang, 2005b: A review of biomass burning emissions part III: intensive optical properties of biomass burning particles. *Atmos. Chem. Phys.*, **5**, 827-849.
- Reid, J. S., H. H. Jonsson, H. B. Maring, A. Smirnov, D. L. Savoie, S. S. Cliff, E. A. Reid, J. M. Livingston, M. M. Meier, O. Dubovik, and S. C. Tsay, 2003a: Comparison of size and morphological measurements of coarse mode dust particles from Africa. *J. Geophys. Res.*, **108**, 8593.
- Reid, J. S., J. E. Kinney, D. L. Westphal, B. Holben, E. J. Welton, S. Tsay, D. P. Eleuterio, J. R. Campbell, S. A. Christopher, P. R. Colarco, H. H. Jonsson, J. M. Livingston, H. B. Maring, M. L. Meier, P. Pilewskie, J. M. Prospero, E. A. Reid, L. A. Remer, G. Russell, D. Savoie, A. Smirnov, and D. Tanrè, 2003b: Analysis of measurements of Saharan dust by airborne and ground-based remote sensing methods during the Puerto Rico Dust Experiment (PRIDE). *J. Geophys. Res.*, **108**, 8586.
- Reischl, G. P., 1991: The relationship of input and output aerosol characteristics for an ideal differential mobility analyser particle standard. *J. Aerosol Sci.*, **22**, 297-312.
- Robock, A., 1988: Enhancement of surface cooling due to forest fire smoke. *Science*, **242**, 911-913.
- , 1991: Surface cooling due to forest fire smoke. *J. Geophys. Res.*, **96**, 20869 - 20878.
- Rosenfeld, D., 2006: ATMOSPHERE: Aerosols, Clouds, and Climate. *Science*, **312**, 1323-1324.
- Rosenfeld, D., Y. Rudich, and R. Lahav, 2001: Desert dust suppressing precipitation: A possible desertification feedback loop. *PNAS*, **98**, 5975-5980.
- Roth, C., U. Berlauer, and J. Heyder, 1989: Particle size analysis of log-normally distributed ultrafine particles using a differential mobility analyser. *J. Aerosol Sci.*, **20**, 547-556.
- Satheesh, S. K., and V. Ramanathan, 2000: Large differences in tropical aerosol forcing at the top of the atmosphere and Earth's surface. *Nature*, **405**, 60-63.
- Satheesh, S. K., and K. K. Moorthy, 2005: Radiative effects of natural aerosols: A review. *Atmosph. Env.*, **39**, 2089-2110.
- Sato, M., J. Hansen, D. Koch, A. Lacis, R. Ruedy, O. Dubovik, B. Holben, M. Chin, and T. Novakov, 2003: Global atmospheric black carbon inferred from AERONET. *Proceedings of the National Academy of Sciences of the United States of America*, **100**, 6319-6324.
- Schütz, L., and R. Jaenicke, 1974: Particle Number and Mass Distributions above  $10^{-4}$  cm Radius in Sand and Aerosol of the Sahara Desert. *J. Appl. Met.*, **13**, 863-870.

- , 1978: Comprehensive Study of Physical and Chemical Properties of the Surface Aerosols in the Cape Verde Islands Region. *J. Geophys. Res.*, **83**, 3585-3599.
- Seinfeld, J. H., and S. N. Pandis, 1998: *Atmospheric Chemistry and Physics: From Air Pollution to Climate Change*. John Wiley & Sons, Inc, 1326 pp.
- Sheridan, P. J., W. P. Arnott, J. A. Ogren, E. Andrews, D. B. Atkinson, D. S. Covert, Moosm, uuml, H. Iler, A. Petzold, B. Schmid, A. W. Strawa, R. Varma, and A. Virkkula, 2005: The Reno Aerosol Optics Study: An Evaluation of Aerosol Absorption Measurement Methods. *Aerosol Sci. Technol.*, **39**, 1-16.
- Shettle, E. P., and R. W. Fenn, 1979: *Models for the Aerosols of the Lower Atmosphere and the Effects of Humidity Variations on their Optical Properties*. Vol. 79 0214, Air Force Cambridge Research Laboratory, 100 pp.
- Shine, K. P., 2000: Radiative Forcing of Climate Change. *Space Science Reviews*, **94**, 363-373.
- Sokolik, I. N., and O. B. Toon, 1996: Direct radiative forcing by anthropogenic airborne mineral aerosols. *Nature*, **381**, 681-683.
- , 1999: Incorporation of mineralogical composition into models of the radiative properties of mineral aerosol from UV to IR wavelengths. *J. Geophys. Res.*, **104**, 9423-9444.
- Sokolik, I. N., O. B. Toon, and R. W. Bergstrom, 1998: Modeling the radiative characteristics of airborne mineral aerosols at infrared wavelengths. *J. Geophys. Res.*, **103**, 8813-8826.
- Sokolik, I. N., D. M. Winker, G. Bergametti, D. A. Gillette, G. Carmichael, Y. J. Kaufman, L. Gomes, L. Schuetz, and J. E. Penner, 2001: Introduction to special section: Outstanding problems in quantifying the radiative impacts of mineral dust. *J. Geophys. Res.*, **106**, 18015-18028.
- Stein, C., 2000: Aufbau und Kalibrierung eines flugzeuggetragenen Instruments zur größen aufgelösten Messung der ultrafeinen Aerosolfraktion, Umwelttechnik, Fachhochschule Mittweida, 85 pp.
- Stein, C., F. Schröder, and A. Petzold, 2001: The Condensation Particle Size Analyzer: A New Instrument for the Measurement of Ultrafine Aerosol Size Distributions. *J. Aerosol Sci.*, 381-382.
- Stier, P., J. H. Seinfeld, S. Kinne, and O. Boucher, 2007: Aerosol absorption and radiative forcing. *Atmos. Chem. Phys. Discussions*, **7**, 7171-7233.
- Stier, P., J. Feichter, E. Roeckner, S. Kloster, and M. Esch, 2006: The evolution of the global aerosol system in a transient climate simulation from 1860 to 2100. *Atmos. Chem. Phys.*, **6**, 3059-3076.
- Stocks, B. J., J. A. Mason, J. B. Todd, E. M. Bosch, B. M. Wotton, B. D. Amiro, M. D. Flannigan, K. G. Hirsch, K. A. Logan, D. L. Martell, and W. R. Skinner, 2002: Large forest fires in Canada, 1959-1997. *J. Geophys. Res.*, **108**, 8149.
- Stohl, A., M. Hittenberger, and G. Wotawa, 1998: Validation of the lagrangian particle dispersion model FLEXPART against large-scale tracer experiment data. *Atmosph. Env.*, **32**, 4245-4264.
- Stohl, A., C. Forster, A. Frank, P. Seibert, and G. Wotawa, 2005: Technical note: The Lagrangian particle dispersion model FLEXPART version 6.2 *Atmos. Chem. Phys.*, **5**, 2461-2474.
- Stohl, A., C. Forster, H. Huntrieser, H. Mannstein, W. W. McMillan, A. Petzold, H. Schlager, and B. Weinzierl, 2007: Aircraft measurements over Europe of an air pollution plume from Southeast Asia – aerosol and chemical characterization. *Atmos. Chem. Phys.*, **7**, 913-937.
- Stohl, A., C. Forster, S. Eckhardt, N. Spichtinger, H. Huntrieser, J. Heland, H. Schlager, S. Wilhelm, F. Arnold, and O. Cooper, 2003: A backward modeling study of intercontinental pollution transport using aircraft measurements. *J. Geophys. Res.*, **108**, 4370.
- Stohl, A., E. Andrews, J. F. Burkhart, C. Forster, A. Herber, S. W. Hoch, D. Kowal, C. Lunder, T. Mefford, J. A. Ogren, S. Sharma, N. Spichtinger, K. Stebel, R. Stone, J. Stroem, K. Torseth, C. Wehrli, and K. E. Yttri, 2006: Pan-Arctic enhancements of light absorbing aerosol concentrations due to North American boreal forest fires during summer 2004. *J. Geophys. Res.*, **111**, 1-20.
- Strapp, J. W., W. R. Leaitch, and P. S. K. Liu, 1992: Hydrated and Dried Aerosol-Size-Distribution Measurements from the Particle Measuring Systems FSSP-300 Probe and the Deiced PCASP-100X Probe. *Journal of Atmospheric and Oceanic Technology*, **9**, 548-555.

- Tanré, D., J. Haywood, J. Pelon, J. F. Léon, B. Chatenet, P. Formenti, P. Francis, P. Goloub, E. Highwood, and G. Myhre, 2003: Measurement and modeling of the Saharan dust radiative impact: Overview of the Saharan Dust Experiment (SHADE). *J. Geophys. Res.*, **108**, 8574.
- Tegen, I., and A. A. Lacis, 1996: Modeling of particle size distribution and its influence on the radiative properties of mineral dust aerosol. *J. Geophys. Res.*, **101**, 19237-19244.
- Tegen, I., M. Werner, S. P. Harrison, and K. E. Kohfeld, 2004: Relative importance of climate and land use in determining present and future global soil dust emission. *Geophys. Res. Lett.*, **31**, L05105.
- Tegen, I., B. Heinold, M. Todd, J. Helmert, R. Washington, and O. Dubovik, 2006: Modelling soil dust aerosol in the Bodélé depression during the BoDEx campaign *Atmos. Chem. Phys.*, **6**, 4345-4359.
- Toon, O. B., and T. P. Ackerman, 1981: Algorithms for the calculation of scattering by stratified spheres. *Appl. Opt.*, **20**, 3657-3660.
- Treffeisen, R., P. Tunved, J. Strom, A. Herber, J. Bareiss, A. Helbig, R. S. Stone, W. Hoyningen-Huene, R. Krejci, A. Stohl, and R. Neuber, 2007: Arctic smoke - aerosol characteristics during a record smoke event in the European Arctic and its radiative impact. *Atmos. Chem. Phys.*, **7**, 3035-3053.
- Trentmann, J., G. Luderer, T. Winterrath, M. Fromm, R. Servranckx, C. Textor, M. Herzog, H. F. Graf, and M. O. Andreae, 2006: Modeling of biomass smoke injection into the lower stratosphere by a large forest fire (Part I): reference simulation. *Atmos. Chem. Phys.*, **6**, 5247-5260.
- Turner, J. S., 1973: *Buoyancy Effects in Fluids*. Cambridge University Press, 368 pp.
- Turquety, S., J. A. Logan, D. J. Jacob, R. C. Hudman, F. Y. Leung, C. L. Heald, R. M. Yantosca, S. Wu, L. K. Emmons, D. P. Edwards, and G. Sachse, 2007: Inventory of boreal fire emissions for North America in 2004: Importance of peat burning and pyroconvective injection. *J. Geophys. Res.*, **112**, 1-13.
- Twomey, S., 1974: Pollution and the planetary albedo. *Atmosph. Env.*, **8**, 1251-1256.
- Veihelmann, B., M. Konert, and W. J. van der Zande, 2006: Size distribution of mineral aerosol: using light-scattering models in laser particle sizing. *Appl. Opt.*, **45**, 6022-6029.
- Virkkula, A., N. C. Ahlquist, D. S. Covert, W. P. Arnott, P. J. Sheridan, P. K. Quinn, and D. J. Coffman, 2005: Modification, Calibration and a Field Test of an Instrument for Measuring Light Absorption by Particles. *Aerosol Sci. Technol.*, **39**, 68-83.
- Wandinger, U., D. Müller, C. Böckmann, D. Althausen, V. Matthias, J. Bösenberg, V. Weiß, M. Fiebig, M. Wendisch, A. Stohl, and A. Ansmann, 2002: Optical and microphysical characterization of biomass-burning and industrial-pollution aerosols from multiwavelength lidar and aircraft measurements. *J. Geophys. Res.*, **107**, 8125.
- Wang, J., and S. A. Christopher, 2006: Mesoscale modeling of Central American smoke transport to the United States: 2. Smoke radiative impact on regional surface energy budget and boundary layer evolution. *J. Geophys. Res.*, **111**, 1-17.
- Weingartner, E., H. Saathoff, M. Schnaiter, N. Streit, B. Bitnar, and U. Baltensperger, 2003: Absorption of light by soot particles: determination of the absorption coefficient by means of aethalometers. *J. Aerosol Sci.*, **34**, 1445-1463.
- Wendisch, M., H. Coe, D. Baumgardner, J. L. Brenguier, V. Dreiling, M. Fiebig, P. Formenti, M. Hermann, M. Kraemer, Z. Levin, R. Maser, E. Mathieu, P. Nacass, K. Noone, S. Osborne, J. Schneider, L. Schuetz, A. Schwarzenboeck, F. Stratmann, and J. C. Wilson, 2004: Aircraft Particle Inlets: State-of-the-Art and Future Needs. *Bull. Amer. Meteor. Soc.*, **85**, 89-91.
- Wernli, H., and H. C. Davies, 1997: A lagrangian-based analysis of extratropical cyclones. I: The method and some applications. *Q. J. R. Meteorol. Soc.*, **123**, 467-489.
- Westphal, D. L., and O. B. Toon, 1991: The short-term temperature response to smoke &nbsp;from oil fires. *Geophys. Res. Lett.*, **18**, 1873 - 1876.
- Whitby, K. T., 1978: The physical characteristics of sulphur aerosols. *Atmosph. Env.*, **12**, 135-159.

Yin, Y., and L. Chen, 2007: Long-range transport of mineral aerosols and its absorbing and heating effects on cloud and precipitation: A numerical study. *Atmos. Chem. Phys. Discussions*, **7**, 3203-3228.



---

# Index

---

<b>A</b>		extinction	24
accumulation mode	20	<b>F</b>	
aerosol	17	FLEXPART	59
aerosol inlet	44	FSSP-300	39
aerosol mixing state		<b>G</b>	
coated particles	22	Grimm OPC	42
external mixture	22	<b>H</b>	
internal mixture	22	Hatch-Choate equations	22
volatility analyses	75	<b>I</b>	
aerosol optical depth	2	indirect effects	
aerosol optical model	78	first indirect effect	1
ageing	18	second indirect effect	1
Aitken mode	20	semi-direct effect	1
<b>B</b>		irradiance	23
biomass burning	2	ITOP	56
forest fires	2	forest fire aerosol	83
<b>C</b>		<b>L</b>	
coarse mode	20	Lagrangian field experiments	54
constant-level sequences	55	lofted (aerosol) layer	5
CPC	32	lofted plume	<i>see lofted (aerosol) layer</i>
<b>D</b>		log-normal distribution	21
deposition	31, 59	<b>M</b>	
Diffusion Screen separators (DS)	35	moment	20
direct effect	1	monodisperse aerosol	20
DMA	37	<b>N</b>	
<b>E</b>		nucleation mode	20
effective diameter	22	<b>P</b>	
equivalent diameter	20	PCASP-100X	40
aerodynamic equivalent diameter	20		
Stokes diameter	20		
excess-CO	59		

polydisperse aerosol	20	secondary aerosol	17
potential temperature	87	self-stabilising hypothesis	12
primary aerosol	17	settling velocity	19
PSAP	42	size distribution parameterisation	21
<b>R</b>		standard conditions	<i>see STP conditions</i>
radiative forcing	2	STP conditions	67
radiative-convective mixed layer	121	<b>T</b>	
<b>S</b>		thermal denuder (TD)	44
SAMUM	62	<b>V</b>	
desert dust aerosol	93	volatility analyses	<i>see aerosol mixing state</i>
sealed ageing hypothesis	13		

---

# Lebenslauf

---

## **Persönliche Daten**

Name	Bernadett Barbara Weinzierl
Geburtsdatum	13/12/1979
Geburtsort	Rosenheim

## **Schulbildung/Studium**

11/2004 – 06/2006	Ausbildung zur Privatpilotin, Flugsportgruppe im DLR e.V., Oberpfaffenhofen
Seit 09/2004	Doktorandin am Institut für Physik der Atmosphäre, DLR, Oberpfaffenhofen
03/2000 – 04/2002	Kirchenmusikausbildung, Amt für Kirchenmusik, München
11/1999 – 05/2004	Studium der Meteorologie, Ludwig-Maximilians-Universität, München
09/1990 – 06/1999	Ignaz-Günther-Gymnasium, Rosenheim
09/1986 – 07/1990	Grundschule, Halfing

## **Prüfungen**

14/07/2006	PPL-A Privatpilotenlizenz nach JAR-FCL deutsch, Klassenberechtigung Motorsegler
27/06/2006	PPL-A Privatpilotenlizenz nach JAR-FCL deutsch, Klassenberechtigung Motorflugzeug
27/05/2004	Diplom im Fach Meteorologie (Thema der Diplomarbeit: „Tropical convergence lines“)
10/04/2002	Kirchenmusik-Prüfung nach der Prüfungsordnung C
25/06/1999	Abitur